Analysis of Primary Stripper Foils at the Spallation Neutron Source by an Electron Beam Foil Test Stand

A Dissertation Presented for the

Doctor of Philosophy

Degree

The University of Tennessee, Knoxville

Eric Paul Barrowclough

December 2017

Dedication

To my loving wife, Maggie, and my family, especially my parents, who have given me overwhelming love and support throughout this process.

Abstract

Diamond films are used at the Spallation Neutron Source (SNS) as the primary charge exchange foils (i.e., stripper foils) of the accelerated 1 GeV (Gigaelectron volts) hydride ions. The most common type of film used is a nanocrystalline diamond film, typically 17 mm x 45 mm (millimeter) with an aerial density of 350 $\mu g/cm^2$ (microgram per square centimeter). The diamond film is deposited on a corrugated silicon substrate using plasma-assisted chemical vapor deposition. After the growth of the diamond film, 30 mm of the silicon substrate is etched away, leaving a freestanding diamond foil with a silicon handle that can be inserted into SNS for operation. Each stripper foil is typically used for a month of operation before being replaced by another stripper foil. Since SNS is a user facility, it is very difficult and expensive to experiment with different stripper foil properties that influence the lifetime. Therefore in 2009, a test stand was designed and developed that would research various stripper foil properties and their potential performance in SNS. This test stand consisted of a thirty thousand electron volt (keV) electron gun that would be used to study stripper foil degradation and how this impacts foil lifetime. An electron gun was chosen because of its ability to replicate the thermal load on the stripper foils as well as the sheer size of the electron gun that would allow it to become a tabletop test stand. The electron gun capabilities include: current up to 5 mA (milliampere), 0.300 mm^2 focused spot size, and rastering in the x- and y-directions. A 30 keV and 1.6 mA/mm^2 (milliampere per square millimeter) electron beam deposits the same power density on a diamond foil as a 1.4 MW (megawatt) SNS beam. Rastering of the electron beam exposes a similar area of the foil as SNS beams. Experiments were conducted using the foil test stand to study: foil flutter and lifetime; effects of corrugation patterns, aerial densities, foil crystallite size (micro

vs. nano), and boron doping; temperature distributions and film emissivity; and conversion rate of nanocrystalline diamond into graphite.

Table of Contents

List of Tables

List of Figures

List of Abbreviations and Symbols

${}_1^1H$ or H^+ or p^+	Proton
%	Percentage
°C	Degree Celsius
${}_2^4He^{+2}$ or α	Alpha Particle
A	Ampere
A	Richardson's constant for each cathode material [amperes per square centimeter per square Kelvin ($A/cm^2/K^2$)]
AC/DC	Alternating Current/Direct Current
ACFC	Arizona Carbon Foil Company
ANL	Argonne National Laboratory
AR	Accumulator Ring
BWS	BlueWave Semiconductor
C	Coulombs
CADAD	Controlled AC/DC Discharge Method
cm	Centimeter (1×10^2 cm = 1 m)
CM	Commercially Available Diamond
cm^{-1}	Wavenumber
cm^2	Square Centimeter (1×10^4 cm^2 = 1 m^2)
CO_2	Carbon Dioxide
CVD	Chemical Vapor Deposition
CW	Continuous Wave Beam
DLC	Diamond-Like Carbon
DM	Diamond
e^-	Electron
eV	Electron Volt
FC	Faraday Cup
FDT	Foil Development Team
FLIR	Forward Looking Infrared
Ft	Feet
FTS	Foil Test Stand
g	Gram
g/cm^3	Density
GeV	Gigaelectron Volt (1×10^{-9} GeV = 1 V)
GUI	Graphical User Interface
H^-	Hydrogen Ion
H^0	Hydrogen Atom
H_2	Hydrogen

H_2O	Water
HBC Foil	Hybrid Boron Mixed Carbon Foil
HEBT	High Energy Beam Transport
Hg	Mercury
HOPG	Highly Oriented Pyrolytic Graphite
Hz	Hertz (Measurement of Frequency)
J	Emission Current Density [Amperes per Square Centimeter (A/cm^2)]
J	Joule
J-PARC	Japan Proton Accelerator Research Center
J/kg*K	Unit for Specific Heat
K	Kelvin (-273.15 K = 0 °C)
KEK	High Energy Accelerator Research Organization
keV	Kiloelectron volt (1×10^{-3} keV = 1 eV)
kV	Kilovolt (1×10^{-3} kV = 1 V)
LA	Limiting Aperture
LaB_6 or LAB6	Lanthanum (VI) Hexaboride
LANL	Los Alamos National Laboratory
LBNL	Lawrence Berkeley National Laboratory
LEBT	Low Energy Beam Transport
Linac	Linear Accelerator
m	Meter
m^2	Square Meter
mA	Milliamperes (1×10^{3} mA = 1 A)
mC	Millicoulombs (1×10^{3} mC = 1 C)
mCADAD	Modified Controlled AC/DC Arc Discharge Method
MEBT	Medium Energy Beam Transport
MeV	Megaelectron Volt (1×10^{-6} MeV = 1 eV)
$MeV*cm/g^3$	Unit for Stopping Power
MHz	Megahertz (1×10^{-6} MHz = 1 Hz)
MLF	Material and Life Science Facility
mm	Millimeter
MPECVD	Microwave Plasma Enhanced Chemical Vapor Deposition
MR	Main Ring
ms	Millisecond (1×10^{3} ms = 1 s)
MV	Megavolt (1×10^{-6} MV = 1 V)
MW	Megawatt (1×10^{-6} MW = 1 W)
n	Neutron
Ne^+	Neon Ion
nm	Nanometer (1×10^{9} nm = 1 m)

NTRC	National Transportation Research Center
ORNL	Oak Ridge National Laboratory
P	Pulsed Beam
P/R	Pulsed and Rastered Beam
PFC	Primary Foil Changer
ppp	Protons Per Pulse
RCS	Rapid-Cycle Synchrotron
RF	Radiofrequency
RGA	Residual Gas Analyzer
rms	Root Mean Square
s	Second
SEM	Scanning Electron Microscope
SLAC	Stanford Linear Accelerator Center
SNS	Spallation Neutron Source
SRF	Superconducting Radiofrequency
SRS	Stanford Research Systems
T	Cathode Temperature (K)
torr	Unit of Pressure (1 torr = 133.32 Pascal = 133.32 Newton/m^2)
TRIUMF	TRI University Meson Facility
UTK	University of Tennessee at Knoxville
V	Volt
W	Walt
W/mK	Unit for Thermal Conductivity
W_a	Discharged Amount of Carbon from the Anode
W_c	Discharged Amount of Carbon from the Cathode
α_λ	spectral absorptance – the ratio of the spectral radiant power absorbed by an object to that incident upon it (value between 0.0 and 1.0)
ε_{ave}	Average Emissivity
ε_λ	Spectral Emittance
κ	Boltzmann's constant = 8.6 x 10^{-5} eV/K
λ	Wavelength
μA	Microamperes (1 x 10^6 μA = 1 A)
μg	Microgram (1 x 10^6 μg = 1 g)
μg/cm^2	Aerial Density
μm	Micrometer (1 x 10^6 μm = 1 m)
μm^2	Square Micrometer (1 x 10^{12} μm^2 = 1 m^2)
μs	Microsecond (1 x 10^6 μs = 1 s)

ϱ_λ	spectral reflectance – the ratio of the spectral radiant power reflected by an object to that incident upon it (value between 0.0 and 1.0)
τ_λ	spectral transmittance – the ratio of the spectral radiant power transmitted through an object to that incident upon it (value between 0.0 and 1.0)
ϕ	Work Function of Cathode [electron volt (eV)]

Chapter 1. Introduction

1.1 Introduction into Stripper Foils

Researchers have spent over a century developing methods and techniques to generate and accelerate charged particle beams. These charged particle beams are useful probes of material structure and properties and at the highest energies continue to push the limits of knowledge on the fundamental properties and makeup of matter. Since the development of the first series of particle accelerators, scientists and engineers have continued to research and develop methods to increase the performance and capability of accelerators. In certain accelerators, one or more stripper foils are used to convert the charged particle beam from one charged state to another. These stripper foils vary in both size and composition, with the most common stripper foil composition being carbon. In this body of work, experiments were conducted to better understand the lifetime and the physical and chemical transformations that occur in the primary stripper foil used in the Spallation Neutron Source (SNS) at Oak Ridge National Laboratory (ORNL). There are two stripper foils utilized in SNS: a primary stripper foil and a secondary stripper foil. The primary stripper foil is composed of nanocrystalline diamond. It performs the initial stripping of electrons from the H- accelerated beam, converting it into a proton beam which collides with the mercury target to generate the neutrons used in test stations

that make up the facility. In this dissertation, the results, analysis and interpretation of experiments are presented which probed the performance of the primary stripper foils at various beam powers, how the physical properties of the primary stripper foils influence their lifetime, and what chemical and physical changes the primary stripper foils undergo during SNS operation. These results yield an enhanced understanding of how material properties are linked to stripper foil performance and are expected to guide future development in stripper foil design that should lead to improved performance of the primary stripper foils in SNS.

1.2 History and Theory of Particle Accelerators

1.2.1 First Particle Accelerator

Earnest Rutherford can be considered the grandfather of particle physics and particle accelerators. In 1910, Rutherford performed the famous experiment where he bombarded a gold foil with alpha particles ($^4_2He^{+2}$). In this study, Rutherford found that some of the particles went through the foil and others bounced back [1]. This led to the conclusion that an atom's mass is located at a small, dense center known as the nucleus. Later in the 1920's, Rutherford used 5 million electron volt (MeV) alpha particles generated by the radioactive decay of

uranium atom to disintegrate the nitrogen nuclei.

After Rutherford's discovery, Cockcroft and Walton begin to develop particle accelerators while working at the Cavendish Laboratory in Cambridge, England. In 1930, Cockcroft and Walton calculated the amount of energy an alpha particle needed to penetrate a nucleus. Since it required a large amount of energy, Cockcroft and Watson decided that protons would be better candidates than alpha particles to accelerate since the energy requirement was significantly less [2]. By the end of 1932, Cockcroft and Watson successfully built an accelerator that could accelerate protons (${}_1^1H$ or p^+) to 800 kiloelectron volts (keV) and disintegrate a lithium atom into two α-particles. A Soviet research team confirmed these results in Kharkov months later [2, 3].

Around the same time, Robert J. Van de Graaff developed a device to produce and maintain high voltages using similar ideas and principles to that of Cockcroft-Walton accelerator. The first Van de Graaff generating device was demonstrated in 1931. Particle accelerator facilities that currently utilize Van de Graff generators are capable of producing and maintaining voltages as high as 15 megavolts (MV) [4, 5].

Although Van de Graaff generators successfully accelerated particles, it was difficult to maintain a reliable high voltage source over an extended period of time using this approach. An alternative for accelerating particles was proposed using a series of lower voltages. In an early paper, the Norwegian engineer, Rolf Wideröe, designed a system that switched voltage polarity to alternately attract and repel positively charged particles [6]. As the positively charged particles were pulled in, the potential would switch from a negative to a positive, forcing the positively charged particles forward (i.e., accelerating the particles). Wideröe proposed that by adding several of these systems in a series would allow the acceleration of particles up to 25 kilovolts (kV) [6].

In 1929, Ernest Lawrence translated Wideröe's paper and used the design plans to develop one of the first linear accelerators. In 1931, with the help of David Sloan, Lawrence built a series of thirty electrodes that could accelerate mercury ions up to 1.26 MeV [7]. A schematic diagram of the linear accelerator built by Sloan and Lawrence is in Figure 1.1. Sloan continued to work on improving the design and capability of the linear accelerator, and developed a linear accelerator that could accelerate mercury ions up to 2.85 MeV. Progress was restricted until sources of high power at high frequency were developed (megawatt power range with frequencies in the megahertz or greater).

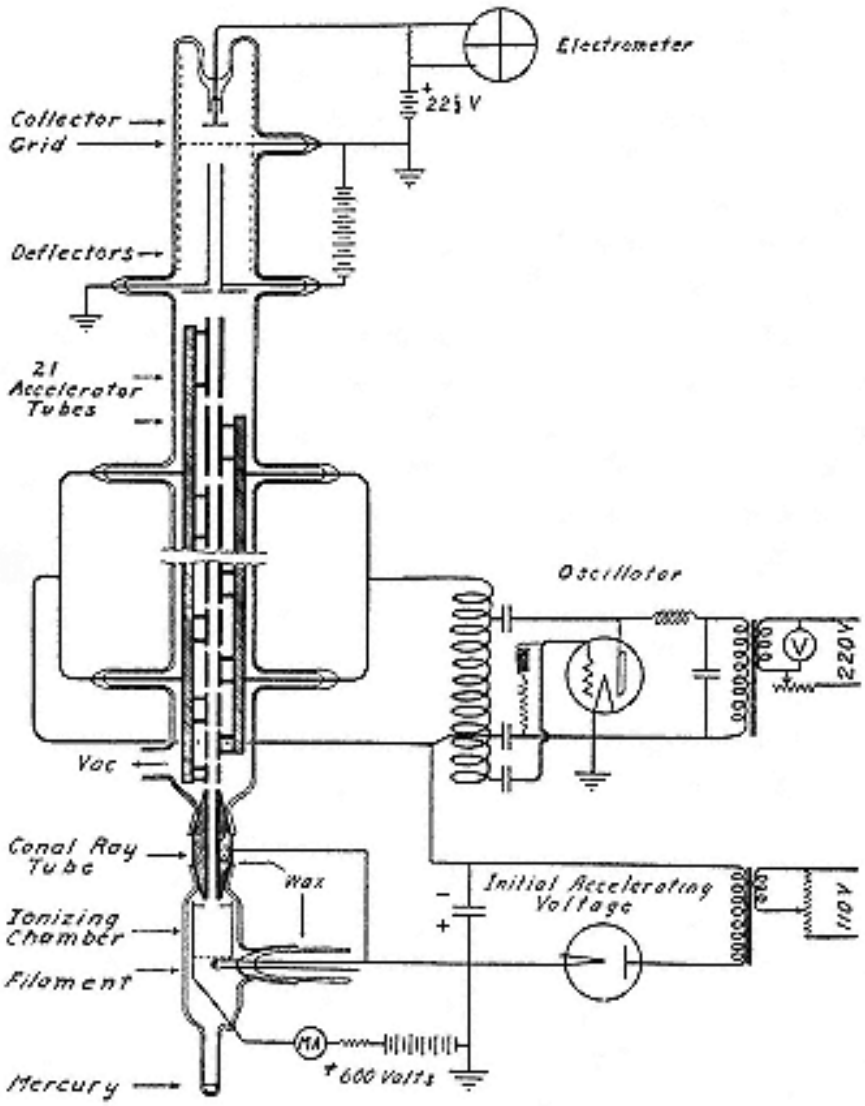

Figure 1.1 - The linear accelerator of Sloan and Lawrence (1931)

In the mid 1940's, several researchers began to develop a magnetron that had the capability of multi-kilowatt power levels and frequencies as high as 30,000 megahertz (MHz). Additionally, other researchers began to develop higher power sources that had greater stability than magnetrons. This allowed researchers to develop the Stanford Mark I, Stanford Mark II, and the Stanford Mark III [8]. The Stanford Mark I was approximately 14 feet (ft) long with a 0.9 megawatt (MW) power source with a frequency of 3,000 MHz, and was capable of accelerating electrons to 6.0 MeV. The Stanford Mark II was similar to the Stanford Mark I, except it was only 12 ft long and had a radiofrequency (RF) power source that could provide 20 MW of power to accelerate electrons to 40 MeV. The Stanford Mark III is still in operation, and is a 300 ft long linear accelerator that is capable of accelerating electrons to 1.2 Gigaelectron volt (GeV). One notable experiment that took place on the Stanford Mark III was R. Hofstadter's measurement on the form factors of the neutron and proton. This work led to Hofstadter receiving the Nobel Prize in 1961 [9, 10].

Following the success of the Stanford Mark III, researchers started to develop the Stanford Linear Accelerator Center (SLAC), which is twenty times as powerful as the Stanford Mark III. The total length of SLAC is approximately two miles and has an acceleration energy of 20 GeV. Since the development of

SLAC, it has become a key focal point for high-energy physicists, leading to several important discoveries and Nobel Prizes [11].

1.2.2 J-PARC

Two recently developed accelerator facilities of interest to this body of work are the Japan Proton Accelerator Research Center (J-PARC) and the SNS. Both J-PARC and SNS generate neutrons by the spallation process. W.H. Sullivan and Glenn T. Seaborg [12] at the Lawrence Radiation Laboratory in Berkeley, California first used the word "spallation" to describe the process of a high-energy particle colliding with a nucleus to emit a significant amount of neutrons and fragments. SNS will be discussed in further detail in the proceeding sections.

J-PARC is comprised of three proton accelerators which are used to generate various secondary particle beams used at three experimental facilities. The accelerators include a 400 MeV linear accelerator (Linac), a 3 GeV synchrotron (also known as a rapid-cycle synchrotron (RCS)), and a 50 GeV synchrotron known as the Main Ring (MR). The three experimental facilities are use in research on materials and life science, neutrinos, and hadrons. Construction of the accelerators and experimental facilities began in 2007 and

reached completion in April of 2009. J-PARC's mission is to provide a diverse source of high-power secondary beams for researchers from around the world. An artistic sketch of J-PARC and its facilities is depicted in Figure 1.2 and a schematic diagram of J-PARC is shown in Figure 1.3 [13]. In addition, a conceptual drawing of how the accelerated particle transforms throughout the facility is shown in Figure 1.4 [13].

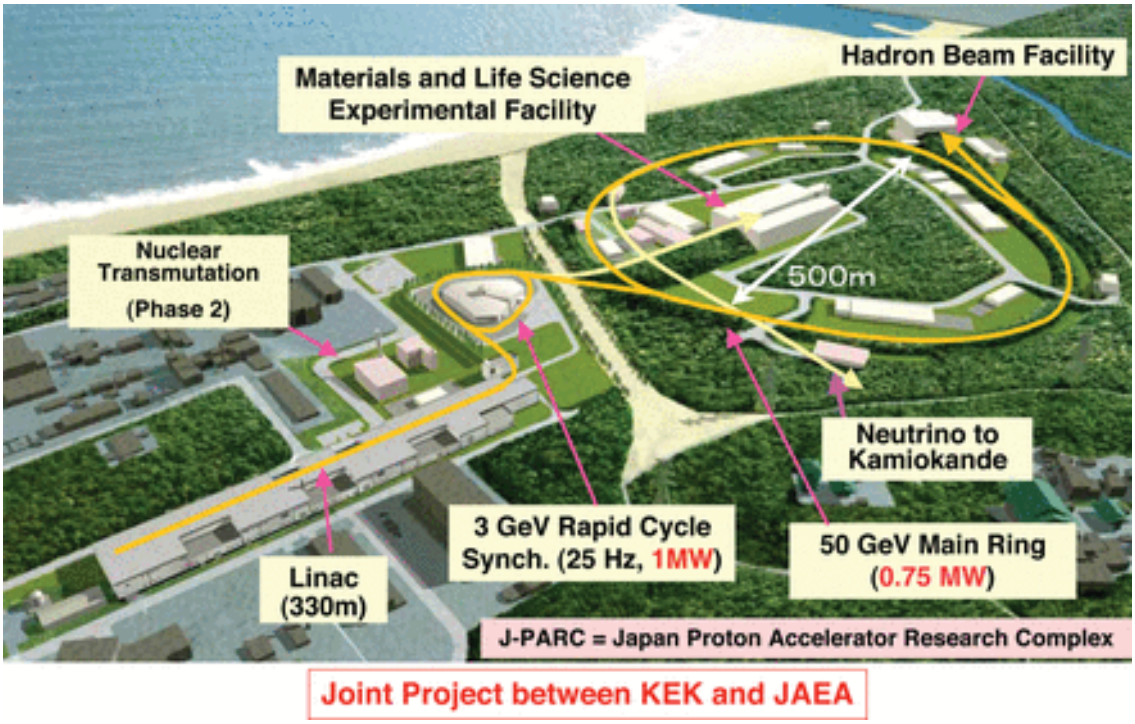

Figure 1.2- Depiction of the Japan Proton Accelerator Research Complex

J-PARC is of special interest because of the similar design to SNS and the use of thin carbon foils to strip electrons from a high energy H^- beam. J-PARC's facility design starts with an ion source to produce a negatively charged

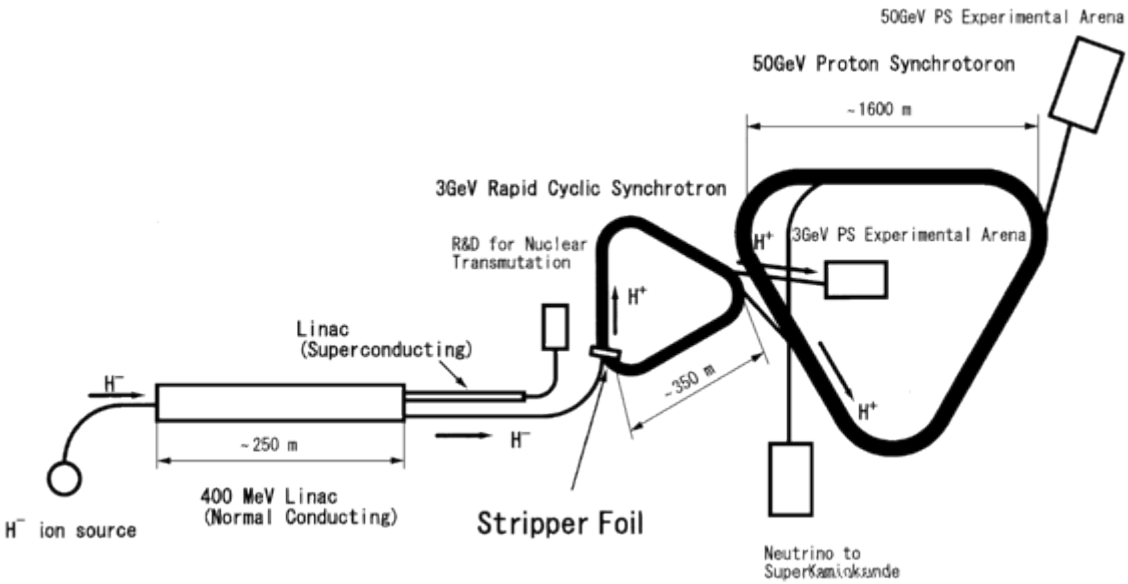

Figure 1.3 – Schematic layout of the accelerator complex of J-PARC

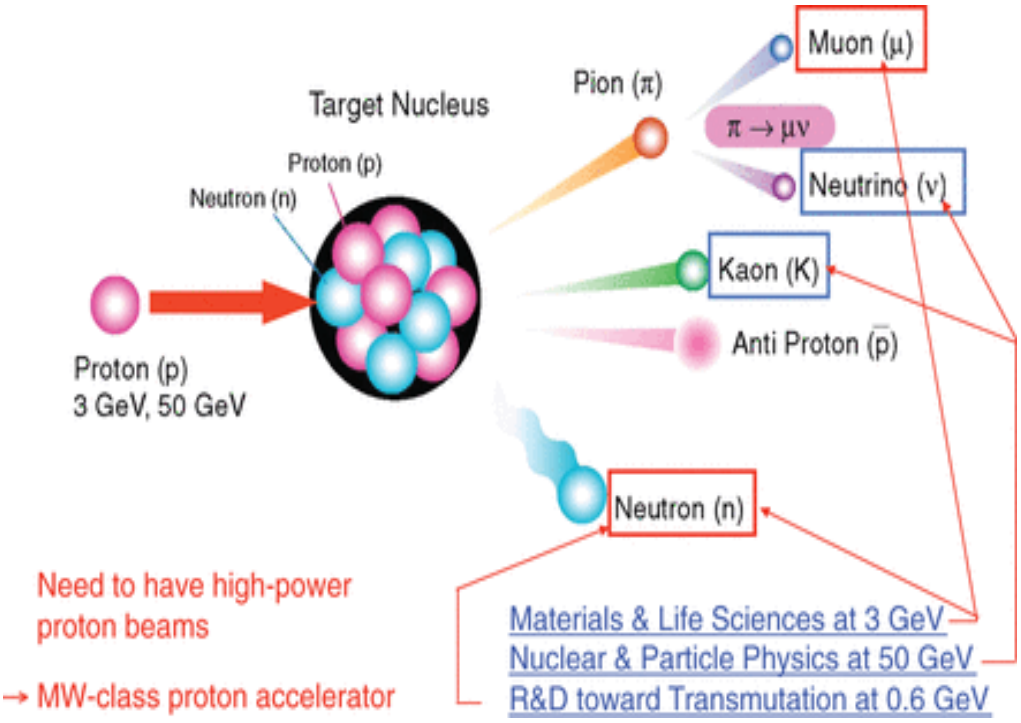

Figure 1.4 - Diagram of a 3 GeV accelerator proton impacting a Target Nucleus and spalling off various particles, specifically a neutron.

hydrogen ion (H^-) [14]. The H^- is extracted as a pulsed beam and accelerated over various stages of the facility to reach 400 MeV, before it is injected into the RCS. When it enters the RCS, it passes through a Hybrid Boron mixed Carbon (HBC) foil that strips the H^- beam of its electrons. The HBC foils are approximately 1 μm thick, with a corresponding aerial density of 200 $\mu g/cm^2$. The three outcomes for the H^- beam as it passes through the foil are:

$$(1)\ H^- \rightarrow H^+ + 2e^-$$

$$(2)\ H^- \rightarrow H^0 + 1e^-$$

$$(3)\ H^- \rightarrow H^-$$

In the first case, both electrons (e^-) are stripped and separated from the resulting proton (H^+); the protons are then sent into the RCS. The second case is where only one e^- is stripped; the resulting hydrogen atoms (H^0) are sent to a secondary foil. The third case is where no electrons are stripped from the H^- beam; the H^- ions are also sent to a secondary foil. While in the RCS, the H^+ beam circulates approximately 10 times where it is accelerated, focused, and shaped by eleven RF accelerating cavities to 3 GeV. The beam circulates in the RCS to allow additional pulses to be added to the beam from the Linac, to increase its overall intensity. As it circulates though, it passes through the stripper foil and causes a

slight beam loss. Conditions are set to minimize these beam losses and to optimize beam intensity. When the H^+ beam typically reaches an intensity of ~4.2 x 10^{11} protons per pulse (ppp), it can be extracted into the Material and Life Science Facility (MLF) or the MR. At the MLF, the 3 GeV H^+ beam is directed from the RCS onto a mercury target, generating neutrons by the spallation process to be used for materials research. The remaining portion of the H^+ beam that is not extracted into the MLF is sent into the MR. In the MR, it is circulated and accelerated further to 50 GeV by seven RF cavities. After being accelerated to 50 GeV, it can be extracted either to the Hadron Facility or the Neutrino Facility to be used for further scientific and materials research [15].

1.3 Spallation Neutron Source (SNS)

In the early 1990's, the Department of Energy (DOE) made the decision to design, develop, and operate a neutron scattering research facility that was an order of magnitude more powerful than any neutron source in the world at the time. This facility became known as the Spallation Neutron Source (SNS) [16, 17]. After several years of development and research, construction began at ORNL for the building of SNS in December of 1999. After approximately six years of construction, SNS was completed in May of 2006. The first three SNS

research instruments became available in August of 2007, and since then a total of seventeen instruments have been built which are used by an average of 700 researchers per year as of 2011 [18]. SNS is a world-class particle accelerator research facility that delivers an intense pulsed neutron beam for use by researchers from around the world. The pulsed neutron beam is used for several areas of research and industrial development, including but not limited to material science, biology, chemistry, and physics. This research has led to advances in both research and commercial products; for example, in characterizing medicines, and in developing powerful lightweight magnets and plastics to be used in automobiles and planes. An illustration of SNS that identifies the corresponding national laboratories that designed the five main sections is depicted in Figure 1.5.

1.3.1 Purpose of SNS

SNS is an one-of-a-kind research facility that uses an accelerator-based system to deliver microsecond pulsed proton beams to a mercury target to produce the world's most intense pulsed beam of neutrons. This allows researchers to perform neutron-based measurements at a higher resolution, greater sensitivity, faster analysis time, and the ability to apply these to more complex sample environments than ever before [19]. A depiction of the

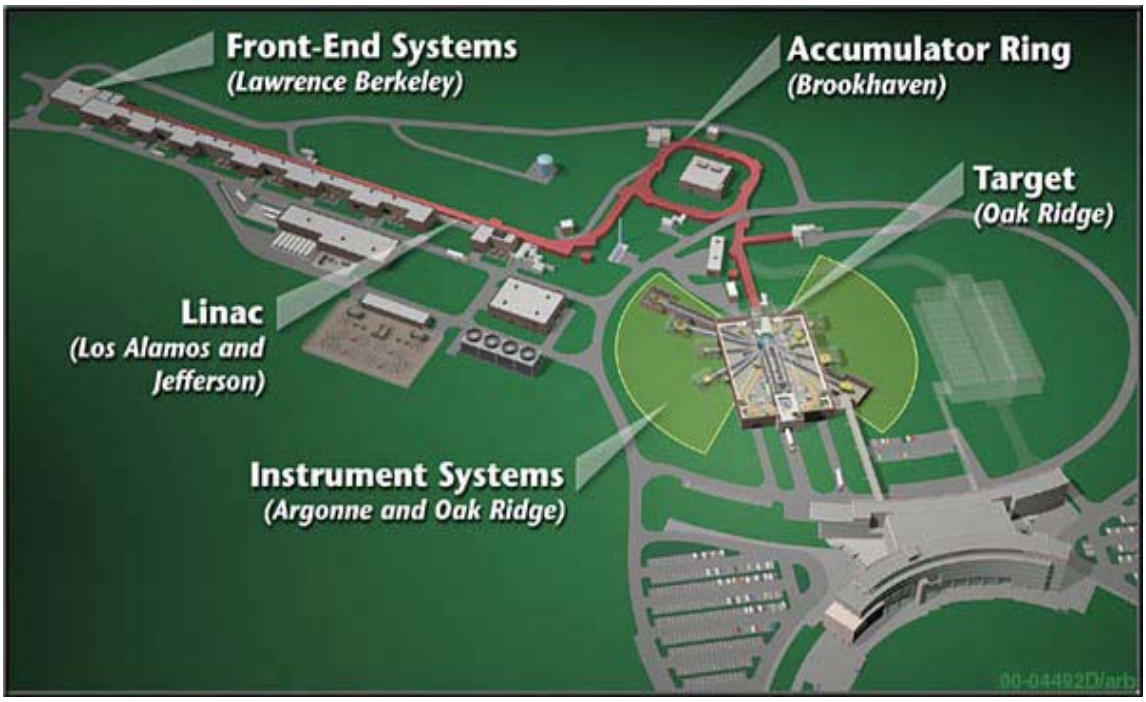

Figure 1.5 - Overview of SNS with labels identifying the five major sections along with the main collaborators.

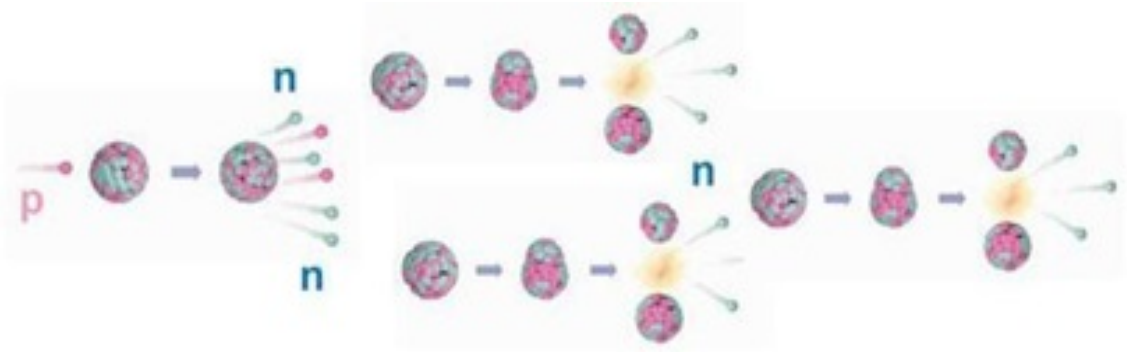

Figure 1.6 - Diagram of an accelerated proton (p) hitting a target nucleus and spalling off neutrons (n). The neutron subsequently goes on to spall several more neutrons from the target nuclei.

spallation process is illustrated in Figure 1.6.

1.3.2 Design of SNS

SNS can be divided into five main sections: Front-End Systems, Linear Accelerator, Accumulator Ring, Target, and Instrument Systems [20]. The Front-End Systems consists of the ion source, an electrostatic Low Energy Beam Transport (LEBT) that includes the first-stage beam chopper, a four-vane Radio-Frequency-Quadrupole (RFQ) to accelerate the beam up to 2.5 MeV, and a Medium Energy Beam Transport (MEBT) and second-stage chopper; which were all developed and tested at Lawrence Berkeley National Laboratory (LBNL) before being delivered to ORNL in June of 2002 [21].

1.3.2.1 H^- Source

The ion source creates the hydride plasma by radiofrequency and confines it with a multicusp magnetic field [22, 23, 24, 25]. The ion source delivers a 2.5 MeV, 35 – 50 mA hydride ion in a pulse to the linear accelerator at a pulse frequency and width of 60 Hz and 1 ms, respectively. A depiction of the ion source at SNS is illustrated in Figure 1.7 [26].

1.3.2.2 Linear Accelerator

The linear accelerator (Linac) uses a combination of conducting and superconducting cavities to accelerate and focus the beam from 2.5 MeV to 1,000 MeV (1 GeV) [27, 28]. The Linac was designed by Los Alamos National Laboratory (LANL) and is made up of several klystrons and super conducting cavities. The H^- ion source is kept at a pulse frequency of 60 Hz and macro-pulse width of 1 ms, with a peak current of 52 mA. The beam is chopped to give an average beam current within the macro pulse of 36 mA (68% chopping factor). Once the hydride beam is accelerated up to the final beam energy (typically 968 MeV ≈ 1 GeV) from the superconducting radiofrequency (SRF) and superconducting cryomodules, it is sent into the High Energy Beam Transport (HEBT). The HEBT transports the accelerated beam into the Accumulator Ring [22, 23, 27, 28, 29, 30, 31].

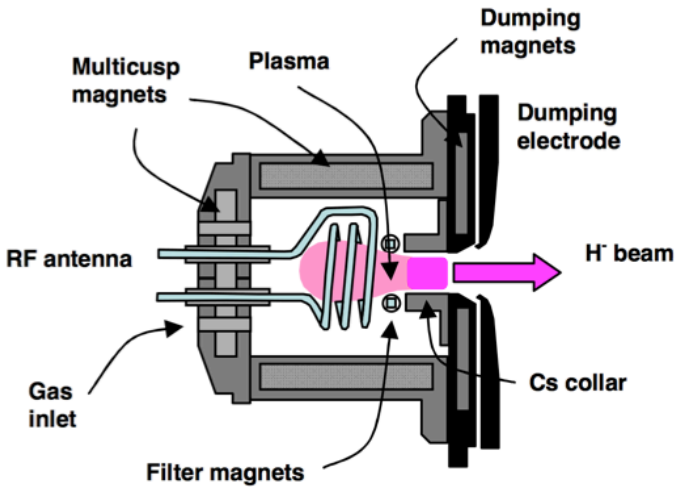

Figure 1.7 - Schematic diagram of SNS Ion Source.

1.3.2.3 Accumulator Ring and Primary Stripper Foil

The Accumulator Ring (AR) is the third main section of SNS designed by Brookhaven National Laboratory (BNL), following the Front End and Linac [32]. The two main functions of the AR are to send the H^- beam through a stripper foil to remove the two electrons and then intensify the resulting proton beam. It takes approximately 1 μs for a 1.0 GeV proton to complete one cycle in the AR, and therefore a proton generated from the beginning of the 1 ms macro pulse of H^- will circulate approximately 1,200 times in the AR before the entire macro pulse is accumulated in the ring [33, 34]. Protons generated from stripping of the entire macro pulse are accumulated in the AR, creating a huge increase in beam intensity. When the fully accumulated proton beam is extracted from the AR, the highly intensified beam is time compressed to 1 μs.

When the beam passes through the foil, there is potential for the H^- ion beam to undergo the same three reactions as the J-PARC stripper foil. An illustration of the process that an H^- ion beam undergoes after being stripped of its two electrons is illustrated in Figure 1.8. When stripping of the electrons from the H^- ion occurs, the stripped electrons (sometimes referred to as convoy electrons) descend downward to the electron collector in a helical pattern. Several different electrodes are used to ensure that the electrons enter the

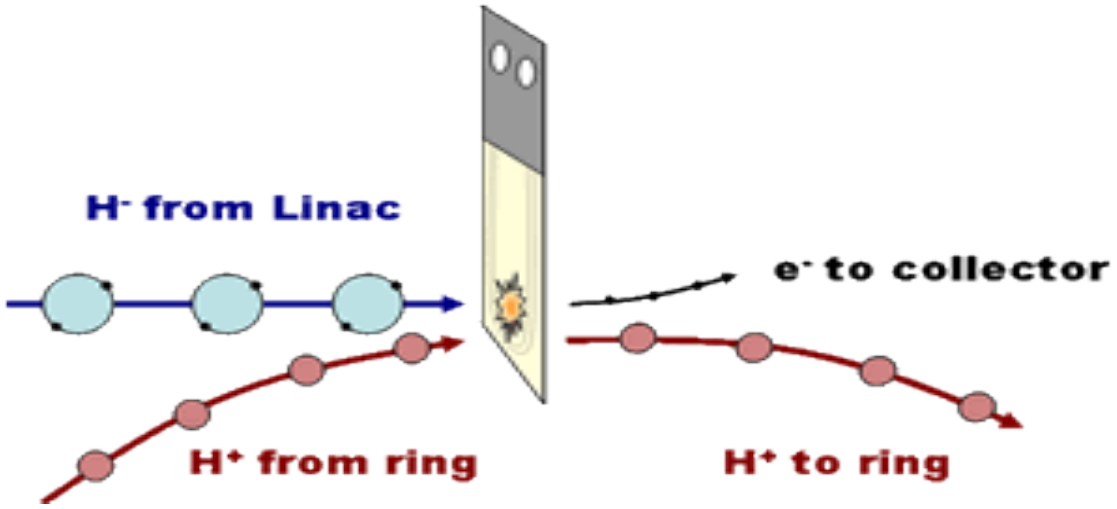

Figure 1.8 - Illustration of the H^- beam path through a stripper foil

electron collector. If the stripped electrons miss the electron collector, the electrons can be reflected back up to the stripper foil and the foil bracket. Issues with this have been observed in SNS operation and will be discussed later in this dissertation. An illustration of the path that the stripped electrons were designed and predicted to take after being stripped is illustrated in the Figure 1.9 [35]. When an H^- ion is partially stripped, the electron is directed downward to the electron collector and the H^0 atom is sent into the secondary foil. When an H^- ion passes through the foil unstripped, it too is intercepted by this secondary foil. As noted earlier, the protons generated by complete stripping of electrons from the H^- beam in the entire macro pulse are circulated in the AR to intensify and time compress the proton beam. When released from the AR, this results in a pulsed beam of 1.0×10^{14} protons per pulse when operating at 1.4 MW and a 1 mA

average H^- beam current [36, 37, 38].

One of the major challenges for successful operation of SNS is the stripper foil, more specifically the primary stripper foil. From this point forward, the primary stripper foil will be referred to as "foil." SNS has implemented several different designs and chemical compositions of foils. Up till now, the most commonly used foil has been made of nanocrystalline diamond grown on a silicon substrate by plasma enhanced chemical vapor deposition (PECVD).

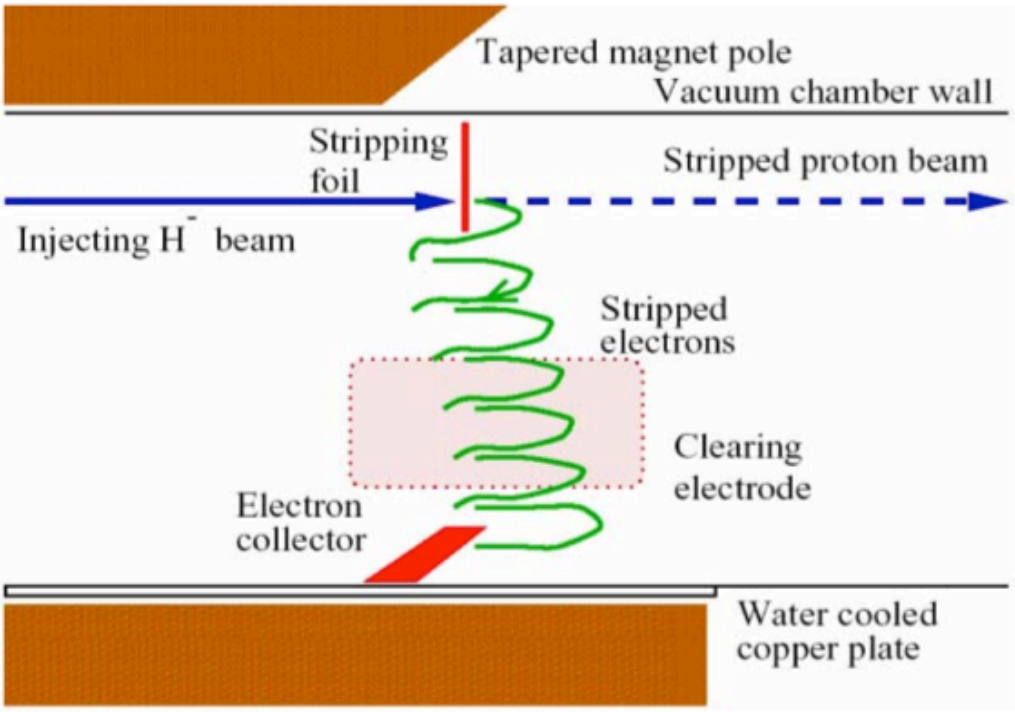

Figure 1.9 – Schematic mechanism of the electron collector at SNS.

The standard dimensions of the foil are 17 mm x 45 mm x 1 μm (thick). Once the foil is grown, a large section (17 mm x 30 mm) of the silicon substrate is etched away to leave a freestanding, nanocrystalline diamond portion that is supported on only one side. The remaining silicon (17 mm x 15 mm) is known as the silicon handle and is used to attach the foil to the foil bracket assembly. The foil bracket assembly has been modified several times since the beginning of SNS operations, with the most current design being a L-shaped bracket made of titanium. Once the foil is attached to the foil bracket assembly, it is loaded into the Primary Foil Changer (PFC), which holds up to twelve foils. The PFC is interconnected to SNS under vacuum and has the capability to transfer and adjust foils in and out of the beam line. It is designed like a bicycle chain with points along the chain for attachment of the brackets. The bicycle chain is remotely manipulated to adjust the position of the foils. A more detailed analysis of the foils and the various foil components will be discussed in a further section. Photographs of the AR, the PFC housing, and a foil prior to being placed into the PFC are shown in Figure 1.10, Figure 1.11, and Figure 1.12, respectively.

The final proton beam has approximately 1.0×10^{14} protons per pulse. These protons are then delivered to the Target at a frequency of 60 Hz. This corresponds to an average beam power of 1.4 MW. Facilities have been set aside

Figure 1.10 - Accumulator Ring coming around the bend into the LINAC.

Figure 1.11 - Primary Stripper Foil Changer (PFC). The PFC houses the foils that used within SNS during production.

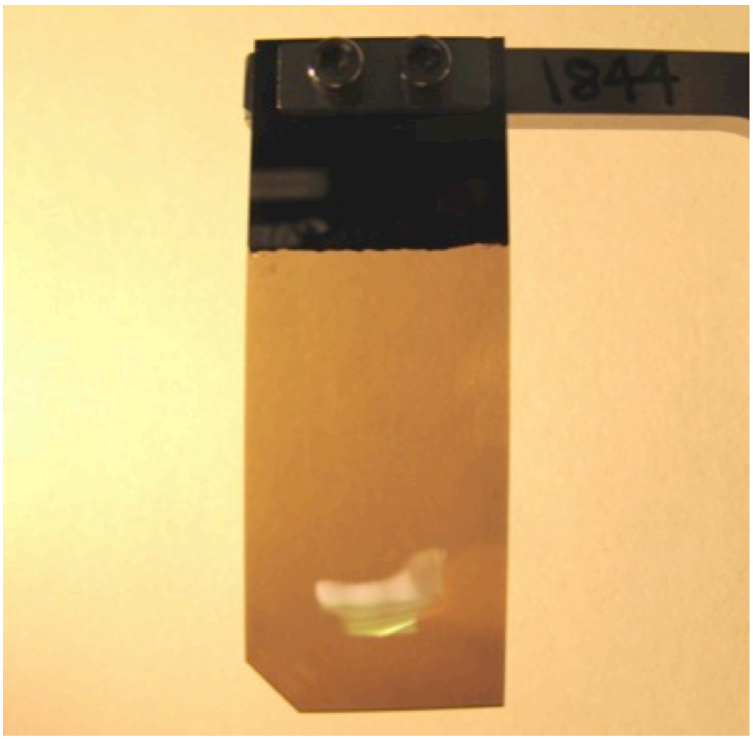

Figure 1.12 - Photograph of a foil prior to be inserted into SNS for production.

for future upgrades that would allow twice as many protons to be stored within the accumulator ring per pulse to deliver a 2 MW proton beam to the target.

It is very important that a large percentage (proof-of principle tests and experience has shown > 99%) of the H^- beam is stripped completely of its two electrons and that SNS behaves consistently between different SNS cycles. In order to monitor how the beam is behaving between different cycles, the operators leave two standard diamond stripper foils in the PFC to characterize the beam. One foil has a higher aerial density ("thicker") than the nominal 350 $\mu g/cm^2$, and the other has a lower aerial density ("thinner") than the nominal 350

$\mu g/cm^2$. The operators utilize the same thick and thin foil over several cycles to compare how different beam settings affect the overall beam dynamics and stripping efficiency. Additional discussion will take place on the current issues and problems that are affecting the lifetimes of foils in a further section.

1.3.2.4 Target

The mercury Target, Stage #4, as mentioned above was designed at ORNL to accept a 1.4 MW H^+ pulsed beam from the AR at a frequency of 60 Hz and width of 1 ms. Collisions of the H^+ beam would then spall (i.e., knockoff) neutrons off from the mercury Target. This was a very challenging problem due to the intense radiation that the Target area would undergo and the difficulties of working with liquid mercury. Due to the intense energy being delivered to the Target, it must be able to quickly and efficiently dissipate this energy [39]. At the same time, it must be able to provide a vast amount of neutrons to the source. With this in mind, a target composed of liquid mercury (Hg) was chosen for its high neutron count per atom (80), its ability to dissipate the heat, and its capability of withstanding high doses of radiation. When the protons hit the mercury Target, each proton spalls off approximately 12 – 14 neutrons from a mercury atom. If a typical solid target made of tantalum or tungsten was chosen instead, it would be susceptible to detrimental radiation damage and thermal

shock. By having a liquid target that is circulated, it has the capability to self-cool itself by constantly removing heat from the impact region. Additionally, the circulation will prevent high radiation damage from occurring since the impact region is constantly being replenished and replaced. The Target contains approximately 14 tons of liquid mercury that is circulated continuously through a series of channels within the enclosed system. By keeping the system enclosed, it allows the potential use of a single target for several years. Unfortunately, current target designs and manufacturing techniques require it to be replaced on average twice a year due to the mechanical and structural stress that the various components undergo. Furthermore, liquid mercury is extremely cumbersome to work with; reasons include the potential health hazard that may arise if not handled correctly and the pitting that can occur inside the Target from not properly regulating the flow of such a dense material. If the flow of mercury were not properly regulated, its high-density would cause pitting inside of the Target that would severely limit the lifetime of the Target by increasing the probability of leaks and contamination issues [20, 33]. A diagram and photograph of the mercury Target at SNS is shown in Figure 1.13 and Figure 1.14, respectively [31].

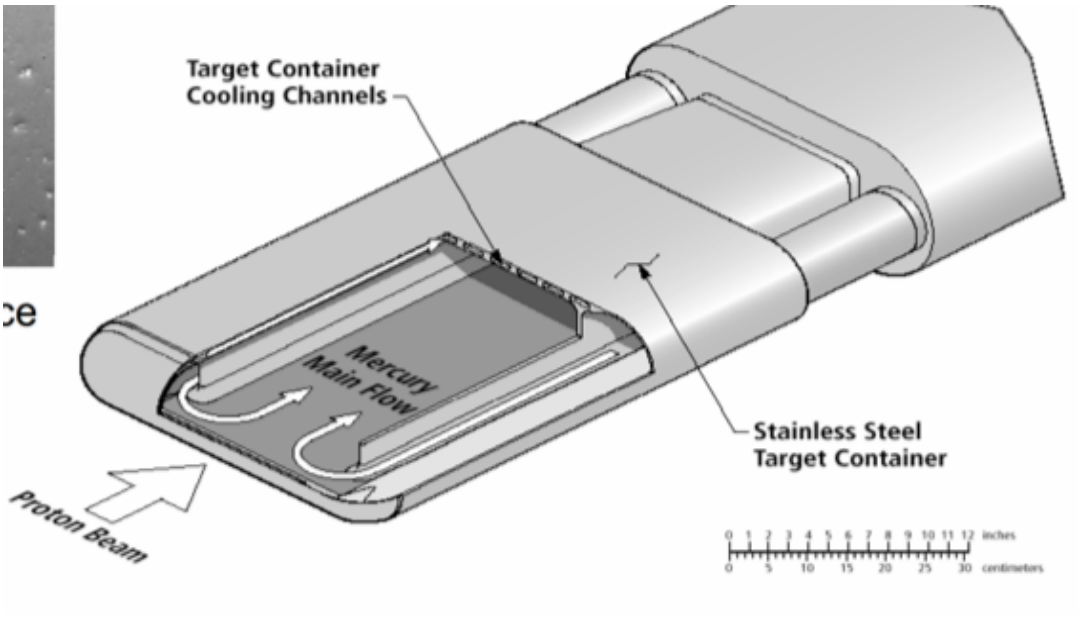

Figure 1.13 - Diagram of the mercury Target used at SNS.

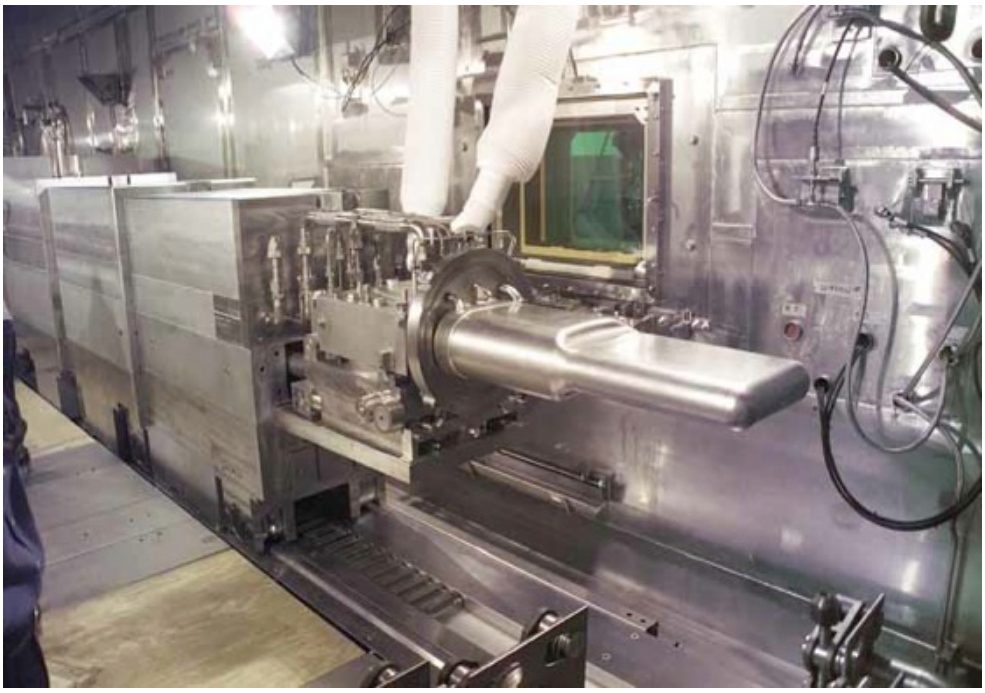

Figure 1.14 - Photograph of the mercury Target being installed by remote manipulators within SNS.

1.3.2.5 Neutron Instrumentation

For the final stage, Stage #5, Argonne National Laboratory (ANL) was charged to design and develop the preliminary neutron scattering instrumentation along with working with ORNL to develop the experimental facilities. Neutrons emitted from the Target are focused and then cooled by either water or liquid helium to provide the different instruments with a range of neutron energies. Since the initial instrumentation development, additional research groups have developed several more instruments to give a total of seventeen instruments currently under operation at SNS, two in construction and commissioning phase, and three more in the design and proposal phase. The instruments currently in operation include a series of diffractometers, reflectometers, and spectrometers that provide a wide range of analysis and characterization for samples [40, 41]. The samples that are tested in SNS come from areas of research including but not limited to chemistry, polymers, life sciences, material chemistry, and applied engineering [20, 42]. A schematic diagram of SNS Instrument Hall and a partial showing of the instruments presently available are illustrated in Figure 1.15 [43].

The SNS project relied on several organization and national laboratories working together for a common goal: to build the world's most intense source of

neutrons. This allowed the successful design, building, and current operation of SNS; this accomplishment was similar in magnitude to what was accomplished by the Manhattan Project during the Second World War [25].

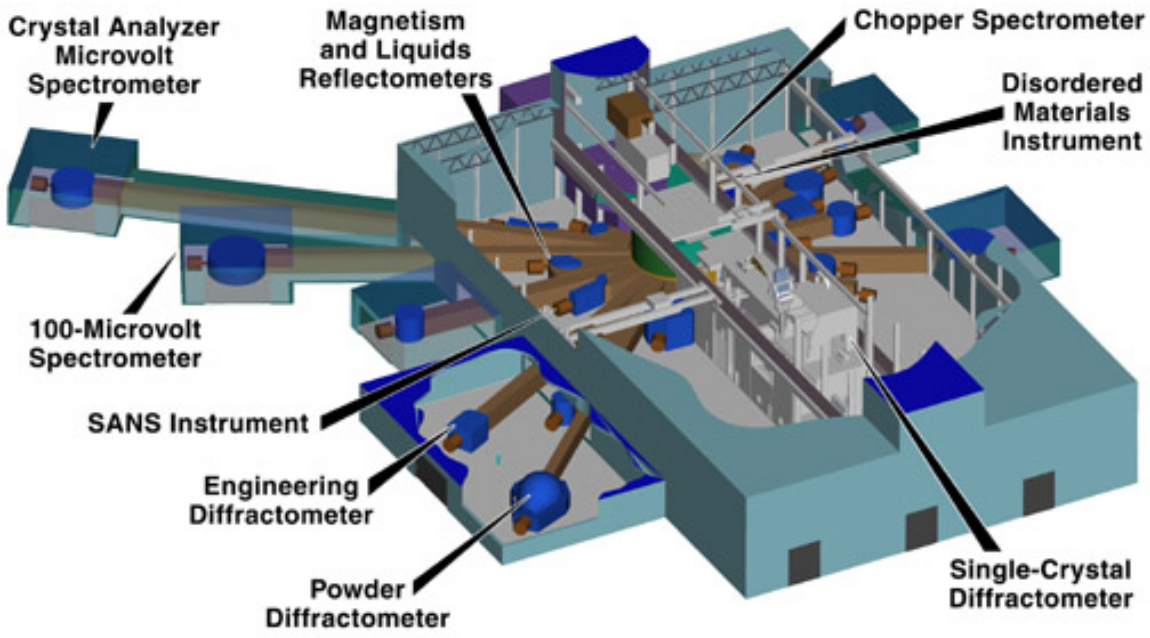

Figure 1.15 - Schematic diagram of SNS Instrument Hall.

1.3.3 SNS Operations

SNS has been in operation since 2007 and has been operating at 1 MW or greater for the past several years. SNS beam began production with a maximum power on Target of 0.200 MW in 2007. After SNS was tuned and conditioned for higher power levels, the power was steadily increased to 1.100 MW from 2007 to

2010, and operated for over a year of operation between 0.900 and 1.100 MW. From 2009 to 2010, several issues arose within SNS that limited the power level to approximately 0.850 MW. These issues included failures within the Target and the destruction of several primary stripper foils from the improper ventilation of the PFC. From the end of 2011 until early 2013, the beam power was increased back to 1.000 MW and maintained. In early 2013, additional concerns with Targets limited SNS to a power level of 0.900 MW. After these issues were resolved, the beam reached an historic level of greater than 1.200 MW. Since 2013, several milestones have been reached within SNS. One of the most important milestones reached was the successful operation of SNS at 1.400 MW for two weeks prior to a scheduled shutdown. Although SNS has successfully operated at 1.400 MW, several issues have limited SNS from consistently operating at this power level. Therefore, operating power has been limited to guarantee the availability of the beam to researchers until these issues are resolved. SNS is currently able to deliver a 1.0 MW of beam power with the existing system and foil conditions, with the goals of having an operational beam power of 1.4 MW and developing the technology to have beam powers of 3.0 and 5.0 MW [31].

1.4 Primary Stripper Foils

When SNS was being designed it was recognized that the primary stripper foil would be a critical element in its operation. C.J. Liaw and coworkers at BNL (BNL had responsibility for the AR design) performed some preliminary testing on the lifetimes of carbon-based foils using conditions that simulated SNS loads [44, 45]. Liaw and coworkers calculated the maximum temperature that a carbon stripping foil would experience under SNS operation and determined a temperature between 2,350 – 2,578 K depending on foil thickness [46]. In the lifetime testing, all of the carbon foils made from amorphous carbon lasted less than 100 hours. Foils with the desired thickness of 400 $\mu g/cm^2$ without carbon fiber supports lasted as short as 10 hours. However, a 1 μm thick (approximately 350 $\mu g/cm^2$) microcrystalline diamond foil performed the best, lasting over 400 hours. One problem with this foil was it could only be used in a window configuration, supported on all sides by the silicon substrate it was grown on. When it was attempted to create a single edge supported foil, the foil scrolled up tightly and was unusable. Drs. Feigerle (UTK) and Shaw (ORNL), who already worked in diamond film growth, were contacted to solve this problem and from that began the ORNL stripper foil program [47].

1.4.1 The UTK-ORNL Stripper Foil Project

Two approaches were taken to address foil scrolling: 1. Growth of chemical vapor deposition (CVD) diamond on lithographically patterned silicon substrates to create corrugations in the films and impart increased structural rigidity, and 2. Use of nanocrystalline diamond films. Methods for growing nanocrystalline diamond films had recently been reported by Dieter Gruen and coworkers [48]. Scrolling of released microcrystalline diamond films was believed to be the result of stresses introduced by the columnar characteristic of microcrystalline diamond growth, where grains grew and expanded after initial nucleation. Nanocrystalline diamond films, on the other hand, can be grown under conditions where nucleation continues throughout growth producing films without columnar character.

The majority of the foils used in the SNS beam line since it first came on line in 2006 have been nanocrystalline diamond foils patterned with corrugations and produced by UTK and ORNL researchers (Shaw and Feigerle). Except for some early foils which were grown in a hot filament reactor at UTK, all of these were grown by microwave plasma enhanced chemical vapor deposition (MPECVD) in a commercial ASTeX reactor. MPECVD is a technique where the microwave plasma activates gaseous precursors to generate growth species for

deposition of a solid-state film onto a chosen substrate [20, 49, 50, 51]. The plasma created by MPECVD is typically produced above the substrate by creating a radio frequency (RF) glow discharge. The chemical reactions that take place within the plasma have two fundamental purposes: to create the chemically active species necessary for film growth and to deliver the necessary energy to provide uniform nucleation, particle migration, and heterogeneous kinetics across the substrate [20, 47, 49, 50, 51, 52, 53].

MPECVD was chosen as the preferred method of growth to eliminate metal contamination in the films that had been shown in hot-filament growth [59 – 60]. Some foils of differing design have also been tested in SNS including: carbon foils by Arizona Carbon Foil Company, Diamond-Like Carbon foils by TRIUMF; nanocrystalline diamond foils grown by hot filament chemical vapor deposition at BlueWave Semiconductors; and Hybrid Boron mixed Carbon (HBC) foils by Sugai. All of these foils used have had a range of thickness (i.e., aerial densities), size, and dimension; with a select number of foils being supported by fibers.

Modification of the growth parameters and substrate preparations used in microcrystalline diamond film growth was necessary for the development of the

nanocrystalline diamond films to get complete and uniform coverage of the surface [52]. The process for creating a nanocrystalline diamond foil has been extensively developed [50, 54, 55, 56, 57, 58, 59, 60, 61]. The general process for development is to first clean and then pattern a (100) silicon substrate with one of the several lithography designs, most commonly a U-shaped. The lines in the lithography pattern are typically at a density of 100 lines/inch, but a variety of patterns have been investigated. After the silicon substrate is patterned, the silicon substrate goes through an anisotropic chemical etch. The etch produces trenches that have an approximate depth of 5 μm with walls that are at a 55-degree inclination. A cross-sectional photograph of a corrugated diamond foil with an approximate corrugation depth of 20 μm is shown in Figure 1.16. Additionally, a photograph of the silicon wafer containing multiple pre-cut silicon substrates with an U-shaped lithography pattern is shown in Figure 1.17. Once a lithography pattern is chosen and implemented, the silicon wafer is cut to the appropriate dimension (17 mm x 45 mm) and seeded with diamond seeds. This is done by placing the substrate into an ultrasonic bath with a diamond abrasive slurry. The slurry creates diamond nucleation sites on the silicon substrate. The density of the nucleation sites depends on the size of the diamond particles in the slurry, with a desire to provide a high enough density that the diamond particles will grow together prior to achieving the desired film

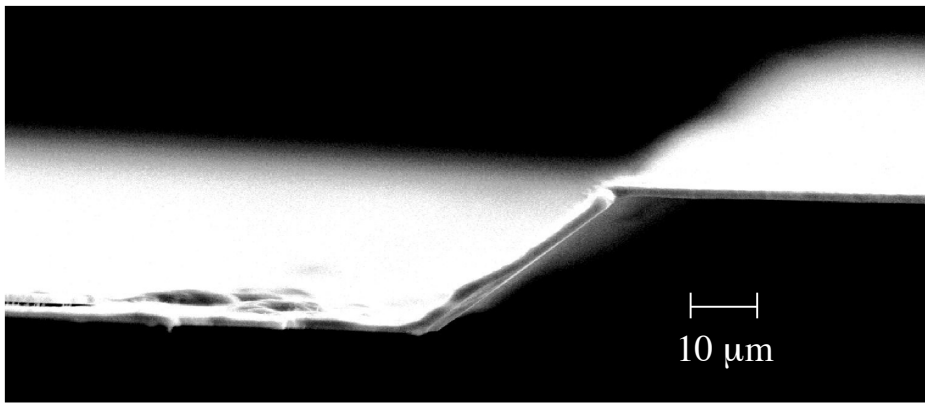

Figure 1.16 - Cross-section of a corrugated foil with an approximate corrugation depth of 20 m.

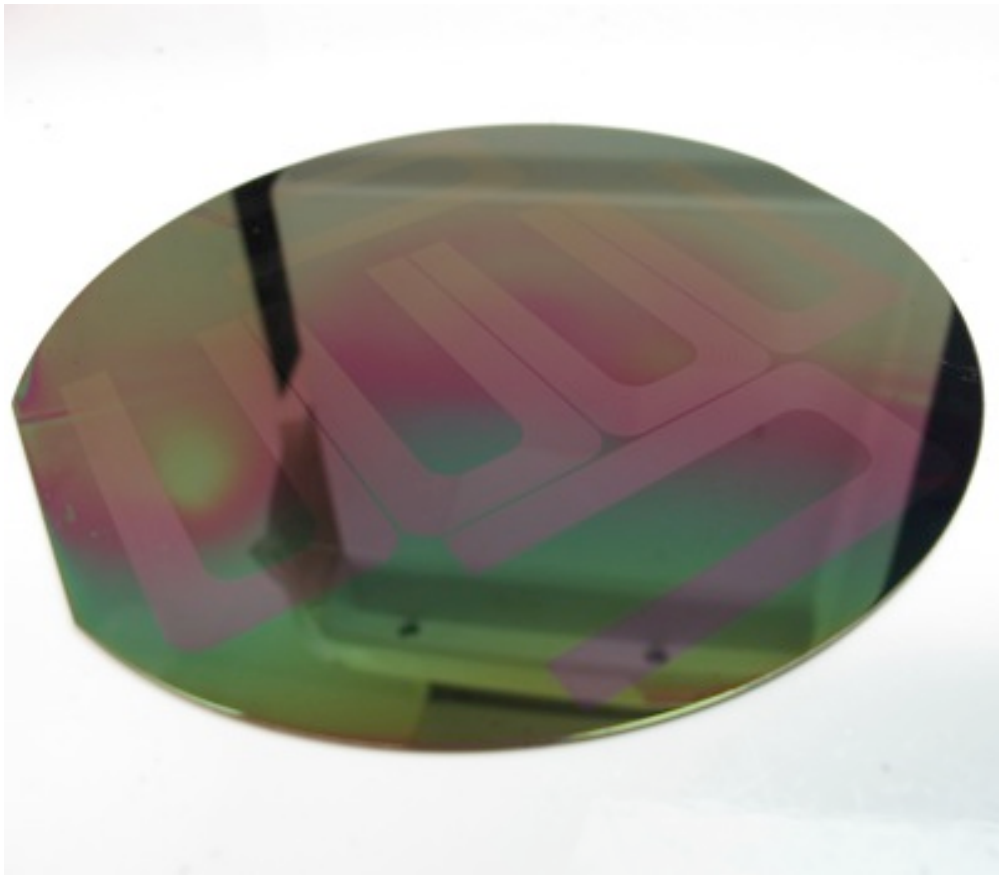

Figure 1.17 - The common U-shaped lithography that has been patterned on a four-inch silicon substrate.

thickness.

Prior to nanocrystalline films, the practice was to mechanically scratch the surface with a diamond paste to deposit seeds onto a silicon substrate. In order to increase the films nucleation density and improve the uniformity of the films, a slurry recipe designed by Hoffman containing a mixture of large and small diamond particles was employed [62]. This slurry of diamond nanoparticles was implemented by placing both the slurry of diamond nanoparticles and the silicon substrate into an ultrasonic bath. The ultrasonication provided a uniform and high nucleation density on the silicon substrate. More recently, the slurry has been changed to contain explosion diamond. This slurry mixture provides smaller diamond particles that are ideal for nanocrystalline diamond growth. The silicon substrate is then placed into the ASTeX 2.45 GHz microwave plasma-enhanced chemical vapor deposition growth chamber and grown at a reactor power and pressure of 1,000 W and 130 Torr, respectively. By using and adjusting mixture of methane gas, hydrogen gas, and argon gas (up to 95 percent), a 1.0 μm thick nanocrystalline diamond film may be grown in about one hour.

After a set period of time (approximately 1 hour) of growth, the newly

deposited film on the silicon substrate is brought back to room temperature and removed from the MPECVD chamber. From here, the deposited film is analyzed by SEM to determine the crystallinity, profiled to determine the surface roughness, and then weighed and alpha-ranged to determine the thickness and uniformity of the films. Next, a portion of the film's silicon substrate is etched away to leave a free-standing diamond area that is typically 17 mm x 30 mm. The remaining 15 mm of the silicon substrate that is left behind provides a handle for the film to be loaded into SNS's PFC. At this stage of the process, the films are very fragile since the typical aerial density is 350 $\mu g/cm^2$ (i.e., thickness of ~1 μm). Great care must be taken to restrict all quick movement and turbulent air flows that will cause the free-standing diamond portion of the film to break away from the silicon handle. The rigidity of the diamond films grown allows them to be inserted into SNS beam without having any fiber supports. On a couple occasions, SNS personnel have supported the diamond films with carbon fibers to help reduce foil shaking ("foil flutter"). However, the fibers were not able to withstand the high intensity of SNS beam and were unable to provide any significant reduction in foil flutter. Fluttering and additional problems that have affected foils within SNS will be discussed in another section. A photograph of the foil after it has gone through the entire development process is shown in Figure 1.18.

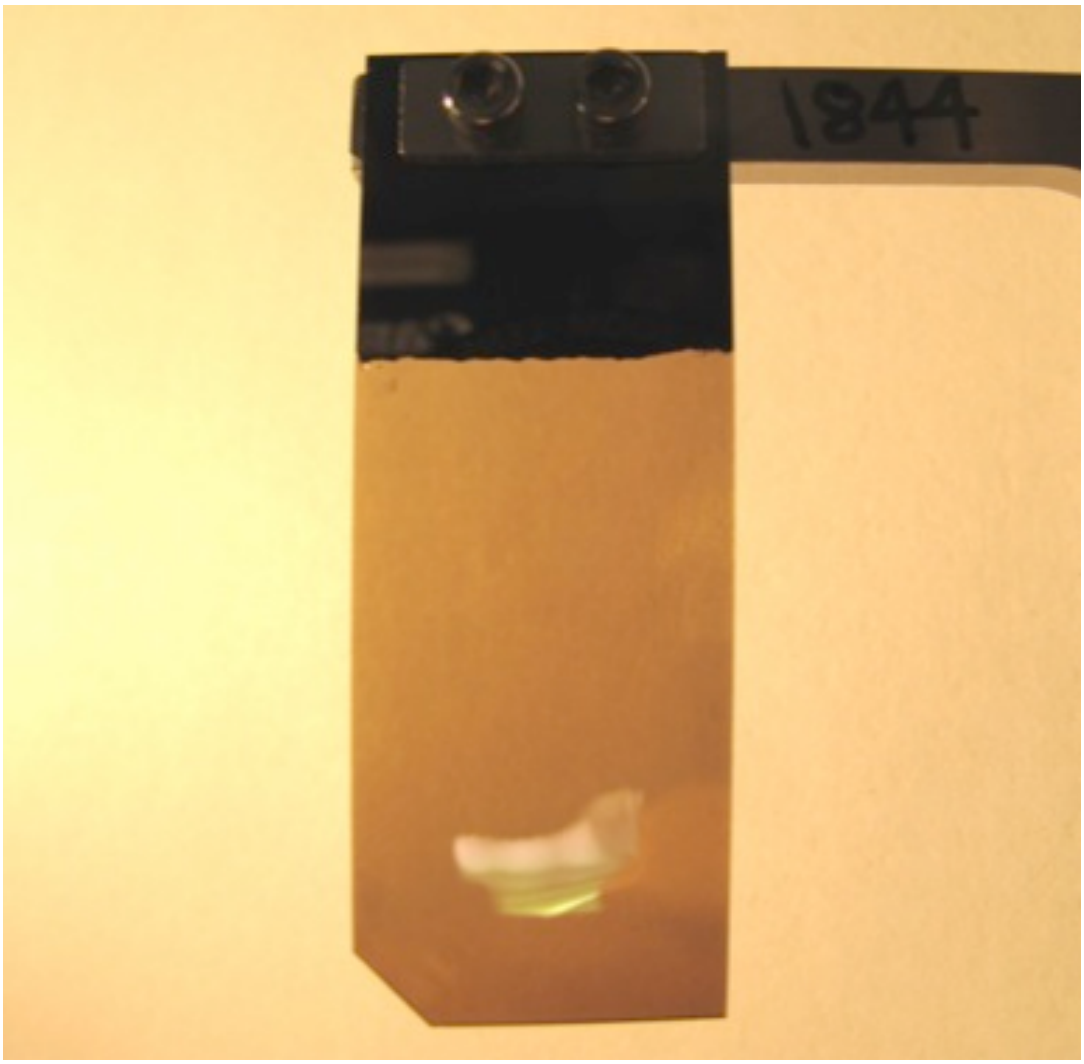

Figure 1.18 - Nanocrystalline Diamond foil grown at ORNL preproduction SNS mode.

The foils created and developed at ORNL are unlike most other foils used in particle accelerators, in that the foils do not require to be supported by fibers and three out of four of their edges are free of any support. Initial nanocrystalline diamond foils grown on silicon had issues of curling after their silicon substrates were etched away. To overcome this, Shaw and Feigerle introduced different lithography patterns onto the foils that would help keep the

foils flat after their silicon substrates were etched away. Several different lithography patterns have been designed, with a standard U-shape pattern being the most commonly used. Further information on the different lithography patterns and their success will be discussed in a later section.

The early-developed polycrystalline (microcrystalline and nanocrystalline) foils from ORNL were tested at BNL and proved to have a large advantage over other carbon foil types. Polycrystalline foils have a more rigid design, which decreases the amount of fluttering and beam loss; and are capable of withstanding higher beam temperatures before failure. Since 2006, the polycrystalline foils have been the primary foil utilized at SNS. These foils have shown to be quite successful, lasting a complete SNS run cycle and withstanding SNS design parameters: a pulsed beam at a frequency and width of 60 Hz and 1 ms, respectively, and a power level of 1.4 MW on the Target.

There have been several foils developed at ORNL and implemented into SNS that have been very successful. Two of these foils that survived beam powers of greater than 1.0 MW include a microcrystalline diamond foil (Foil #1073) and a nanocrystalline diamond foil (Foil #1108), both with a standard U-shape lithography pattern. The total charge placed on the microcrystalline and

nanocrystalline foils were 4,820 and 7,359 coulombs, respectively. Post beam photographs of Foils #1073 and #1108 are shown in Figure 1.19 and Figure 1.20, respectively. The darkening of the bottom right corner of the foil is the actual location where the injection and circulating beams pass through foil. In addition to the darkening, severe wrinkling and curling has occurred leading to tears along the edge of the freestanding diamond portion.

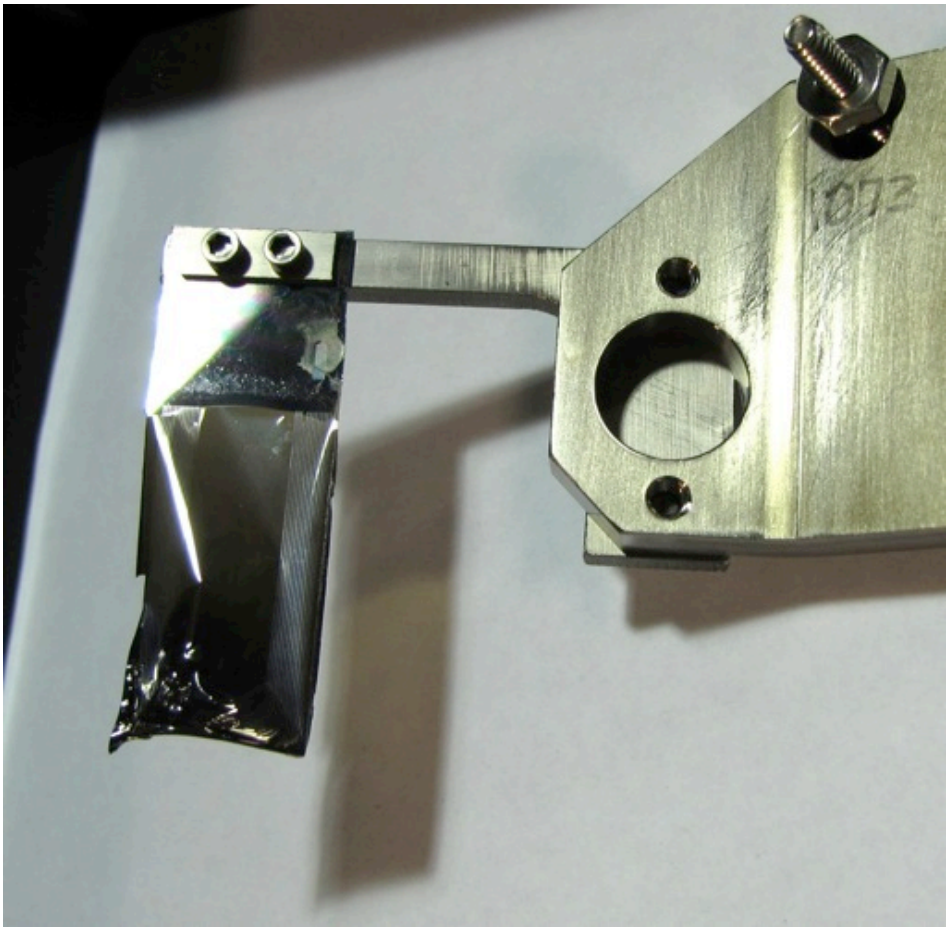

Figure 1.19 - Foil #1073 - Champion Foil #1 - A microcrystalline diamond stripper foil post-SNS production.

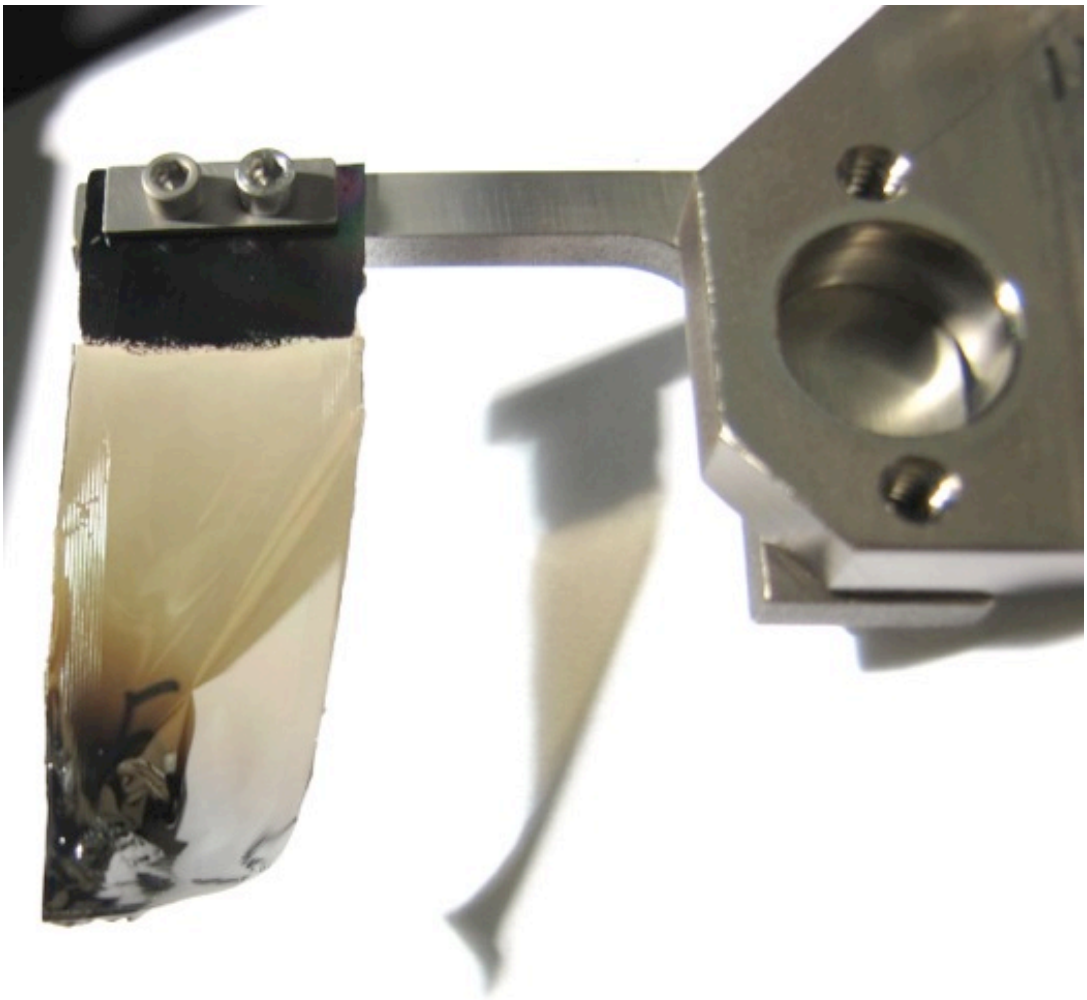

Figure 1.20 - Foil #1108 - Champion Foil #2 - Nanocrystalline diamond stripper foil post-SNS production.

1.4.2 Additional Stripper Foils used in SNS

Several other foils have been tested and characterized at SNS in situ, in a laboratory test stand at SNS, and at LANL [63, 64]. These foils include carbon foils from the Arizona Carbon Foil Company (ACFC), TRI University Meson Facility (TRIUMF), and BlueWave Semiconductor.

1.4.2.1 ACFC

The carbon foils from Arizona Carbon Foil Company (ACFC) were once tested in SNS. The ACFC foils are developed by high temperature evaporation-condensation onto a glass slide and have been used extensively throughout the world since 1964 because of their high quality and reliability [62, 65]. The ACFC foils have a turbostratic crystal structure. A turbostratic crystal structure is the case when graphene sheets are randomly stacked together and is illustrated in Figure 1.21 [62, 63, 64, 65, 66].

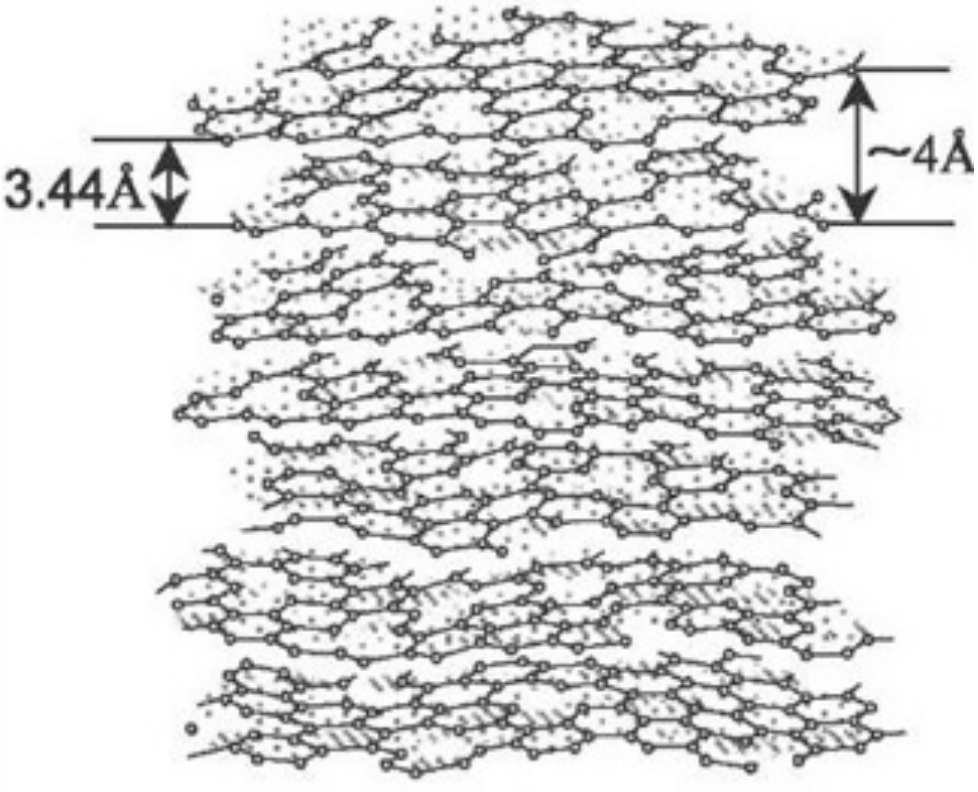

Figure 1.21 - Turbostratic Crystal Structure of the Arizona Carbon Foil.

The lifetimes of ACFC foils has been extensively measured at several particle accelerator facilities and were initially used at SNS to characterize and calibrate the beam and its stripping efficiency [62, 67, 68, 13]. Additional discussion on these tests will take place in Chapter 3. The ACFC foils used within SNS were placed on an aluminum bracket and held in place by 7 μm carbon fibers [65]. After a brief period where a cumulative power of only 199.6 MW was placed on the foil, the ACFC failed and was replaced by the early-developed microcrystalline foils from ORNL. The ACFC foils were installed three more times into the PFC, but the ACFC foils were never used again for production.

1.4.2.2 TRIUMF

TRI University Meson Facility (TRIUMF) developed the second type of carbon foils utilized within SNS [62, 68]. TRIUMF's staff developed a multilayer foil that had alternating layers of amorphous and Diamond-Like Carbon (DLC). The amorphous layers were created by carbon arc discharge, and the DLC layers were developed by the pulsed laser deposition (PLD) method [67]. The PLD method works by having a Nd:YAG infrared laser penetrate a glass vacuum window to the top of a bell jar. The laser is then defocused onto several optical mirrors and lenses that refocus the beam onto a sputter target. When the newly

focused laser beam hits the sputter target, it causes carbon particles to evaporate and deposit on nearby substrates. The length of time this process undergoes dictates the overall thickness of the film [67]. A single TRIUMF foil was tested within SNS in 2007. The high intensity and repetition rate of SNS beam decreased the structural integrity of the TRIUMF foil, preventing it from being used for a long period of time before being substituted out for another type [63, 64].

1.4.2.3 BlueWave Semiconductor

The next type of foil used within SNS is a nanocrystalline diamond foil grown by hot filament chemical vapor deposition by Blue Wave Semiconductor (BWS) [69]. Utilizing a silicon substrate patterned with a standard U-shape lithography pattern from ORNL, the BWS films were grown and displayed great uniformity across the substrate similar to the films grown by MPECVD. Films grown by BWS were shipped back to ORNL to have the silicon substrate etched away prior to being loaded into SNS for testing. The first BWS foil loaded within SNS performed very well and showed promise as a viable alternative to MPECVD. One concern of the BWS foils is that hot filament growth has the potential to introduce contaminants into the foil that come from the filament (e.g., tungsten) [70]. Although the foils performed well and any impurities that

may exist seemed to have no impact on the foil lifetime, it has not been determined if there are any long term effects from these impurities within SNS. A photograph of the BWS nanocrystalline foil after the silicon substrate is partially etched away is shown in Figure 1.22.

Figure 1.22 - BlueWave Semiconductor nanocrystalline diamond foil post-growth/etch.

1.4.2.4 HBC

The last type of foil that has been used within SNS is the Hybrid Boron mixed Carbon (HBC) foil developed by Isao Sugai et al. of the High Energy Accelerator Research Organization (KEK) in Japan. The HBC foils were grown by a technique devised at KEK known as the Controlled AC/DC Arc Discharge Method (CADAD) [13, 62, 63, 64, 71, 72, 73]. The CADAD method works by alternating arc discharge between an anode and a cathode. Typically films grown from an anode produce carbon clusters that have an average size of 3 nm. The smaller size makes these films very strong against mechanical shock but the film becomes fragile when placed within the beam. On the other hand films grown from the cathode produce larger carbon clusters, typical size being 500 nm. These films are able to withstand high intensity beams but are very sensitive to mechanical shock. Therefore, Sugai et al. decided to develop films that alternate between growth from an anode and growth from a cathode [13]. It was found that the lifetimes of the foils became sensitive to the following ratio:

$$\text{Lifetime Ratio} = \frac{Wc}{Wc+Wa}$$

Where:

W_c = discharged amount of carbon from the cathode

W_a = discharged amount of carbon from the anode

After several growths, it was found that the best conditions of foil growth were when the lifetime ratio was greater than 50%. Unfortunately, this limited the thickness of foils that could be grown before the foils began coming off of the glass substrate to approximately 130 ± 40 μg/cm^2. Therefore, the graphite rods were doped with various atoms, in particular boron (B) up to 20%. These foils became known as the Hybrid Boron mixed Carbon Stripper Foils (HBC foil). The HBC foils are limited to a maximum aerial density of approximately 170 – 200 μg/cm^2 before the films begin to peel away from their glass substrate. Sugai and coworkers performed lifetime measurements using a 3.2 MeV Ne^+ beam with a current of 2.5 ± 0.5 μA and a spot size diameter of 3.5 mm, determining how the HBC foils would compare to other commonly used stripper foils used in accelerators [74, 75, 76]. The foils tested included HBC foils of 200 – 380 μg/cm^2, diamond foils (DM foils) of 350 μg/cm^2, diamond foils of 680 – 780 μg/cm^2, and commercially available thick foils (CM-foils) of 200 – 400 μg/cm^2. Under these specific beam conditions, Sugai et al. was able to show that the HBC foils had a much longer lifetime than commercially available foils, diamond foils, and undoped carbon foils made by the CADAD method [77]. Table 1.1 list results from that study.

A set of HBC foils were used for a brief period within SNS during the 2014

Table 1.1 - Maximum and Average lifetime of HBC, Diamond (DM), and commercially available (CM) foils measured with a 3.2 MeV Ne+ ion beam of 2.5± 0.5 μA on a 3.5 mm diameter beam spot.

Type of foils	HBC-Foil	DM-Foil	CM-Foil
Max lifetime (mC/cm^2)	7,100	97	22
Average (mC/cm^2)	5,400	89	20

cycle. To meet SNS's aerial density requirement of 350 μg/cm^2, two HBC foils of approximately 170 μg/cm^2 thickness were used in conjunction with one another. Since the foils did not have a way of being mounted directly to the foil bracket, a set of carbon fibers were used to hold the two foils together on the bracket. Following the standard ramp up protocol within SNS, the HBC foils began to show immediate issues with foil flutter. After a short period in production mode, the foils were deemed non-operational due to their severe foil flutter. When the foils were taken out of SNS, it was found that the two foils that had been joined together by carbon fibers were no longer together and had essentially bowed out from one another. Since the foils were now no longer in parallel together, SNS was essentially experiencing a single foil of ~170 μg/cm^2. The separation of the two foils and the significant foil flutter, lead to high beam losses and a substantial decrease in stripping efficiency. Photographs of the HBC foils before and after being placed into SNS are shown in Figure 1.23 and Figure 1.24, respectively [13, 72]. The HBC stripper foils have had great success at J-

PARC, but had very little success on the two tests performed under SNS beam conditions.

1.4.3 Comparison of Stripper Foils

Several types of foils have been used at SNS since it was placed into production mode in 2006, as mentioned in the preceding sections. A list of the types and quantities of foils used, along with the thickness ranges and the amount of charge the foils experienced while in SNS are in Table 1.2. By far the most commonly used foil within SNS is the nanocrystalline diamond foil developed at ORNL. This foil has become the "go-to-foil" when SNS operators require a reliable and predictable foil. This foil has been extensively studied and characterized to help predict how it will perform under a variety of SNS conditions, and has been able to survive SNS design power level of 1.400 MW. The major limitation of this foil that was mentioned in the preceding section is the mechanical defects that are formed from post-growth handling and development. Despite these foils being made of one of the strongest material known to man (i.e., diamond), these foils are still very fragile. The freestanding diamond portion of the foil has been known to break off from the silicon handle from a turbulent air current or if the etching process to remove the silicon substrate becomes too rapid. Other foils that performed very well, but less

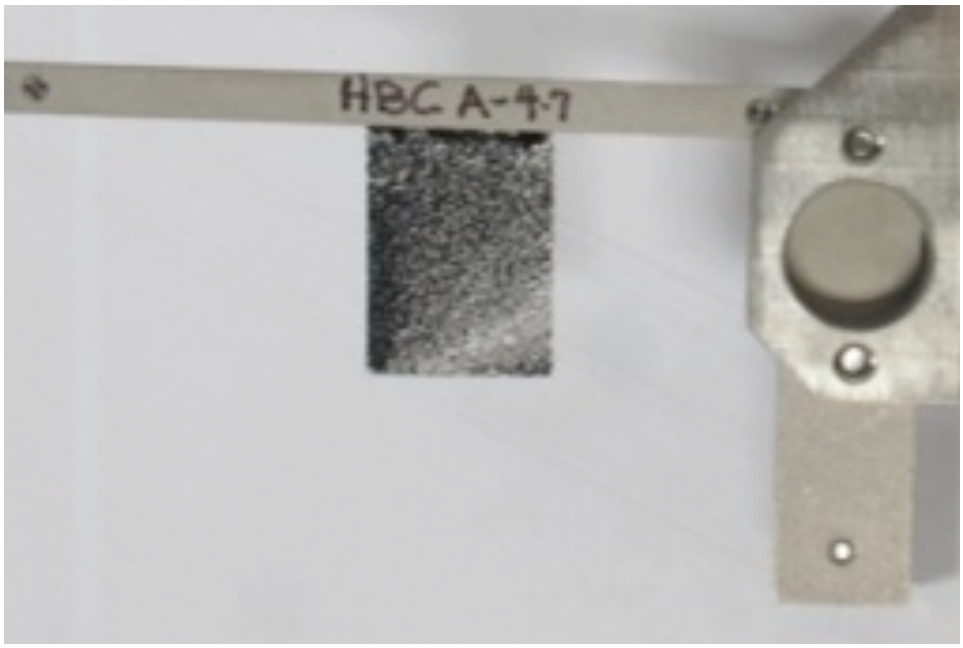

Figure 1.23 – Sugai's HBC foils supported by carbon fibers prior to being placed into SNS for production mode.

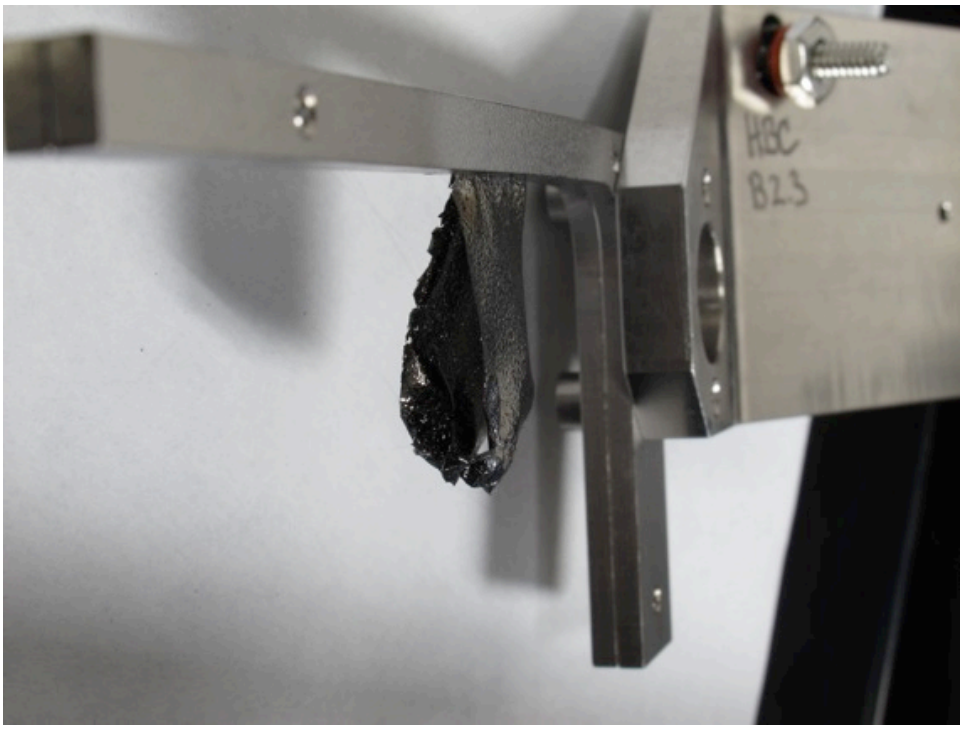

Figure 1.24 - Sugai's HBC foil postproduction mode in SNS. The two HBC foils separated despite being held in together by carbon fibers.

Table 1.2 - Primary Stripper Foils Used-to-Date Within SNS.

Foil Type	Number of Foil Used	Thickness Weight ($\mu g/cm^2$)			Charge to Target (Coulombs)		
		Minimum	Average	Maximum	Minimum	Average	Maximum
Diamond Like Carbon ACFC	4	260	260	260	N/A	N/A	N/A
Boron-Doped Nanocrystalline Diamond - ORNL	6	302	334	356	0.092	1666.529	6952.879
Microcrystalline Diamond ORNL	15	265	329	463	94.000	912.849	2561.337
Nanocrystalline Diamond ORNL	41	265	317	391	48.600	1180.642	3177.000
TRIUMF	1	N/A	N/A	N/A	-	16.000	-
HBC KEK - Sugai	2	340	345	350	39.822	711.121	1382.420
Nanocrystalline Diamond BlueWave Semiconductor	1	-	327	-	-	1707.49	-

frequently, include: the microcrystalline diamond and boron-doped nanocrystalline diamond made at ORNL, and the nanocrystalline diamond foils made by BlueWave Semiconductor. Certain foil types have not performed as well under SNS operational conditions. These foils include the carbon foils from TRIUMF, the diamond like carbon foils from ACFC, and the HBC foils by Sugai. These three foils perform well at other facilities in which the beam intensity is much lower. Additionally, these three foils require fiber supports. The use of fibers, mainly carbon fibers, helps keep the foil flat and rigid to provide a uniform surface for stripping. Unfortunately, at high intensities, the fibers tend to break and the foil subsequently flutters intensely. This intense foil fluttering makes the operation of the SNS machine very difficult, and therefore the foil is typically replaced with a more rigid foil. The ACFC as mentioned previously, were initially used to characterize SNS machine and help determine beam loss prior to developing a standard for a nanocrystalline diamond foil. After a standard was created for the nanocrystalline diamond foil on stripping efficiency, the uses of ACFC became obsolete and haven't been used within SNS since its early days. The TRIUMF foil was used once with very little success and quickly failed due to large foil flutter. The HBC foils developed by Sugai have been implemented twice within SNS. The HBC foils have had great success at KEK and J-PARC, which has a similar design to SNS but at a much lower

intensity. Despite this success, the higher intensity beam at SNS is too detrimental to the HBC foils. The HBC foils experience high foil flutter and high beam loss, making these foils unusable for SNS operation.

In conjunction with a variety of foils being implemented within SNS, several types of lithography patterns have been designed and used on the diamond foils developed at ORNL. The various lithography patterns have been researched to provide better stabilization for the foils to prevent and/or minimize foil flutter. These lithography patterns include U-shaped (50 and 100 lines per inch), checkerboard, Full U, U Sine, U with square corners, random ellipses, and concentric rings. A pictorial representation of the types of lithography patterns currently developed is in Figure 1.25. The success of the different types of lithography patterns will be discussed in a proceeding chapter.

Research of the impact that other physical features have on the performance of the films has been studied. These other features include how the edges of the freestanding diamond portion affect foil flutter. When the diamond film is grown on the silicon substrate, the film is deposited on the top of the substrate as well as along the sides of the substrate. When the silicon substrate is etched away from the diamond, it typically leaves a uniform edge around the

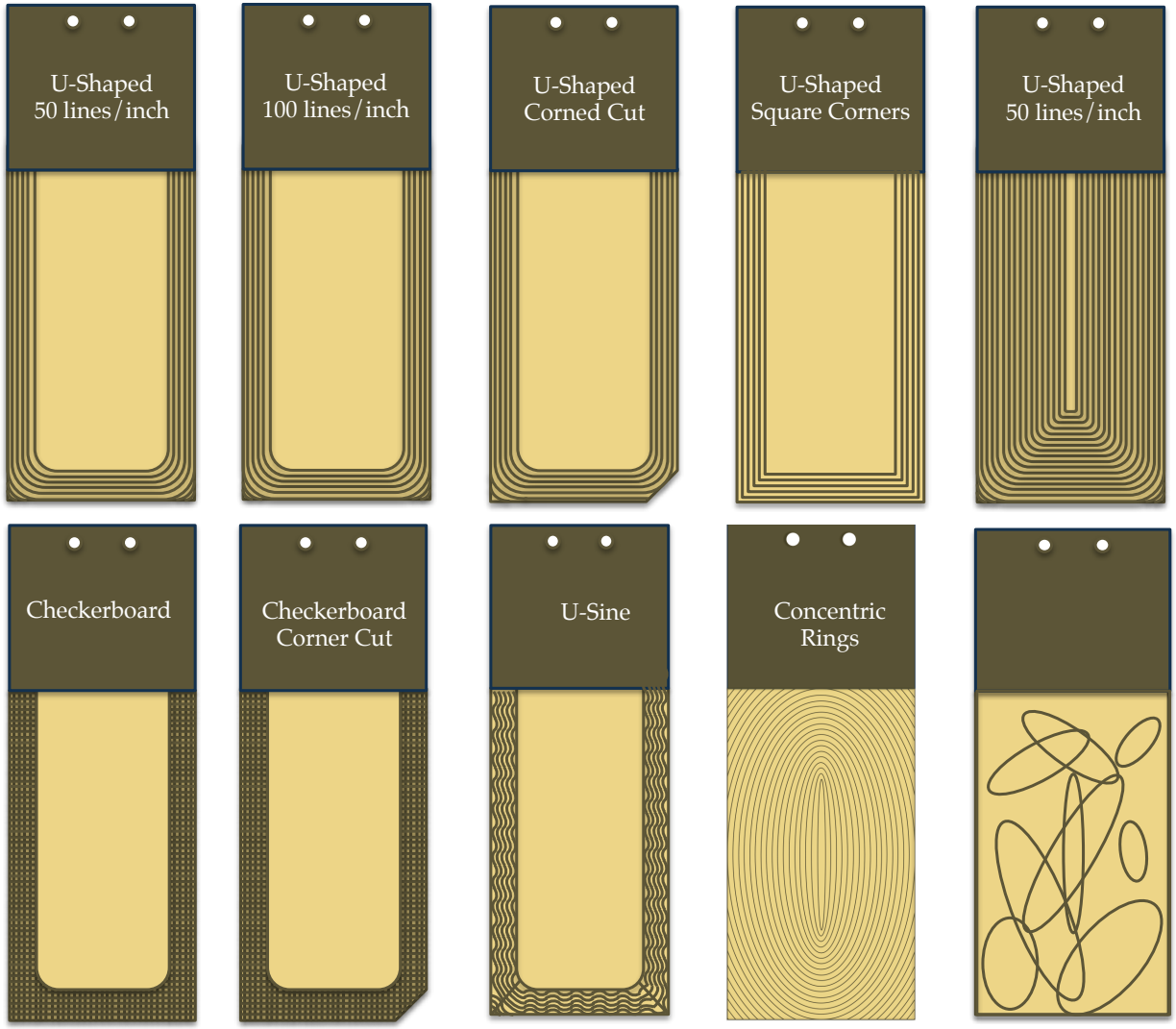

Figure 1.25 - Depiction of some of the various types of lithography patterns developed at ORNL.

etched away from the diamond, it typically leaves a uniform edge around the sides of the foil that has been labeled as the "box-top lid," due to the remarkable similarity to a lid on a shoebox. This box-top lid is typically 1 μm thick, which corresponds to the thickness of the silicon substrate. Researchers at SNS were initially concerned that this increase in thickness along the edge would increase beam loss and scattering. Therefore, portions of the film's box-top lid was removed, along with a 90-degree cut at one of the bottom corners to help eliminate some beam loss as the injection and circulating beams passed through the film. The 90-degree cut was performed both pre- and post-growth. In order to compare how the removal of the box-top lid affected foil performance, additional foils were developed that had a continuous box-top lid around the foil. The effects that the lithography patterns and the box-top lids had on the performance of the foils will be discussed in a proceeding chapter. A pictorial representation of the foils and their various types of box-top lids are illustrated in Figure 1.26 to Figure 1.29.

1.4.4 Champion Stripper Foils

There have been a few foils in SNS lifetime that have lasted almost an entire SNS run cycle, and have been given the term "champion foil." There have also been numerous foils that survived SNS for a month without failing and were

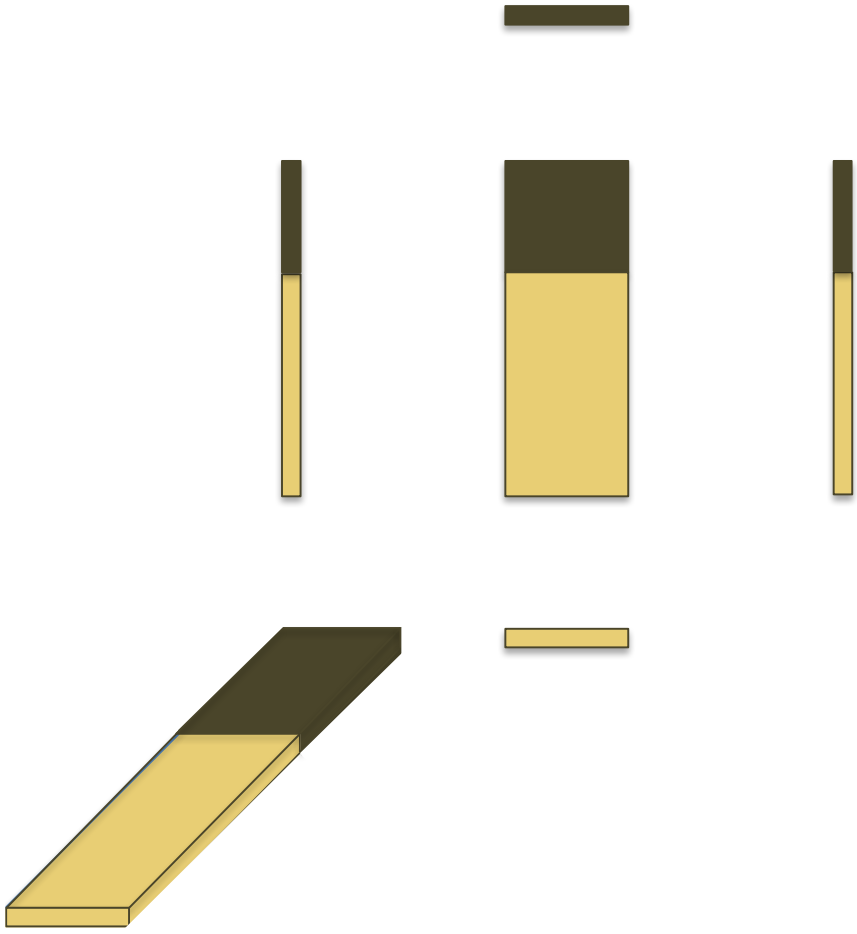

Figure 1.26 - Diagram of a diamond foil with a full box top edge.

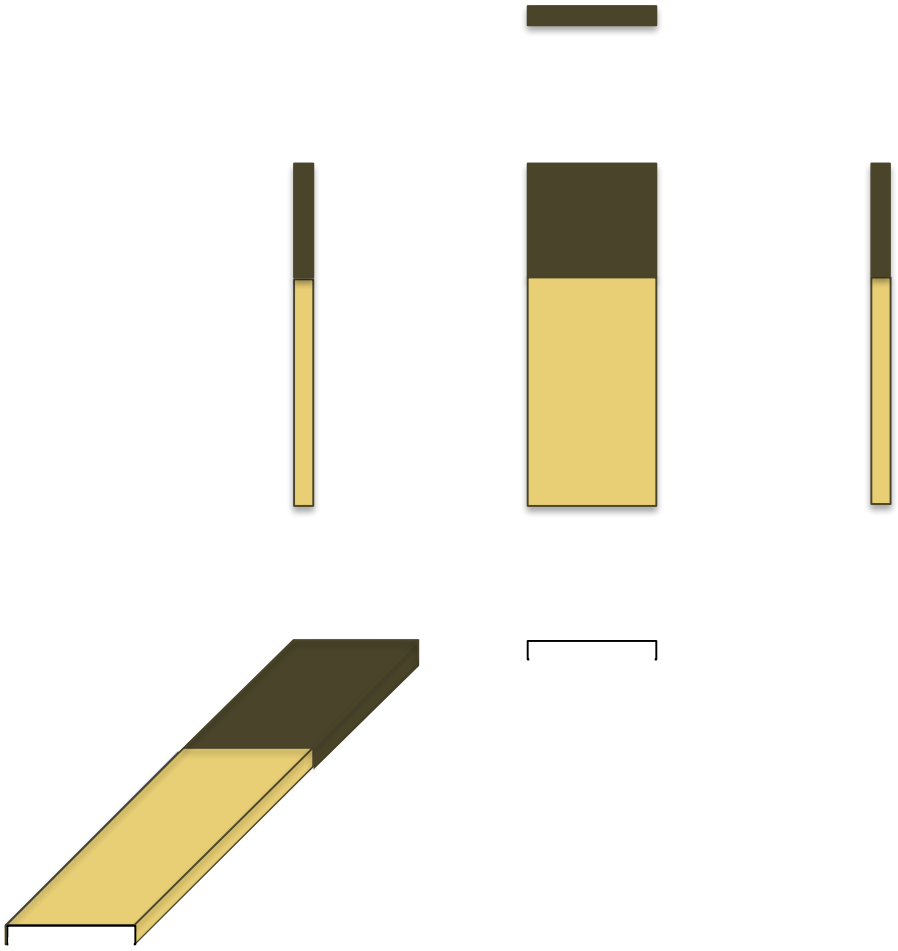

Figure 1.27 - Diagram of a diamond foil with the box top edge along the sides but removed from the bottom.

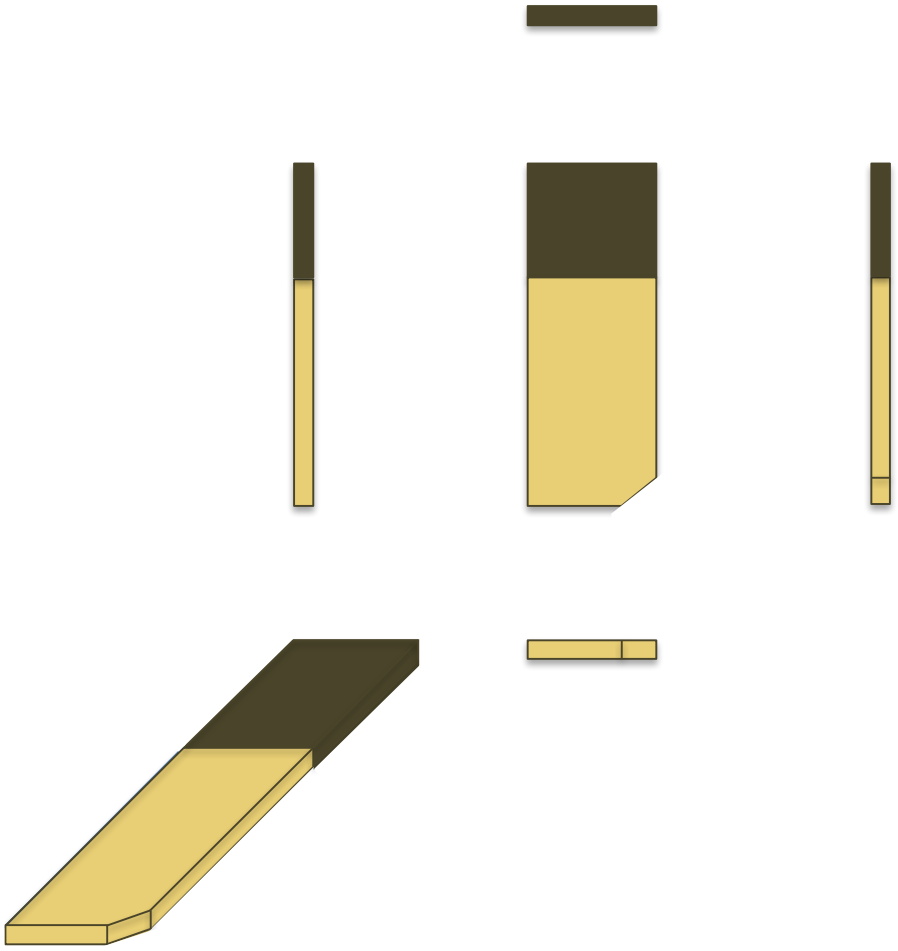

Figure 1.28 - Diagram of diamond foil with corner cut pre-growth to allow a continuous box-top lid.

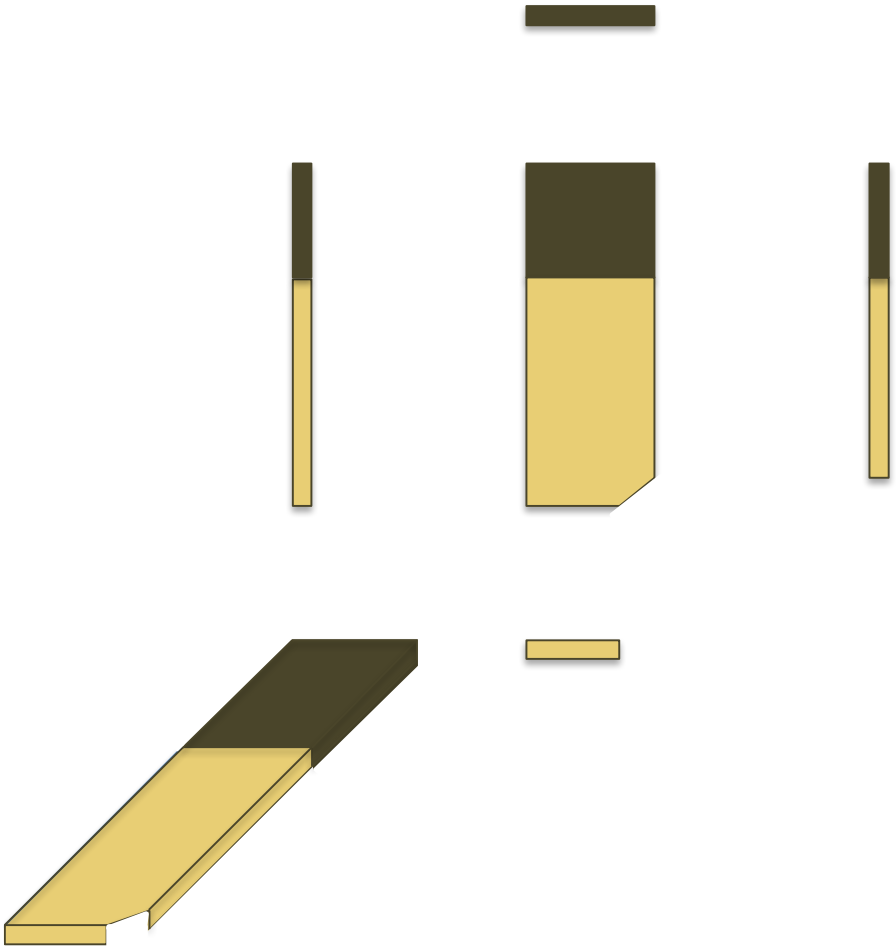

Figure 1.29 - Diagram of diamond foil with corner cut post growth, leaving a partially incomplete box-top lid

only removed from production to try a different foil. These foils have a variety of properties that led to their success.

The first champion foil was Foil #1073, which was a nanocrystalline diamond foil made by MPECVD at ORNL. Foil #1073 had the following properties: an aerial density measured by alpha ranging of 344 $\mu g/cm^2$, an U-shaped lithography pattern of 50 lines/inch, a box-top lid on all sides, a total size of 17 mm x 45 mm with the standard free diamond portion of 17 mm x 30 mm, and was a relatively continuous film as revealed by SEM. After the silicon substrate was etched away: the foil remained flat with no curling, showed no tears along the box-top lid, and was a perfect foil without any noticeable physical defects. The foil was attached to a titanium foil bracket and loaded into the PFC on August 5, 2009. Conditioning of the foil started on September 3, 2009, and was placed into production on September 8, 2009, until the end of SNS run cycle on December 22, 2009. During the approximate four-month cycle, the foil received the following: an average beam energy of 928.00 MeV, a total charge of 4,820 Coulombs, a total power deposition of 1,254.658 MW, and a peak power level of 1,038.400 kW or 1.038 MW. This foil never failed during operation but was rather removed from the beam due to the end of SNS run cycle. A post-production photograph of Foil #1073 is shown in Figure 1.30.

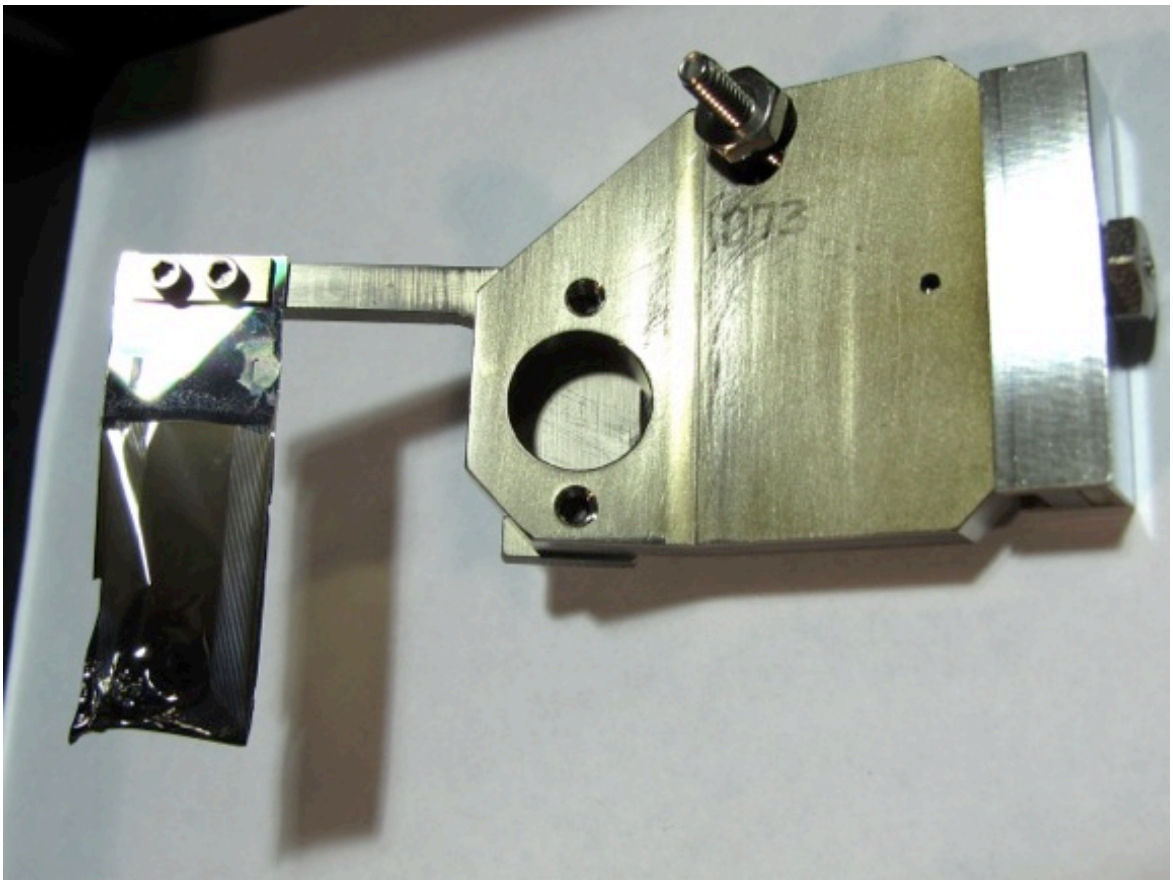

Figure 1.30 - Foil #1073 after being used in SNS during production mode.

The second champion foil was Foil #1108, and it was also a nanocrystalline diamond foil made by MPECVD at ORNL. Foil #1108 had the following properties: an aerial density measured by alpha ranging of 332 μg/cm^2, an U-shaped lithography pattern of 50 lines/inch, a box-top lid on all sides, a total size of 17 mm x 45 mm with the a free diamond portion of 17 mm x 35 mm, and was a relatively continuous film as revealed by SEM. After the silicon substrate was etched away: the foil remained relatively flat with a slight curling, showed a small vertical tear on box-top lid near the silicon edge, and contained no

additional physical defects. The foil was attached to a titanium foil bracket and loaded into the PFC on August 5, 2009. Conditioning of the foil started on February 18, 2010, and was placed into production on February 23, 2010 until the end of SNS run cycle on June 30, 2010. During the approximate four-month cycle, the foil received the following: an average beam energy of 925.05 MeV, a total charge of 7,359 Coulombs, a total power deposition of 1,890.792 MW, and a peak power level of 1,085.499 kW or 1.086 MW. Similar to Foil #1073, Foil #1108 never failed during operation but was rather removed from the beam due to the end of SNS run cycle. A post-production photograph of Foil #1108 is shown in Figure 1.31.

The third champion foil was Foil #B1616, which was a boron-doped microcrystalline diamond foil made by MPECVD at ORNL. Foil #B1616 was doped with 10 ppm diborane and had the following properties: a blue appearance, an aerial density measured by alpha ranging of 308 $\mu g/cm^2$, an U-shaped lithography pattern of 100 lines/inch, a box-top lid on all sides except where the corner of the foil was cut off post-growth, a total size of 17 mm x 45 mm with the a free diamond portion of 17 mm x 31 mm, and was a relatively continuous film as revealed by SEM. Unlike the first two champion foils, Foil #B1616 was etched without the use of tape to protect the silicon substrate (which

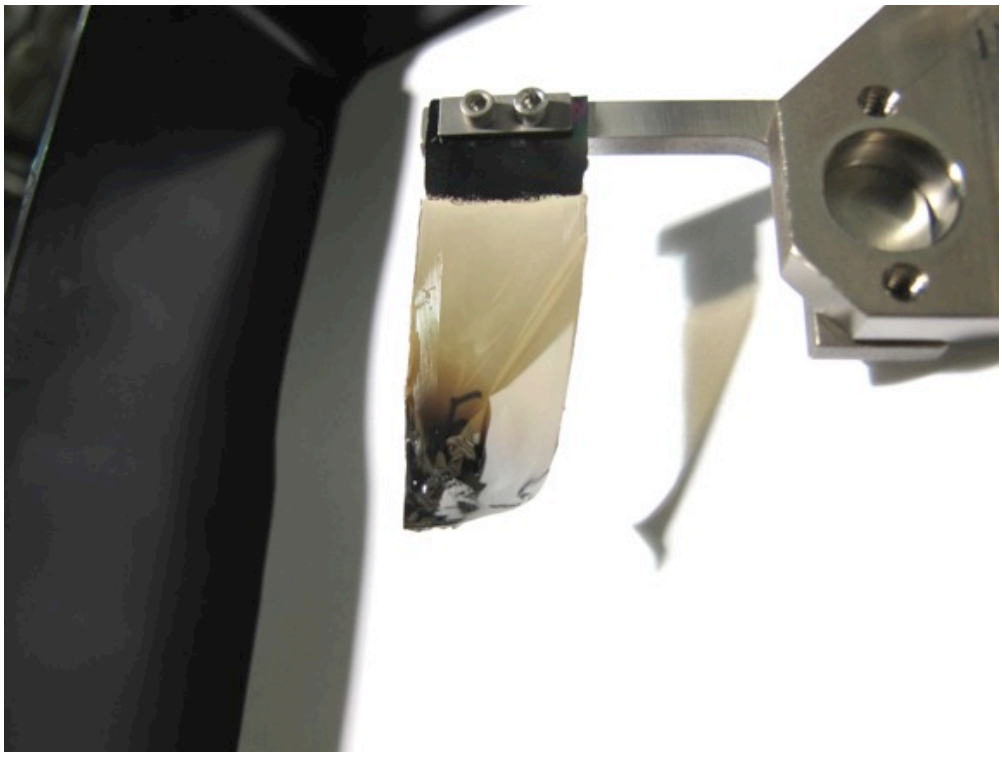

Figure 1.31 - Foil #1108 after being used in SNS for production; intense curling of the foil occurred.

#B1616 was etched without the use of tape to protect the silicon substrate (which reduced the amount of outgassing that occurred when conditioning on the foil began). After the silicon substrate was etched away: the foil remained relatively flat, had a horizontal rip 4 mm below the silicon handle on the bracket size, and contained no additional physical defects. The foil was attached to a titanium foil bracket and loaded into the PFC on January 31, 2012. Conditioning of the foil started on March 13, 2012, and was placed into production from March 13, 2012, to April 9, 2012. The foil performed very well in this initial month of production and was switched out to try a different foil. After this different foil had issues,

Foil #B1616 was placed back into production mode on April 13, 2012, and used for the remaining of SNS cycle that ended on June 20, 2012. The foil overall had the following characteristics while in production: very little foil flutter, curling of the foil that worsened and then flattened out, and hot spots along the bottom edge for a short period of time. During the approximate five-month cycle, the foil received the following: an average beam energy of 910.80 MeV, a total charge of 6,952.879 Coulombs, a total power deposition of 1,757.860 MW, and a peak power level of 1,051.026 kW or 1.051 MW. Similar to the first two champion foils, Foil #B1616 never failed during operation but was rather removed from the beam due to the end of SNS run cycle. The foil was removed from the PFC on July 17, 2012.

The fourth champion foil was Foil #1499, and it was also a nanocrystalline diamond foil made by MPECVD at ORNL. Foil #1499 had the following properties: an aerial density measured by alpha ranging of 344 $\mu g/cm^2$, an U-shaped lithography pattern of 100 lines/inch, a corner cut post-growth, a box-top lid on all sides except for the 45 degree angle on the corner, a total size of 17 mm x 45 mm with the a free diamond portion of 17 mm x 30 mm, and was a relatively continuous film as revealed by SEM. After the silicon substrate was etched away, the foil was floppy because it was missing 8 mm of its box-top lid right

below the silicon handle. The foil was attached to a titanium foil bracket and loaded into the PFC on August 7, 2012. Conditioning of the foil started on January 5, 2013, and was placed into production from February 5, 2013 until being switched out on April 2, 2013. The foil performed very well, with hot spots visible only on the first day and a measured stripping efficiency of 98.2%. During the approximate two-month cycle, the foil received the following: an average beam energy of 910.80 MeV, a total charge of 3,498 Coulombs, a total power deposition of 1,757.860 MW, and a peak power level of 1,051.026 kW or 1.051 MW. Similar to the other champion foils, Foil #1499 never failed during normal operation but was rather used for a high hit density test on April 1, 2013, for 7 hours and 22 minutes. The foil was removed from the PFC on July 23, 2013.

The fifth champion foil was Foil #1872, and it was also a nanocrystalline diamond foil made by PECVD at ORNL. Foil #1872 had the following properties: an aerial density measured by alpha ranging of 339 $\mu g/cm^2$, an U-shaped lithography pattern of 100 lines/inch, a corner cut post-growth, a box-top lid on all sides except for the 45 degree angle on the corner, a total size of 17 mm x 45 mm with the a free diamond portion of 17 mm x 29.5 mm, and was a relatively continuous film as revealed by SEM. After the silicon substrate was etched away without the use of tape, the foil had a slight twist on the bracket

side but had no visible tears or other physical defects. The foil was attached to a titanium foil bracket and loaded into the PFC on July 23, 2013. Conditioning of the foil started on February 18, 2014, and was placed into production from February 18, 2014 until being switched out on April 6, 2014. The foil performed very well, with a slight fluttering during its first few weeks of production but then stabilized for the last few weeks of operation. The foil was still in good shape when removed from production. During the approximate two and half month cycle, the foil received the following: an average beam energy of 910.80 MeV, a total charge of 4,633 Coulombs, a total power deposition of 2,108.927 MW, and a peak power level of 1,421.391 kW or 1.421 MW. Similar to the other champion foils, Foil #1872 never failed during operation but was rather removed from the beam due to the end of SNS run cycle. The foil was removed from the PFC on July 31, 2014.

The sixth champion foil was Foil #1402, and it was also a nanocrystalline diamond foil made by MPECVD at ORNL. Foil #1402 had the following properties: an aerial density measured by alpha ranging of 320 $\mu g/cm^2$, an U-shaped lithography pattern of 100 lines/inch, a corner cut post-growth, a box-top lid on all sides except for the 45 degree angle on the corner, a total size of 17 mm x 45 mm with the a free diamond portion of 17 mm x 30 mm, and was a relatively

continuous film as revealed by SEM. After the silicon substrate was etched away with the use of tape, the foil had a hole on the beam side that was approximately 16.5 mm from the bottom and 6 mm from the side. The foil was attached to a titanium foil bracket and loaded into the PFC on August 5, 2010. Conditioning of the foil started on November 2, 2010, and was placed into production from November 9, 2010, until being switched out on December 22, 2010. The foil performed very well, with a slightly increase beam ramp of 400 kW to 900 kW over a 1.5 days. The foil was still in good shape when removed from production. During the approximate one and half month cycle, the foil received the following: an average beam energy of 925.00 MeV, a total charge of 3,177 Coulombs, a total power deposition of 802.878 MW, and a peak power level of 1,085.688 kW or 1.086 MW. Similar to the other foils, Foil #1402 never failed during operation but was rather removed from the beam due to the end of SNS run cycle. A post-production photograph of Foil #1402 is shown in Figure 1.32.

In addition to these six champion foils, there were several other foils that performed very well and lasted an average of one month while SNS was in production mode before being switch out for another foil. The additional champion foils are listed in the following table, Table 1.3. The most common foil used within SNS, the nanocrystalline diamond foil made at ORNL by MPECVD

with an U-shaped lithography pattern, had the overall best performance.

1.4.5 Post-analysis of stripper foils

Analysis of the foils that have been used within SNS has been rather difficult because of the high radioactivity of the foils and the potential for the foils to break. If a used foil were to break, it has the potential to be swept up in an air current and cause radiation contamination in the surrounding

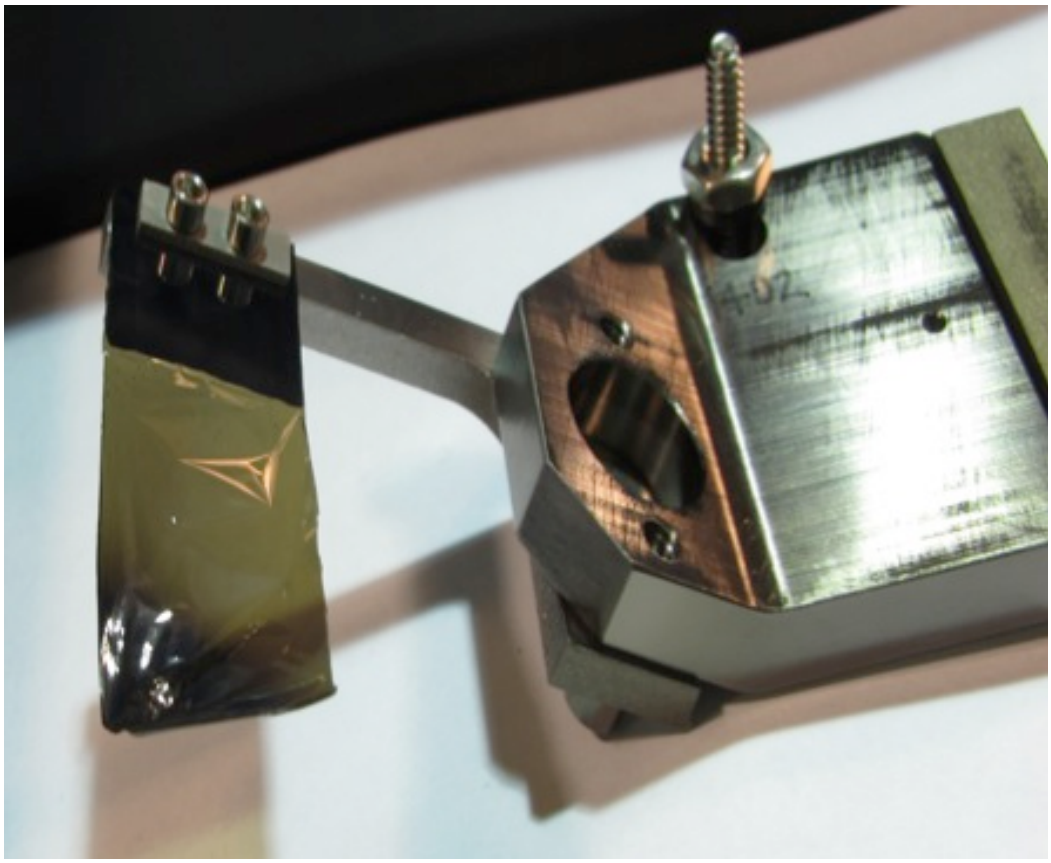

Figure 1.32 - Photograph of Foil #1402 after being used in SNS for production.

Table 1.3 - Additional Champion Foils used with SNS

Foil #	Foil Type	Pattern	Corner Cut	Overall Size (mm x mm)	Free-Standing (mm x mm)	Aerial Density by α-Ranging ($\mu g/cm^2$)	Average Beam Energy (MeV)	Charge on Target (Coul.)	Power on Target (MW)	Peak Power on Target (MW)
1143	ND	U-50	No	17 x 45	17 x 35	368.0	925.00	2010	536.477	1.018
1443	ND	U-100	After	17 x 45	17 x 30	326.0	925.00	1646	426.289	0.931
1437	ND	U-100	After	17 x 45	17 x 30	326.0	925.00	2120	553.787	0.881
1439	ND	U-100	After	17 x 45	17 x 30	326.0	925.00	2162	545.575	0.846
1467	ND	U-100	After	17 x 45	17 x 30	344.0	925.00	1405	360.886	0.839
1477	ND	U-100	After	17 x 45	17 x 30	320.0	925.00	1666	428.094	0.845
1497	ND	U-100	After	17 x 45	17 x 30	344.0	925.00	1614	414.645	0.835
1508	ND	U-100	After	17 x 45	17 x 28	344.0	925.00	1294	332.383	0.837
1524	ND	U-100	After	17 x 45	17 x 30	320.0	925.00	1457	374.273	1.017
1474	ND	U-100 Checker	After	17 x 45	17 x 30	368.0	925.00	2271	583.597	1.044
1495	ND	U-100	After	17 x 45	17 x 30	356.0	918.51	2245	568.086	1.036
B1674	BD	U-100	After	17 x 45	17 x 30	356.0	910.80	2480	616.980	1.034
B1752	BD	U-100	After	17 x 45	17 x 30	350.0	910.80	2449	97.881	1.039

Table 1.3 - Additional Champion Foils used within SNS - Continued

Foil #	Foil Type	Pattern	Corner Cut	Overall Size (mm x mm)	Free-Standing (mm x mm)	Aerial Density by α-Ranging ($\mu g/cm^2$)	Average Beam Energy (MeV)	Charge on Target (Coul.)	Power on Target (MW)	Peak Power on Target (MW)
1792	ND	U-100	After	17 x 45	17 x 30	320.0	910.80	1633	425.464	0.870
1501	ND	U-100	After	17 x 45	17 x 30	320.0	910.80	1925	501.637	0.873
1554	ND	U-100	No	17 x 45	17 x 30	368.0	910.80	1884	477.819	0.866
1822	ND	U-100	Before	17 x 45	17 x 30	352.0	910.80	1869	478.485	0.917
1839	ND	U-100	Before	17 x 45	17 x 29.5	352.0	910.80	1842	483.819	1.398
HBC B-2.3	HBC	-	No	17 x 25	17 x 25	350.0	910.80	1382	358.293	0.862
1862	ND	U-100	Before	17 x 45	17 x 30.5	364.0	910.80	2582	669.223	0.868
1505	ND	U-100	After	17 x 45	17 x 30	344.0	910.80	2120	240.215	1.063

environment. Despite this issue, careful handling of the foils has allowed post-beam analysis of almost all the foils by photographs and a select number of foils by a scanning electron microscope (SEM). Post-beam analysis foils have shown a wide-range of damage, ranging from a slight wrinkling and darkening of the foil to a complete removal of the freestanding foil from the silicon handle. It has been noted on several occasions that the foils that experience severe foil flutter within SNS typically have a mechanical defect that is causing the foil to shake. These mechanical defects include a horizontal rip across the freestanding portion of the foil, a vertical tear along the edge of the foil (i.e., box-top lid), a break between the freestanding portion and the silicon handle, and severe curling or wrinkling of the foil. Some of these defects are shown in the following post-beam analysis photographs in Figure 1.33 and Figure 1.34.

Additional analysis of one of these foils, Foil #1792, by a scanning electron microscope (SEM) was completed to determine if and how the crystallinity of the foil changed after being placed in SNS beam line. The SEM took images of the foil in multiple locations, including both irradiated and non-irradiated areas. It was shown that prior to the foil being irradiated by SNS beam, the foil had uniform clusters and particle distributions. Post-irradiation by SNS beam, the foil's crystallinity changed from multiple clusters on the order of several

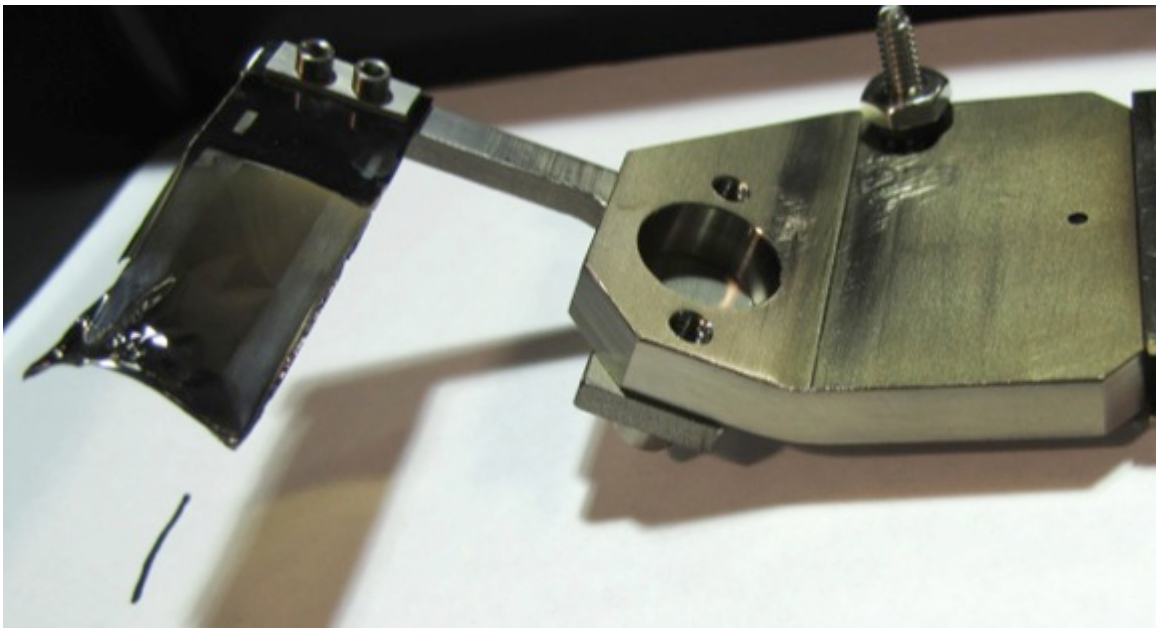

Figure 1.33 - Illustration of various tears and rips in Foil #1073 after being used in SNS.

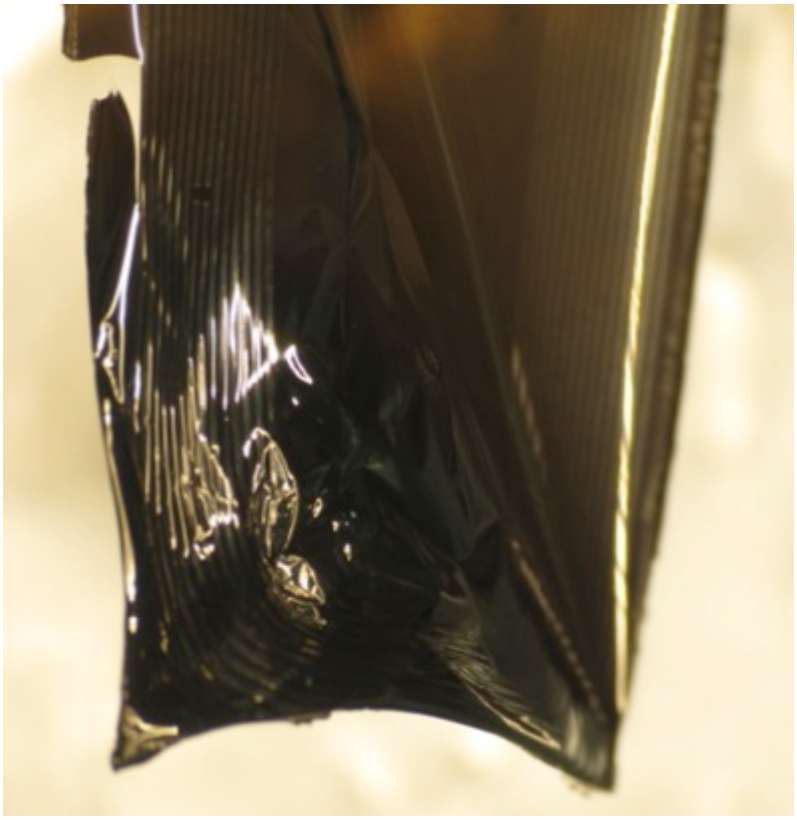

Figure 1.34 - Photograph of Foil #1073 curling that the stripper foils undergo when place into SNS under high thermal loads.

nanometers to several hundred nanometers. A SEM image of a spot that has and hasn't received irradiation from SNS beam is shown in Figure 1.35.

1.5 SNS Current Conditions and Problems

The current status of SNS is providing researchers with a 1.0 to 1.4 MW beam of protons to the mercury Target. The protons spall neutrons off from the mercury within the Target. The neutrons are then focused onto several different instruments for research. From 2014 to 2015, several obstacles delayed the progress of SNS to provide a constant design value of 1.4 MW. Some examples that SNS employees have faced during that time frame included several Target failures; water contamination in various portions of the Linac; and multiple components that have either failed completely or have limited operation. Despite these issues, SNS employees have been able to successfully diagnosis and resolve these problems. Allowing SNS personnel to continue delivering the scientific community the most intense pulsed neutron beams in the world.

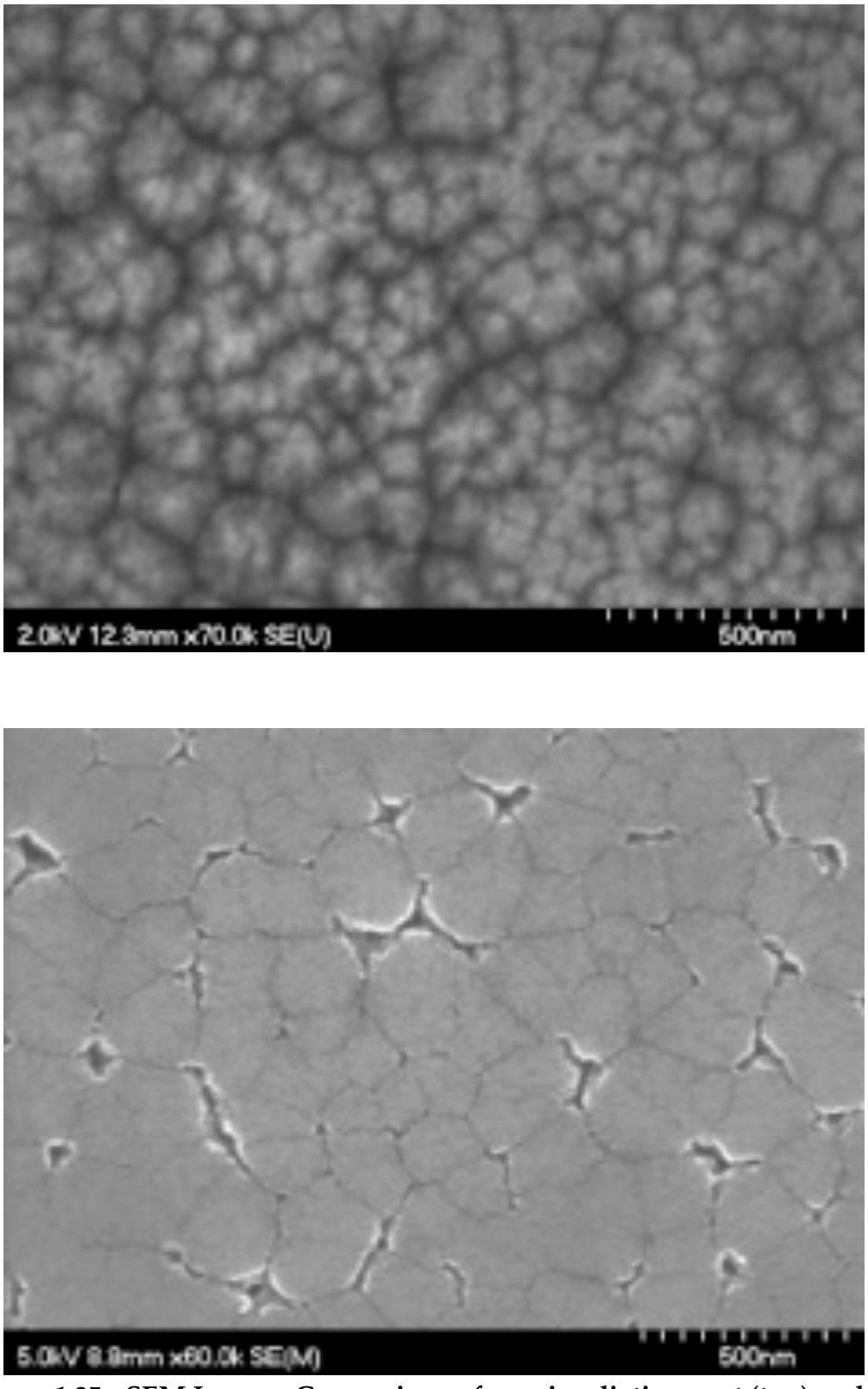

Figure 1.35 - SEM Image - Comparison of non-irradiation spot (top) and an irradiated spot (bottom)

1.6 Purpose of Foil Development Team

The Foil Development Team was developed in 2001 and it consists of members from ORNL, SNS, and UTK. This group has highly skilled technicians in foil growth and development, experts in chemical vapor deposition, and experts in accelerator physics. The mission of this group is to: design and develop foils for the use in SNS to help maintain current operating conditions of 1.0 to 1.4 MW, develop foils for future SNS upgrades of 2.0 and 3.0 MW, and characterize these foils throughout their entire lifecycle. One aspect of this team that is of particular interest is to determine how well the foils will perform under increasing beam conditions. This includes the use of an electron beam test stand to help determine how foils will perform under both present and future thermal loads within SNS.

Chapter 2. Foil Test Stand - Experimental

2.1 Introduction and Purpose of FTS

The Spallation Neuron Source (SNS) at Oak Ridge National Laboratory (ORNL) has successfully operated since 2006 with only a few interruptions. SNS currently uses a standard nanocrystalline diamond foil that typically has an aerial density of 350 $\mu g/cm^2$ and a U-shaped lithography pattern (refer to previous chapter for description of lithography patterns). In recent years, SNS employs a foil for one month of operation before replacing it. This accounts for approximately eight to ten foils per year. After SNS started full operation in 2006, there was great need to have the instrument reliable for the various users coming from around the world. Therefore, it was difficult to experiment with different foil composition and types that are currently being developed, and severely limited the foil development program. In 2009 the Foil Development Team (FDT), composed of individuals from ORNL, SNS, and the University of Tennessee at Knoxville (UTK), deemed it necessary to develop a table top test stand that would allow a more adaptable approach to testing foil properties than what could be done during normal operation at SNS [78, 79, 80]. This test stand would allow a variety of foils to be examined, along with determining the various properties that influence the success of a foil within SNS. Since having an accelerated H^- beam was not feasible as a table top source, there was need to

have a source that would both meet the size restriction and still apply the same thermal load that the foils experience during operation. Therefore, it was calculated that a thirty thousand electron-volt (30 keV) beam could apply a spot on a foil with a high enough current density to simulate the thermal load of SNS [78, 79]. This device became known as the Electron Beam SNS Foil Test Stand, or more commonly the Foil Test Stand (FTS).

2.2 Description of Foil Test Stand

The Foil Test Stand (FTS) was designed and built by members of the Foil Development Team (FDT) in 2009, to further the advancement of the foil development program. The FTS consists of several different components, including a 30 keV electron gun, a faraday cup and limiting aperture, a residual gas analyzer, various vacuum components, an actuator and bracket that allows up to four foils to be attached, an infrared camera, a high definition video recorder, and a stainless steel vacuum chamber that houses several of these components [78, 79]. An illustration of the FTS that indicates where each major component is located with respect to one another is shown in Figure 2.1.

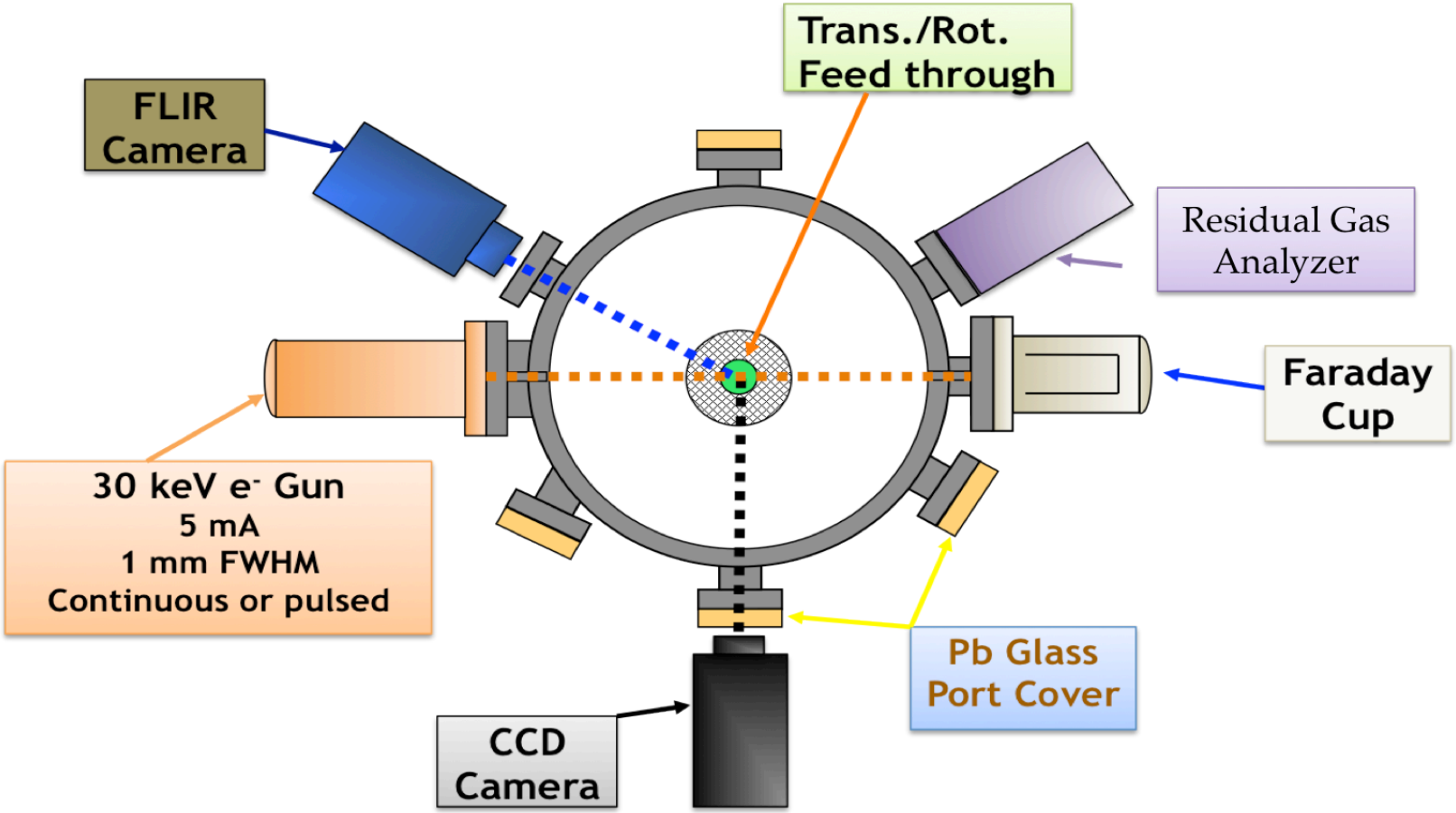

Figure 2.1 - Illustration of the Foil Test Stand

2.2.1 Instrumentation

2.2.1.1 Electron Gun

One of the most important units on the FTS is the electron gun and its corresponding power sources. The electron gun was a prototype developed by Kimball-Physics and is capable of producing a 30 keV electron beam with currents up to 5 milliamperes (mA). The electron gun consists of several different components to help focus and control the beam. There are four main components: the triode, focus, beam collimation, and deflection.

The first component of the electron gun, the triode, is made up of three different sections that are in sequence with one another: the cathode, the grid or Wehnelt, and a grounded anode [78, 79, 81]. The cathode is a thermionic emitter made up of a heated 300 square micrometer (μm^2) lanthanum hexaboride (LaB_6 or LAB6) crystal. The original LaB_6 cathodes produced by Kimball-Physics were made into a conical shape with the tip of the cone flattened to produce a 15 micrometer (μm) diameter surface with a <100> orientation. The flattened portion provides the best electron emission and therefore would produce a focused spot size diameter of 15 μm. In order to increase the focused spot size of the electron beam, the LaB_6 crystal conical portion was flattened to give a spot

size diameter of 19.5 μm. This in turn leads to a focused spot size of approximately 300 μm^2. The LaB_6 crystal is biased (cathode voltage) to establish the beam energy. An example of a LaB_6 crystal used in an electron gun is illustrated in Figure 2.2 [78, 79, 81].

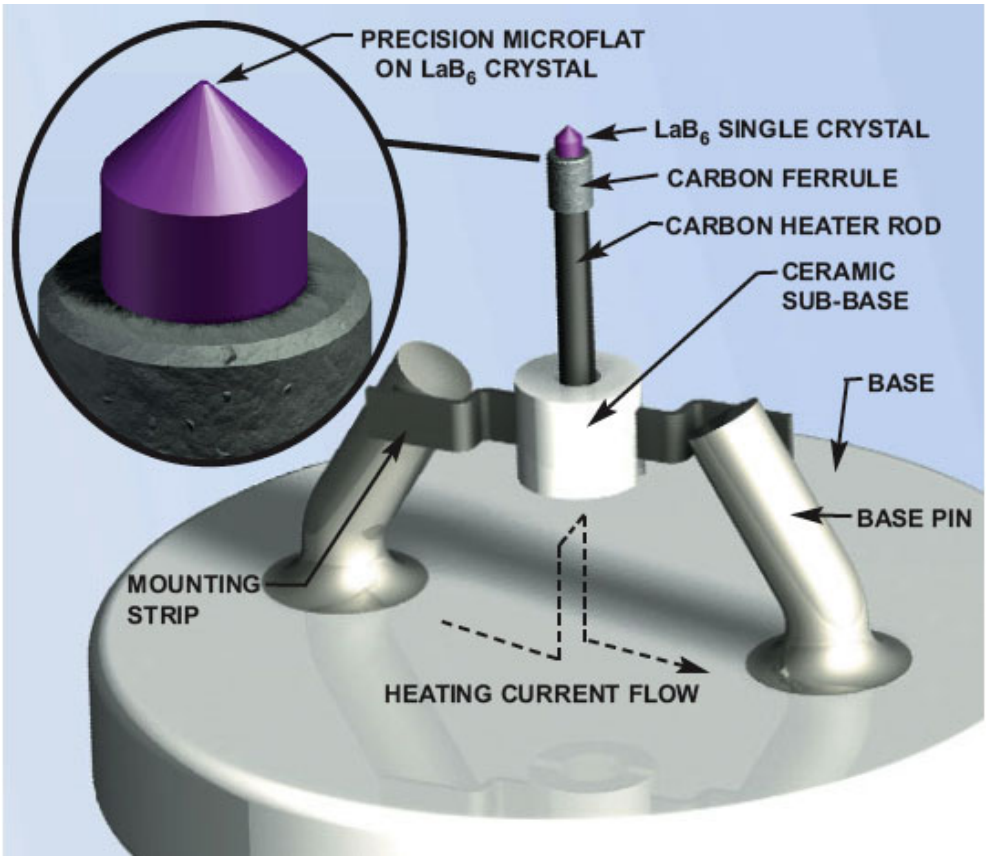

Figure 2.2 - Cathode of Kimball Physics Electron Gun

The emission that is obtainable is a function of the cathode's temperature and energy. If the temperature is low and the energy is high, it is operating in a temperature-limited mode described by the Richardson-Dushman equation [81, 82, 83, 84]:

$$J = AT^2e^{-\phi/\kappa T}$$

Where:

J = emission current density [amperes per square centimeter (A/cm^2)]

A = Richardson's constant for each cathode material [amperes per square centimeter per square Kelvin ($A/cm^2/K^2$)]

T = cathode temperature (K)

ϕ = work function of cathode [electron volt (eV)]

κ = Boltzmann's constant = 8.6×10^{-5} eV/K

There is an exponential relationship between the inverse temperature and electron emission. Therefore, to increase emission, the temperature of the cathode must be increased and the emission will continue to increase with temperature until reaching a space charge limit. Operation can also be space charge limited when the temperature is high and the energy is low. While in this mode, emission is dependent upon the amount of energy applied to the system. If the temperature of the cathode is held constant and the energy is increased, emission will increase until it reaches a temperature-limited mode. This is similar to the space charge limited mode in that the emission no longer increases with an increased applied energy, but only increases if the temperature of the cathode is increased. Operating the cathode in either a temperature or space

charge limited mode has both desirable and undesirable effects. The temperature-limited mode allows for longer cathode lifetimes, but the beam current will tend to fluctuate. The space charge limited mode allows for less current fluctuations, but shorter cathode lifetimes due to the higher temperatures involved. The dependence of current on voltage and temperature are illustrated in Figure 2.3 [81, 82, 83, 84].

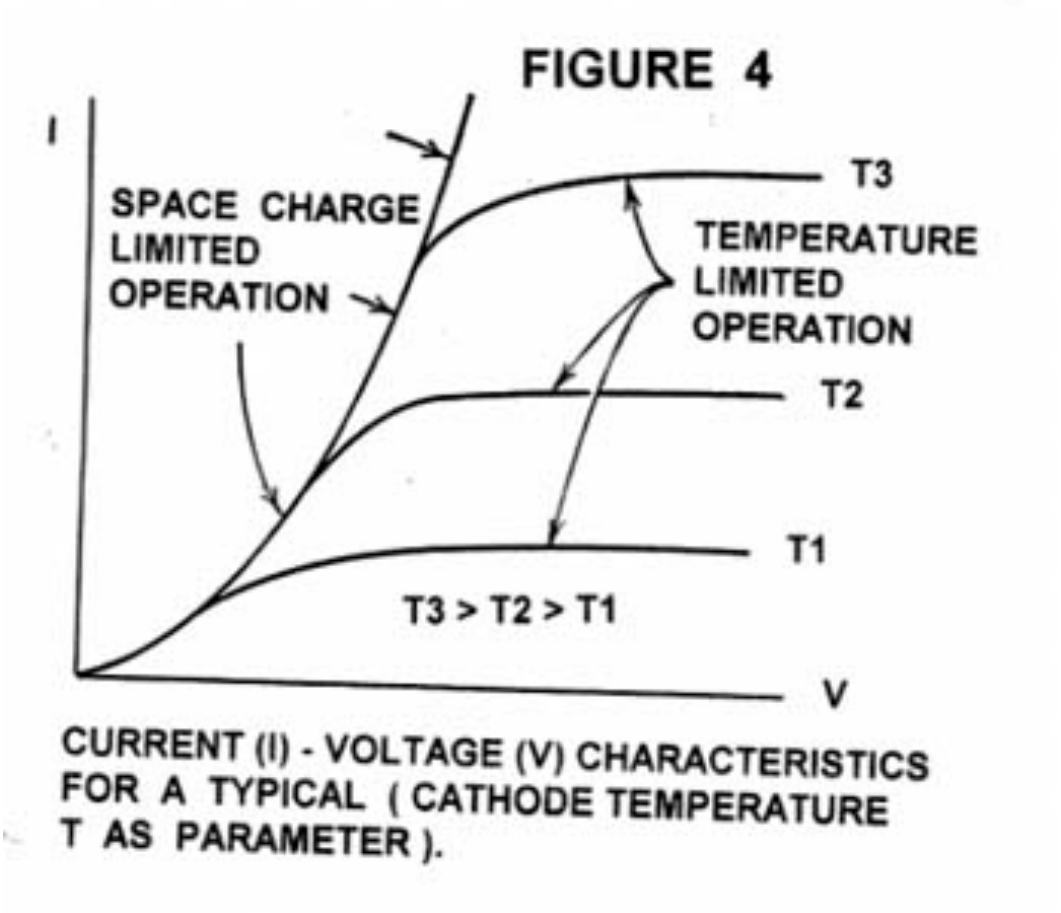

Figure 2.3 - Current (I) versus Voltage (V) characteristics for a typical cathode.

The second section of the triode is Wehnelt, more commonly called the control grid or Grid. The grid is a cylinder device that encases the cathode and helps shape the emission. The third section of the triode is the anode, which is an aperture plate held at ground potential. By aligning the anode and cathode up with one another, the electron's energy and direction can be fine-tuned.

The second component of the electron gun is the focus, which is a set of three tubes in series to form an Einzel lens. An Einzel lens is when the first and last tubes are held at the same (here ground) potential, while the middle tube potential varies. This enables the electron gun to be focused at different energies and working distances. It also allows an increase of the spot size by defocusing the beam. A diagram of an Einzel Lens and the paths ions take to a focal point are illustrated in Figure 2.4 [85].

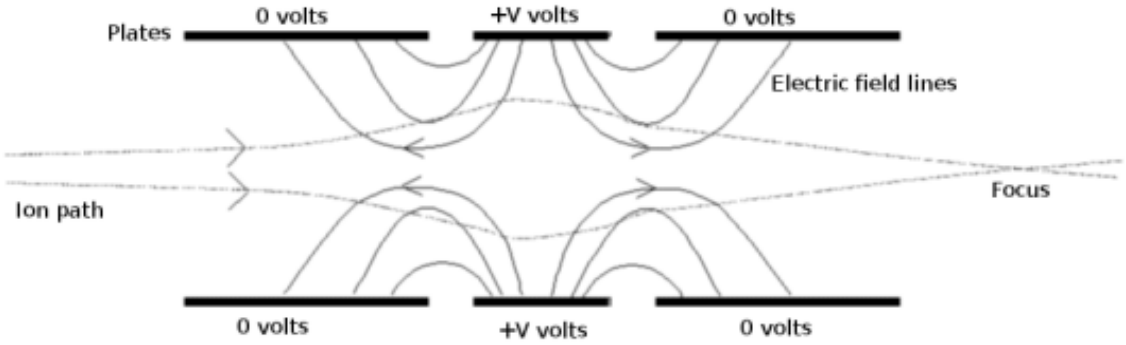

Figure 2.4 - Einzel Diagram

The third component of the electron gun is the beam collimator, which forms a parallel output beam. A collimated beam, allows spot size and beam current density to remain constant while the distance to the target is varied.

The final component of the electron gun is the deflection assembly, which consists of orthogonal pairs of deflection plates (x- and y- deflection) that are in series with one another. Applying voltage to the deflection assembly allows the beam's position to be controlled on the target. Voltage applied to the deflection plates may be altered back and forth to raster the beam. Rastering increases the total spot size that the beam will cover. Since the two pairs of deflection plates are in series with one another, first the y-deflection plates and second the x-deflection plates, the amount of voltage that must be supplied to each of these to move the beam a similar amount is different. Additionally, a higher voltage must be applied to the deflection plates at higher beam energies to move the beam a similar amount than at lower beam energies. Although it is sometimes necessary to largely deflect the beam, it should be noted that larger deflections might cause beam distortion. Therefore, the electron gun is optimized to limit the amount of deflection.

The electron gun is powered by a combination of a Kimball-Physics EGPS-

4215 power supply and a Glassman High Voltage Supply. This combination supplies the electron gun the necessary high voltage needed to each of its components. The FTS is a very dynamic tool that is used to analyze and characterize a variety of foils that have the potential to be used within SNS. The FTS has the capability to replicate the current and future thermal loads that the foils experience within SNS. In order to meet the necessary spot size requirement, it is required that the beam from the electron gun be rastered in both the x- and y-direction. Rastering of the electron beam allows for a larger, but still uniform, sample size to be placed on the foil. Table 2.1 lists the capabilities of the electron gun as specified by the manufacture, including the standard voltage and current ranges for the different components within the gun. Figure 2.5 shows a photograph of the electron gun [81].

Electron emission from the gun is measured by a Faraday Cup (FC) mounted on a port aligner. The FC is a long cylinder with a stainless steel outer shield and a copper inner cylinder. A limiting aperture (LA) is mounted at the entrance of the FC to regulate the size of the beam that is sampled. The FC captures the electrons that go through the LA and indicates how well the beam is focused and tuned. Since the FC experiences a large amount of energy, it is necessary to regulate the temperature of the FC with deionized

Table 2.1 - EMPS-4215 Power Supply Ranges

EMPS – 4215 Power Supply Ranges	
Parameter	**Standard LaB_6 Cathode**
Additional High Voltage Supply (Slave Energy)	0 to -30 kV (At 5 mA)
Energy	0 V to -30 kV
Source (voltage)	0 V to 3.0 V
Source (current)	0 A to 6 A
Emission Current	0 mA to 5 mA
Grid	0 V to -500 V
Focus	0 V to -20 kV
X-Deflection	-300 V to +300 V
Y-Deflection	-300 V to +300 V

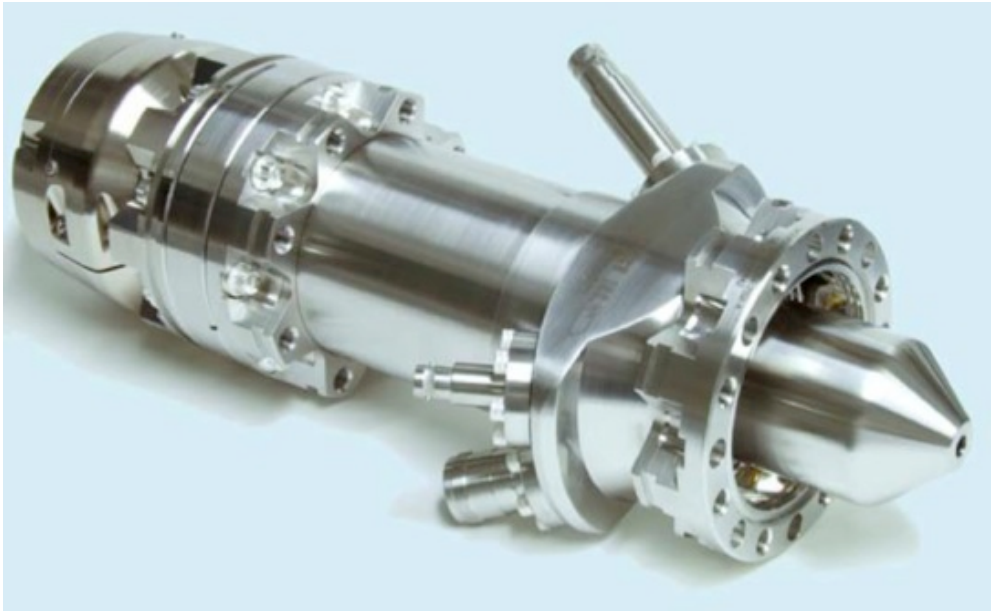

Figure 2.5 – Overall view of the electron gun.

water. Bias voltages maybe applied to both the FC and LA to help direct the electrons. A schematic diagram of the FC and LA are illustrated in Figure 2.6 [81].

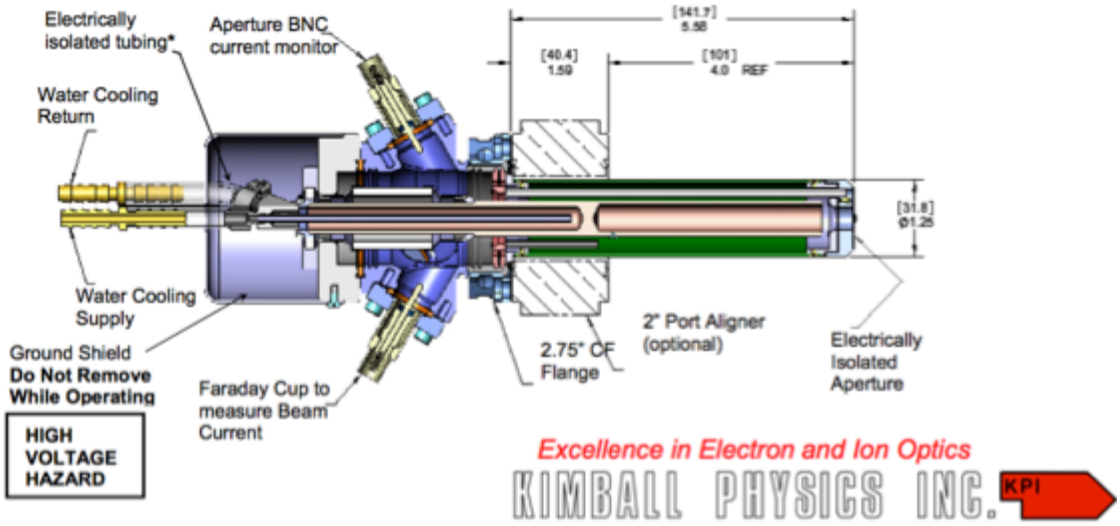

Figure 2.6 - Schematic view of the faraday cup and corresponding components.

2.2.1.2 Residual Gas Analyzer

The FTS also includes a residual gas analyzer (RGA) from Stanford Research Systems (SRS). The RGA is a small mass spectrometer that is connected directly to the vacuum system and used to analyze the various gases within the vacuum chamber. This is useful for vacuum system diagnostics and to monitor degassing of foils when heated [86, 87, 88, 89].

2.2.1.3 Vacuum System

The foil test stand was built using a custom cylindrical stainless steel vacuum chamber made by MDC Vacuum Products, LLC. It consists of an eight-inch-long, ten-inch outer diameter tube; with twelve-inch diameter conflate flanges at each end. Additional vacuum ports are placed around the periphery of the tube to allow attachment of the electron gun, the faraday cup, the RGA, vacuum gauges, and various view ports. A reducing flange (12 inches to 8 inches) is attached to the bottom, which allows an eight-inch turbo molecular pump to be attached. The turbo molecular pump pumps the system down. After initial assembly or opening the system to atmosphere, the system is vacuum baked out at with a minimum temperature of 100 °C for 12 hours to remove water vapor (H_2O), carbon dioxide (CO_2), and other residual gases from the system [98]. After the vacuum bake-out, the vacuum system typically achieves a base pressure of 1.0 to 1.5 x 10^{-10} torr. In Figure 2.7, a photograph of the top view of the FTS Chamber with the top lid removed. At the bottom of the image is the FC/LA, in the center is the turbo molecular pump with a protection screen, and at the top is the electron gun. The other ports on the left and right side of the chamber are used as viewports and access points for vacuum gauges. On the topside of the vacuum chamber is a twelve-inch diameter lid that has a one and half inch diameter port with a linear actuator and Z-stage attached. The

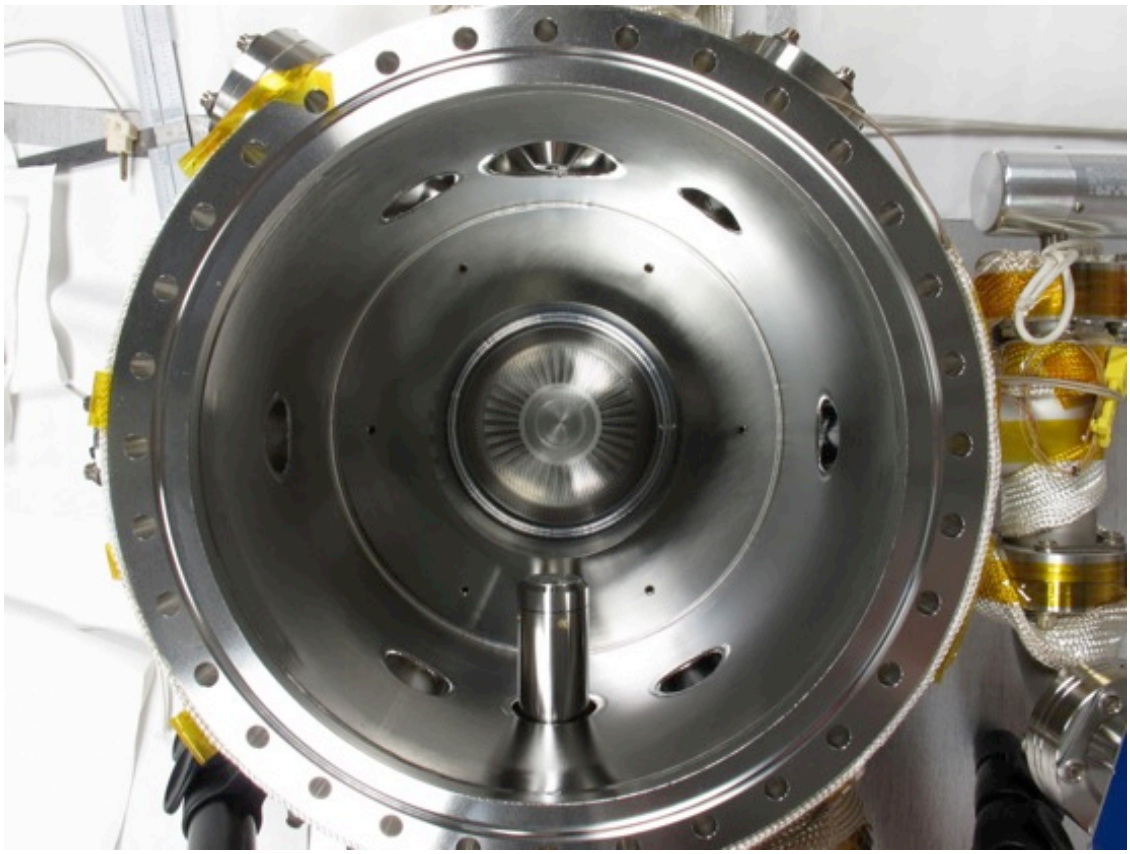

Figure 2.7 - Top view of the FTS chamber, including the FC/LA (bottom), turbo molecular pump (center), and electron gun (top).

linear actuator and the Z-stage have a travel distance of one inch and eight inches, respectively. This allowed the ability to design a sample holder with four positions that can be occupied by a combination of foils and a phosphorous disk. The phosphorous disk would be installed over a fourth foil when it is necessary to line and calibrate the electron gun, otherwise it is deemed unnecessary and four foils may be installed. The ability to install multiple foils into one foil load cycle allows for more consistent and accurate results. Once the number and types of foils are chosen and loaded into the vacuum chamber, the vacuum

chamber is wrapped in heating tapes and aluminum foil for the twelve-hour bake out, removing most of the residual gases (e.g., H_2O, CO_2, H_2) [89]. Occasionally other gases will appear to be off-gassing from the chamber, including turbo molecular pump oil and hydrochloric acid (HCl). Following the bake out, the chamber is allowed to gradually cool to room temperature before the start of any experiments. In Figure 2.8 there are several images of the process of loading the foils onto the foil holder and the bake out of the chamber that follows. It is important to bake out the chamber for a minimum of twelve hours to remove all contaminants and reach a vacuum chamber base pressure in the low 10^{-10} torr.

2.2.1.4 LabVIEW

In order to efficiently and effectively control all the vacuum instrumentation (e.g., the electron gun, FC/LA), the system employs a custom designed graphical user interface (GUI) from LabVIEW. The GUI controls the electron gun's beam energy and current, along with the necessary bias applied to the FC/LA. This GUI was initially designed by Kimball Physics, but has since been further customized to better suit the needs of the FTS and its operators. A screenshot of the LabVIEW GUI that is currently employed by the FTS is shown in Figure 2.9.

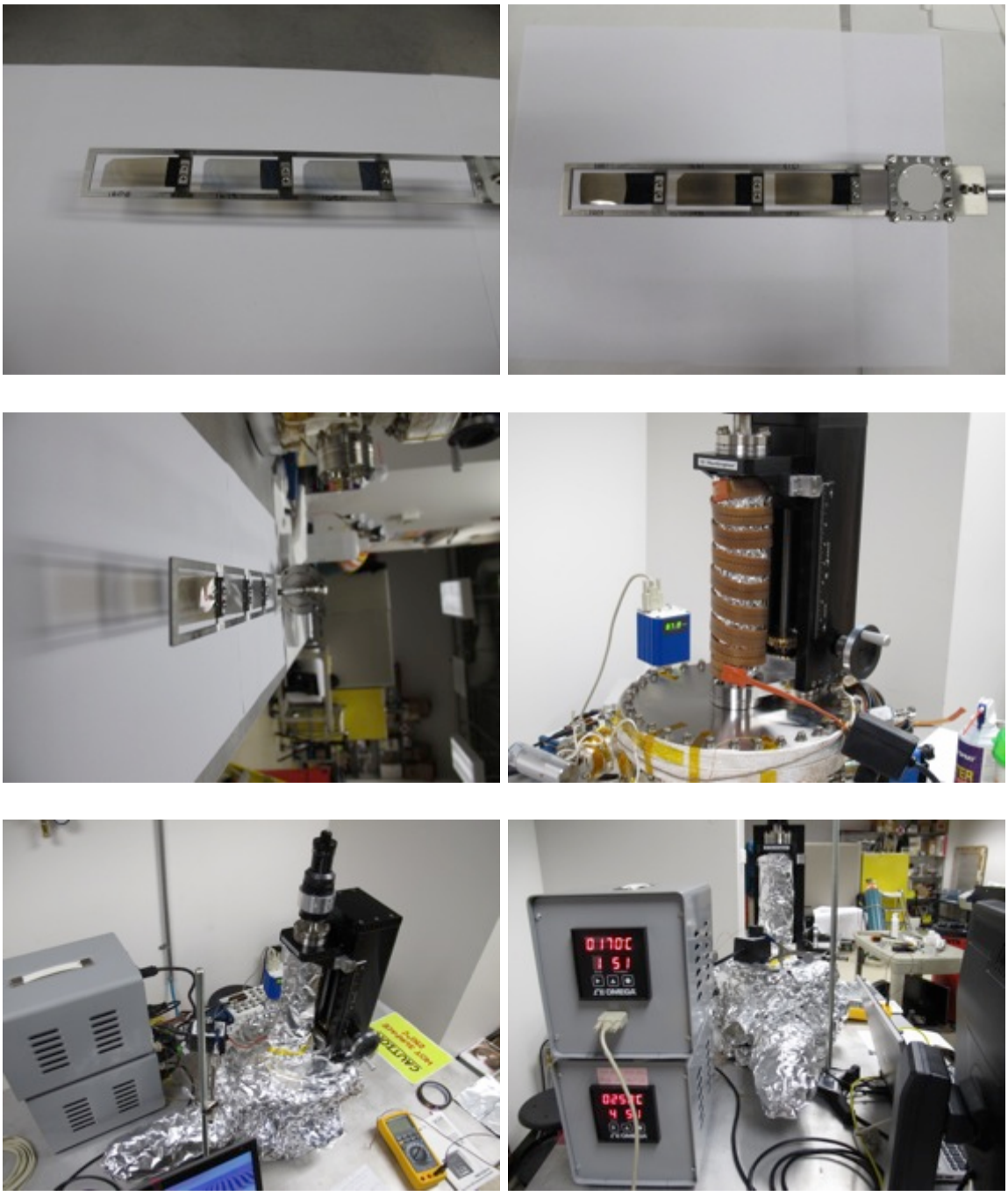

Figure 2.8 - Various aspects of the FTS: multi-sample foil holder without phosphorous screen, multi-sample holder with phosphorous screen, multi-sample holder alignment, wrapping multi-motion feedthrough with heater tape for bake out, wrapping of chamber with aluminum foil to provide uniform heating of chamber, and controlling of bake out with Omega controller.

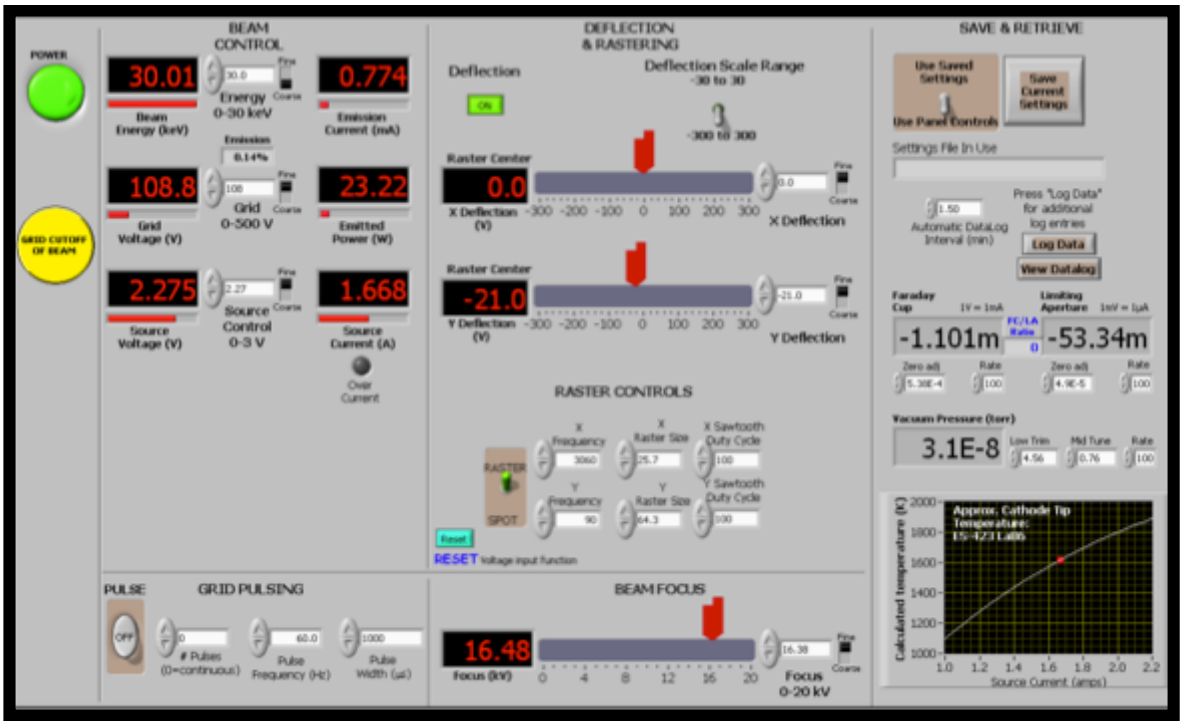

Figure 2.9 - FTS electron gun graphical user interface in LabVIEW.

2.2.1.5 Cameras

The second most important components after the electron gun are the infrared camera and high definition video camera. The infrared camera from FLIR (Model SC5600) uses an indium antimonide crystal as its sensor and has the ability to measure temperatures that range on a sample from 300 to 2,500 °C [90]. It has the ability to measure a wide temperature range because it may use up to two different filters, providing three specific temperature ranges. The three temperature ranges are the following: Range #1 uses no filters and has a temperature range from 5 to 300 °C; Range #2 uses a 50 mm filter and has a temperature range from 300 to 1,500 °C; and Range #3 uses a 150 mm filter and

has a temperature range from 1,500 to 2,500 °C. The majority of this work utilizes Filter #2 for measuring the temperature of the foils for the various tests. In addition to being able to make an in-situ measurement of a sample's temperature, it has the ability to calculate the emissivity and spot size. Since the emissivity of the foil can change when exposed to the electron beam, it is important that the emissivity is known to get an accurate temperature measurement. Additionally, it is important that the spot size of the beam is known to calculate the power density of the electron gun to relate it to SNS. The infrared camera's capability to measure the spot size is corroborated with measurements from a high magnification compact light microscope.

The high definition video recorder from JVC is also employed to monitor the foils. This video recorder has the capability to record both videos and pictures of foils throughout the whole process. This includes prior to the foils being loaded; after the foils are loaded; after the vacuum chamber is baked out; and before, during, and after all tests are performed on the foils. By being able to monitor and record the foils at the different stages, it allows a very complete and thorough analysis of how the foils change due to various beam conditions.

2.2.2 Comparison to SNS

The FTS is a very dynamic tool that is used to analyze and characterize a variety of foils that have the potential to be used within SNS. The FTS has the capability to replicate the present, and future, thermal loads that the foils will experience within SNS [78, 79]. In order to meet the necessary spot size requirement, it is required that the beam from the electron gun be rastered in both the x- and y-direction. Rastering of the electron beam allows for a larger, but still uniform, spot size to be placed on the foil [81]. In order to compare the FTS to SNS, it is necessary to determine what energy and current the electron gun from the FTS must apply to reach an equivalent thermal load to SNS.

2.2.2.1 Calculation and Theory

As was stated in previous sections, SNS was designed to produce a 1.0 GeV beam with a power of 1.4 MW, and a pulse rate and width of 60 Hz and 975 μs, respectively. This corresponds to a beam delivering 1.0×10^{14} protons per pulse (ppp) to the foil [78, 79]. In addition to the foil being impacted by the 1.0×10^{14} ppp from the linear accelerator, the foil also experiences a foil load from the circulating beam within the accumulator ring. On average the foil will experience each proton seven to ten times from the accumulator ring and accounts for the majority of the load that the foil experiences. Therefore, a well-

tuned SNS beam that is at the design-power of 1.4 MW will have a peak hit density on the foil of 4.5 x 10^{13} protons per square millimeter (p/mm^2) [78, 79]. Since the pulse width of SNS beam is 1 ms (1 ms = 1x 10^{-3} s), then the peak proton beam density per unit time is approximately:

$$4.5 \times 10^{13}\ \text{p/mm}^2 \div 1 \times 10^{-3}\ \text{s} = 4.5 \times 10^{16}\ \text{p/mm}^2\text{/s}$$

To better understand this number of 4.5 x 10^{16} p/mm^2/s, it can be converted to units of amperes. In units of amperes, this number corresponds to a peak beam current density of 7.2 mA/mm^2 [78, 79].

2.2.2.2 Stopping Power

In order to compare the thermal load the foil will experience within SNS H^-/H^+ to that of the FTS electron beam (e^-), the stopping powers of the two different beams were compared. A 1.0 GeV beam of protons stopping power in amorphous carbon (density is ~2.0 g/cm^3) is approximately 1.946 MeV*cm^2/g. The stopping power versus the energy of a proton in amorphous carbon is shown in Figure 2.10 [91]. On the other hand, the stopping power of a 30 keV electron beam in amorphous carbon of the same density is 8.575 MeV*cm^2/g. The stopping power versus the energy of an electron in amorphous carbon is shown

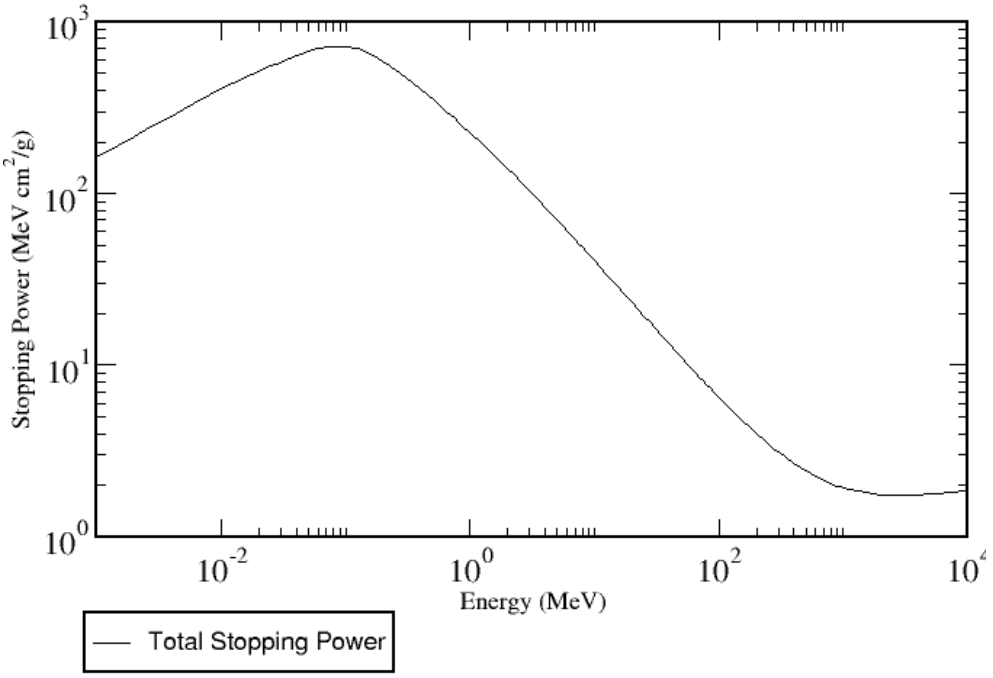

Figure 2.10 - Stopping power of a 1 GeV Proton (1.946 MeV cm² g^{-1}) in amorphous carbon (density = 2.0 g cm^{-3})

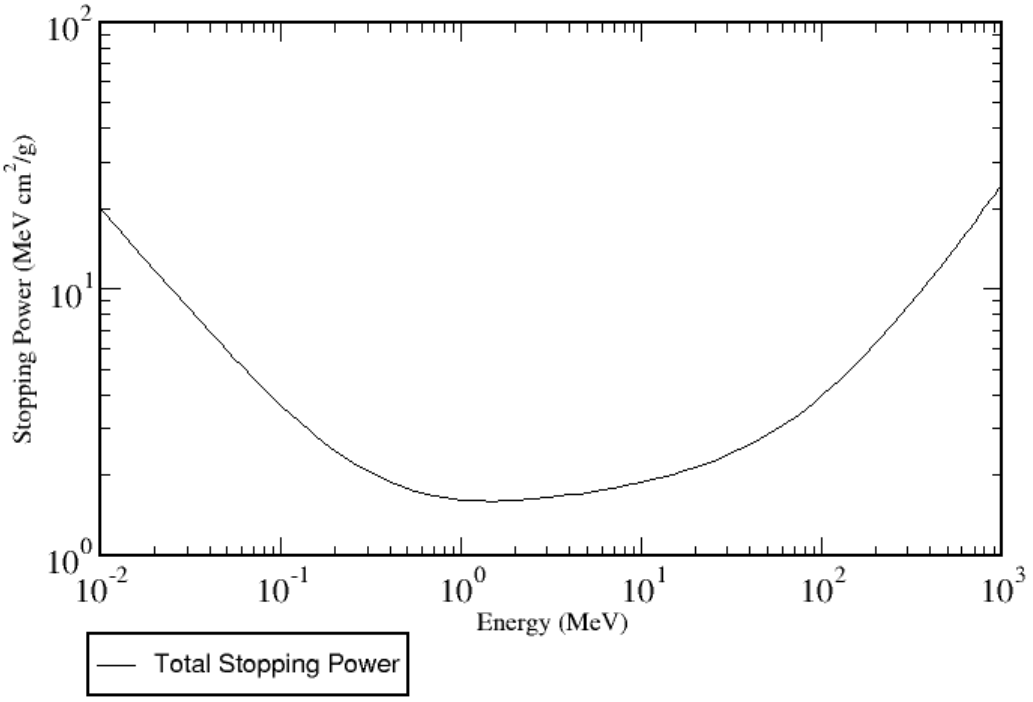

Figure 2.11 - Stopping power of a 30 keV Electron (8.575 MeV cm² g^{-1}) in amorphous carbon (density = 2.0 g cm^{-3})

in Figure 2.11 [91].

The stopping power of 30 keV electrons is ~4.43 times higher than that of a 1 GeV protons. Since the stopping power in amorphous carbon is much greater for electrons than protons, it requires a low-energy electron to achieve the same effect as a high-energy proton. Therefore, to have a similar power density to that of a 7.2 mA/mm^2 proton beam, it is necessary to have an electron beam that can produce a power density of 1.6 mA/mm^2.

1.4 MW SNS Beam ≈ 1.6 mA/mm^2 Electron Beam

A concern with using electrons to simulate the thermal load the foils experience within SNS is the range of the electrons within the foils. It is important that the range of electrons is greater than the thickness of the foil to prevent additional scattering effects within the foil. The typical foils used within SNS are nanocrystalline diamond with an average aerial density of 350 $\mu g/cm^2$. A corresponding volume density of crystalline diamond is ~3.5 g/cm^3. This gives a foil that is approximately 1 x 10^{-6} meters thick (or 1 μm). The range of 30 keV electrons is 1.996 x 10^{-3} g/cm^2 (or 1,996 $\mu g/cm^2$), which is almost six times (5.70 times) the average foil aerial thickness [78, 79]. Therefore, it is believed that

having a low power electron beam has no additional effects from electrons (e.g., no additional scattering of the electrons within the foil). In addition to being able to deliver a peak density of 1.6 mA/mm^2 to simulate a 1.4 MW SNS beam, it is also important that the electron gun is capable of delivering a similar spot size to that of the peak SNS beam size. The peak SNS beam size has an approximate root mean square (rms) in both the x- and y- direction of 3.00 mm, which corresponds to a beam area of 27 mm^2. Unfortunately to get the appropriate power density for the entire SNS beam (rms = 3.00 mm), it would require the electron beam to produce a 43 mA beam to get the appropriate power density (1.600 mA/mm^2). However, the peak SNS beam size has been determined by a Zeiss microscope on several foils that have been used within SNS. Figure 2.12 is a photograph taken by the Zeiss microscope of a foil that has been in SNS. The peak beam size is outlined and measured to have a radius of approximately 1.50 mm and spot size of 7.2 mm^2. For a 7.2 mm^2 spot size, it would require either a single electron beam to produce a 11.5 mA beam or the rastering of a smaller electron beam. Since the first option is not necessarily practical for a tabletop electron source, it was decided that the spot size would be maximized for an area of approximately 1 mm^2 and the beam would be rastered. The rastering would cover the entire 7.2 mm^2 area and would be at a high enough frequency to prevent any unwanted cooling on the foil. This allowed the installation of a 30

keV electron gun, with a maximum emission current of 5 mA, to meet the design requirements [81].

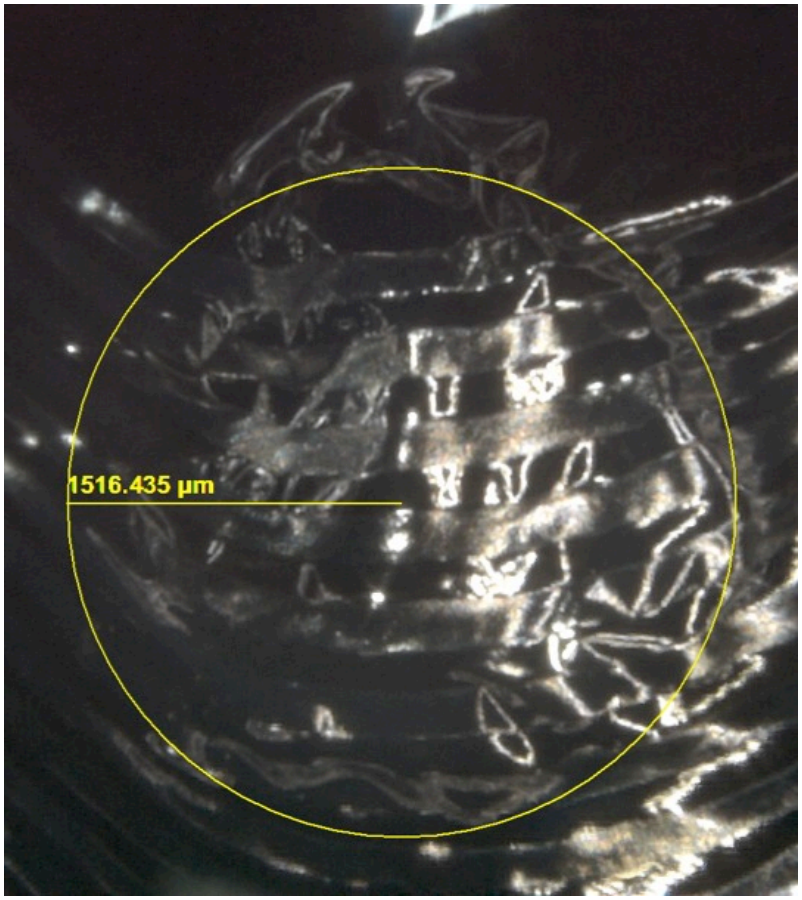

Figure 2.12 - Determination of SNS spot size with Zeiss microscope measurement software.

2.3 Experimental

Prior to conducting initial experiments on the primary stripper foils, it was first necessary to determine the capabilities of the electron gun and the other FTS components. The electron gun was a prototype developed by Kimball

Physics. It was therefore essential to determine the limits of the electron gun and its ability to simulate the SNS beam. First off, it is necessary to recall SNS beam conditions that need to be emulated to provide an accurate comparison.

The SNS beam is pulsed at 60 Hz with a pulse width of 1.00 ms; it has a design beam energy of 1.0 GeV corresponding to a stopping power in amorphous carbon of 1.946 MeV cm^2 g^{-3}, and a power density for a 1.4 MW proton beam of 7.2 mA/mm^2. The SNS beam size can range from a few millimeters to several millimeters in diameter. Therefore, it was decided that the peak SNS beam size would be used, and it corresponds to a diameter of approximately 3.0 mm (area of ~7.07 mm^2) as measured post-production using a Zeiss microscope.

A thirty keV electron has a stopping power in amorphous carbon of 8.575 MeV cm^2 g^{-3}. The stopping power of a 30 keV electron is 4.43 times larger; therefore, to simulate a 1 GeV proton power density of 7.2 mA/mm^2, it is required to have a 30 keV electron power density of 1.6 mA/mm^2. The Kimball Physics electron gun is specified to have a maximum current output of 5 mA and a focused beam spot size of 0.300 mm^2. If a pulsed beam was defocused to an approximate spot size of 7.2 mm^2, to get the appropriate 1.6 mA/mm^2 power

density it would require an electron beam current of approximately 11.2 mA. This is over two times the specified maximum beam current on the electron gun. Additionally, it was found that as the electron beam became defocused an annulus was formed. This is expected since the majority of the electrons being discharged are coming from the circumference of the 0.300 mm^2 LaB_6 crystal. In order to overcome both the limited spot size and power density, it was decided that the electron beam would be rastered in both the x- and y-direction.

Rastering of the electron beam, or commonly called rasterization, is a technique that has been used for several years to increase the amount of area that an electron beam can cover. One of the most common devices that use the technique of rastering of a beam is an old television (i.e., a tube television). The older televisions raster electron beams in both the X- and Y-direction. Typically, the rastering is much quicker in one direction over the other, "painting the beam" in a Z-like pattern. The Kimball Physics electronics allows the electron gun to be rastered in both the X- and Y-direction at a frequency up to 15,000 Hz [90]. Initial work was completed to determine what frequency ratio of X:Y was required to optimize the electron beam. Several X:Y ratios were tried that ranged from 150:1 to a 1:1, vice versa. In order to provide a uniform temperature on the foil, the maximum rastering frequency was employed. Table 2.2 lists some of the

rastering frequencies and the corresponding rastering ratios tested.

Table 2.2 - Some of the raster frequencies and ratios tried with the electron gun.

Higher X Frequency			Higher Y Frequency		
X Frequency (Hz)	**Y Frequency (Hz)**	**Ratio (X:Y)**	**X Frequency (Hz)**	**Y Frequency (Hz)**	**Ratio (X:Y)**
14,550	97	150:1	97	14,550	1:150
14,900	149	100:1	149	14,900	1:100
14,650	293	50:1	293	14,650	1:50
14,860	743	20:1	743	14,860	1:20
14,955	997	15:1	997	14,955	1:15
14,990	1,499	10:1	1,499	14,990	1:10
14,913	1,657	9:1	1,657	14,913	1:9
14,984	1,873	8:1	1,873	14,984	1:8
14,987	2,141	7:1	2,141	14,987	1:7
14,862	2,477	6:1	2,477	14,862	1:6
14,998	2,999	5:1	2,999	14,998	1:5

In addition to the table of common raster frequencies and ratios researched, it was also of interest to determine which ratio had the most uniform beam coverage on the foil. Therefore, the average area that a 60 Hz beam with a pulse width of 1 ms could cover in a one second interval was calculated for various rastering ratios. Figure 2.13, Figure 2.14, and Figure 2.15 display the

beam patterns and the area covered on the foil for the 1:7 ratio, 1:8 ratio, and a 1:9 ratio, respectively. Additionally, Figure 2.16 is a diagram showing the rastering ratio versus the total area covered by the beam, with the greatest beam coverage from the 1:7, 1:8, and 1:9 ratios. Initial experiments that used a raster ratio greater than 15:1 or 1:15, caused increase problems with foil flutter and caused non-uniformity in the beam area. Therefore, to overcome these two issues, it was found that a ratio of 1:7 or 7:1 provided the best beam uniformity with the least amount of foil flutter. Since the SNS beam is not rastered, it was a concern that the additional foil flutter is being caused in the FTS by the rastering of electron beam. Therefore, tests were conducted without rastering that utilized either a continuous wave (CW) beam or a pulsed beam. It was found in these tests that foil flutter still existed at similar frequency and severity. In addition to having the best beam uniformity and least amount of foil flutter, the 1:7/7:1 ratio synchronized very well with the FLIR infrared camera and the JVC high definition video recorder.

While the appropriate rastering ratio was chosen, it was also necessary to determine the appropriate rastering sizes in the x- and y-direction. Since a focused spot size is 0.300 mm^2, it was necessary to find how much the voltage must be applied to each of the x- and y-deflection plates. Since the x-deflection

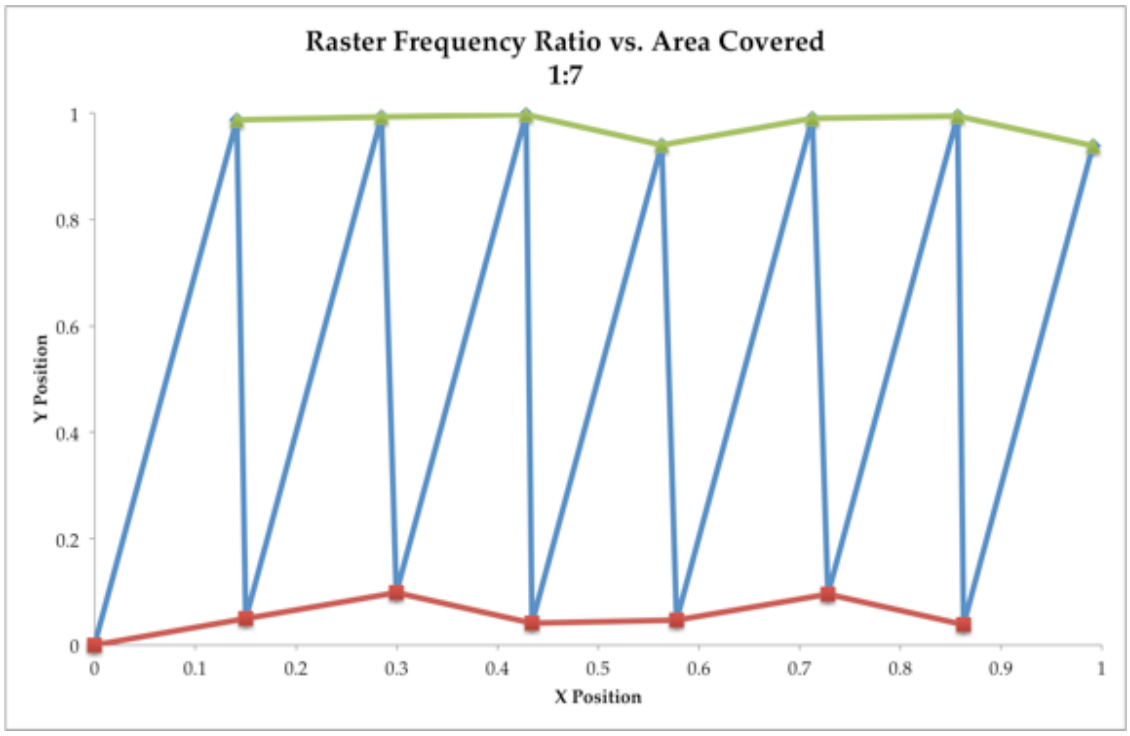

Figure 2.13 - Raster Frequency Ratio versus Area Covered (1:7)

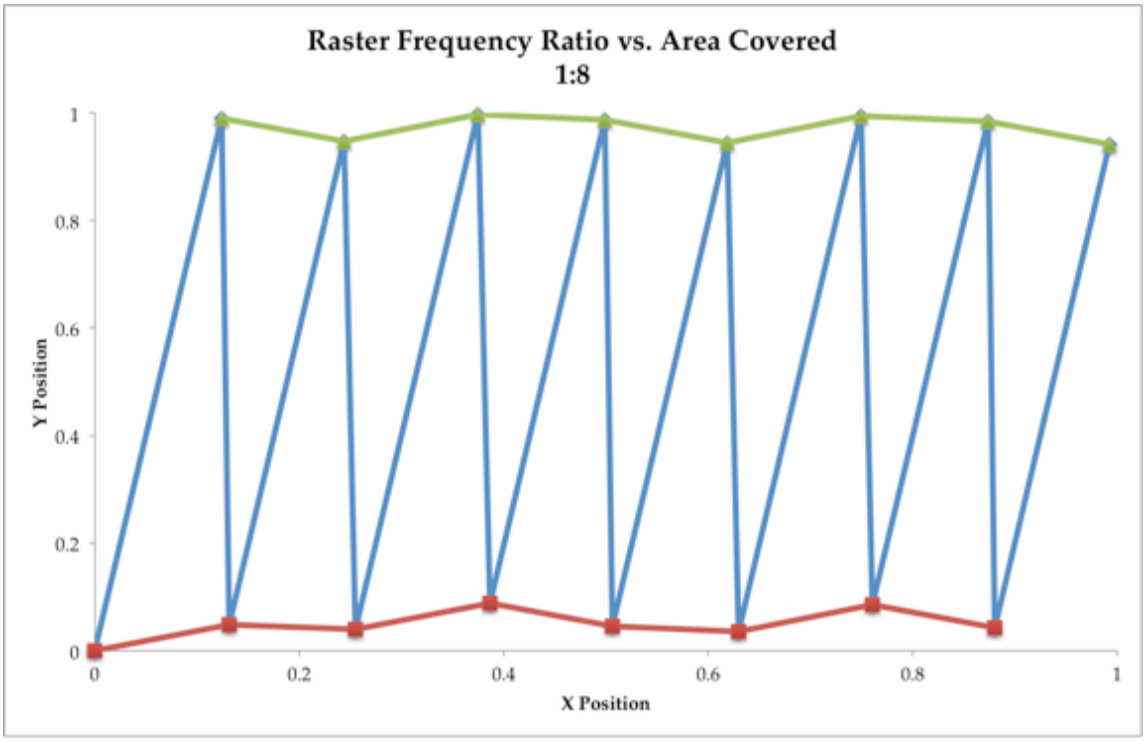

Figure 2.14 - Raster Frequency Ratio versus Area Covered (1:8)

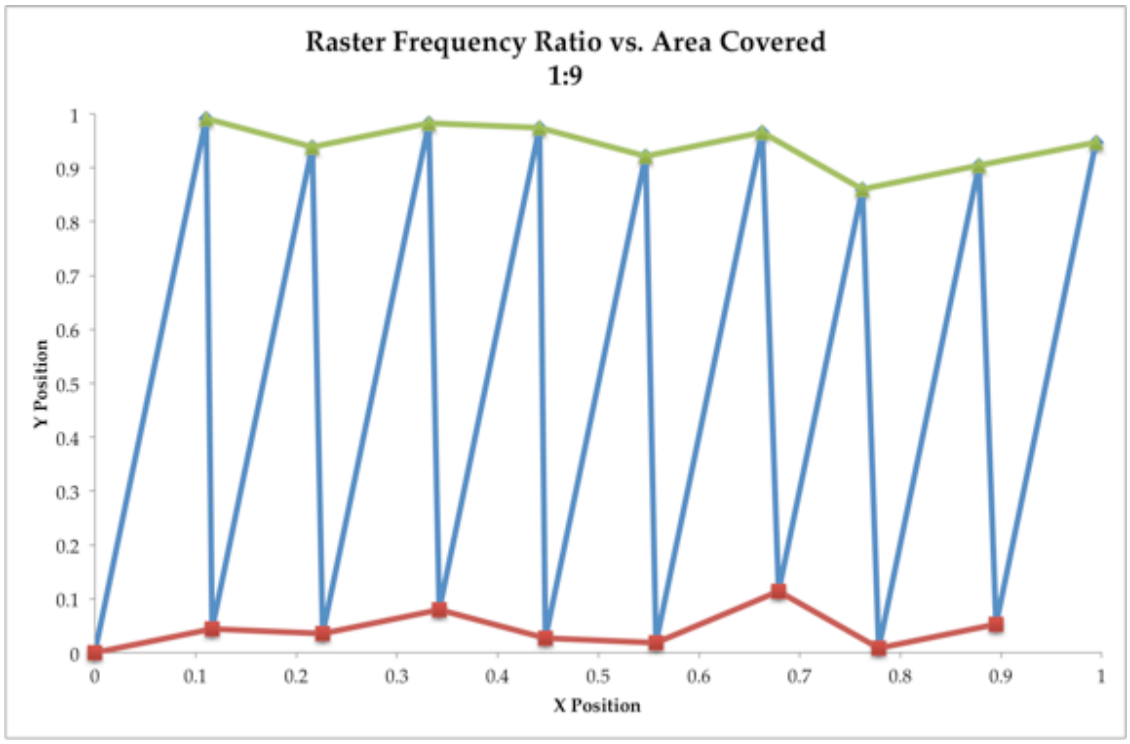

Figure 2.15 - Raster Frequency Ratio versus Area Covered (1:9)

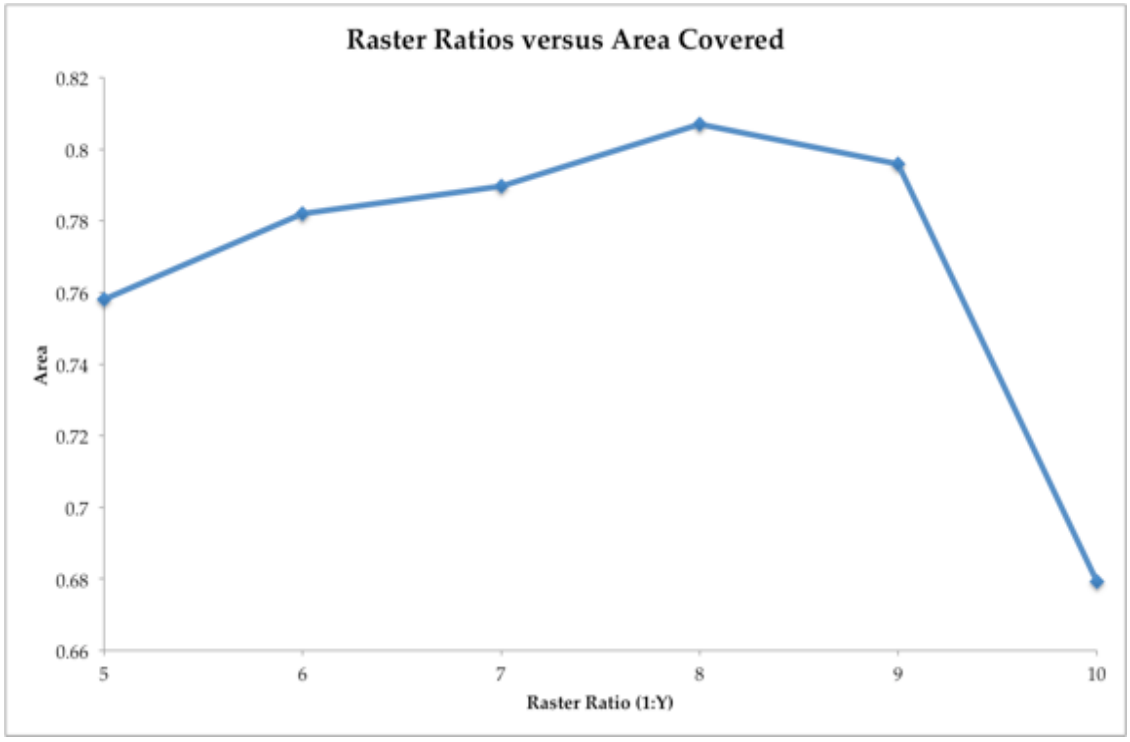

Figure 2.16 - Raster Ratios versus Area Covered

plates are closer to the filament, they require less voltage to be applied than the y-deflection plates to have a similar impact on the beam direction. It was found that a voltage of 51.5 V and 119.0 V applied to the x- and y-deflection plates, respectively, gave the appropriate spot size radius of 1.5 mm^2. Although this set of voltage gave the appropriate spot size, it was often adjusted to provide a smaller spot size when testing the foils to allow for a greater number of tests to be completed on a single foil.

Once the appropriate raster frequencies and sizes were determined, it was also important to determine the general protocol for testing several types of foils. Most of the foils tested within the FTS were diamond foils developed at ORNL, with similar sizes and parameters. This allowed for repeatable tests to be conducted on the foils, along with determining which parameters seemed to have the most influence on foil lifetime. Since one of the main purposes of the FTS is to help predict how foils will respond when placed into SNS for production, it was necessary to provide a similar testing protocol. Therefore, a testing protocol was developed to provide uniformity and consistency between each experiment.

When the foils are loaded into SNS and prior to the foils being used for

production, the operators of SNS condition the foil. Conditioning of the foil involves the gradual increase of beam power onto the foil to help accommodate the material transformation that is occurring within the foil. It was discovered in SNS that a foil that experienced either a burst of power or a hasty conditioning would become severely damaged and the overall foil lifetime would decrease. The results were confirmed several times within the FTS, both intentionally and unintentionally, in which an unconditioned spot received a burst of energy and placed a hole within the foil. Therefore, a Gradual Ramp Up of the beam both within SNS and FTS is necessary.

The typical ramp up within the FTS includes using a series of increasing currents for approximately five minutes before increasing the current on the beam to the next level. Table 2.3 is a list of currents, listed as both a continuous wave beam and 60 Hz pulsed beam, that are commonly used when ramping up the electron beam within the FTS. Since the power density is dependent upon both the current applied and the appropriate spot size, the FTS is easily capable of providing a wide range of power densities onto the foil. This will be important when predicting how the foils will behave at higher SNS beam power levels and upgrades.

Table 2.3 - Gradual Ramp Up of Beam Settings

Step	Continuous Wave Beam (mA)	60 Hz Pulsed Beam (mA)
1	0.272	0.017
2	0.640	0.040
3	1.120	0.070
4	1.600	0.100
5	2.160	0.135
6	2.720	0.170
7	3.200	0.200
8	3.760	0.235
9	4.320	0.270
10	4.800	0.300

Chapter 3. Foil Test Stand – Temperature, Emissivity, and Material Transformation

3.1 Introduction

The focus of this project is to understand the chemical and physical transformations that a foil experiences when heated by energy deposition from the SNS beam. Therefore, it is important to understand the temperatures that the foil experiences and what thermally driven transformations occur within the foil. Understanding foil transformations are important in determining foil lifetime and performance within SNS, and it is hoped that with this understanding, ways to improve the lifetime and performance of foils can be found. The FTS is capable of placing a similar thermal load on the foil as would be produced by the SNS beams, allowing a wider array of tests and characterization techniques to be conducted on the foil that are not available within SNS.

3.1.1 Temperature Studies at Brookhaven National Laboratory

While SNS was under development, Brookhaven National Laboratory (BNL) researchers (Liaw, Lee, and Tuozzolo) modeled and tested several types of carbon stripper foils. Liaw et al. first modeled the thermal load that a carbon foil would be subjected to under SNS beam conditions. By modeling the thermal load, Liaw et al. were able to determine the temperature a foil would experience [92]. Applying these results, Liaw et al. used one of BNL's accelerated H^- beam

lines to test several types of foils and determine the lifetime of each foil type. The H^- beam line was accelerated to 750 keV and pulsed at a frequency and length of 7.5 Hz and 0.5 ms, respectively. Liaw et al. chose beam currents that would produce a similar thermal load on the foils as modeled for SNS. A comparison of the beam parameters for SNS and BNL are shown in Table 3.1. At that time, the most common stripper foil used in other accelerators was made of amorphous carbon developed by the method of arc discharge deposition. Therefore, Liaw et al. tested a variety of foil types to determine how long each type would survive under SNS simulated beam conditions. The foils included two types of amorphous carbon foils and one type of diamond. The foils tested included: carbon foils from Arizona Carbon Foil Company (ACFC) made by the arc discharge deposition method, carbon foils by Los Alamos National Laboratory (LANL) made by the mCADAD method, and diamond foils on a silicon wafer prepared by Goodfellow Corporation.

Liaw et al. mounted the foils onto an aluminum square bracket. On a portion of the foils, Liaw et al. added carbon fibers to determine if this additional support had an effect on length of the foil lifetime. The ACFC foils had aerial densities ranging from 200 – 400 $\mu g/cm^2$, with lifetimes from a few hours to seventy-five hours. The foil lifetime decreased as the temperature on the foil

Table 3.1 – Beam Parameters of the SNS and BNL Beams

	SNS Inject H^- Beam	**BNL Linac H^- Beam**
Kinetic Energy	1,000 MeV	0.750 MeV
Pulse Length	1.0 ms	0.5 ms
Pulse Frequency	60.0 Hz	6.7 Hz
Maximum Current	32.00 mA	2.02 – 2.20 mA
Beam Size	3 mm x 2 mm	3 mm diameter

increased and exceeded 2,500 K, with a negligible lifetime at 4,000 K. The carbon foils from LANL all had an approximate aerial density of 200 $\mu g/cm^2$ and an average lifetime of less than fifty hours. A single diamond film, with an approximate thickness of 1 μm and aerial density of 350 $\mu g/cm^2$, lasted over four hundred hours. A chart depicting the lifetimes of each foil tested is shown in Figure 3.1 [92]. Additionally, the lifetimes of ACFC foils over a range of beam currents (i.e., temperatures applied to the foil) were measured. It was found that as beam current increased from 1 mA to 5.9 mA (which caused an increase in the beam temperature on the foil from approximately 1,500 K to 4,000 K), the expected lifetime of the foil decreased dramatically. Results of the ACFC foils' lifetime at increasing temperatures are shown in Figure 3.2 [92].

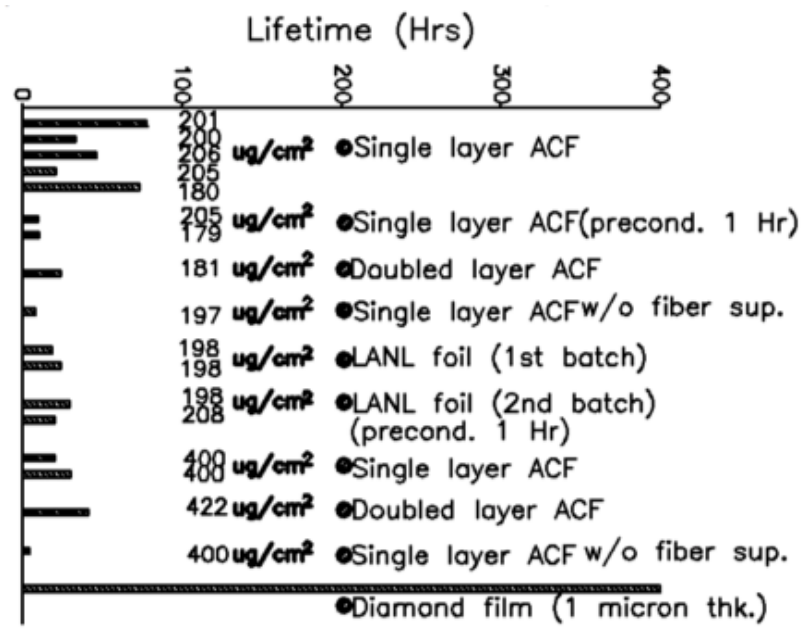

Figure 3.1 - Summary of Carbon Foil Lifetime Tests.

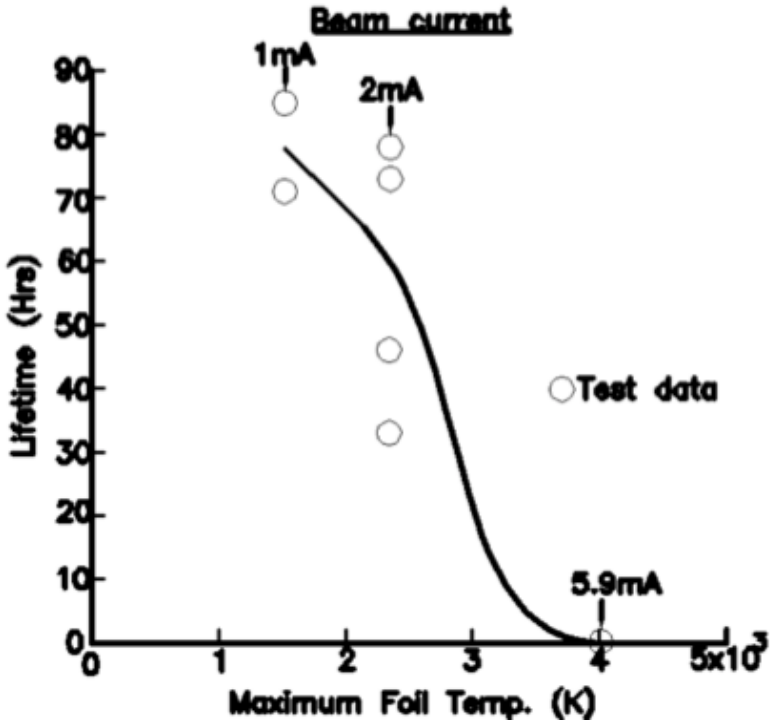

Figure 3.2- Carbon foil lifetime vs. Maximum foil temperature for Arizona 200 μg/cm² foil.

As shown in Figure 3.2, the lifetime of a carbon foil decreases considerably once the temperature on the foil exceeds 2,500 K. From these early results at BNL, it was decided that the use of the amorphous carbon foils from ACFC and LANL would not suffice for the high power levels at SNS. In addition, the results of Figure 3.1 demonstrated the longevity of diamond foils under simulated SNS beam conditions. Therefore, a diamond foil was chosen as the primary stripper foil to be used within SNS.

Additional research was still required to provide a better understanding of the temperature range that the foil would experience and developing a method to grow freestanding diamond foils with a single silicon edge for support. A freestanding diamond foil with a single silicon edge is important since both the SNS injection (3 mm x 2mm) and circulating (several mm in diameter) beams were designed to impact the lower portion of the foil. If this area of the foil had both silicon and diamond present, it would cause additional scattering, beam loss, and an increase in radiation contamination. This additional scattering and beam loss are the result of the differences in thickness (silicon = ~ 1 mm and diamond = ~1 μm) and in stopping power of the two materials for a 1 GeV proton beam (silicon = 1.801 MeV*cm^2/g and diamond = 1.937 MeV*cm^2/g). The increase in radiation contamination is caused by silicon

having a much lower melting point than diamond and not being able to withstand the very high SNS beam temperatures. These high beam temperatures would cause the silicon to melt, potentially contaminating the beam line and any nearby instrumentation in the process. Additionally, in the BNL study, Liaw et al. needed only to etch away an inner square of the silicon substrate to test the diamond foil since the H^- beam line could be directed at a small portion of the foil [44, 46, 92]. This etching produced a "diamond window," giving the foil more support since it was supported on all four sides as opposed to the single edge SNS design. Unfortunately, utilizing a foil with a window is not practical under the current SNS design scheme for reasons mentioned above. Therefore, additional research was needed after this study to develop a diamond foil supported by just a single edge.

3.1.2 Temperature Modeling of Foils at Spallation Neutron Source

Mike Plum and Yasuhiro Takeda, researchers at SNS, have modeled the temperatures that develop in a foil under various SNS beam conditions, determining how foil composition (e.g., diamond and graphite) and thickness influence the overall temperature. From their model, Plum and Takeda concluded that foil lifetime is influenced by the maximum temperature a foil experiences [93]. As expected, the highest temperature on the foil is where both

the injection and circulating beams pass through the foil.

Using a finite element method developed by ANSYS, a simulation software package, Plum and Takeda were able to develop a map of the temperature distribution on the foil. This allowed Plum and Takeda to determine the maximum temperature developed on a stripper foil under a set of SNS beam conditions. Plum and Takeda noted that there was a significant difference between the two types of carbon material examined (i.e., diamond and graphite). Since the primary mechanism for heat dissipation on the foil is radiative cooling, this difference in temperature is largely influenced by the radiative energy emission of each carbon type. The rate of radiative energy emission from a sample is dependent upon its emissivity, which in turn influences the temperature on the sample. For example, by applying the same energy deposition to two samples of different emissivities, the sample with the lower emissivity will develop a higher temperature. Since diamond has a much lower emissivity than graphite, diamond will be raised to a higher temperature at the same energy deposition than will graphite.

The first case modeled a diamond foil to determine the influences of thermal conductivity, specific heat, and emissivity on temperature. The material

properties of diamond and graphite are given in Table 3.2, and the beam parameters are given in Table 3.3.

Table 3.2 - Material properties of the Foil

Material	**Diamond**	**Graphite**
Foil Size	45 mm x 17 mm	45 mm x 17 mm
Thickness	400 μg/cm^2 = 1.14 μm	400 μg/cm^2 = 1.78 μm
Emissivity	0.3	0.8
Thermal Conductivity (At 300 K)	1,800 W/mK	179 W/mK
Specific Heat (At 300 K)	516 J/kg*K	720 J/kg*K
Density	3,510 kg/m^3	2,250 kg/m^3

Table 3.3 - Beam Parameters

Beam Energy	1.0 GeV
Protons Per Pulse over 1 ms	1.5 x 10^{14} ppp
Pulse Frequency	60.0 Hz
Pulse Width	1 ms
Spot Size	Gaussian-like beam

A series of four simulations were performed to determine the influences of thermal conductivity and specific heat on the maximum temperature of a diamond foil. The first simulation kept both thermal conductivity and specific heat constant, finding a maximum temperature of 1,950 K. The second simulation kept thermal conductivity constant at 1,800 W/mK and varied specific

heat from that of diamond to graphite (from 516 J/kg*K to 720 J/kg*K), finding a maximum temperature on the foil of 1,375 K. The third simulation varied the thermal conductivity (from 1,800 W/mK to 179 W/mK) and kept the specific heat constant at 516 J/kg*K, finding a maximum temperature of 2,167 K. The fourth simulation simultaneously varied both the thermal conductivity (from 1,800 W/mK to 179 W/mK) and the specific heat (from 516 J/kg*K to 720 J/kg*K), finding a maximum temperature of 1,572 K. In this set of four simulations, it was found that the specific heat had the largest effect on the maximum temperature of a foil (i.e., a higher specific heat generates a lower maximum temperature). Additionally, it was found that reducing the thermal conductivity of the foil significantly increased the maximum temperature on the foil. However, the influence from thermal conductivity was less than the influence of specific heat.

Plum and Takeda also simulated how the emissivity of a material affects foil temperature. In their simulation, Plum and Takeda varied the emissivity of the diamond foil (0.1 to 1.0), while keeping the other foil properties constant (as depicted in Table 3.2 and Table 3.3). The results showed that by increasing the emissivity of the foil (from 0.1 to 1.0), the maximum temperature on the foil decreased from approximately 2,000 K to 1,250 K. At higher temperatures on the foil, radiative cooling becomes the dominant mechanism. At lower temperatures

on the foil, conduction cooling is the dominant mechanism. In Figure 3.3, a graph depicting how foil temperature decreases as a function of emissivity is shown.

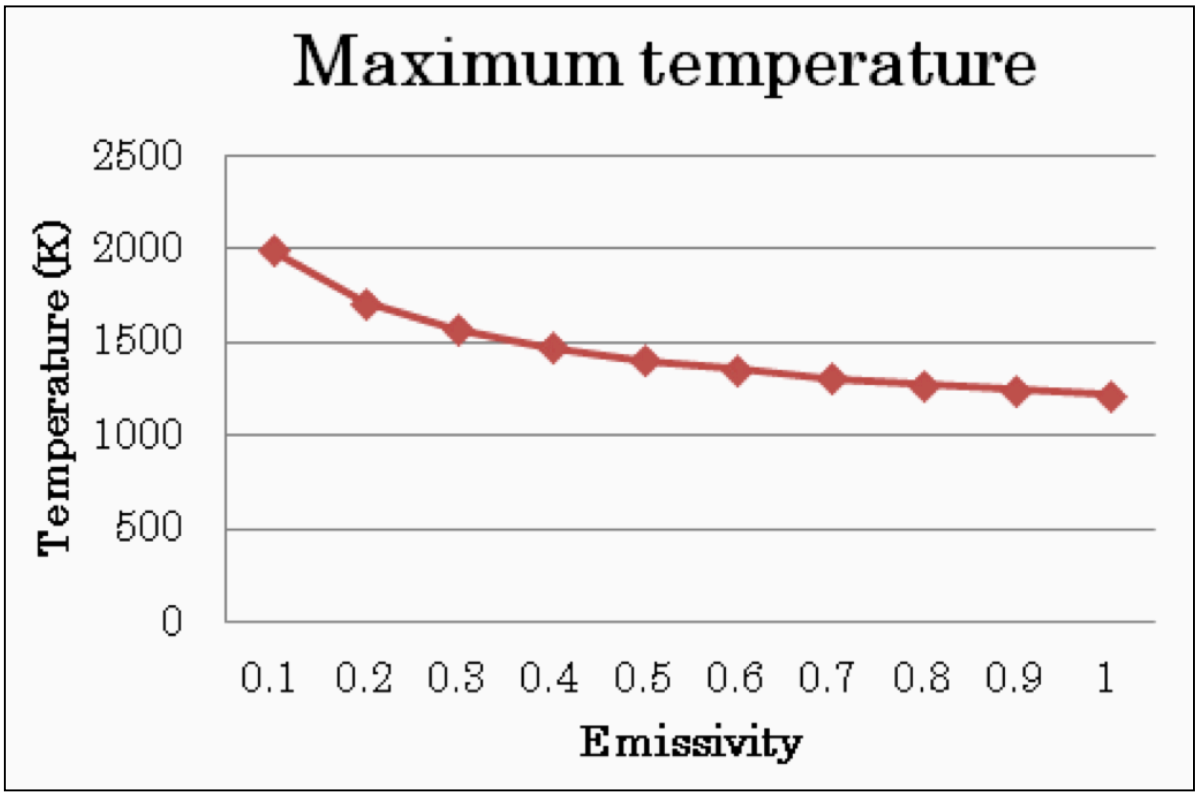

Figure 3.3 – Maximum temperature on a diamond foil as a function of Emissivity.

3.2 FTS Experiments

The FTS was used to simulate the assorted thermal loads that span the range of SNS beam powers on a variety of foils. In addition, the temperature, emissivity, and carbon state of the foils were determined by both in situ and post analysis methods. The emissivity measurements provide key data for establishing more precise in situ optical pyrometry temperature measurements in the FTS. As the foils begin to transform when exposed to high beam powers, their emissivities begin to change. This change in emissivity affects both optical pyrometry measurements and the radiative cooling. To better understand these changes, the FTS placed a variety of beam conditions on foils to measure how the emissivity changes and then the changes in emissivity were measured with a blackbody source. The foils were then analyzed by Raman spectroscopy to characterize how the carbon state changed based upon different beam exposures.

3.2.1 Preparation of Samples

A set of FTS beam conditions were developed that would produce similar thermal loads (energy deposition and temperature) on a foil as would be experienced within SNS. The change in emissivity and carbon state of the foils at the various power levels were measured for three nanocrystalline diamond foils

(#1662, #1987, and #1989). For each power level, experiments were designed to probe these changes as a function of both time and thermal load. During each experiment, the foil temperature was measured continuously and spatially using the optical pyrometry capabilities of the infrared camera. After the experiments, the foils were removed from the FTS and the emissivity, chemical state, and crystallinity of the carbon material were determined from absorption and Raman measurements.

3.2.1.1 Foil #1662

For Foil #1662, two series of spots were created on the foil by increasing the beam power using two methods: (1) Stair Step method and (2) Gradual (linear) method. The FTS was used over SNS for reasons discussed in preceding sections (e.g., time, radiation, and maneuverability of the SNS beam). The purpose of this experiment was to determine how well the foil would perform at higher SNS beam powers, and how the emissivity, chemical state and crystallinity changed with respect to beam power and time. Other than changes in beam current and exposure time, a standard beam setting was used for these experiments:

- Spot size of 2.65 mm^2

- 30 keV beam that was both pulsed and rastered simultaneously
    - Pulse frequency = 60 Hz
    - Pulse width of 1 msec
    - Rastering in both the horizontal and vertical direction at a frequency ratio of 1:7

The first series of spots were created using the Stair Step method for increasing the beam current. The Stair Step method would begin by initially applying a conditioning beam current of 0.272 mA to a spot on the foil. After the spot was conditioned, the beam current was incrementally increased and held for an additional 5.0 minutes at each increment. This process was continued up to the current limit of the FTS electron gun (approximately 5.0 mA). These spots where identified as #XS, where "S" represents the Stair Step method and "X" represents the appropriate position in the series.

For example, Spot #1S received a beam current of 0.272 mA for 5.0 minutes (SNS equivalent of 0.094 MW, foil temperature of 710 K). After the five minutes for Spot #1S, the foil was adjusted to provide a clean and unused area for Spot #2S. In a similar method, Spot #2S was conditioned for 5.0 minutes at a beam current of 0.272 mA, followed by an additional 5.0 minutes of a 0.640 mA

beam (SNS equivalent of 0.220 MW, foil temperature of 925 K). Once again, the foil was adjusted to provide a clean and unused area for Spot #3S. Spot #3S received the same conditioning and beam conditions as Spot #2S, followed by an additional 5.0 minutes of a 1.120 mA beam (SNS equivalent of 0.385 MW, foil temperature of 1,175 K).

The process was continued for the remaining ten spots to give a "stair step" look at beam current. This approach helped determine the effect that beam current has on the maximum temperature and the overall emissivity of the foil. A list of the FTS electron gun's parameters for the Stair Step approach are shown in Table 3.4, and includes the following:

1. Maximum Peak Emission Currents (mA) at 30 keV
2. Measured Maximum Average Emission Current for the pulsed beam
3. Corresponding duration that the beam was on the foil
4. SNS beam power equivalence for the Maximum Peak Emission Current

A second series of spots was also produced on Foil #1662 using a linear, or "Gradual Ramp Up," of the beam power. Each spot in the Gradual Ramp Up approach would be initially conditioned for 5.0 minutes at a beam current of

0.272 mA (SNS = 0.094 MW). After the initial five minutes of conditioning, the beam power would be linearly increased to the same maximum beam current setting and total ramp time used in the Stair Step approach. The rate of current ramp achieved is described in Equation 3.1 below:

Equation 3.1

$$Ramp\ Up\ Rate = \frac{[Final\ Maximum\ Peak\ Emission\ Current - 0.272\ mA]}{[Total\ Duration - 5\ minutes]}$$

Table 3.4 - Emission Current Settings for Emissivity Determination Experiment for Foil #1662 (Stair Step Ramp Up Method)

Spot	Maximum Peak Emission Current (mA)	Measured Maximum Average Emission Current (mA)	Time (min)	SNS Equivalence (MW)
#1S	0.272	0.017	5.0	0.094
#2S	0.640	0.040	Spot #1 + 5.0	0.220
#3S	1.120	0.070	Spot #2 + 5.0	0.385
#4S	1.600	0.100	Spot #3 + 5.0	0.550
#5S	2.160	0.135	Spot #4 + 5.0	0.743
#6S	2.720	0.170	Spot #5 + 5.0	0.936
#7S	3.200	0.200	Spot #6 + 5.0	1.101
#8S	3.760	0.235	Spot #7 + 5.0	1.293
#9S	4.320	0.270	Spot #8 + 5.0	1.486
#10S	4.800	0.300	Spot #9 + 5.0	1.651

This process was continued until the limit of the FTS electron gun was met (a beam current of approximately 5.0 mA), and the time frame was increased by 5.0 minutes for each additional beam current limit. These spots where identified as #XG, where "G" represents the Gradual Ramp Up method and "X" represents the appropriate position in the series.

For example, the first spot was conditioned for 5.0 minutes at a constant beam current of 0.272 mA (Spot #1G, SNS equivalent of 0.094 MW, foil temperature of 710 K). After the five minutes for Spot #1G, the foil was adjusted to provide a clean and unused area for Spot #2G. Spot #2G was also conditioned for 5. 0 minutes at a beam current of 0.272 mA (SNS = 0.094 MW). After the initial five minutes of conditioning, the beam current was linearly increased from 0.272 mA to 0.640 mA (SNS equivalent of 0.094 MW to 0.220 MW, foil temperature range of 710 K to 925 K) over the next 5.0 minutes (average rate of 0.074 mA/min = 0.025 MW/min)). After this, the foil was adjusted again to provide a clean and unused area for Spot #3G. Spot #3G was also conditioned for 5.0 minutes at a beam current of 0.272 mA (SNS = 0.094 MW). After the initial five minutes of conditioning, the beam current was linearly increased from 0.272 mA to 1.120 mA (SNS equivalent of 0.094 MW to 0.385 MW, foil temperature

range of 710 K to 1,175 K) over the next 10.0 minutes (0.085 mA/min = 0.029 MW/min).

The process was continued for the remaining ten spots to give a "gradual ramp up" look at beam current. This approach helped determine the effect that beam current has on the maximum temperature and the overall emissivity of the foil. Comparison of the Stair Step and Gradual Ramp Up results should help determine if the change in emissivity was a function of the time the foil spent at a specific beam current or if it was more influenced by the maximum peak beam current it experiences. A list of the FTS electron gun's parameters for the Gradual Ramp Up approach are shown in Table 3.5, and includes the following:

1. Maximum Peak Emission Currents (mA) at 30 keV
2. SNS beam power equivalence for the Maximum Peak Emission Current
3. Measured Maximum Average Emission Current for the pulsed beam
4. Corresponding duration that the beam was on the foil
5. Ramp up rate (for both the FTS and SNS equivalence)

Once the two series of spots were created on Foil #1662, it was removed from the FTS for post-analysis characterization. A photograph of Foil #1662, after being

removed from the FTS, is shown in Figure 3.4 (left foil). The spots produced by the Stair Step approach are on the right and the spots produced by the Gradual Ramp Up approach are on the left.

Table 3.5 - Emission Current Settings for Emissivity Determination Experiment for Foil #1662 (Gradual Ramp Up Method)

Spot	Maximum Peak Emission Current (mA)	SNS Equivalence (MW)	Measured Maximum Average Emission Current (mA)	Time (min)	Ramp Up Rate [Equation 3.1] (mA/min)	Ramp Up Rate [Equation 3.1] (MW/min)
#1G	0.272	0.094	0.017	5.0	-	-
#2G	0.640	0.220	0.040	10.0	0.074	0.025
#3G	1.120	0.385	0.070	15.0	0.085	0.029
#4G	1.600	0.550	0.100	20.0	0.089	0.030
#5G	2.160	0.743	0.135	25.0	0.094	0.032
#6G	2.720	0.936	0.170	30.0	0.098	0.034
#7G	3.200	1.101	0.200	35.0	0.098	0.034
#8G	3.760	1.293	0.235	40.0	0.100	0.034
#9G	4.320	1.486	0.270	45.0	0.101	0.035
#10G	4.800	1.651	0.300	50.0	0.101	0.035

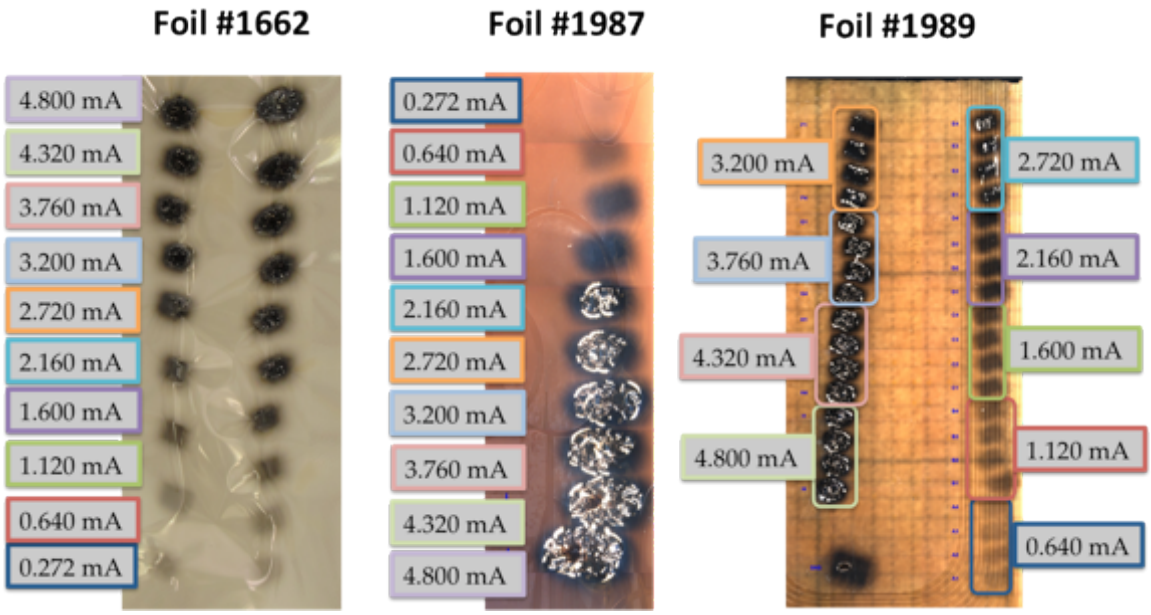

Figure 3.4 - Post-beam exposure. Foil #1662 had both the standard increases in emission currents for 5 minutes. Foil #1987 had 5 minutes of each displayed beam current (no conditioning); Foil #1989 has four spots at each beam current (no conditioning) for 1, 2, 4, and 8 minutes.

3.2.1.2 Foil #1987

For Foil #1987, a series of ten spots with increasing beam current density were placed on the foil within the FTS. The spots on Foil #1987 were neither conditioned at a low beam power nor were the beam currents gradually ramped up on the foil. Instead, the spots received 5.0 minutes at the same final beam currents as were used on Foil #1662. The purpose of this experiment was to determine how well the foil performs at higher beam powers with no conditioning. Additionally, this experiment was used to determine if the emissivity or the chemical state and crystallinity of the carbon material changed in a different manner than Foil #1662. These spots were identified as #XN, where

"N" represents the no conditioning method and "X" represents the appropriate position in the series.

A list of the FTS electron gun's parameters for the No Conditioning approach on Foil #1987 are shown in Table 3.6, and includes the following:

1. Peak Emission Currents (mA) at 30 keV
2. Measured Average Emission Current for the pulsed beam
3. SNS beam power equivalence for the Maximum Peak Emission Current
4. Corresponding duration that the beam was on the foil (5 minutes)

Once the series of spots were placed on Foil #1987, it was removed from the FTS for post-analysis characterization. A photograph of Foil #1987, after being removed from the FTS, is shown in Figure 3.4 (center foil).

3.2.1.3 Foil #1989

For Foil #1989, nine series of spots were placed on the foil with increasing beam currents. Each of the nine series had four spots associated with it that applied the same beam current to each spot for 1.0 minute (Spot #XA, where A =1 minute), 2.0 minutes (Spot #XB, where B = 2 minutes), 4.0 minutes (Spot #XC,

where C = 4 minutes), or 8.0 minutes (Spot #XD, where D = 8 minutes). This experiment was initiated to better determine the rate at which a foil changes from diamond to graphite as the beam emission current increases.

For example, Spots #1A, #1B, #1C, and #1D received a beam emission current of 0.640 mA (0.220 MW) for 1.0 minute, 2.0 minutes, 4.0 minutes, and 8.0 minutes, respectively. After each spot received the appropriate beam conditions

Table 3.6 - Emission Current Settings for Emissivity Determination Experiment for Foil #1987 (No Conditioning Method)

Spot	Peak Emission Current (mA)	Measured Average Emission Current (mA)	SNS Equivalence (MW)	Time (min)
#1N	0.272	0.017	0.094	5.0
#2N	0.640	0.040	0.220	5.0
#3N	1.120	0.070	0.385	5.0
#4N	1.600	0.100	0.550	5.0
#5N	2.160	0.135	0.743	5.0
#6N	2.720	0.170	0.936	5.0
#7N	3.200	0.200	1.101	5.0
#8N	3.760	0.235	1.293	5.0
#9N	4.320	0.270	1.486	5.0
#10N	4.800	0.300	1.651	5.0

for the desired amount of time, the foil was adjusted to provide a clean and unused area for the next spot. This process was repeated for all nine series of beam currents. (i.e., total of 36 spots). A list of the FTS electron gun's parameters used on Foil #1989 are shown in Table 3.7, and includes the following:

1. Corresponding duration that the beam was on the foil (1 to 8 minutes)
2. Peak Emission Currents (mA) at 30 keV
3. Measured Average Emission Current for the pulsed beam
4. SNS beam power equivalence for the Maximum Peak Emission Current

Once the sets of spots were placed on Foil #1989, it was removed from the FTS for post-analysis characterization. A photograph of Foil #1989, after being removed from the FTS, is shown in Figure 3.4 (right foil).

3.2.2 Emissivity and Temperature Measurements

The performance of a foil under SNS beam conditions is largely influenced by temperature. Therefore, a major goal of the FTS is to determine the temperature at different beam conditions and project how well various types of foils will perform at power levels within SNS. In the FTS, the temperature of the foil is measured with the FLIR infrared camera. The FLIR infrared camera

Table 3.7 - Emission Current Settings for Emissivity Determination Experiment for Foil #1989 (Time versus Emission Current)

Spot	Time (min)	Peak Emission Current (mA)	Measured Average Emission Current (mA)	SNS Equivalence for Current (MW)
#1A	1.0	0.640	0.040	0.220
#1B	2.0			
#1C	4.0			
#1D	8.0			
#2A	1.0	1.120	0.070	0.385
#2B	2.0			
#2C	4.0			
#2D	8.0			
#3A	1.0	1.600	0.100	0.550
#3B	2.0			
#3C	4.0			
#3D	8.0			
#4A	1.0	2.160	0.135	0.743
#4B	2.0			
#4C	4.0			
#4D	8.0			
#5A	1.0	2.720	0.170	0.936
#5B	2.0			
#5C	4.0			
#5D	8.0			
#6A	1.0	3.200	0.200	1.101
#6B	2.0			
#6C	4.0			
#6D	8.0			
#7A	1.0	3.760	0.235	1.293
#7B	2.0			
#7C	4.0			
#7D	8.0			
#8A	1.0	4.320	0.270	1.486
#8B	2.0			
#8C	4.0			
#8D	8.0			
#9A	1.0	4.800	0.300	1.651
#9B	2.0			
#9C	4.0			
#9D	8.0			

provides measurements tools to determine beam spot size and the temperature of a sample. Additionally, the FLIR infrared camera is capable of calculating the emissivity of a sample based on known measurements (e.g., using a known emissivity and temperature, it is capable of calculating the emissivity of a sample at the same temperature).

A major factor that influences the temperature of a sample is its emissivity. Emissivity is essentially a "measure of the efficiency in which a surface emits thermal energy [94]." The emissivity of a foil can change at different beam currents if a chemical transformation occurs (e.g., diamond to graphite). Therefore, it is important to know the emissivity of the foil at different stages of operation in SNS to accurately measure the temperature of the foil. The emissivity of a sample is relative to a blackbody source [95]. A blackbody source is a perfect emitter of its thermal energy, giving it an emissivity value of 1.0. The emissivity of a non-blackbody source sample is the fraction of thermal energy that would be emitted from a perfect blackbody source (i.e., emissivity is between 0.0 and 1.0). Because of this, a small change in emissivity may have a large effect on temperature readings when performing optical pyrometry measurements.

3.2.2.1 Emissivity

The emissivity of a translucent material can be determined from measuring the transmission of a blackbody source's radiation through it. This method is based on Kirchhoff's Law [95, 96], and is displayed in Equation 3.2:

Equation 3.2

$$\alpha_\lambda + \rho_\lambda + \tau_\lambda = 1$$

Where:

α_λ = spectral absorptance: the ratio of the spectral radiant power absorbed by an object to that incident upon it (value between 0.0 and 1.0)

ϱ_λ = spectral reflectance: the ratio of the spectral radiant power reflected by an object to that incident upon it (value between 0.0 and 1.0)

τ_λ = spectral transmittance: the ratio of the spectral radiant power transmitted through an object to that incident upon it (value between 0.0 and 1.0)

Additionally, Kirchhoff's law may be used to show that the spectral emittance (ε_λ) and spectral absorptance (α_λ) of a body are equal at any specified temperature and wavelength for a system at thermal equilibrium. This is shown in Equation 3.3:

Equation 3.3

$$\alpha_\lambda = \varepsilon_\lambda$$

Substituting Equation 3.3 into

Equation 3.2 and rearranging yields Equation 3.4 and Equation 3.5:

Equation 3.4

$$\varepsilon_\lambda + \rho_\lambda + \tau_\lambda = 1$$

or

Equation 3.5

$$\tau_\lambda = 1 - \varepsilon_\lambda - \rho_\lambda$$

Therefore, once the spectral transmittance (or transmission) and spectral reflectance are known, the spectral emittance (or emissivity) can be calculated. In order to show that there isn't a dependence upon wavelength when measuring transmission (i.e., temperature dependence), a range of temperatures may be used. If the measured transmission through a material changes significantly for different temperatures, it indicates that the material's emissivity is wavelength dependent (i.e., temperature dependent) and requires the emissivity of a sample to be determined for each temperature in question.

3.2.2.2 Measurement of Emissivity

The emissivity of the Gradual Ramp Up spots (Spots #1G – #10G) prepared on Foil #1662 were determined by measuring the transmission of radiation from a blackbody source. These measurements were obtained under the guidance of Dr. Ralph Dinwiddie, a well-known expert in thermography, at the National Transportation Research Center (NTRC) of ORNL. The following protocol was used for obtaining measurements with the blackbody source:

1. Set blackbody source to known temperature and allow it to equilibrate.

2. Position blackbody source and FLIR camera to optimize filter calibration, (leave the blackbody source and FLIR camera stationary throughout each tested temperature).

3. Measure temperature of blackbody source with FLIR camera.

4. With the temperature of the blackbody source known, place the foil between the blackbody source and FLIR camera. That is, position the foil so that the FLIR camera must now measure the temperature of the blackbody source by viewing it through the foil. Measure the

transmission of the blackbody source through the foil with the FLIR camera.

5. Repeat step #4 for the all spots that have received current and sections of the foil that have received no current.

6. Knowing Kirchhoff's Law and the applied principle for semi-transparent materials, calculate the emissivity of each spot.

In addition, Equation 3.5 may be simplified for translucent materials by assuming the spectral reflectance is negligible (i.e., $\varrho_\lambda = 0$). This simplifies Equation 3.5 to Equation 3.6:

Equation 3.6

$$\tau_\lambda = 1 - \varepsilon_\lambda$$

By simplifying this relationship to Equation 3.6, it allows a direct measurement of the foil's emissivity to take place. In addition, as the foil changes from diamond to graphite-like with increasing beam power (i.e., current density), this method may be used to understand how the emissivity changes with respect to

beam power exposure. A photograph depicting the blackbody experimental setup with the blackbody source [97], FLIR infrared camera, and foil is shown in Figure 3.5.

In order to determine if the emissivity was temperature dependent, four different temperatures were used to calculate the emissivity. The first temperature reading was at 285 °C and the FLIR camera used an indium antimonide (InSb) sensor that was calibrated for a temperature range of 5 – 300 °C (spectral range of 1.5 μm – 5.1 μm) [98]. The next three sets of temperature

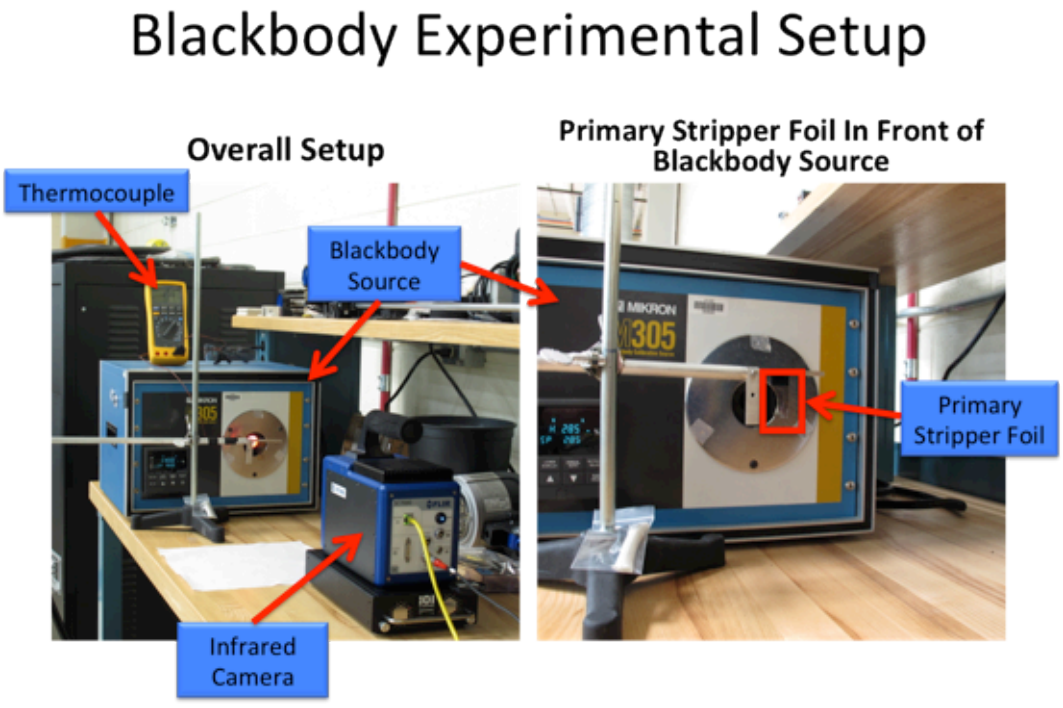

Figure 3.5 - Blackbody Experimental Setup

readings were performed at 500 °C, 750 °C, and 1,000 °C. To obtain measurements at these temperatures, a 50 mm filter (spectral range of 3.97 μm – 4.01 μm) was placed in front of the InSb sensor, allowing measurements to be obtained at a range of 300 – 1,500 °C [98]. The transmissions of the ten spots created by the Gradual Ramp Up method on Foil #1662 were measured with the FLIR camera at Blackbody Source temperatures s of 285 °C, 500 °C, 750 °C, and 1,000 °C and are given in Table 3.8 to Table 3.11. It was assumed that the spectral reflectance was negligible for these results. It was found that the emissivity was fairly consistent for the three higher blackbody source temperatures (i.e., 500 °C, 750 °C, and 1,000 °C). However, when the blackbody source temperature was at 285 °C, there was a slight dissimilarity with the calculated emissivity values from the three higher blackbody source temperatures This difference is assumed to be attributed to the two filters applied, and not a dependency on the wavelength (i.e., not temperature dependent). This is because there were no significant variations when using the same filter for the three higher blackbody source temperatures. In Table 3.12, the average emissivities determined at the three higher blackbody source temperature settings are given for each of the peak emission currents. The 30 keV electron beam placed a spot size of approximately 2.65 mm^2 for each beam emission current. The beam current densities were calculated by dividing the emission current by the spot size, and then correlated

Table 3.8 - Transmission measurements of Foil #1662 at a blackbody source temperature of 285 °C

Spot	Maximum Peak Emission Current (mA)	SNS Equivalence (MW)	Transmission Measurement τ	Emissivity Calculation ε
#1	0.272	0.094	0.827	0.173
#2	0.640	0.220	0.771	0.229
#3	1.120	0.385	0.673	0.327
#4	1.600	0.550	0.538	0.462
#5	2.160	0.743	0.293	0.707
#6	2.720	0.936	0.034	0.966
#7	3.200	1.101	0.019	0.981
#8	3.760	1.293	0.031	0.969
#9	4.320	1.486	0.006	0.994
#10	4.800	1.651	0.011	0.989

Table 3.9 - Transmission measurements of Foil #1662 at a blackbody source temperature of 500 °C

Spot	Maximum Peak Emission Current (mA)	SNS Equivalence (MW)	Transmission Measurement τ	Emissivity Calculation ε
#1	0.272	0.094	0.821	0.179
#2	0.640	0.220	0.766	0.234
#3	1.120	0.385	0.667	0.333
#4	1.600	0.550	0.518	0.482
#5	2.160	0.743	0.351	0.649
#6	2.720	0.936	0.203	0.797
#7	3.200	1.101	0.190	0.810
#8	3.760	1.293	0.192	0.808
#9	4.320	1.486	0.172	0.828
#10	4.800	1.651	0.175	0.825

Table 3.10 - Transmission measurements of Foil #1662 at a blackbody source temperature of 750 °C

Spot	Maximum Peak Emission Current (mA)	SNS Equivalence (MW)	Transmission Measurement τ	Emissivity Calculation ε
#1	0.272	0.094	0.818	0.182
#2	0.640	0.220	0.757	0.243
#3	1.120	0.385	0.660	0.340
#4	1.600	0.550	0.511	0.489
#5	2.160	0.743	0.340	0.660
#6	2.720	0.936	0.199	0.801
#7	3.200	1.101	0.188	0.812
#8	3.760	1.293	0.188	0.812
#9	4.320	1.486	0.170	0.831
#10	4.800	1.651	0.181	0.819

Table 3.11 - Transmission measurements of Foil #1662 at a blackbody source temperature of 1,000 °C

Spot	Maximum Peak Emission Current (mA)	SNS Equivalence (MW)	Transmission Measurement τ	Emissivity Calculation ε
#1	0.272	0.094	0.822	0.168
#2	0.640	0.220	0.754	0.246
#3	1.120	0.385	0.659	0.341
#4	1.600	0.550	0.508	0.492
#5	2.160	0.743	0.332	0.768
#6	2.720	0.936	0.180	0.820
#7	3.200	1.101	0.178	0.822
#8	3.760	1.293	0.175	0.825
#9	4.320	1.486	0.154	0.846
#10	4.800	1.651	0.156	0.844

Table 3.12 - Average emissivity calculations for Foil #1662 at 500 °C, 750 °C, and 1000 °C. In addition, the current density and the associated SNS power level.

Spot	Average Emissivity ε_{ave}	Maximum Peak Emission Current (mA)	Current Density Spot Size = 2.65 mm^2 (mA mm^{-2})	SNS Correlation (MW)
Blackbody	0.999	-	-	-
Foil	0.135	-	-	-
#1	0.176	0.272	0.101	0.094
#2	0.241	0.640	0.242	0.220
#3	0.340	1.120	0.440	0.385
#4	0.489	1.600	0.629	0.550
#5	0.660	2.160	0.849	0.743
#6	0.801	2.720	1.069	0.936
#7	0.812	3.200	1.258	1.101
#8	0.812	3.760	1.478	1.293
#9	0.831	4.320	1.698	1.486
#10	0.819	4.800	1.887	1.651

to a SNS beam power. Recall that the correlation between a 30 keV electron and a 1.0 GeV proton is 1.6 mA mm^{-2} = 1.4 MW. The associated SNS power levels were calculated and are shown in Table 3.12. The measured transmittance of blackbody radiation through the spots prepared on Foil #1662 are plotted versus the electron gun emission in Figure 3.6, and similarly the derived emissivities are shown for each emission current in Figure 3.7.

The emissivity trend increases very rapidly at lower beam currents before leveling out when the current reaches approximately 2.500 mA (an approximate SNS beam power of 0.900 MW). This leveling out is visibly noticeable as well. Once the emissivity was measured for all the beam currents, the emissivity corrected temperature of the foil at the various settings could be determined. Figure 3.8 depicts how the temperature and emissivity change with respect to the beam current density being applied to the foil. The temperature of the foil increases steadily, whereas the emissivity increases rapidly before leveling off. The maximum measured temperature and emissivity are less than 2,000 °C and 0.85, respectively. In additional tests on the foils, a significant increase in the current density (e.g., increase in the overall maximum temperature) has been applied to the foils and the foils have performed well (e.g., the fluttering of the foils was minimal, no significant increase in distortion of the foil, and no

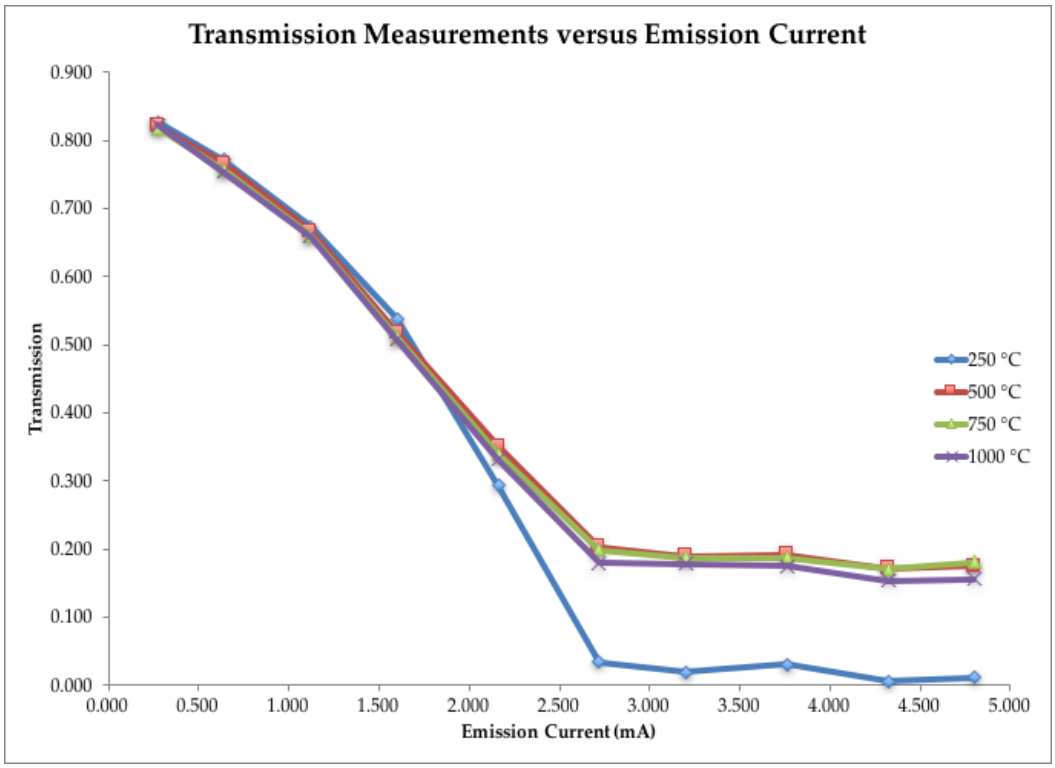

Figure 3.6 - Transmission Measurements versus Emission Current for Foil #1662

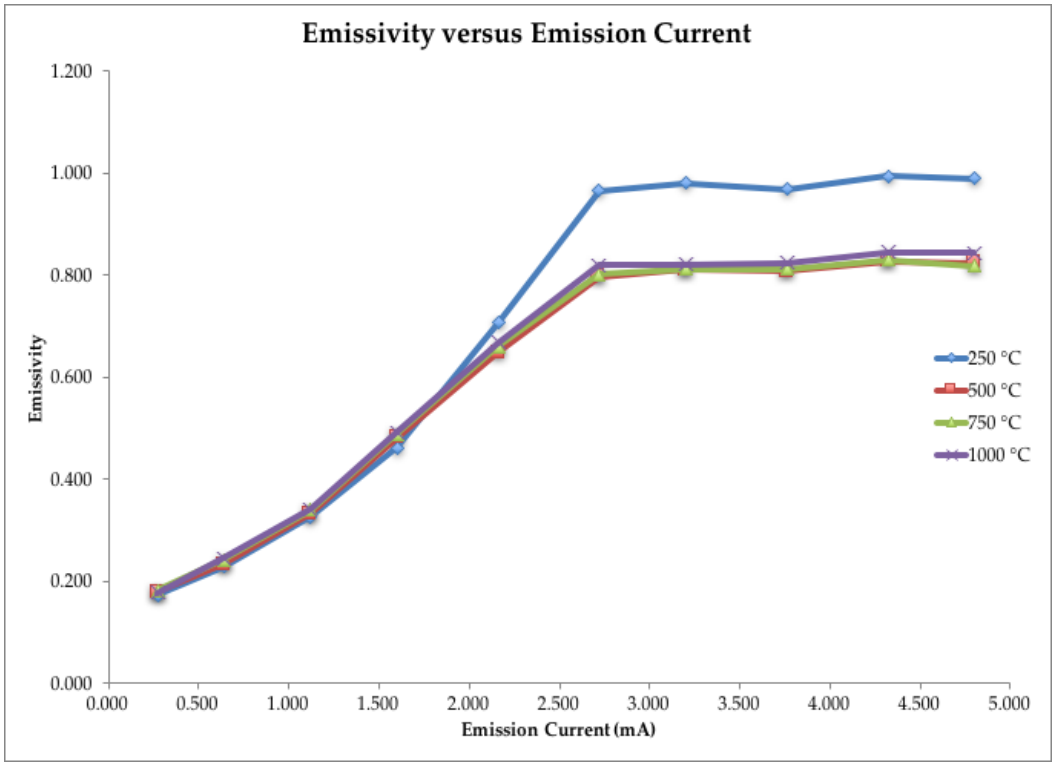

Figure 3.7 - Emissivity Calculation versus Emission Current for Foil #1662

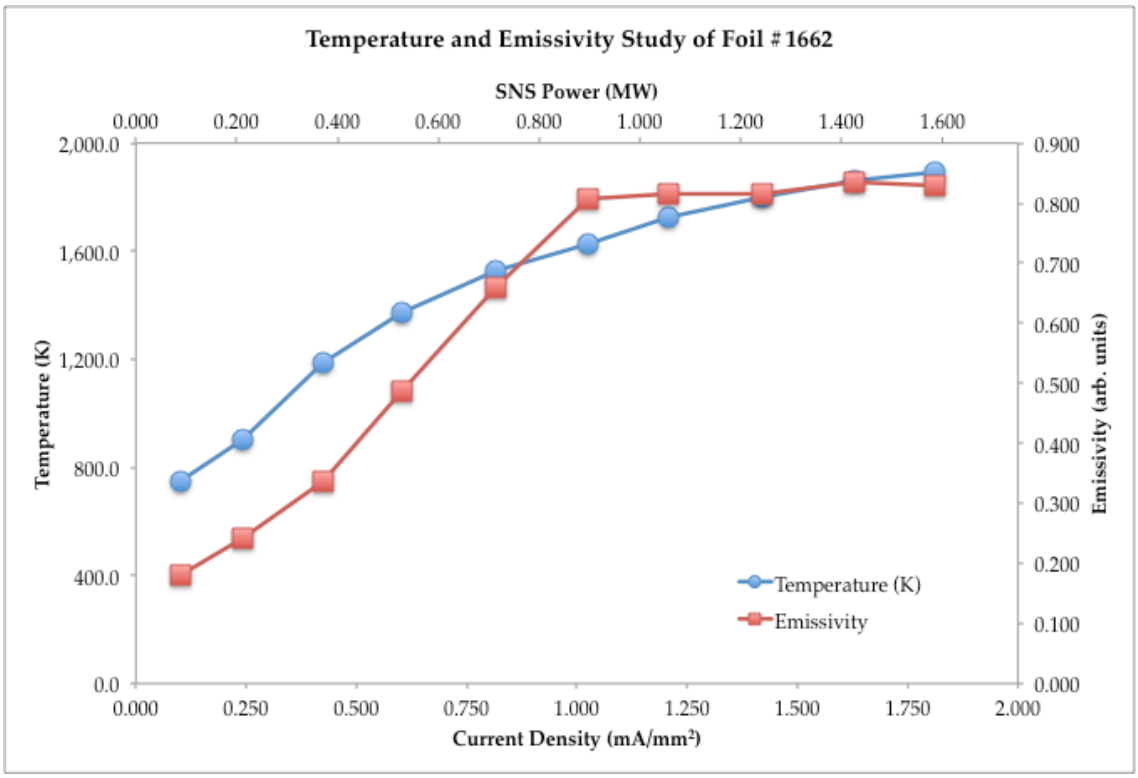

Figure 3.8 - Temperature and Emissivity at Electron Beam Current and Corresponding SNS Power Level for Foil #1662

additional increase in the number of pinholes). These higher beam currents and temperatures on the foils indicate that the current stripper foil design will survive at the future SNS upgrades for higher beam powers (SNS beam power upgrades above 1.4 MW).

The assumption that the spectral reflectance is negligible may not be appropriate for diamond due to its large index of refraction (n = 3.5). Snell's law predicts that the reflectance of diamond should be ~ 17%, which is significantly larger than the 4% reflectance obtained for optical glass. Measurement of the

reflectance of nanocrystalline diamond Foil #1815 using a white light source gave a value of ~25%. This cursory experimental measurement of reflectance is in qualitative agreement with Snell's Law. The results of lowering the emissivity by the calculated Snell's Law value for the reflectance of diamond are shown in Table 3.13. Unfortunately, this yields a negative value for the emissivity of the nanocrystalline diamond foil. While explicit error limits were not determined for these measurements of emissivity, the magnitude of the negative emissivity suggests that errors of +/- 0.05 are likely. If error limits of this magnitude are assumed, the emissivity of nanocrystalline diamond would be in agreement with previous research in which the emissivity of CVD diamond was determined to be 0.02 – 0.03 [95, 99, 100]. While it is not usually a factor of concern, the emissivity can be thickness dependent for very thin films, where it will decrease when the film thickness decreases. This decrease in the film's emissivity is caused by the smaller amount of material present. Typically, emissivity is considered to be a character of the surface of the sample. In actuality, it is dependent upon both the surface and depth of the sample (e.g., a macroscopic property of the material).

When a sample is emitting waves, the waves' emission, absorption, transmission, and reflection through the sample are influenced by the thickness,

Table 3.13 - Average emissivity calculations for Foil #1662 at 500 °C, 750 °C, and 1,000 °C for negligible spectral reflectance versus 17% spectral reflectance

Spot	Average Emissivity Calculated with no Reflectance ε_{ave}	Average Emissivity Calculated with Reflectance ε_{ave}
Blackbody	0.999	0.999
Foil	0.135	-0.035
#3	0.340	0.170
#4	0.489	0.319
#5	0.660	0.490
#6	0.801	0.631
#7	0.812	0.642
#8	0.812	0.642
#9	0.831	0.661
#10	0.819	0.649

up to its "critical thickness." Once a material reaches its critical thickness, the emissivity of the sample is no longer thickness dependent and has reached its bulk emissivity. Metals typically have a critical thickness around a hundred nanometers, whereas dielectrics can have a critical thickness up to a few centimeters [95, 96, 99, 100]. The thickness dependence of a thin layer of diamond grown on a silicon substrate has been studied and the results are shown in Figure 3.9 [95], where the emissivity of diamond decreases significantly around 4 – 5 μm, indicating the critical thickness of diamond [100]. In this study,

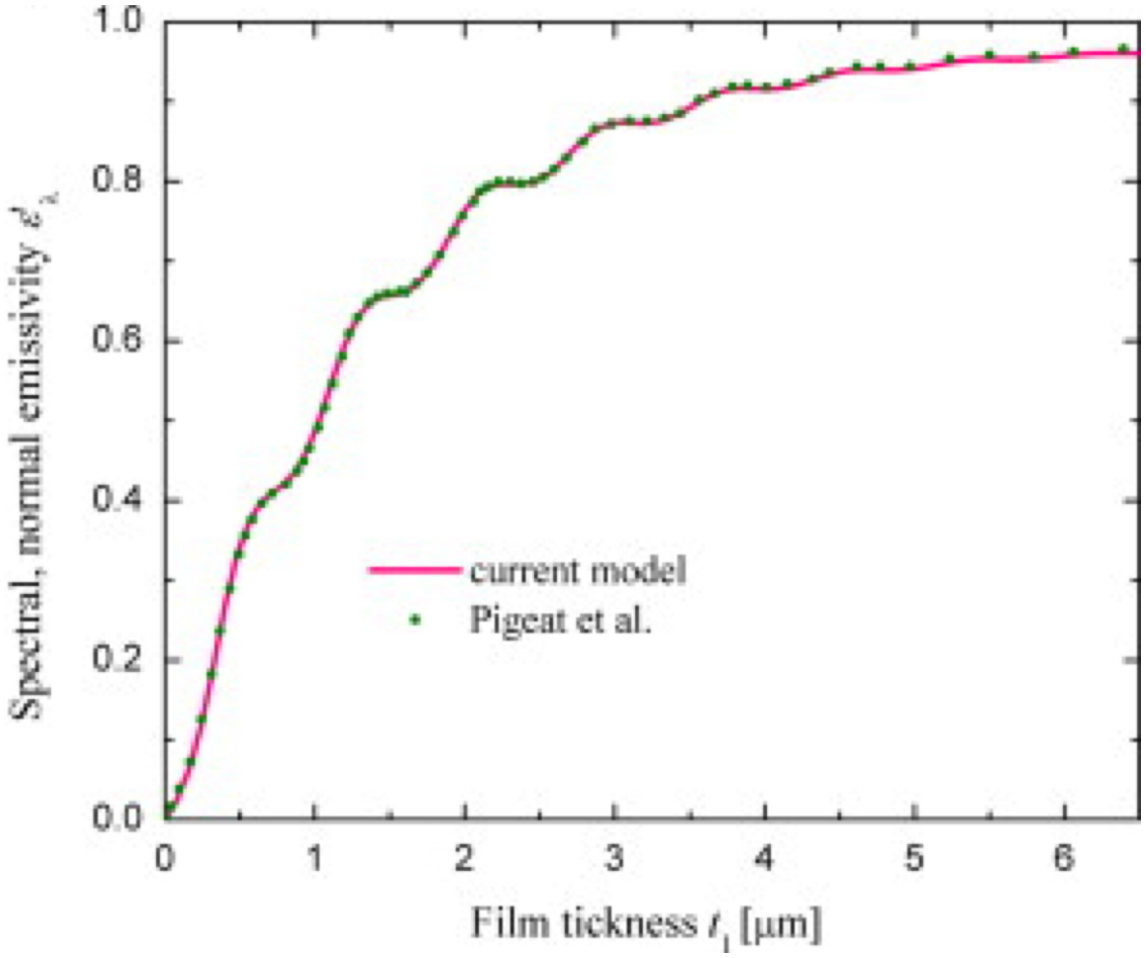

Figure 3.9 - Spectral, normal emissivity of a diamond layer deposited on a silicon substrate.

Edalatpour and Francoeur used a direct method to model the thickness dependence on the emissivity of diamond and compared the results to known values of diamond [95]. Therefore, the 1 μm thick nanocrystalline diamond films studied in this dissertation are below the critical thickness of 4 – 5 μm. Therefore, any measured emissivity would be likely be lower than the bulk emissivity of diamond as shown in Figure 3.10. However, as the foil becomes more graphitic from beam exposure, it also becomes more metallic. This results

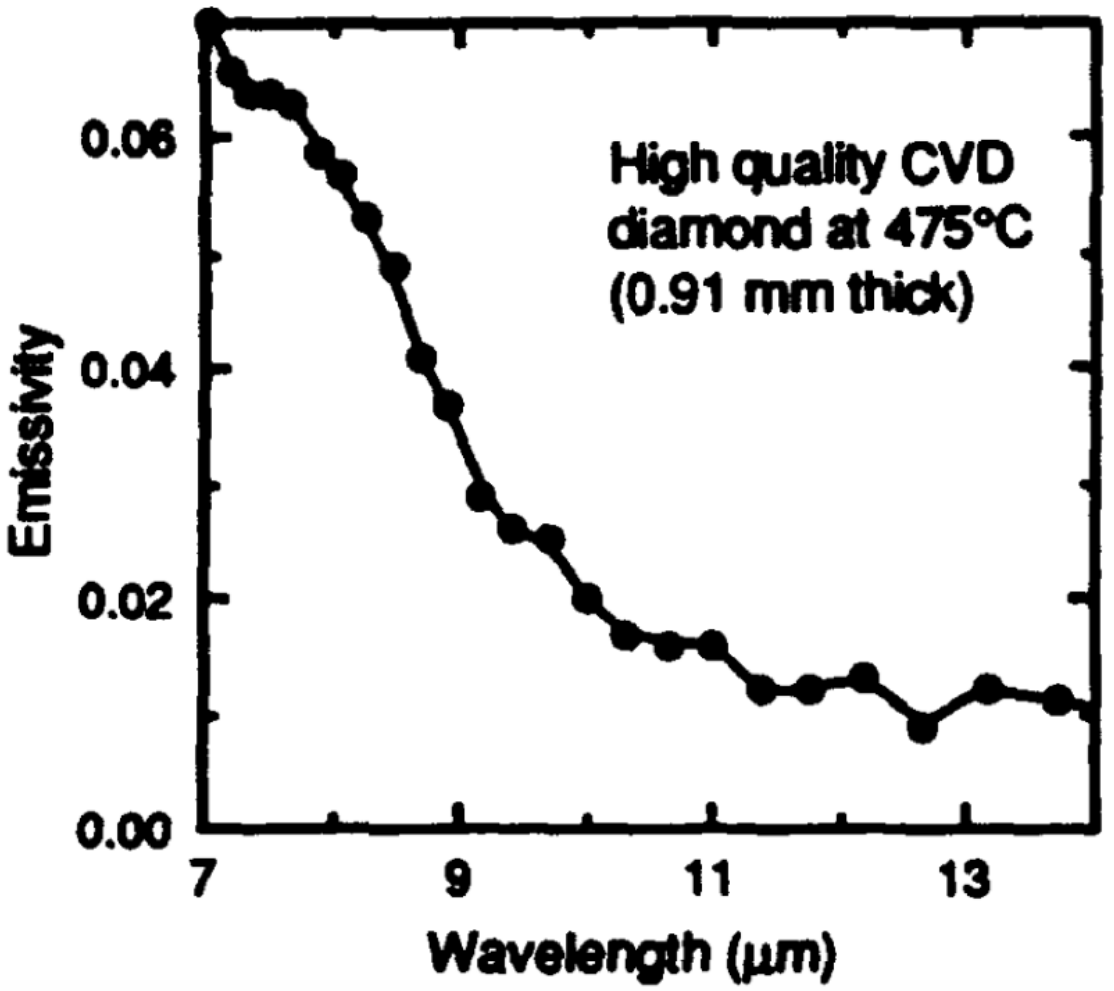

Figure 3.10 - Emissivity of High Quality CVD Diamond at 475 °C (thickness = 0.91 mm).

in a reduction in the critical thickness of the foil at this spot. For the spots treated with higher emission currents, the foil may be reaching bulk emissivity properties (e.g., emissivity is no longer thickness dependent). Additional work on the critical thickness of semi-transparent and transparent materials has been reported [101, 102, 103, 104, 105]. In addition to the study by Edalatpour and Francoeur, Daniel Harris at the Naval Air Warfare Center Weapons Division measured the emissivity of CVD diamond [99, 100]. In his report, Harris found

the emissivity of CVD diamond to be between 0.02 to 0.03 with a sample thickness between 0.35 mm to 0.37 mm. Additionally, Harris found the dependence of emissivity on wavelength, and plotted it in Figure 3.10 for a 0.91 mm thick high-quality CVD diamond at 475 °C [100]. As the emissivity of the foil changes with respect to beam current density, it was also expected that the crystalline structure was undergoing a change as well. The crystalline structures of the diamond foils were expected to be changing because as the foils received an increasing beam current density, the foils would begin to darken and wrinkle. The cause of the wrinkling was thought to be that the diamond was transforming into a graphitic material. Since the density of diamond and graphite are very different (3.5 g cm^{-3} and 2.0 g cm^{-3}, respectively), the foil required more area to allow the same amount of material to inhabit it as it transformed. Subsequently only select areas of the foil were experiencing the beam, causing the majority of the foil to remain unchanged from its diamond state. Since the graphite like material of the foil needed to expand, it would typically pucker up and cause additional stress wrinkles in the foil. This puckering of the foil can be seen in the many photographs in Chapter 1 as well as Figure 3.4.

3.3 Raman Spectroscopy

Although both photographs and videos were able to monitor some of the physical changes that foils were undergoing when exposed to various FTS beams, it was important to understand if the chemical state and crystallinity were changing and if the mechanism of this change could be determined. Therefore, it was decided to analyze the foils with Raman Spectroscopy.

Raman spectroscopy is a technique that relies on the inelastic scattering of a single wavelength (i.e., monochromatic) light source to study the vibrational and rotational modes of gases, vibrational modes of liquids, and phonon modes of solids. The monochromatic light source typically employed is a laser, in which the light becomes scattered when it interacts with a sample. The light has the ability to either scatter elastically or inelastically. If the light scatters elastically, it scatters at the wavelength of the laser and is referred to as Rayleigh scattering. If the light scatters inelastically (i.e., interacts with the sample), the light can scatter at longer wavelengths (Stokes scattering) or shorter wavelengths (Anti-Stokes scattering) relative to the excitation. This inelastic scattering is referred to as Raman Scattering. Typically, elastic scattering is many orders of magnitude more intense than the inelastic Raman scattering. Therefore, the

elastic or Rayleigh scattered peak is removed from detection by a filter, or series of gratings. Modern CCD spectrometers also typically utilize CCD detectors to gain the advantage of parallel detection and improved sensitivity for detection of the lower intensity, inelastically scattered photons.

3.3.1 Background

Raman spectroscopy has been widely used as a technique to characterize diamond thin films. Raman spectroscopy has the capability of distinguishing between various forms of carbon, including sp^2 carbon and sp^3 carbon, and to measure the overall quality of thin films (e.g., a higher ratio of sp^3 carbon to sp^2 carbon indicates a higher quality nanocrystalline film). In a research paper by Knight and White [106], it describes how Raman spectroscopy has become the norm for analyzing diamond films. In their study, Knight and White utilize an argon ion laser (λ = 514 nm) to excite a variety of carbon samples. These samples include natural diamonds, synthetic diamonds and diamond films, diamond-like carbons, crystalline graphite, and noncrystalline carbons of various kinds. The corresponding Raman peaks to each carbon sample are listed in Table 3.14. In addition to showing a broad range of carbon samples, their study showed that the quality of diamond film grown was largely dependent on a small percent change in methane gas and temperature. A lower temperature (~990 °C versus

Table 3.14 - Visible Raman spectroscopy (λ = 514 nm) of a Variety of Carbon Samples

Carbon Sample	Raman Line First Order Band (Peak shape)	Raman Line Second Order Band (Peak shape)
Natural Diamonds	1332 cm^{-1} (Sharp)	2450 cm^{-1} (Sharp)
Diamond Film (2% CH_4, 80 Torr, 1200 ˚C)	1346 cm^{-1} (Broad) 1574 cm^{-1} (Broad)	-
Diamond Film (1.5% CH_4, 40 Torr, 970 ˚C)	1333 cm^{-1} (Sharp) 1597 cm^{-1} (Broad)	-
Diamond Film (1% CH_4, 80 Torr, 990 ˚C)	1332 cm^{-1} (Sharp) 1400 – 1600 cm^{-1} (Broad)	-
Diamond Film (0.5% CH_4, 80 Torr, 980 ˚C)	1332 cm^{-1} (Sharp)	-
Diamond-Like Carbon	1555 cm^{-1} (Broad)	Very broad
Single Crystal Graphite	1580 cm^{-1} (Sharp)	-
Polycrystalline Graphite	1357 cm^{-1} (Broad) 1587 cm^{-1} (Sharp)	2700 – 2724 cm^{-1} (Broad)
Highly Oriented Pyrolytic Graphite (HOPG)	1576 cm^{-1} (Sharp)	2719 cm^{-1} (Broad)
Natural Graphite Crystal	1580 cm^{-1} (Sharp)	2724 cm^{-1} (Broad)
Glassy Carbon	1343 cm^{-1} (Sharp) 1591 cm^{-1} (Sharp)	2680 cm^{-1} (Broad) 2924 cm^{-1} (Broad)
Charcoal	1360 cm^{-1} (Broad) 1584 cm^{-1} (Broad)	Very broad

1,200 °C) and a smaller percentage of methane (≤ 1.5% versus ≥ 2%) leads to higher quality microcrystalline diamond films.

The visible Raman spectrum (λ = 514 nm) of a microcrystalline diamond film grown on a silicon substrate is shown by the black trace in Figure 3.11. In the spectrum of the microcrystalline diamond foil, the major sharp peak at 1332 cm^{-1} represents the sp^3 bonded carbons in the foil and is indicative of diamond. Whereas, the broad peak ranging between 1450 – 1620 cm^{-1} represents sp^2 bonded carbon, located either in the bulk or within the grain boundaries. The laser beam used in the Raman spectra of the film does not discriminate between the grains and grain boundaries when sampling the film. The non-diamond peaks (e.g., sp^2 carbon) that are observed most likely have contributions from the grains boundaries (e.g., sp^3 carbon), as well as the potential for non-diamond contamination in the grains. According to Prawer and Nemanich, they cite the following, "in addition to the first-order Raman line at 1332 cm^{-1}, peaks appear which for the most part reflect sp^2 bonded components of the films, either in the bulk or in the boundaries" [107]. Now the issue of the trans-polyacetylene grain boundary peaks maybe different. When you grow nanocrystalline material, the fraction of the material that is grain boundary is expected to increase significantly due to the inherently smaller particle size. The final peaks are those

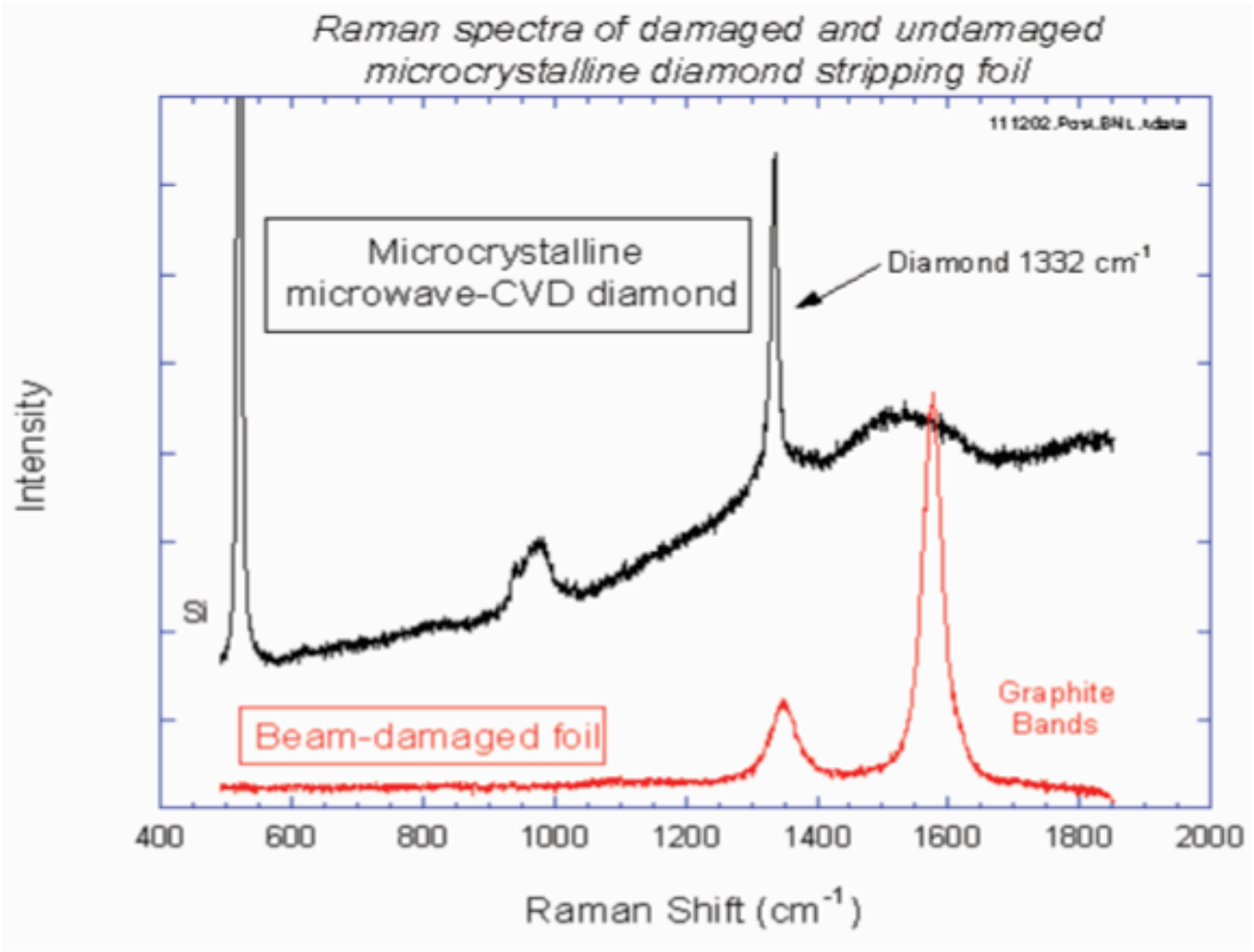

Figure 3.11 - Raman Spectra of microcrystalline diamond foil before and after beam induced heating.

associated with silicon, since the silicon substrate since it has not been etched away. The peaks associated with silicon include the sharp, first order peak at 520 cm^{-1}, and the broad, second order peak between 920 cm^{-1} – 1000 cm^{-1}. Additionally, Figure 3.11 shows the same diamond foil after its silicon substrate was etched away and then exposed to a 650 keV H^- test beam at BNL (red trace). [108] Since the silicon substrate was etched away prior to beam exposure, the silicon peaks are no longer present in the spectrum. After the foil was exposed to the 650 keV H^- test beam, the following occurs:

1. Decrease in the diamond peak at 1332 cm^{-1}
2. Disappearance of broad, amorphous carbon peak at 1480 cm^{-1} – 1560 cm^{-1}
3. Development of graphite's D-band peak of graphite at 1580 cm^{-1}.

This indicates that exposure of the diamond film to the beam and the high thermal load it creates, produces a transformation from diamond to graphite. This is expected at high heats due to diamond's thermodynamic instability. Therefore, it can be assumed that when high thermal loads are applied to a diamond foil, it may transform the film into a more graphite-like material. The understanding of how and when diamond transforms into graphite has been study since 1924, in which it was found that diamond under a vacuum

environment (e.g., free of oxygen), begins to transform to graphite at a temperature range between 1,500 and 1,800 °C [108]. When the diamond is not under a vacuum environment (e.g., the presence of oxygen), diamond will begin to transform to graphite at temperatures above 600 °C [108].

A large majority of this project utilized nanocrystalline diamond foils grown at ORNL. Therefore, it was essential to determine a baseline Raman spectrum for the nanocrystalline diamond films and how the films transform when exposed to varying levels of heat (i.e., beam powers). All Raman spectra were obtained with a source beam size of 2 – 4 μm, using a microscope objective of 50x to 100x. Raman spectroscopy was also routinely used to monitor whether nanocrystalline diamond growth was achieved and the overall quality of the foil. In Figure 3.12, a visible Raman spectrum (λ = 514 nm) of a nanocrystalline diamond foil pre- and post-beam exposure by a 30 keV electron beam in the FTS is shown. In contrast to the microcrystalline diamond spectrum in Figure 3.11, the sharp diamond peak at 1332 cm^{-1} is barely discernable from the much broader peak in this region that spans from ~1250 to 1400 cm^{-1} in the spectrum of the nanocrystalline diamond film. In addition, another strong broad feature develops near 1560 cm^{-1} which is attributed to sp^2 carbon. New features, that are indicative of a nanocrystalline diamond film emerge at approximately 1140 cm^{-1}

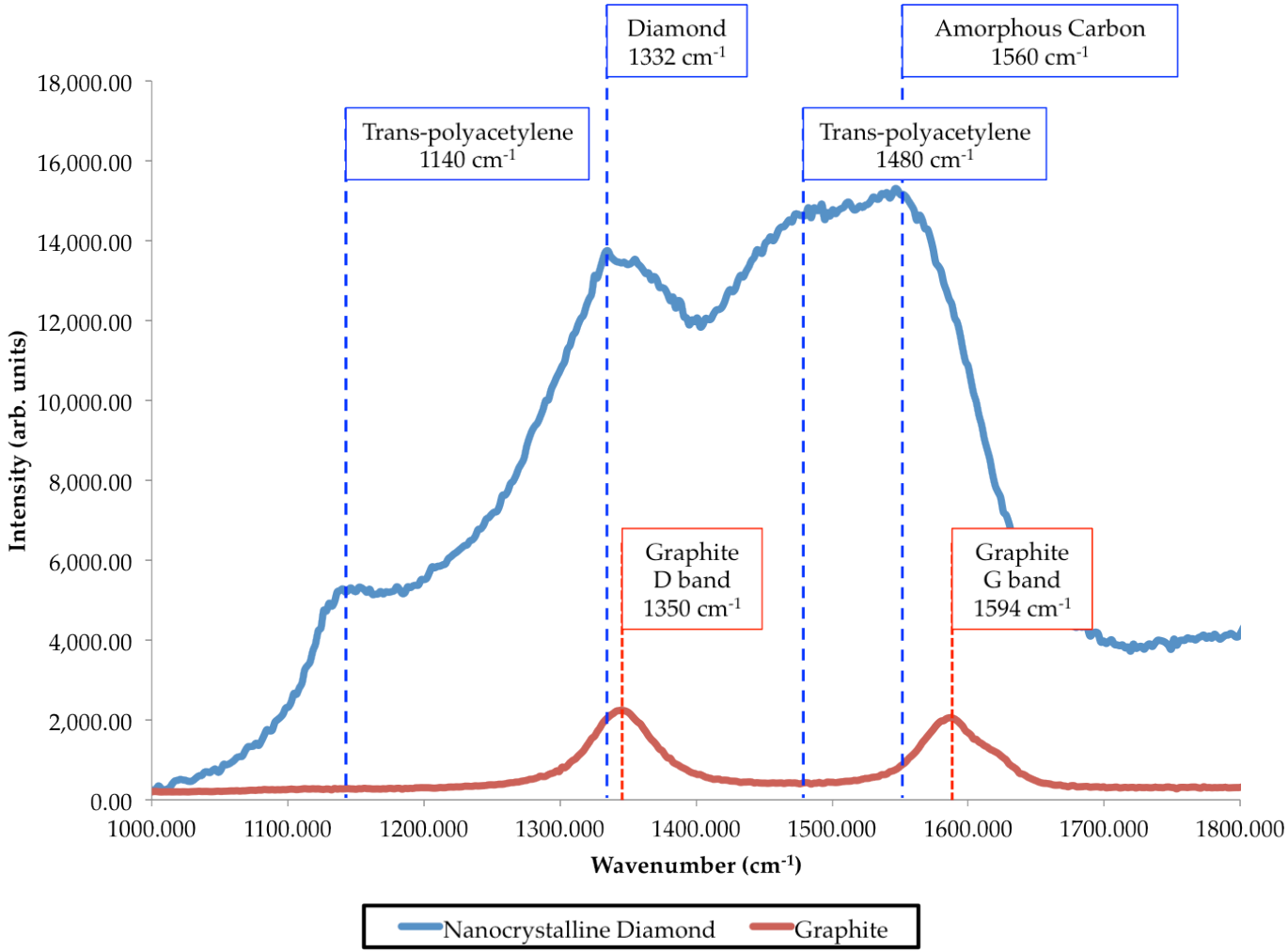

Figure 3.12 - Visible Raman spectra of nanocrystalline diamond foil pre-beam exposure (blue) and post-beam exposure (red).

and 1480 cm^{-1}, and have been identified with the trans-polyacetylene grain boundaries in the film [107, 109, 110, 111, 112, 113, 114]. Since the trans-polyacetylene peak is only a characteristic of nanocrystalline diamond, it can be used to determine whether a microcrystalline or nanocrystalline diamond film was grown. In this sample, the film's silicon substrate was etched away prior to any Raman spectrum being obtained. Therefore, no silicon peaks appear in the spectrum. As shown in this experiment, when a microcrystalline diamond foil is exposed to a high thermal load it will transform from having peaks associated with diamond to peaks associated with graphite. This is very similar to what happens in nanocrystalline diamond foils. In the post-beam exposure spectrum of the nanocrystalline diamond foil in Figure 3.12 (red), the peaks associated with diamond and trans-polyacetylene all but disappear and the peaks associated with the D and G bands of graphite dominate. Additional analysis of the various shifts and changes in peaks will be discussed in a further section.

The visible Raman spectrum provides insight into the transformation of the foil from nanocrystalline diamond to graphite. By monitoring the foil at increasing beam current densities (e.g., increasing temperature), the loss of the trans-polyacetylene grain boundaries indicates the onset of the transformation. Additionally, the visible Raman spectrum works well for determining whether

or not a foil is microcrystalline or nanocrystalline. Since the peaks associated with trans-polyacetylene dominate the visible spectrum, it is difficult to track the rate and the mechanism at which a foil transforms from a diamond to graphite. By switching to a laser source in the ultraviolet region (λ = 257 nm), it was found to be a better probe of the changes that the foil undergoes because it does not show the peaks associated with either trans-polyacetylene or the D-band of graphite. The reason why the spectra appear to be so different is due to the changes in the cross section for Raman scattering of diamond and graphite at each of these wavelengths. In the visible region (i.e., λ = 514 nm), the cross-section of graphite is nearly fifty times that of diamond [106, 115, 116, 117, 118, 119, 120, 121, 122]. Therefore, the peaks of graphite dominate the overall spectrum. Whereas in the ultraviolet region (i.e., λ = 257 nm), the cross-section of diamond becomes approximately the same as that of graphite [123, 124, 125]. Since the cross-section of both diamond and graphite are similar, this allows diamond to become one of the dominant species in the spectrum.

The Raman spectrum of a nanocrystalline diamond foil recorded with 257 nm excitation before and after FTS beam exposure is shown in Figure 3.13. Prior to any thermal loads applied to the nanocrystalline diamond foil, a sharp peak exists for diamond at 1332 cm^{-1} and a broad G-band peak of graphite

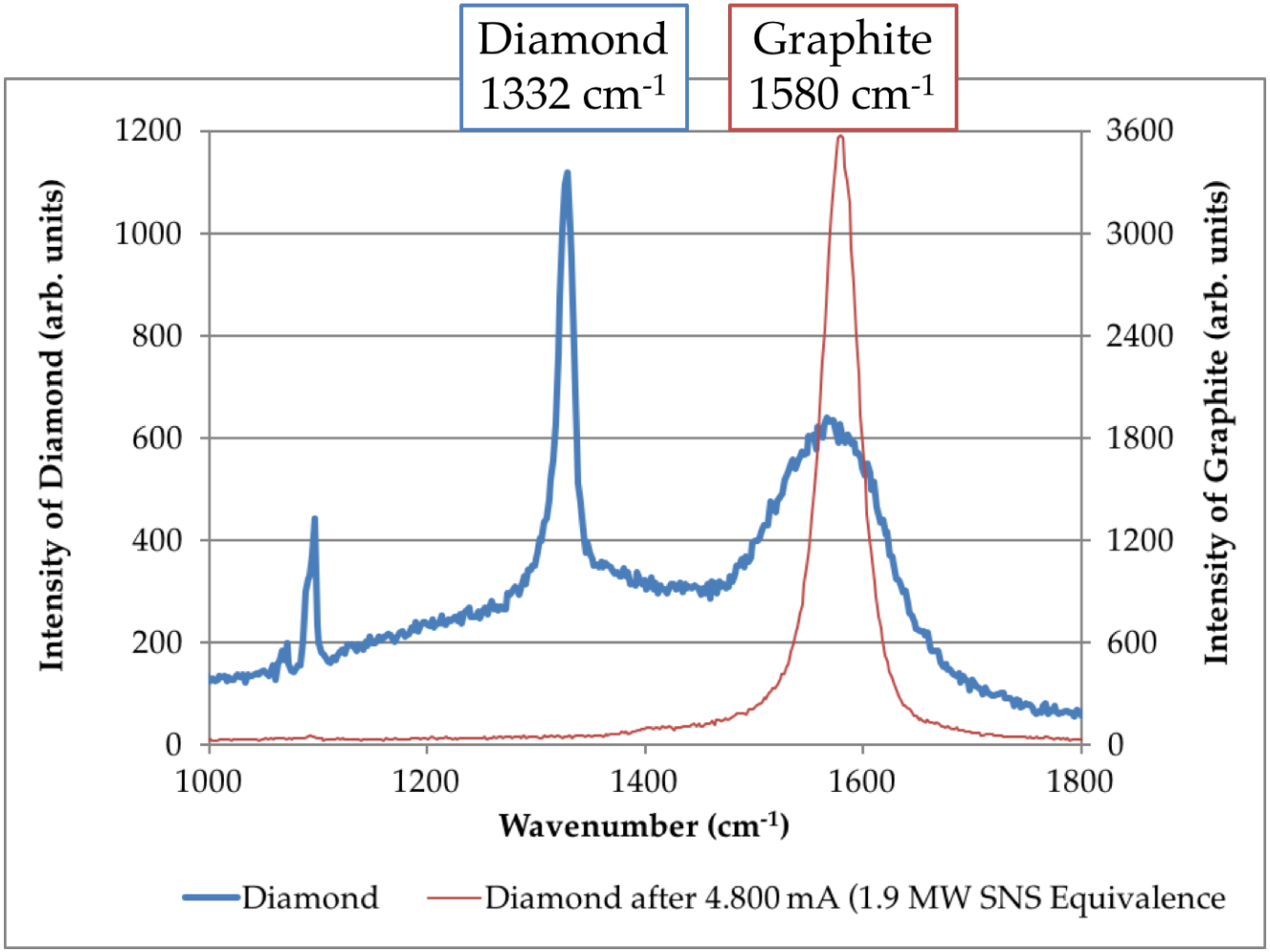

Figure 3.13 - UV Raman spectra of a nanocrystalline diamond foil pre-beam exposure (blue) and post-beam exposure (red).

around 1580 cm^{-1}. After the foil has been exposed to a very high thermal load, the single G-band peak of graphite peak at 1580 cm^{-1} dominates the spectrum. This illustrates how operating the Raman Spectrometer in the ultraviolet allows for a cleaner identification of the peaks associated with diamond and graphite. In addition to ultraviolet Raman spectra taken of a nanocrystalline diamond pre-beam and post-beam exposure, spectra of several carbon standards were taken to establish benchmarks for UV Raman spectra of various types of carbon. The carbon standards included a diamond shard, a Type IIb diamond, glassy carbon, a graphite rod, and highly oriented pyrolytic graphite (HOPG). The peaks for the diamond shard and Type IIb diamond were both at approximately 1332 cm^{-1}. The peak for the glassy carbon was at approximately 1594 cm^{-1}, and the peaks for the graphite rod and HOPG were at approximately 1580 cm^{-1}. The ultraviolet Raman spectra of the carbon standards are illustrated in Figure 3.14.

This research used both visible and ultraviolet Raman, at a wavelength of 514 nm and 257 nm, respectively, to monitor the changes that occur within the foils at the various beam settings. The visible Raman region of diamond films has been extensively studied and was used in initial tests to monitor the change. Unfortunately with nanocrystalline diamond, the less stable carbon atoms in the grain boundaries (i.e., sp^2 carbons) have a significantly larger cross section in the

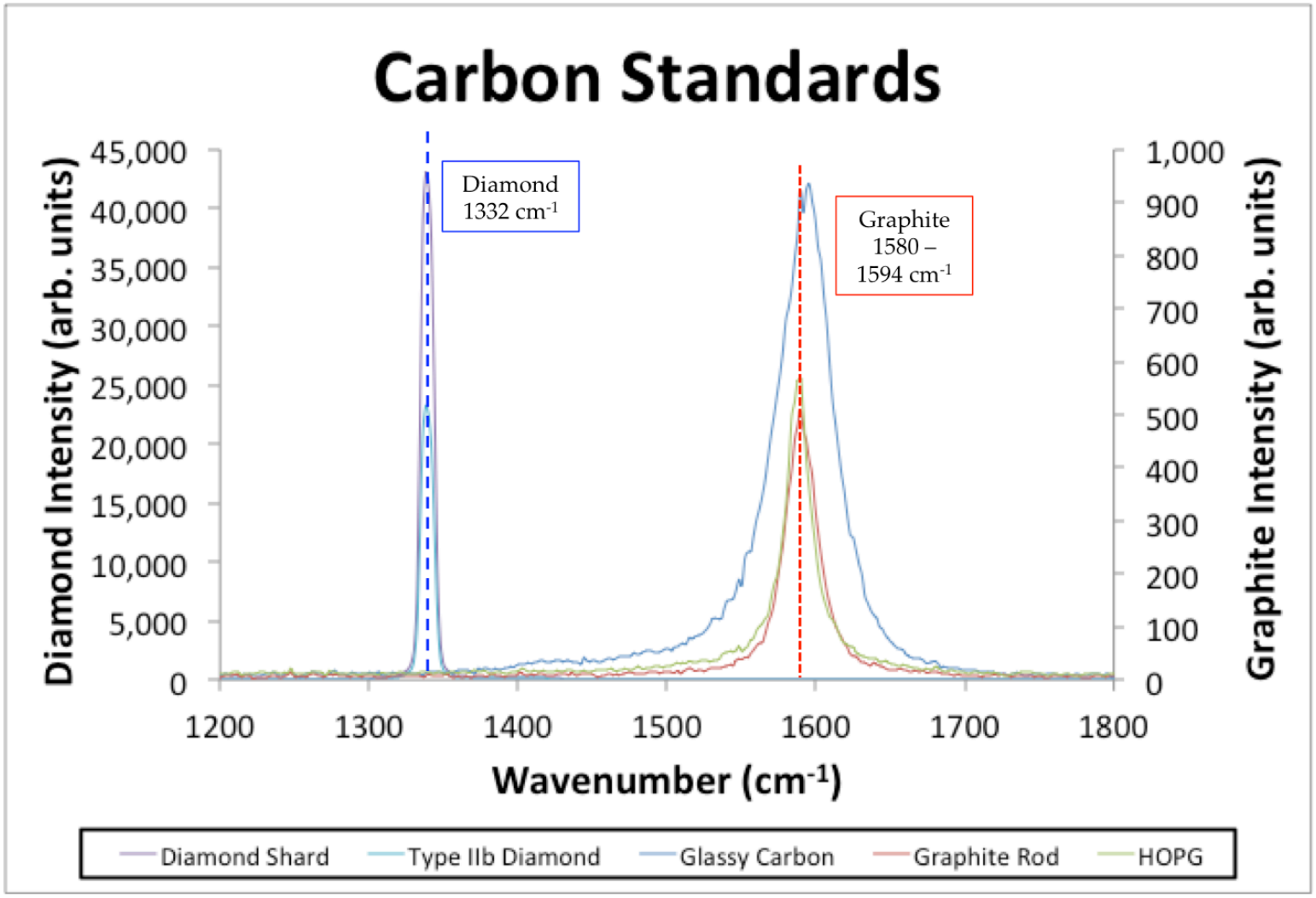

Figure 3.14 - UV Raman spectra of various carbon standards (both diamond and graphite samples).

visible region (λ = 514 nm) than the diamond (i.e., sp^3 carbon) [106, 126, 127]. The cross section of sp^2 carbon in the visible region is approximately 50 to 230 times the associated cross section of sp^3 carbon [109, 110, 122, 123, 124]. This allows the broad Raman bands associated with sp^2 carbon to dominate the spectrum and make the peaks associated with diamond and graphite difficult to isolate. By switching from visible Raman (λ = 514 nm) to ultraviolet Raman (λ = 257 nm), it has been shown that the diamond (1332 cm^{-1}**),** and graphite (1580 cm^{-1}) peaks become more prominent. Whereas the broad peaks associated with trans-polyacetylene grain boundaries and the D-band of graphite all but disappear. This is due to associated cross section of graphite and diamond in the ultraviolet, in which the cross section of diamond is approximately equal to graphite [109, 110, 122, 123, 124]. Therefore, ultraviolet Raman spectroscopy may be used to better track the crystalline change that is occurring as the nanocrystalline diamond foil is becoming more graphitic from increased beam exposure.

This study probes the process of that transformation, correlates it to temperature and beam conditions of SNS, and identifies the carbon material produced. By utilizing Raman spectroscopy, foils that have been exposed to a variety of beam conditions in the FTS ware characterized to monitor how the peaks associated with diamond, graphite, and trans-polyacetylene were affected

at these conditions.

3.3.2 Interpretation of Results

3.3.2.1 Foil #1662

Foil #1662 is a nanocrystalline diamond foil developed by Microwave Plasma-Enhanced Chemical Vapor Deposition (MPECVD) at ORNL. It has an aerial density of 363 μg/cm^2 and a U-shaped checkerboard lithography pattern. A 45-degree cut was made on the bottom corner of the foil post growth, giving a full box-top lid on all sides of the freestanding diamond portion except for the cut corner. Two series of spots were created in the FTS on Foil #1662 as described in detail in Section 3.2.1.1. The spots were created by the Stair Step (Spot #1S to Spot #10S, refer to Table 3.4) and the Gradual (Spot #1G to Spot #10G refer to Table 3.5) ramp up methods. Visible Raman spectra were taken of spots created by the Stair Step and Gradual Ramp Up methods and are compared to one another in Figure 3.15 and Figure 3.16. For both Figure 3.15 and Figure 3.16, the visible Raman spectrum of the initial spots show the same peaks commonly associated with nanocrystalline diamond. The features at 1140 cm^{-1} and at 1480 cm^{-1} are associated with the grain boundaries and trans-polyacetylene. The second peak at 1332 cm^{-1} is that of crystalline diamond, and is the major peak

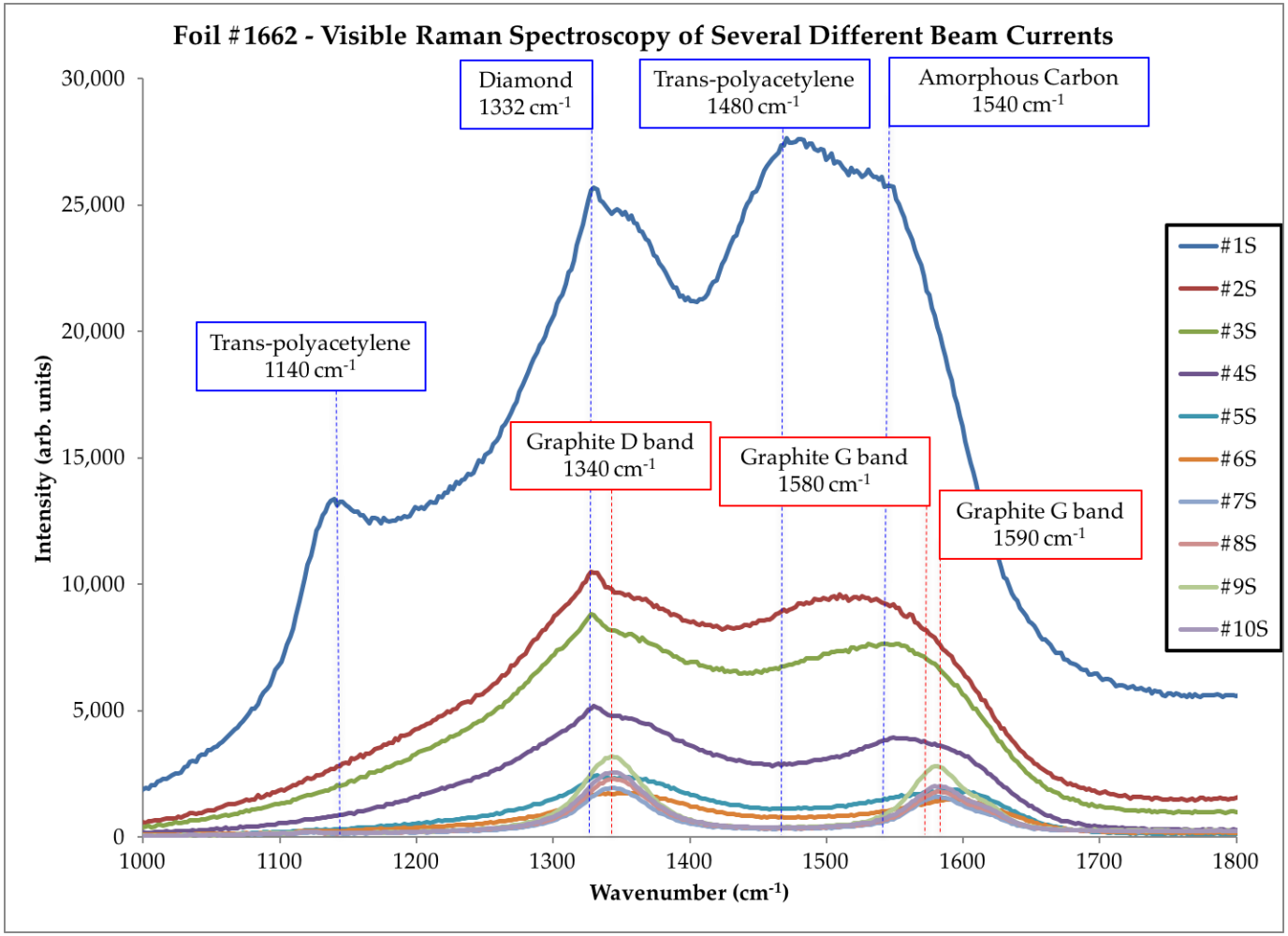

Figure 3.15 - Visible Raman spectra of Foil #1662 after being exposed to increasing beam power density as described in Table 3.4 (Stair Step Approach).

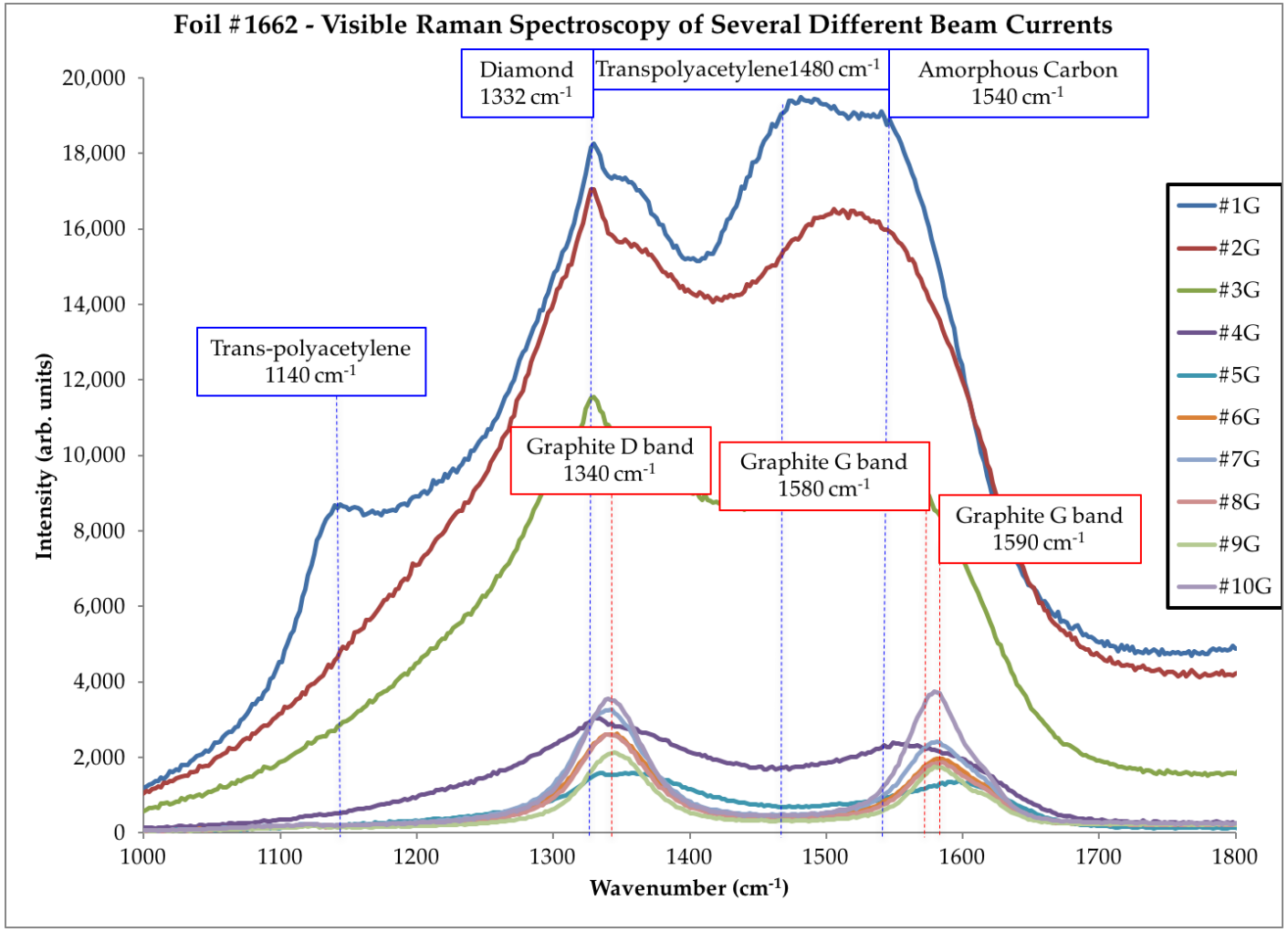

Figure 3.16 - Visible Raman spectra of Foil #1662 after being exposed to increasing power density as described in Table 3.5 (Gradual Approach)

associated with diamond. The next peaks at 1340 cm^{-1}, 1550 cm^{-1}, and 1580 cm^{-1} are associated with the D-band of graphite, amorphous carbon, and the G-band of graphite, respectively. Since the sample is a nanocrystalline diamond film, it is made up of small diamond crystals interconnected by grain boundaries. The smaller the grain size, the larger the fraction of the sample that is grain boundary material. The grain boundaries consist of disordered sp^3 carbon and sp^2 carbon (e.g., graphite, amorphous carbon, and trans-polyacetylene). For both sets of beam conditions, the peaks associated with trans-polyacetylene and amorphous carbon tend to be the first to disappear when exposed to the beam of the electron gun. As the intensity of the beam increases (e.g., more thermal heat is applied), the peak associated with diamond at 1332 cm^{-1} decreases. On the other hand, as the diamond peak is decreasing, the D-band and G-band of graphite increases. After the beam reaches a current of 2.160 mA (SNS equivalent of 0.743 MW, approximate foil temperature of 1,535 K), the peaks associated with diamond have all but disappeared and the D band of graphite (1350 cm^{-1}) increases in intensity. Additionally, the G band of graphite shifts from approximately 1570 cm^{-1} to 1594 cm^{-1}. This peak shift is interpreted as the graphite shifting from an amorphous like graphite to more nanocrystalline graphite [109, 123, 124]. As the beam current and foil temperature continues to increase, the relative intensity of the graphite peaks grows before reaching a maximum at a beam current of 4.320

mA (SNS equivalent of 1.486 MW). Additionally, the G band of graphite shifts from approximately 1594 cm^{-1} to 1580 cm^{-1} when the temperature on the foil gets at or above 1,715 K (an approximate beam current of 3.200 mA or SNS equivalent of 1.101 MW). This fluctuation of the graphite peak indicates that the foil has developed a longer-range graphitic order similar to HOPG, or simply, the foil has transformed from nanocrystalline graphite to graphite. The intensity of the graphite peak subsequently begins to fluctuate at these higher beam currents. This is most likely due to the development of holes in the foil. These holes cause a decrease in the overall intensity of the Raman signal. Additionally, as the spots become darker with each increasing beam current, the ability for the Raman spectrometer to capture all of the scattered light significantly decreases. Once this intensity levels off and/or decreases, it is believed that the foil has found a stable crystalline structure and will undergo no additional thermal changes. In addition to the comparison of both sets of beam conditions and their respective visible Raman spectra, ultraviolet Raman spectra were taken to better monitor how the peaks associated with diamond and graphite change at various beam exposures. In the ultraviolet region, the major peaks in the spectrum are the diamond peak (1332 cm^{-1}) and the G band of graphite peak (1580 cm^{-1}). This is in comparison to the visible region, in which the diamond and G band of graphite peaks are obscured by the grain boundaries peaks (1140 cm^{-1}, 1350 cm^{-1}, and 1550

cm^{-1}). Ultraviolet Raman spectra of the Stair Step and the Gradual Ramp Up methods are shown in Figure 3.17 and Figure 3.18, respectively. Similar to Figure 3.15 and Figure 3.16, after the beam reaches a current of 2.160 mA (SNS equivalent of 0.743 MW, approximate foil temperature of 1,535 K), the peak associated with diamond (1332 cm^{-1}) has all but disappeared. At this same intensity, the G band of graphite shifts from approximately 1570 cm^{-1} to 1594 cm^{-1}. As noted earlier, this peak shift is interpreted as the graphite shifting from an amorphous like graphite to nanocrystalline graphite [109, 123, 124]. As the beam current intensity increases further, the graphite peak shifts from approximately 1594 cm^{-1} to 1580 cm^{-1} when the temperature on the foil gets at or above 1,715 K (an approximate beam current of 3.200 mA or SNS equivalent of 1.101 MW). This fluctuation of the graphite peak indicates that the foil has developed a longer-range graphitic order similar to HOPG, or simply, the foil has transformed from nanocrystalline graphite to graphite. The relative intensity of the graphite peaks continues to increase before reaching a maximum at a beam current of 4.320 mA (SNS equivalent of 1.486 MW). The intensity of the graphite peak subsequently fluctuates at higher beam currents from the development of holes in the foil. Additionally, as the spots become darker, the ability for the Raman spectrometer to capture all of the scattered light significantly decreases. Once this intensity levels off and/or decreases, it is believed that the foil has

Foil #1662 – UV Raman Spectroscopy of spots placed on Foil #1662 from Stair Step Method

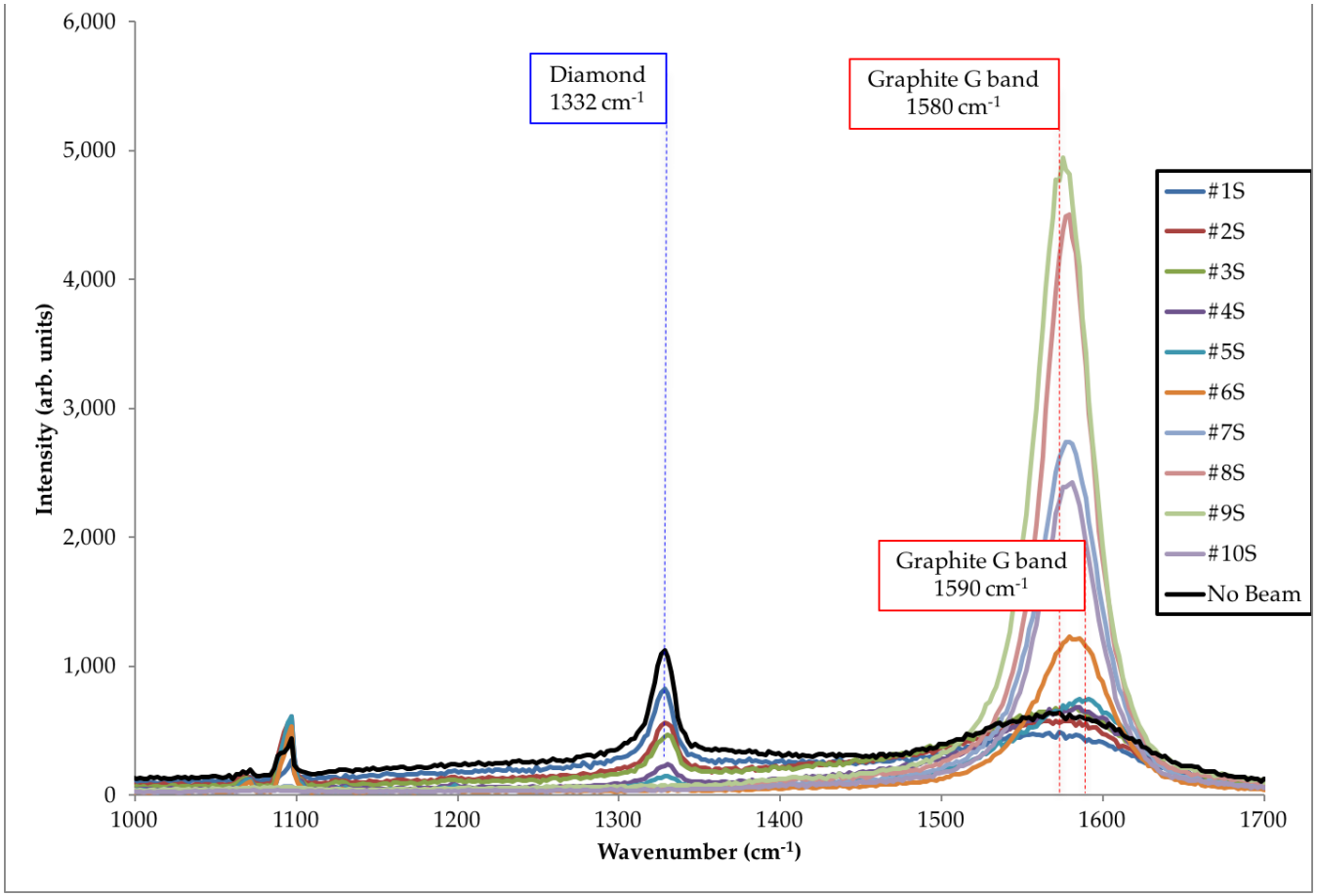

Figure 3.17 - Ultraviolet Raman spectra of Foil #1662 after being exposed to increasing beam power densities as described in Table 3.4 (Stair Step approach).

Foil #1662 – UV Raman Spectroscopy of spots placed on Foil #1662 from Gradual Ramp Up

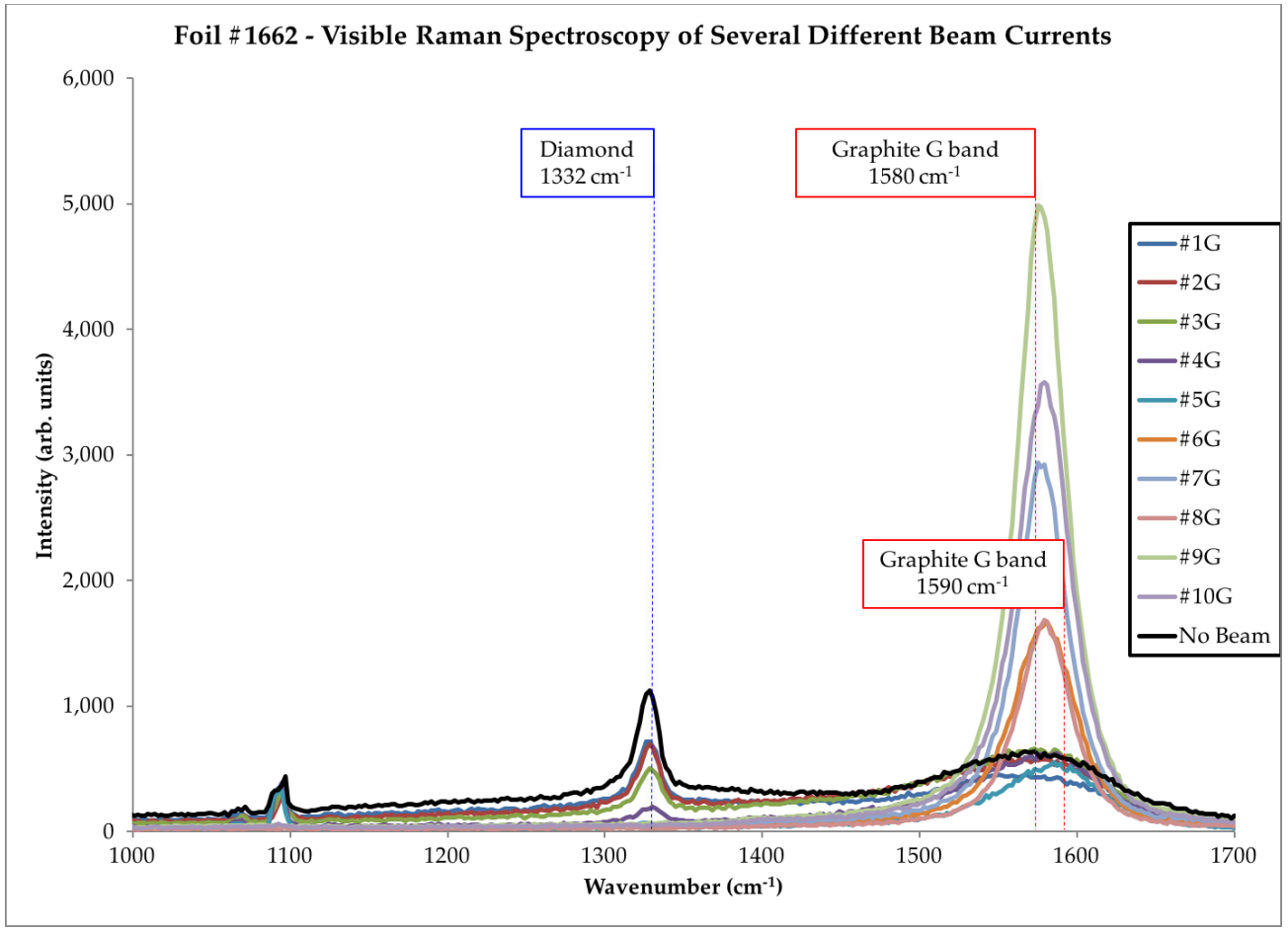

Figure 3.18 - Ultraviolet Raman spectra of Foil #1662 after being exposed to increasing power densities as described in Table 3.5 (Gradual Approach).

found a stable crystalline structure and will undergo no additional thermal changes. Tracking the position of the G-band peak with FTS beam current (and foil temperature) for both visible and UV excitation is useful for highlighting changes in the chemical state and crystallinity of the foil. The position of the G-band for the spots created by the two different ramp up methods is given in Table 3.15. From studying Foil #1662 with both visible (λ = 514 nm) and ultraviolet (λ = 257 nm) Raman spectroscopy, the sequence of thermal transformations are shown in Table 3.15 below. **T**he maximum intensities of G-band of graphite [range of 1520 – 1600 cm^{-1} for the visible (514 nm) and a range of 1560 – 1590 cm^{-1} for the ultraviolet (257 nm)] are found for each spot and the corresponding wavenumber is given. In Figure 3.19, the corresponding wavenumber for each spot is plotted [Gradual Ramp Up – visible (blue), Gradual Ramp Up – ultraviolet (red), Stair Step ramp up – visible (green), and Stair Step ramp up – ultraviolet (purple)]. After the corresponding wavenumber is found for each spot, the difference between the wavenumber of the visible spectrum and ultraviolet spectrum is calculated. This is completed for both methods and then plotted in Figure 3.20 **[**Gradual Ramp Up (blue) and Stair Step (red) Ramp Up Methods]. At the lower beam currents (Spots #1X – #4X, where X = G (Gradual) and X = S (Stair Step)), there is a large difference between the peak location between the ultraviolet and visible regions. When the beam current

Table 3.15 - Monitoring of Foil #1662 G-band with Visible and Ultraviolet Raman Spectra

Method	**Gradual Ramp Up Method**		**Stair Step Ramp Up Method**	
Region	Visible λ = 514 nm	Ultraviolet λ = 257 nm	Visible λ = 514 nm	Ultraviolet λ = 257 nm
Spot #1	1540.57	1568.90	1540.57	1568.90
Spot #2	1534.45	1566.84	1530.37	1573.01
Spot #3	1520.15	1577.12	1526.28	1570.95
Spot #4	1540.57	1573.01	1550.76	1583.29
Spot #5	1548.72	1587.40	1548.72	1583.29
Spot #6	1597.47	1585.35	1595.45	1585.35
Spot #7	1581.26	1581.24	1593.42	1579.18
Spot #8	1581.26	1575.06	1583.28	1577.12
Spot #9	1585.31	1579.18	1583.28	1579.18
Spot #10	1579.23	1575.06	1579.23	1575.06

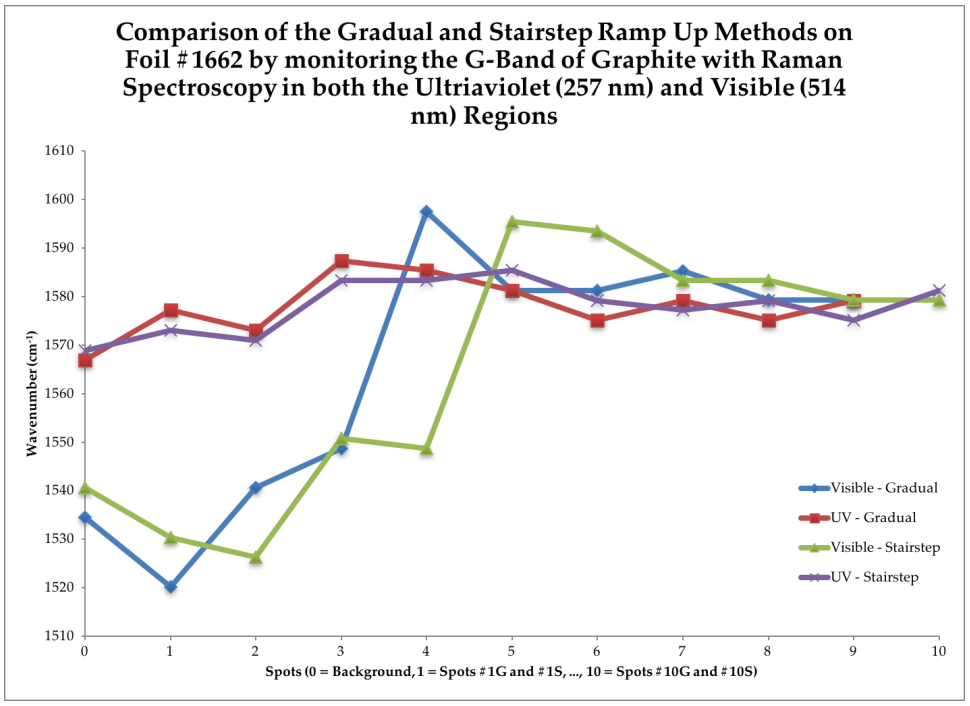

Figure 3.19 - Comparison of the Gradual and Stair Step ramp up methods on Foil #1662 by monitoring the G-band of graphite with Raman spectroscopy.

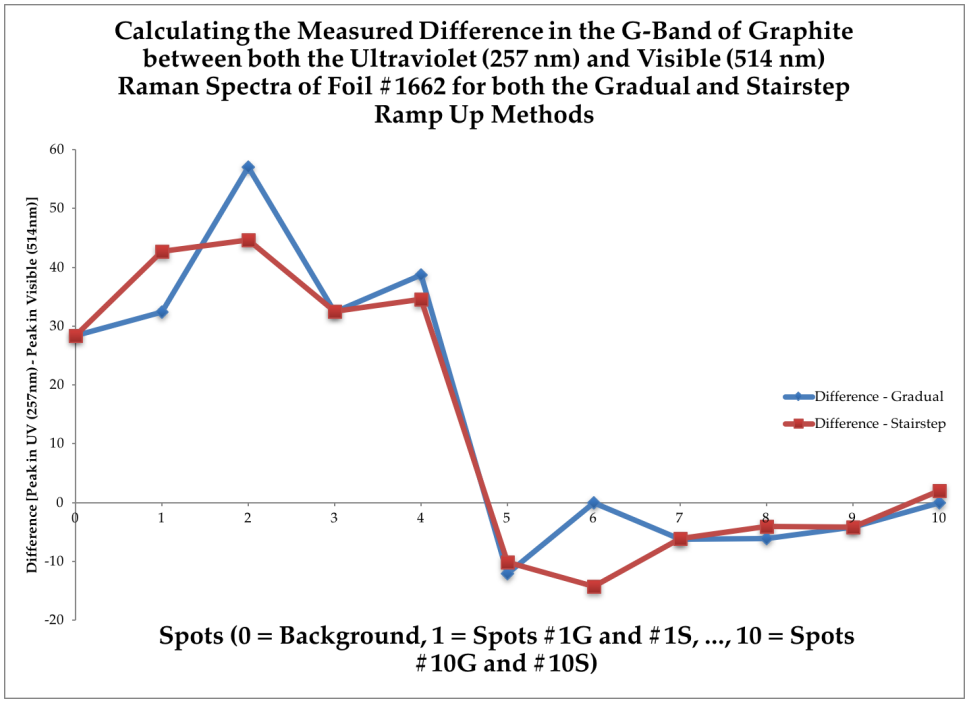

Figure 3.20 - Calculating the measured difference in the G-band of graphite between the ultraviolet (257 nm) and visible (514 nm) Raman spectra of Foil #1662.

reaches approximately 2.160 mA (SNS equivalent = 0.743 MW, Spot #5X), the difference between the ultraviolet and visible regions decreases. This sharp decline in the difference between the G-band position in the visible and ultraviolet Raman spectra is a marker for the transition from nanocrystalline to larger scale graphite. In the various Raman spectra of the different beam conditions for both ramp up methods, this further indicates that the nanocrystalline diamond foil is undergoing a series of changes to its chemical state and crystallinity.

In a study of carbon fibers by Chieu et al., the influence that heat-treatment had on the D-band (1360 cm^{-1}) and G-band (1580 cm^{-1}) of graphite by Raman spectroscopy (λ = 488 nm) was researched [115]. In their study, Chieu et al. tracked how the relative intensity of the D-band (I_D) to the G-band (I_G) compared at temperatures between 1,100 °C to 2,900 °C. Similar to the results in this research, the relative intensity of the D-band decreases at higher temperatures and disappears around 2,900 °C. On the other hand, the relative intensity of the G-band increases and transforms from a broad peak to a sharp peak. The results of their study may be seen in Figure 3.21 and Figure 3.22. Figure 3.21 contains the Raman spectra at the various heat treatment temperatures (T_{HT}), whereas Figure 3.22 compares the ratio of I_D/I_G at the

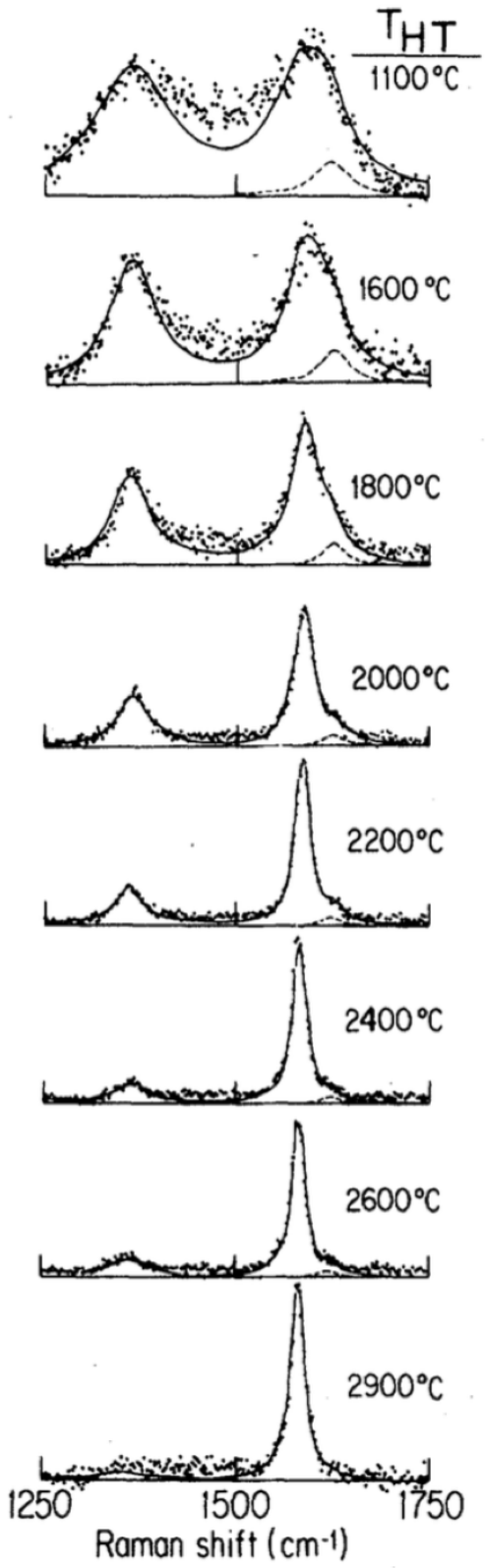

Figure 3.21 - First-order Raman spectra for benzene-derived carbon fibers heat treated at various heat-treatment temperatures (T_{HT}).

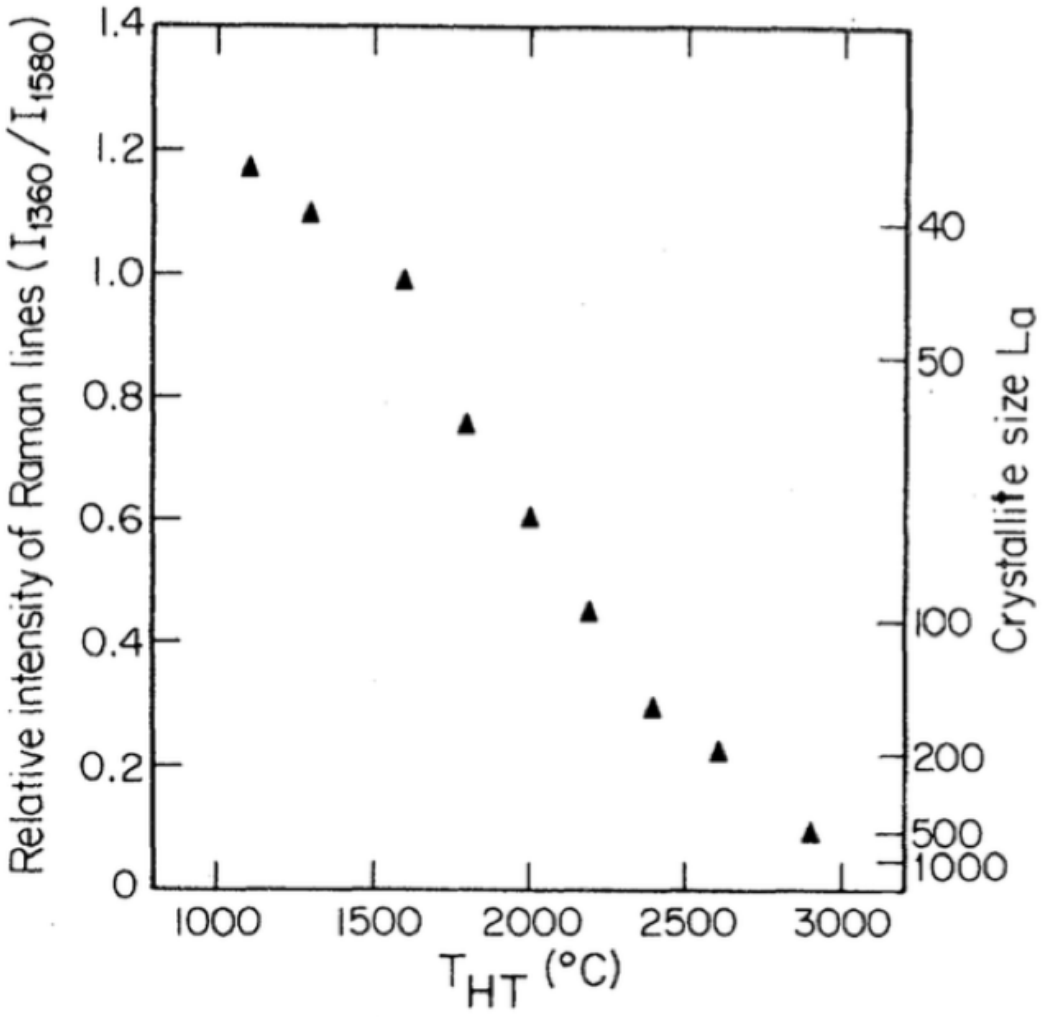

Figure 3.22 - Plot of the intensity ratio of the disorder- induced line at ~1360 cm^{-1} to the Raman-allowed line at ~1580 cm^{-1} vs heat-treatment temperature (THT) for the benzene-derived carbon fibers.

different T_{HT} [115].

From studying Foil #1662 with both visible (λ = 514 nm) and ultraviolet (λ = 257 nm) Raman spectroscopy, the sequence of thermal transformations that occurs while a nanocrystalline diamond foil is exposed to an increasing beam current (e.g., increased temperature), is the following:

1. The peak associated with trans-polyacetylene at 1140 cm^{-1} is the first to disappear when exposed to the FTS beam current. This may be seen in the visible (λ = 514 nm) Raman spectra of Foil #1662, shown in Figure 3.15 and Figure 3.16 for the Stair Step and Gradual Ramp Up Methods, respectively. The disappearance of the trans-polyacetylene peak occurs in both Spots #2S and #2G, in which a maximum beam current of 0.640 mA beam (SNS equivalent of 0.220 MW, foil temperature of 925 K) was applied to the foil. Additionally, the peak associated with trans-polyacetylene and amorphous carbon at at 1480 cm^{-1} and 1540 cm^{-1}, respectively, decrease. Since the peak associated with diamond (1332 cm^{-1}) decreases as well, it may be inferred that the trans-polyacetylene and amorphous carbon are being converted into graphite. As additional current is applied to the foil (Spots #3S – #5S and Spots #3G - #5G), the

trans-polyacetylene and amorphous carbon peaks disappear and a peak associated with some form of graphite begins to develop.

2. The peak associated with nanocrystalline diamond (1332 cm^{-1}) begins to decrease similarly to trans-polyacetylene, but not as quickly. Unlike trans-polyacetylene, as the peak associated with diamond decreases the peak associated with graphite begins to increase and shift to the right on the spectrum (i.e., to 1590 cm^{-1}). This was seen for both the Stair Step and Gradual Ramp Up Methods as shown in Figure 3.15 and Figure 3.16, respectively. The last beam current level that the diamond peak (1332 cm^{-1}) can be identified is at a maximum beam current of 2.160 mA (SNS Equivalent 0.743 MW, foil temperature of 1,535 K) for Spots #5S and #5G. At this beam current, this is the when the peak associated with graphite is shifted farthest to the right and the most intense at this position. The shift in graphite peak has been study by several researchers, including Ferrari and Robertson. In the reports by Ferrari and Robertson [109, 110, 122, 123, 124], the peak at 1590 cm^{-1} is an indication of nanocrystalline graphite. By applying the results of Ferrari and Robertson, it may be inferred that the nanocrystalline diamond peak at 1332 cm^{-1} is transforming into an intermediate form via nanocrystalline graphite (peak at 1590 cm^{-1}). This is

further supported by the ultraviolet spectra taken of Foil #1662 shown in Figure 3.17 and Figure 3.18 for the Stair Step and Gradual Ramp Up Methods, respectively. As mentioned previously, the ultraviolet Raman spectrum of nanocrystalline diamond does not include peaks associated with trans-polyacetylene. This allows the monitoring of the diamond peak (1332 cm^{-1}) and graphite peak (1580 – 1590 cm^{-1}) to be monitored more closely. In the ultraviolet spectra of Foil #1662, the last stage at which the diamond peak is discernable is for Spots #5S and #5G. Additionally, the graphite peaks at these spots have shifted to the right (1590 cm^{-1}) and is has the highest relative peak intensity for this position. This further indicates that the nanocrystalline diamond is transforming into nanocrystalline graphite.

3. The final crystalline change that occurs when the nanocrystalline graphite peak shifts to the left (from 1590 cm^{-1} to 1580 cm^{-1}) and increases in intensity. This increase in intensity and shifting of the nanocrystalline graphite peak indicates that it is transforming into graphite. This begins to occur for Spots #6S and #6G, in which a maximum beam current of 2.720 mA (SNS equivalent of 0.936 MW, foil temperature of 1,635 K) was applied to the foil. This is seen for both the Stair Step and Gradual Ramp

Up Methods as shown in Figure 3.15 and Figure 3.16, respectively, as the peak at 1590 cm^{-1} shift to 1580 cm^{-1}. This is further supported by the ultraviolet Raman spectra of Foil #1662. As the foil receives increasing beam current (e.g., increased thermal load/temperature), the nanocrystalline graphite begins to transforms into graphite (Spots #6S - #10S and Spots #6G - #10G).

3.3.2.2 Foil #1987

Foil #1987 is a nanocrystalline diamond foil developed by MPECVD at ORNL with an aerial density of 395 $\mu g/cm^2$ and a random ellipses lithography pattern. A 45-degree cut was made on the corner of the foil prior to growth, giving a full box-top lid on all sides of the freestanding diamond portion (including the cut corner). Foil #1987 received a very common set of FTS beam conditions with no prior conditioning to determine its performance. The ten spots are described in detail in Section 3.2.1.2 (Spot #1N to Spot #10N, refer to Table 3.6). Ultraviolet Raman spectra were taken of the ten spots and compared in Figure 3.23. The diamond peak (1332 cm^{-1}) was found to decrease and disappear at higher beam currents (i.e., higher power densities) similar to the visible and ultraviolet Raman spectra for Foil #1662. Additionally, the broad peak associated with graphite both shifted from 1480 – 1560 cm^{-1} to around 1594

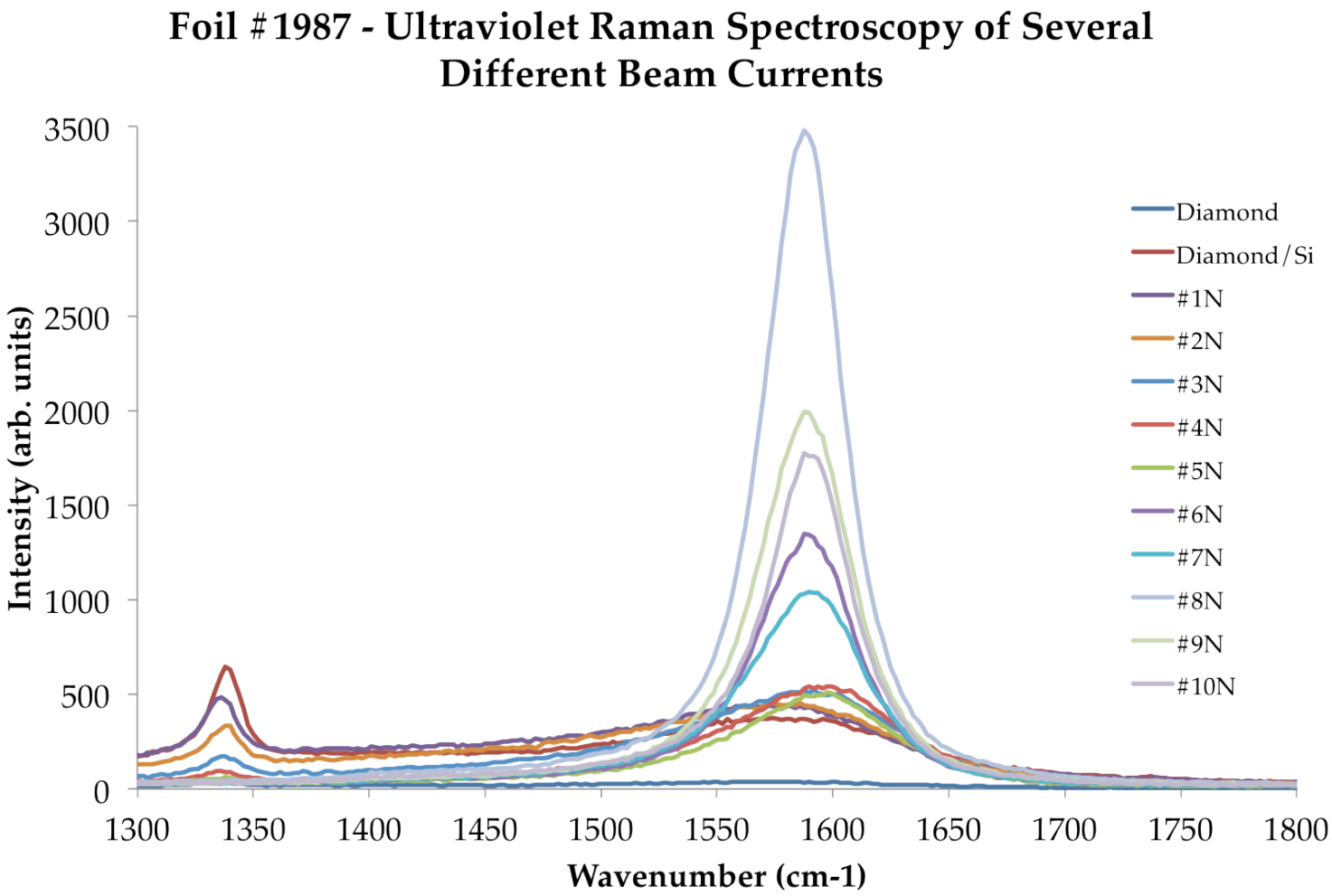

Figure 3.23 - Ultraviolet Raman spectroscopy of several different beam currents (0.272 mA to 4.800 mA or 0.094 MW to1.651 MW).

cm^{-1}, and increased in intensity. This indicates that nanocrystalline graphite has formed when the beam current was around 2.160 mA (SNS equivalent of 0.743 MW and foil temperature of 1,535). When the thermal load was increased further (i.e., increased beam current), the peak once again shifted. This final peak was sharp and shifted to 1580 cm^{-1} when the beam current was around 3.200 mA (SNS equivalent of 1.101 MW and foil temperature of 1,715). This indicates that the nanocrystalline graphite transformed into graphite. This agrees with the results seen for Foil #1662. The ten spectra were combined to illustrate the changes the foil underwent with increasing thermal loads. The change in diamond and graphite are shown in Figure 3.24 and Figure 3.25, respectively. These two figures demonstrate how the foil at increasing beam currents (i.e., increasing power densities) transforms from diamond to graphite-like. Interestingly, it was found that as the beam current on the foil increases the foil transforms from diamond to graphite by going through an intermediate nanocrystalline graphite phase, and is shown in Figure 3.25. A.C. Ferrari and J. Robertson have characterized this mode of transformation for diamond to graphite [109, 123, 124]. Ferrari and Robertson found nanocrystalline diamond transforms first into hydrogenated amorphous carbon (1540 cm^{-1}), second to tetrahedral amorphous carbon (1560 cm^{-1}), thirdly to nanocrystalline graphite (1594 cm^{-1}), and finally to graphite (1579 cm^{-1}) [109, 123, 124].

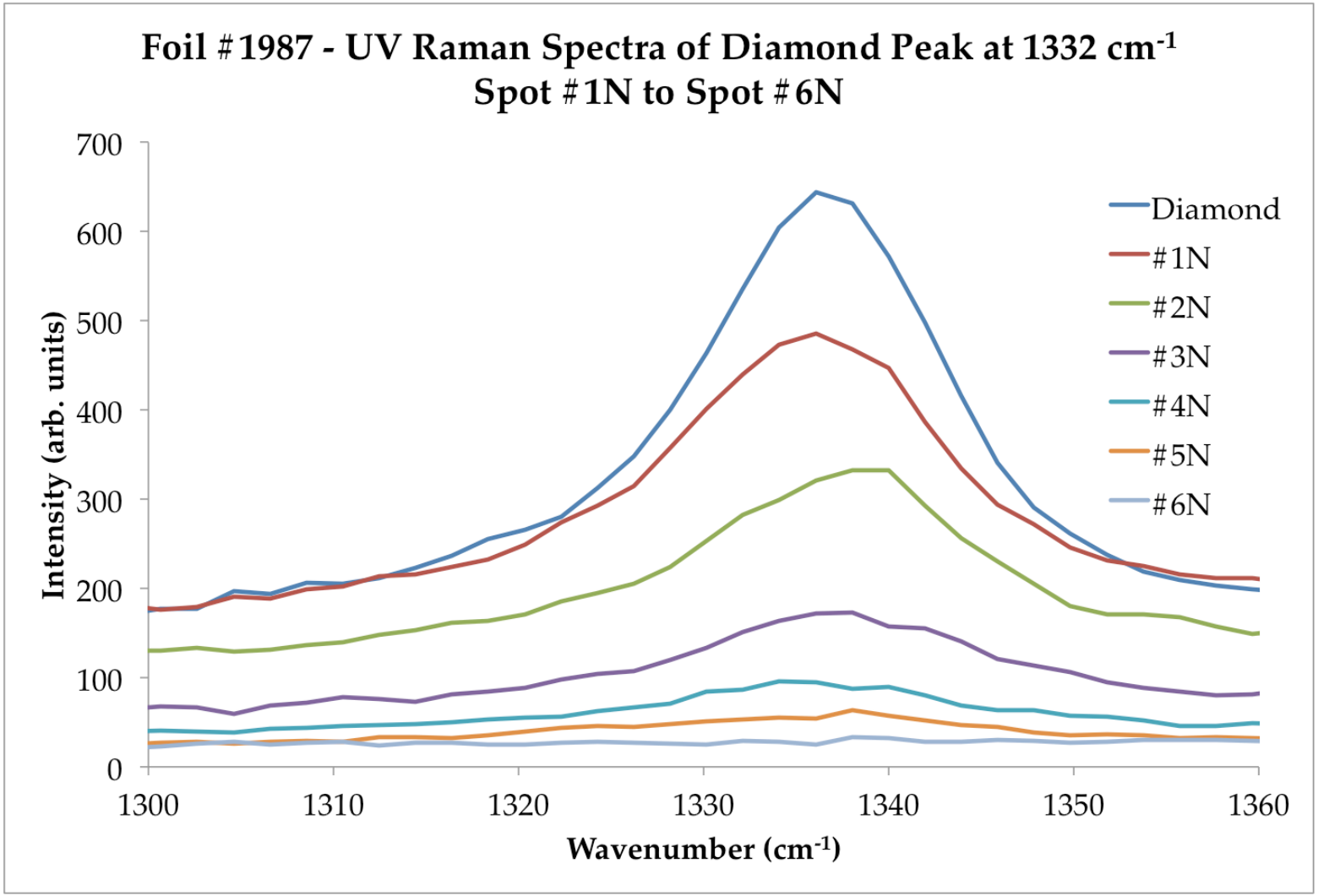

Figure 3.24 - UV Raman spectra of Foil #1987: Diamond peaks at 1332 cm^{-1} for Spot #1N (0.272 mA = 0.094 MW) to Spot #6M (2.720 mA = 0.936 MW).

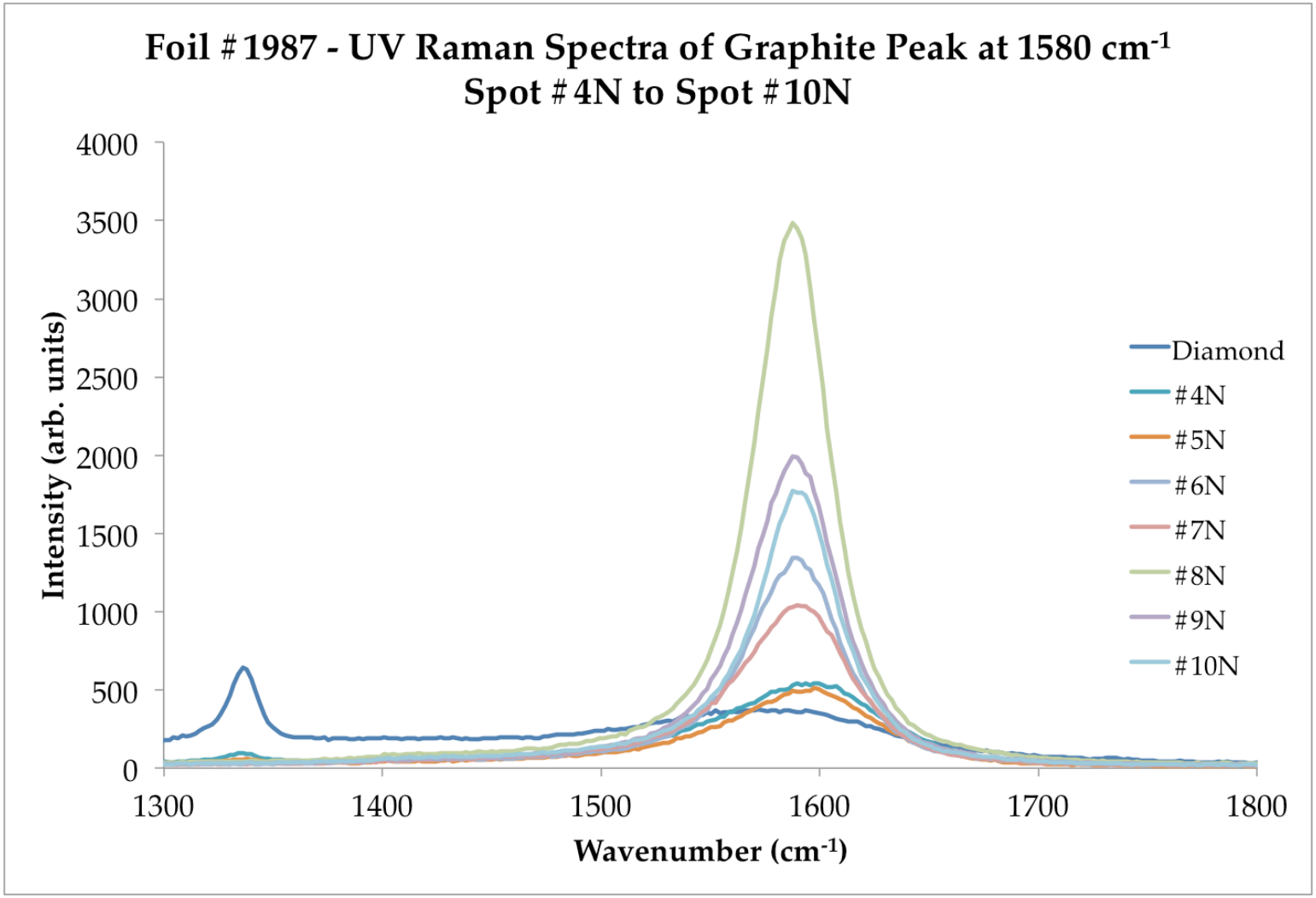

Figure 3.25 - UV Raman spectra of Foil #1987: Graphite peaks around 1580 cm^{-1} for Spot #4N (1.600 mA = 0.550 MW) to Spot #10N (4.800 mA = 1.651 MW).

The tracking of the different peaks is shown in Figure 3.24 to Figure 3.25. In Figure 3.24, the peak associated with diamond at 1332 cm^{-1} is tracked for Spots #1N through #6N. The maximum diamond peak intensity is around 600, which is for an undamaged spot on the foil. The intensity of the peak steadily decreases as higher beam current is applied to the foil, all but disappearing after receiving a beam current level of greater than 2.160 mA (Spot #5N, SNS = 0.743 MW). Additionally the peak associated with graphite at 1580 cm^{-1} can be tracked in Figure 3.25. It is noticed that the peak for graphite becomes distinguishable at a beam current of 1.600 mA (Spot #4N, SNS = 0.550 MW). The intensity of the graphite peak continues to increase up to 4.800 mA (Spot #10N, SNS = 1.651 MW). In addition to the graphite peak increasing in intensity, it was also noticed that the peak tended to have a slight shift. The peak associated with graphite starts out at 1586 cm^{-1} for Spot #4N (1.600 mA, SNS = 0.550 MW), and then shifts to the right to 1588 cm^{-1} for Spot #5N (2.160 mA = 0.743 MW). After Spot #5N, the peak shifts to the left to 1582 cm^{-1} for Spots #6N and #7N (2.720 mA = 0.936 MW and 3.200 mA = 1.101 MW, respectively). The peak continues to shift left before settling at 1580 cm^{-1} for Spot #8N, Spot #9N, and Spot #10N (3.760 mA = 1.293 MW, 4.320 mA = 1.486 MW, and 4.800 mA = 1.651 MW, respectively). This shift in the graphite peak indicates that the foil is undergoing a similar change described by A.C. Ferrari and J. Robertson [109, 123, 124], in which the foil

transforms from diamond and amorphous carbon (1332 cm^{-1} and 1480 to 1560 cm^{-1}) to nanocrystalline graphite (1594 cm^{-1}). From nanocrystalline graphite, it transforms again to graphite (1580 cm^{-1}). This phenomenon has been characterized in both the visible and ultraviolet regions, with the ultraviolet region showing a more distinguished peak shift since the spectrum is not dominated by trans-polyacetylene.

Prior to discovering the peak shift, it was thought that the mechanism for the transformation from diamond to graphite could be easily calculated through a basic kinetic study. Therefore, additional tests were completed on another nanocrystalline diamond foil, Foil #1989.

3.3.2.3 Foil #1989

Foil #1989 is a nanocrystalline diamond foil developed by MPECVD at ORNL, having an aerial density of 322 $\mu g/cm^2$ and a concentric ring lithography pattern. A 45-degree cut was made on the corner of the foil prior to growth, giving a full box-top lid on all sides of the freestanding diamond portion including the cut corner. Foil #1989 received a series of nine electron gun beam current levels applied to the foil by a pulsed and rastered beam. The nine series of spots are described in detail in Section 3.2.1.3 (Spots #1A – #1D to Spots #9A –

#9D, refer to Table 3.7). Ultraviolet Raman spectra were taken of all nine series of spots and are compared in Figure 3.26 through Figure 3.34.

Ultraviolet Raman spectra of Spots #1A – #1D, which received a current level of 0.640 mA (SNS equivalent of 0.220 MW, foil temperature of 925 K), are shown in Figure 3.26. At this current level, the relative intensity of diamond (1332 cm^{-1}) to graphite (1560 cm^{-1}) remained relatively constant. In comparison to an undamaged spot on the foil that received no beam, there was only a small decrease in the intensity of the Raman spectra and a slight darkening of the foil (see Figure 3.4). At this beam current, the duration of the beam on the foil seems to have a slight effect on the intensity of both the diamond and graphite peak. That is, there is a slight decrease in the intensity of the diamond peak at 1332 cm^{-1} and a slight increase of the graphite peak at 1580 cm^{-1}. There does not appear to be a shift in the position of the graphite peak nor an increase in the darkening of the foil from a longer exposure time.

Ultraviolet Raman spectra of Spots #2A – #2D, along with an undamaged section of the nanocrystalline diamond foil, are shown in Figure 3.27. The four spots received a beam current of 1.120 mA (SNS equivalent of 0.385 MW, foil temperature of 1,175 K), for 1 minute to 8 minutes. At this beam current level,

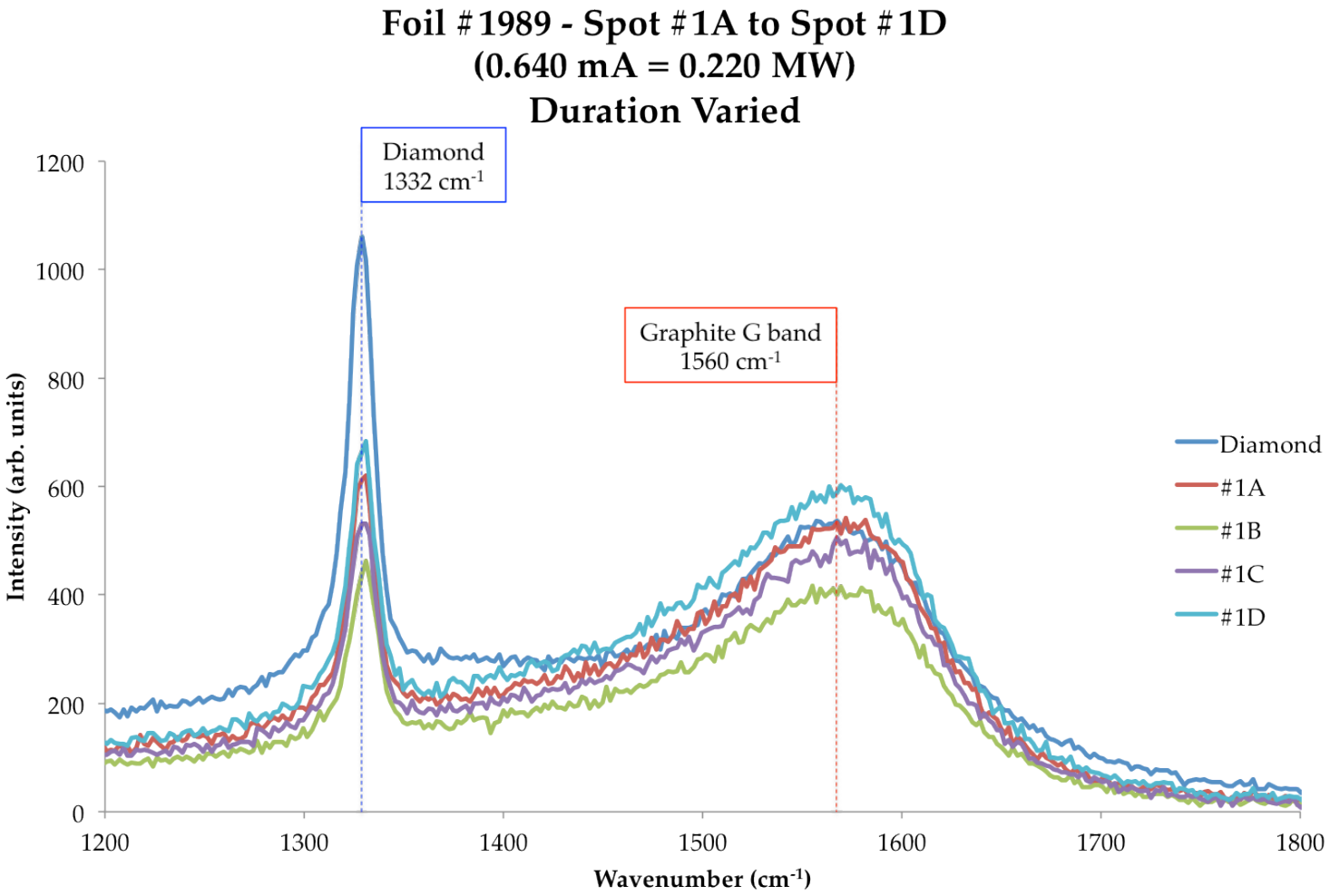

Figure 3.26 - UV Raman spectra of Foil #1989: Diamond peaks at 1332 cm^{-1} and Graphite peaks at 1560 cm^{-1} for Spots #1A to #1D (0.640 mA = 0.220 MW and a beam duration of 1.0 to 8.0 minutes).

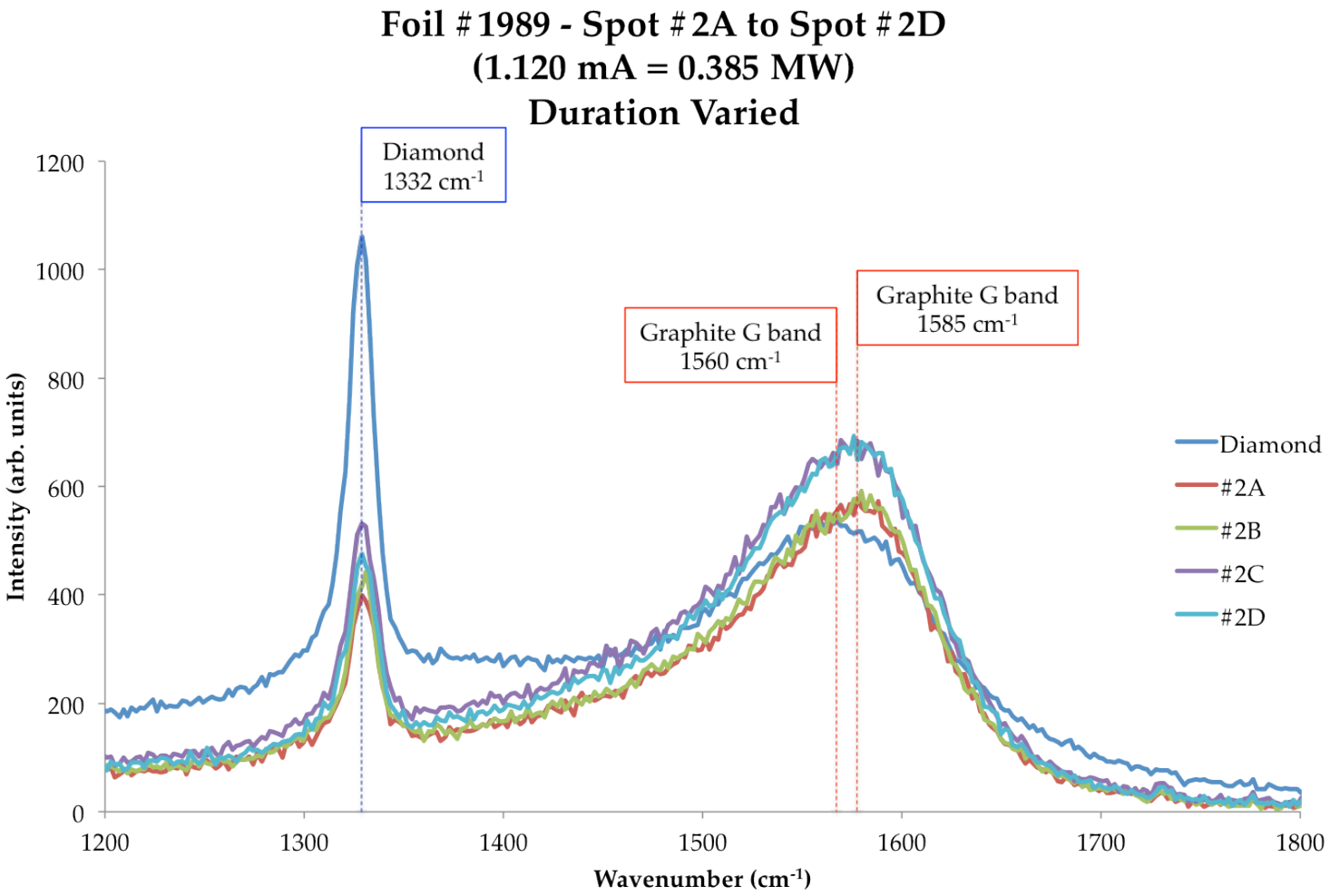

Figure 3.27 - UV Raman spectra of Foil #1989: Diamond peaks at 1332 cm^{-1} and Graphite peaks at 1585 cm^{-1} for Spots #2A - #2D (1.120 mA = 0.385 MW and a beam duration of 1.0 to 8.0 minutes).

the relative intensity of diamond (1332 cm^{-1}) decreased and the amorphous G-peak of graphite (1560 cm^{-1}) increased. The duration of the beam on the foil seems to have a slight effect on the intensity of both the diamond and graphite peaks when the beam is on the foil for greater than 1 minute (e.g., results for 2-, 4-, and 8- minutes are similar). That is, there is a slight decrease in the intensity of the diamond peak at 1332 cm^{-1} and a slight increase and shift of the graphite peak from 1560 cm^{-1} to 1580 cm^{-1}. There was an increase in the darkening of the foil compared to Spots #1A – #1D and the darkening of the foil increased as the exposure time increased (see Figure 3.4).

Ultraviolet Raman spectra of Spots #3A – #3D, along with an undamaged section of the nanocrystalline diamond foil, are shown in Figure 3.28. The four spots received a beam current of 1.600 mA (SNS equivalent of 0.550 MW, foil temperature of 1,375 K), for 1 minute to 8 minutes. At this beam current, the duration of the beam on the foil seems to have no effect on the intensity of both the diamond and graphite peaks. Additionally, the shift in the graphite peak is consistent for all durations (1560 cm^{-1} to approximately 1594 cm^{-1}). Upon visual inspection, the darkening of the foil increased slightly as the beam exposure time increased (from 1 minute for Spot #3A to 8 minutes for Spot #3D), and there was significantly more darkening of the foil compared to Spots #2A – #2D (see

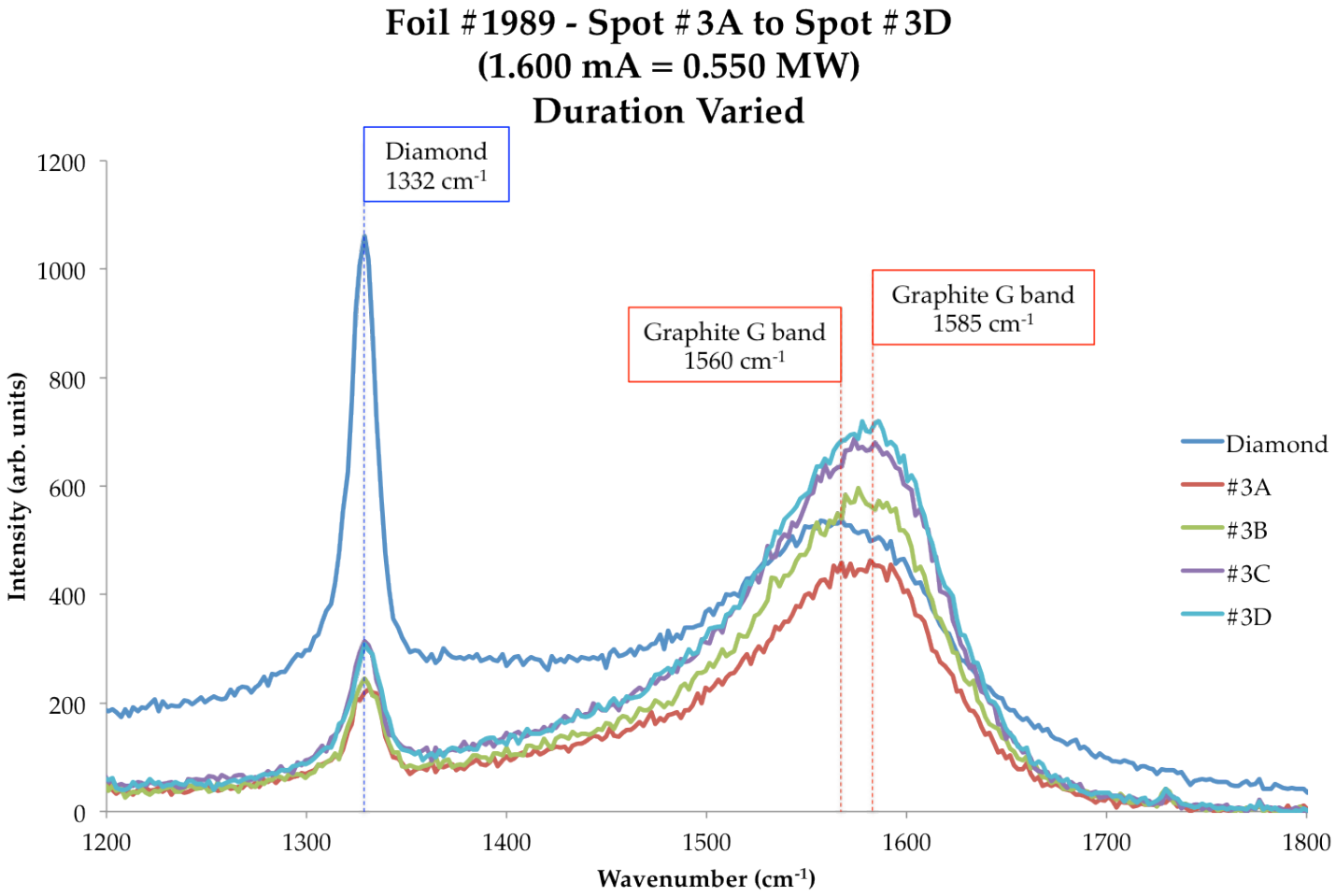

Figure 3.28 - UV Raman spectra of Foil #1989: Diamond peaks at 1332 cm^{-1} and Graphite peaks at 1585 cm^{-1} for Spot #3A to #3D (1.600 mA = 0.550 MW and a beam duration of 1.0 to 8.0 minutes).

Figure 3.4).

Ultraviolet Raman spectra of Spots #4A – #4D, along with an undamaged section of the nanocrystalline diamond foil, are shown in Figure 3.29. The four spots received a beam current of 2.160 mA (SNS equivalent of 0.743 MW, foil temperature of 1,535 K), for 1 minute to 8 minutes. Similar to Spots #3A - #3D, at this beam current the relative intensity of diamond (1332 cm^{-1}) decreased and the G-peak of graphite both increased and shifted to the right from 1560 cm^{-1} to 1585 cm^{-1}. This is an indication that the amorphous graphite peak seen in nanocrystalline diamond is transforming into nanocrystalline graphite. At this beam current, the duration of the beam on the foil seems to have no effect on the intensity of both the diamond and graphite peaks. Additionally, the shift in the graphite peak is consistent for all durations (1560 cm^{-1} to approximately 1585 cm^{-1}). Upon visual inspection, the darkening of the foil did not increase with beam exposure (from Spot #4A to Spot #4D), but there was more darkening of the foil compared to Spots #3A – #3D (see Figure 3.4).

Ultraviolet Raman spectra of Spots #5A – #5D, along with an undamaged section of the nanocrystalline diamond foil, are shown in Figure 3.30. The four spots received a beam current of 2.720 mA (SNS equivalent of 0.936 MW, foil

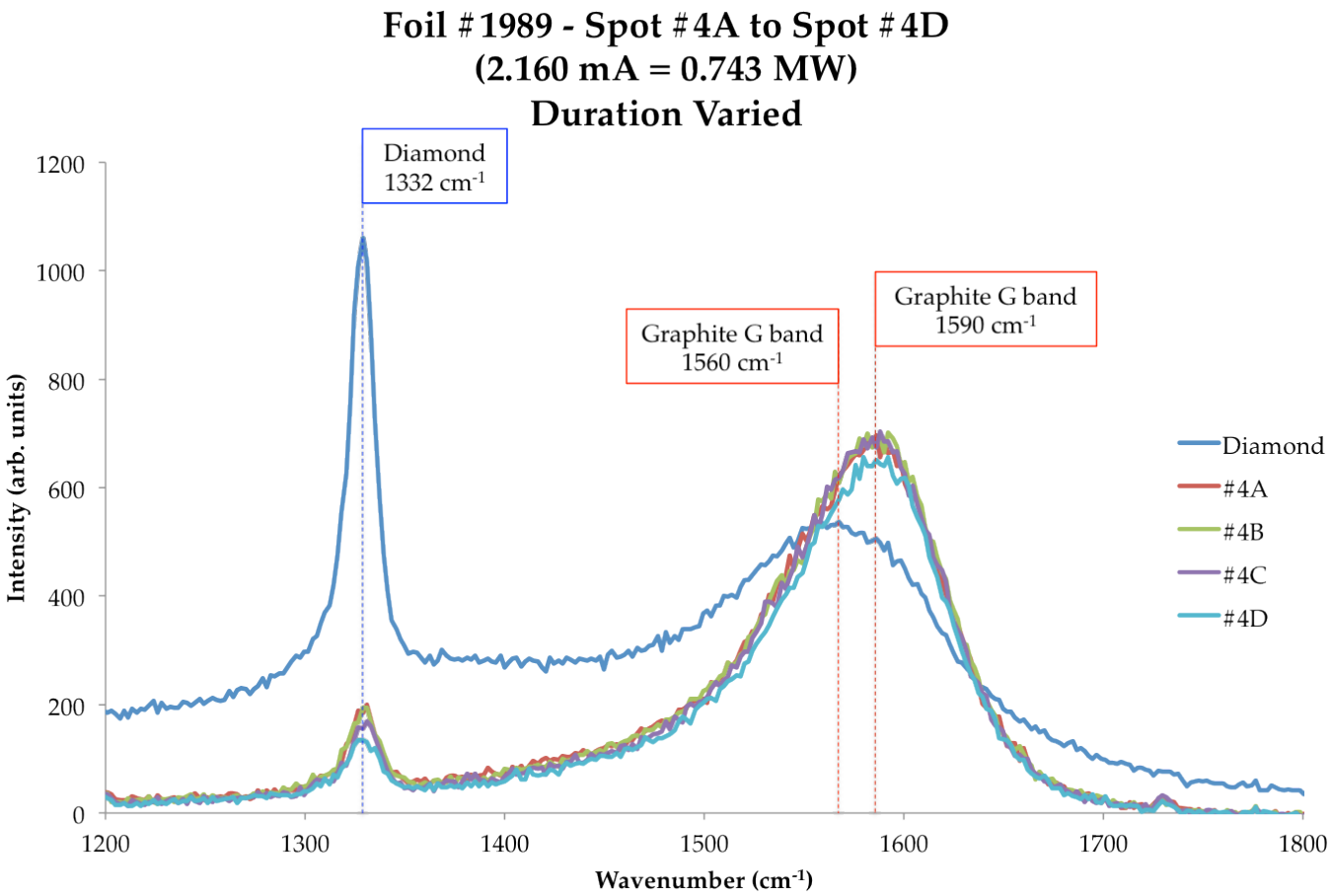

Figure 3.29 - UV Raman spectra of Foil #1989: Diamond peaks at 1332 cm-1 and Graphite peaks at 1590 cm-1 for Spots #4A to #4D (2.160 mA = 0.743 MW and a beam duration of 1.0 to 8.0 minutes).

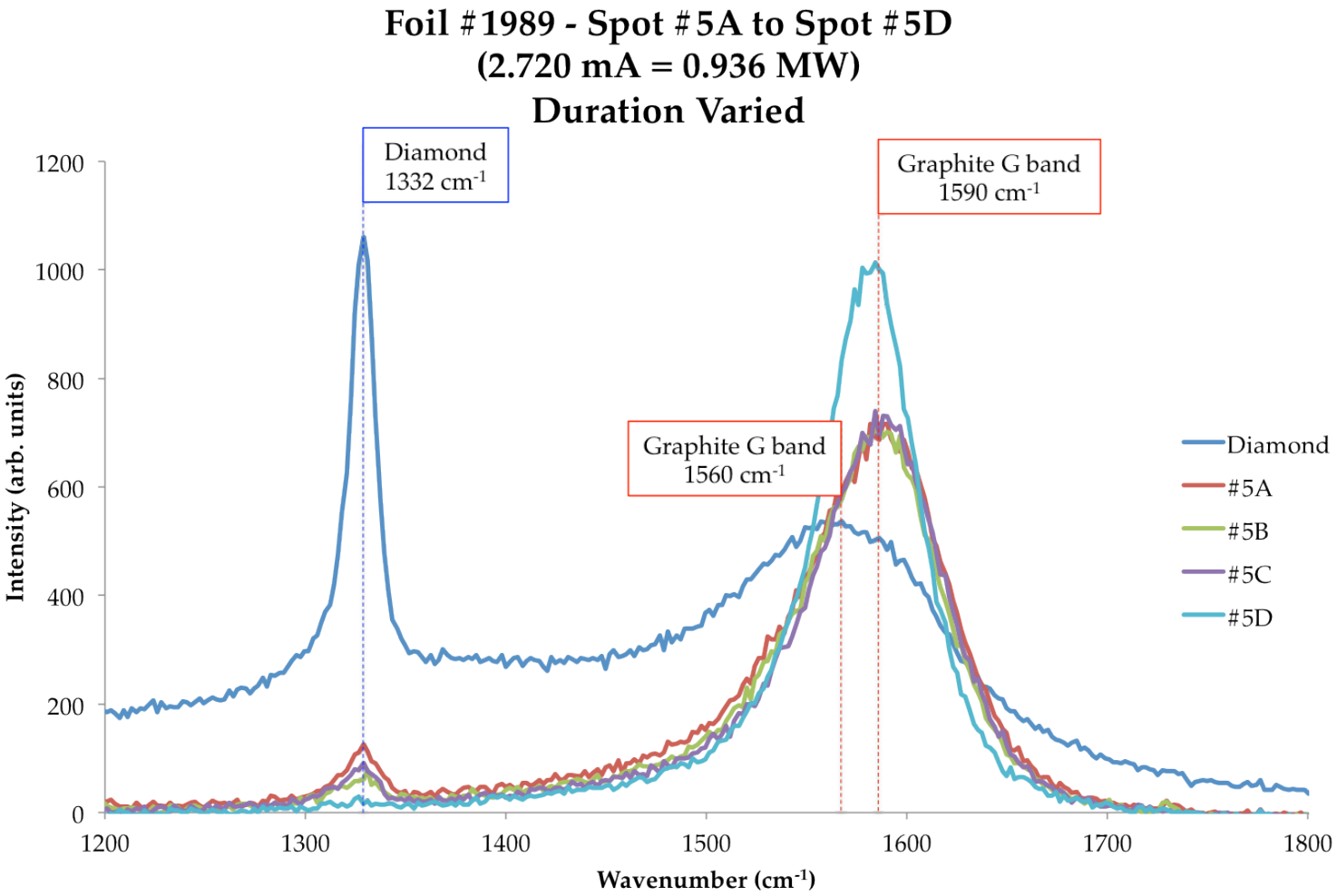

Figure 3.30 - UV Raman spectra of Foil #1989: Diamond peaks at 1332 cm^{-1} and Graphite peaks at 1590 cm^{-1} for Spots #5A to #5D (2.720 mA = 0.936 MW and a beam duration of 1.0 to 8.0 minutes).

temperature of 1,635 K), for 1 minute to 8 minutes. Similar to Spots #4A - #4D, at this beam current the relative intensity of diamond (1332 cm^{-1}) decreased and the G-peak of graphite (1560 cm^{-1}) both increased and shifted to the right. This is an indication that the amorphous graphite peak seen in nanocrystalline diamond has transformed into nanocrystalline graphite. At this beam current, the duration of the beam on the foil seems to have an effect on the intensity on the graphite peak. After one minute (Spot #5A), the peak shifts from 1560 cm^{-1} approximately 1594 cm^{-1}. At each additional time increment, the graphite peak begins to shift back to the left (from 1594 cm^{-1} to 1580 cm^{-1}). This indicates that with enough time and a high enough beam current, the amorphous graphite peak will transform first to nanocrystalline graphite (1594 cm^{-1}) and then to graphite (1580 cm^{-1}). Upon visual inspection, the darkening of the foil slightly increased with longer beam exposure (from 1 minute for Spot #5A to 8 minutes with Spot #5D). Additionally, there was more darkening of the foil compared to Spots #4A – #4D (see Figure 3.4).

Ultraviolet Raman spectra of Spots #6A – #6D, along with an undamaged section of the nanocrystalline diamond foil, are shown in Figure 3.31. The four spots received a beam current of 3.200 mA (SNS equivalent of 1.101 MW, foil temperature of 1,715 K), for 1 minute to 8 minutes. Similar to Spots #5A - #5D,

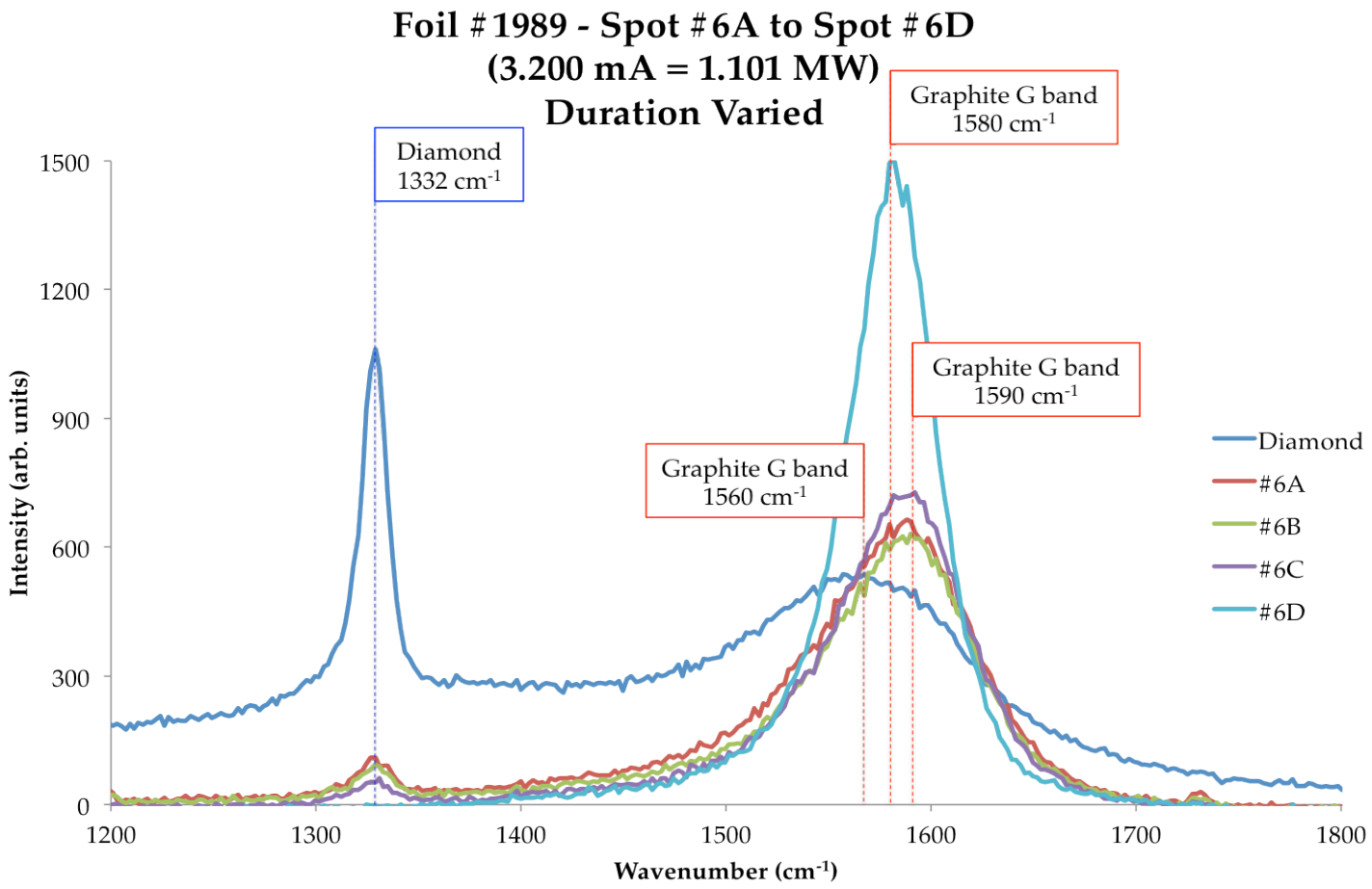

Figure 3.31 - UV Raman spectra of Foil #1989: Diamond peaks at 1332 cm^{-1} and Graphite peaks from 1580 cm^{-1} to 1590 cm^{-1} for Spots #6A to #6D (3.200 mA = 1.101 MW and a beam duration of 1.0 to 8.0 minutes).

Spot #6A - #6D relative intensity of diamond (1332 cm^{-1}) decreased and the G-peak of graphite (1560 cm^{-1}) both increased and shifted to the right. Unlike Spots #5A - #5D, Spots #6A - #6D graphite peak shifted from 1560 cm^{-1} (amorphous) to 1594 cm^{-1} (nanocrystalline graphite) for all durations instead of beginning the shift to 1580 cm^{-1} (graphite). From previous studies, this is an indication shift to 1580 cm^{-1} (graphite). From previous studies, this is an indication that the amorphous graphite peak seen in nanocrystalline diamond is transforming into nanocrystalline graphite. Unlike Spots #5A - #5D, the increased beam duration and increased beam power did not transform the foil from nanocrystalline graphite to graphite. This indicates that neither enough time nor a high enough beam current (i.e., temperature), was delivered to the foil to transform it from nanocrystalline graphite (1594 cm^{-1}) and to graphite (1580 cm^{-1}). Additionally the darkening of the foil compared to Spots #5A – #5D was slightly less upon visual inspection (see Figure 3.4), indicating that Foil #1989 received a lower thermal load despite an increase in the beam current.

Ultraviolet Raman spectra of Spots #7A – #7D, along with an undamaged section of the nanocrystalline diamond foil, are shown in Figure 3.32. The four spots received a beam current of 3.760 mA (SNS equivalent of 1.293 MW, foil temperature of 1,775 K), for 1 minute to 8 minutes. Similar to Spots #6A - #6D, at

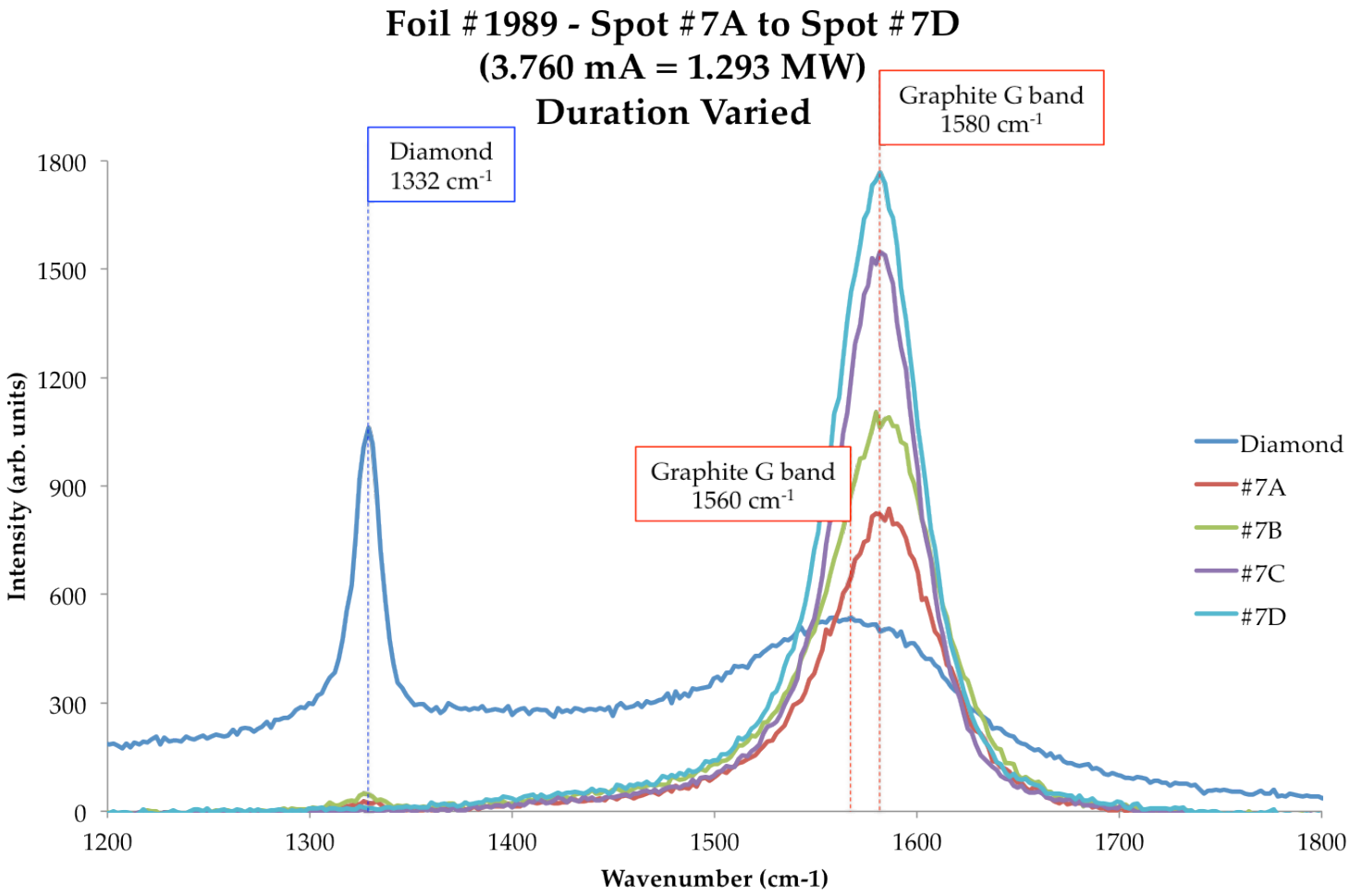

Figure 3.32 - UV Raman spectra of Foil #1989: Graphite peaks at 1580 cm^{-1} for Spots #7A to #7D (2.720 mA = 0.936 MW and a beam duration of 1.0 to 8.0 minutes).

this beam current the relative intensity of diamond (1332 cm^{-1}) decreased and the G-peak of graphite (1560 cm^{-1}) both increased and shifted to the right. This is an indication that the amorphous graphite peak seen in nanocrystalline diamond is beginning to transform into graphite (1580 cm^{-1}). At this beam current, the duration of the beam on the foil seems to have an effect on the intensity on the graphite peak. After one minute (Spot #7A), the peak shifts from 1560 cm^{-1} to approximately 1594 cm^{-1}. At each additional time increment, the graphite peak begins to shift back to the left (from 1594 cm^{-1} to 1580 cm^{-1}). This indicates that with enough time and a high enough beam current, the amorphous graphite peak will transform first to nanocrystalline graphite (1594 cm^{-1}) and then to graphite (1580 cm^{-1}). Upon visual inspection, the darkening of the foil was comparable for all four spots and was not significantly influenced by beam exposure time (Spots #7A - #7D), but with more darkening of the foil compared to Spots #6A – #6D (see Figure 3.4).

Ultraviolet Raman spectra of Spots #8A – #8D, along with an undamaged section of the nanocrystalline diamond foil, are shown in Figure 3.33. The four spots received a beam current of 4.320 mA (SNS equivalent of 1.486 MW, foil temperature of 1,835 K), for 1 minute to 8 minutes. Similar to Spots #7A - #7D, Spot #8A - #8D relative intensity of diamond (1332 cm^{-1}) essentially disappeared

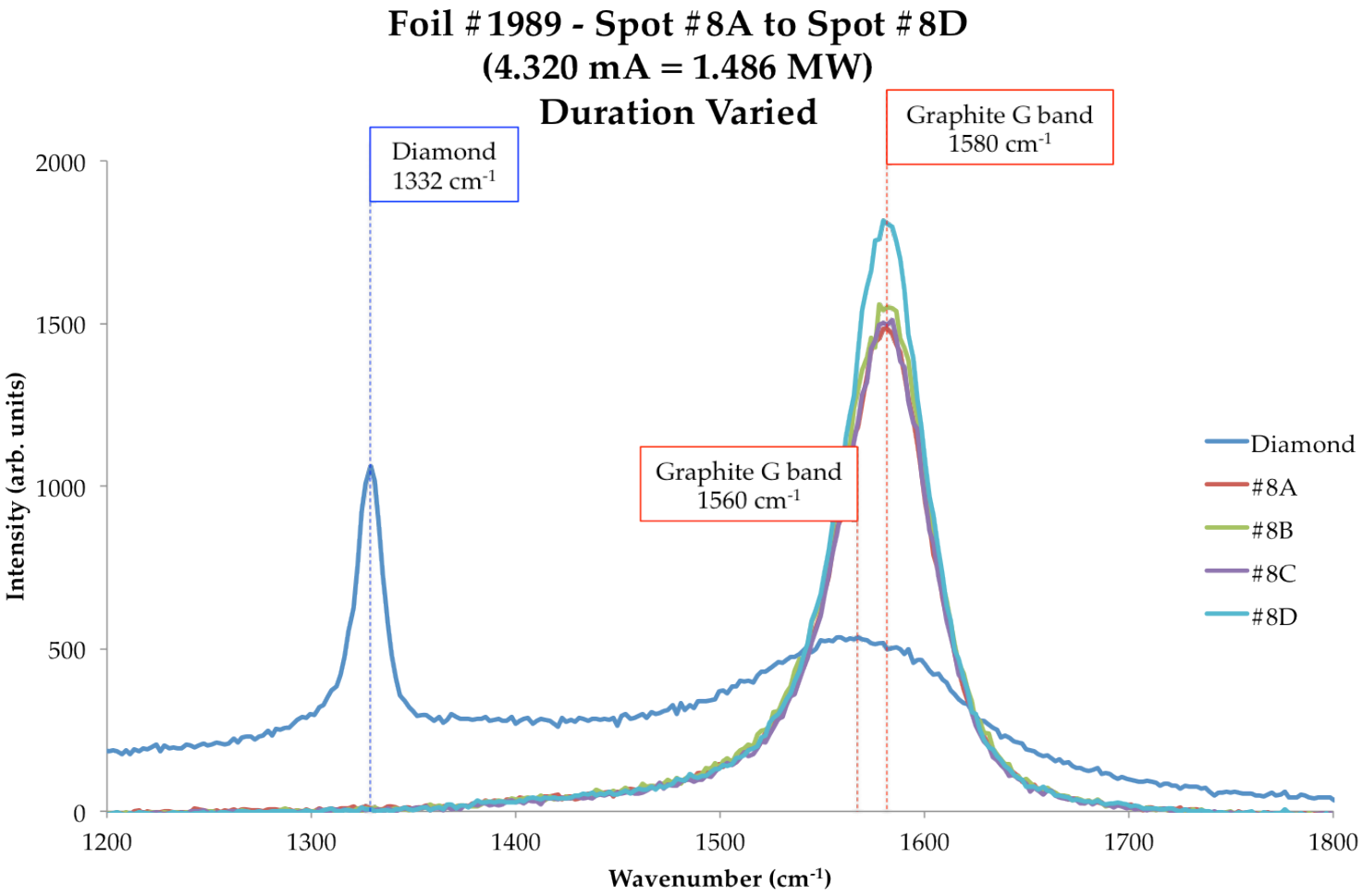

Figure 3.33 - UV Raman spectra of Foil #1989: Graphite peaks at 1580 cm^{-1} for Spots #8A to #8D (4.320 mA = 1.486 MW and a beam duration of 1.0 to 8.0 minutes).

and the G-peak of graphite (1560 cm^{-1}) both increased and shifted slightly to the right. Upon visual inspection, the darkening of the foil was comparable for all four spots and was not significantly influenced by beam exposure time (Spots #8A - #8D), but with more darkening of the foil compared to Spots #7A – #7D (see Figure 3.4).

Ultraviolet Raman spectra of Spots #9A – #9D, along with an undamaged section of the nanocrystalline diamond foil, are shown in Figure 3.34. The four spots received a beam current of 4.800 mA (SNS equivalent of 1.651 MW, foil temperature of 1,890 K), for 1 minute to 8 minutes. Similar to previous spots, Spot #9A - #9D the peak associated with diamond (1332 cm^{-1}) disappeared and the G-peak of graphite (1580 cm^{-1}) both increased and shifted to the right. At this beam current (same for all durations), the peak went straight from amorphous graphite peak to graphite (skipping what appeared to be an intermediate phase, nanocrystalline graphite). It should be noted that as the beam duration increases, the peak associated with graphite both increased in intensity and begins to shifted left on the spectrum. This indicates that the foil is transforming from amorphous carbon to graphite, and this conversion continues as the duration of the beam is increased. This can be attributed to the fact that as the beam is applied to the foil for a longer duration, the area surrounding the

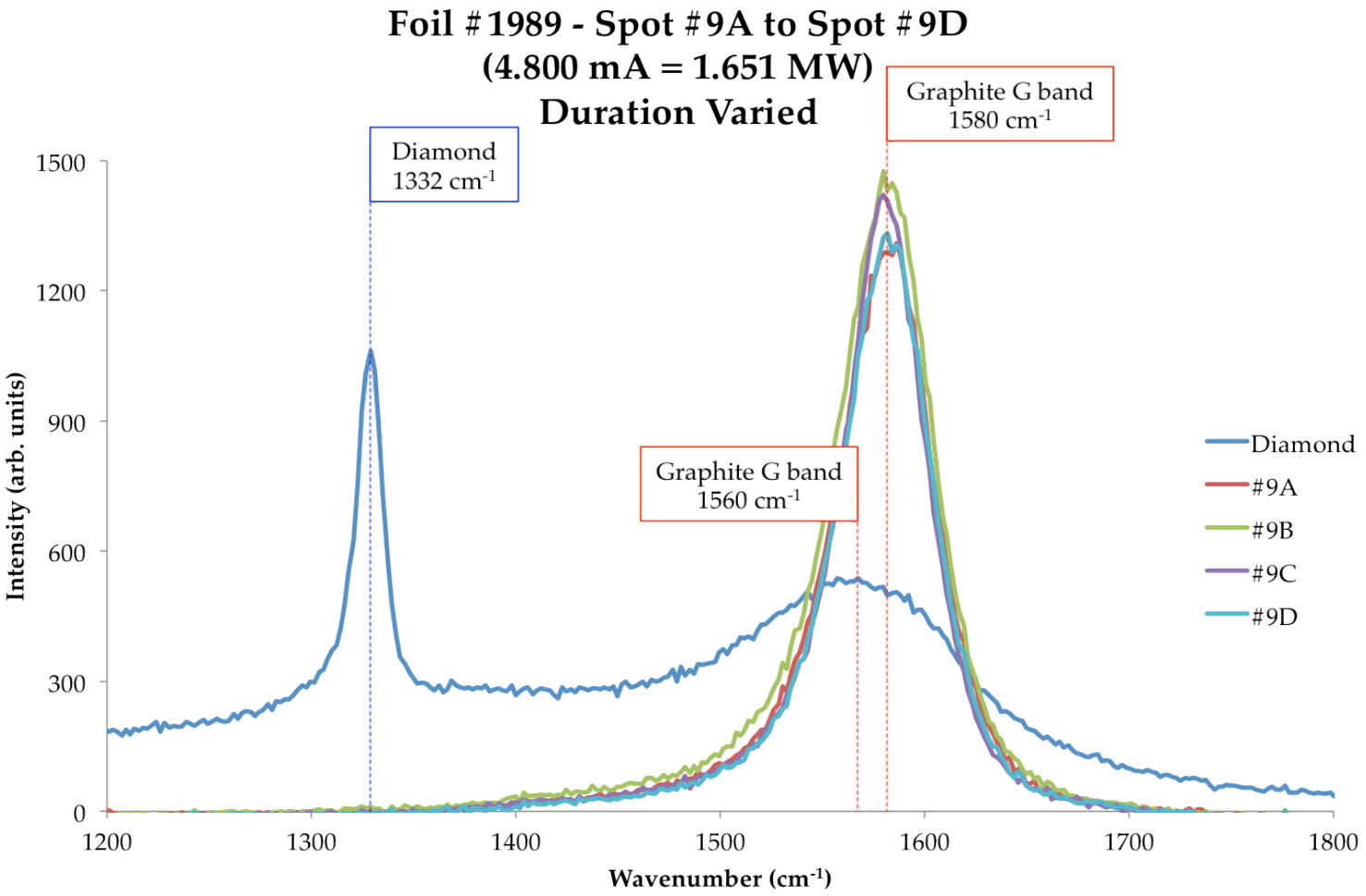

Figure 3.34 - UV Raman spectra of Foil #1989: Graphite peaks at 1580 cm^{-1} for Spots #9A to #9D (4.800 mA = 1.651 MW and a beam duration of 1.0 to 8.0 minutes).

spot on the foil where the beam is hitting begins to transform from the large thermal load. Therefore, when a Raman spectrum is taken, there is a larger percentage of the region that has transformed into the end product. This further corroborates earlier studies that the state of graphite is dependent upon the maximum temperature applied to the foil (as opposed to the duration). Visual inspection of the foil illustrates this when looking at the nine series of spots in Figure 3.4. From this photograph of Foil #1989 post-beam, the degree of darkening on the foil appears to be more influenced by the peak current applied to the foil and less by the time the current is applied.

3.4 Conclusion

Several tests and analyses were completed on stripper foils, with the majority of the data focused on nanocrystalline diamond foils (the most commonly utilized foil at SNS). From this, the chemical and physical transformations that a foil undergoes when heated with high thermal loads is better understood. Under these experiments, the previous unknown foil emissivity and the relative temperatures that the foil experiences under various thermal loads were determined. Additionally, the mechanism for which nanocrystalline diamond transforms into graphite-like material is now better

understood.

When the foil does not undergo any conditioning (e.g., Foil #1989), the foil transforms from nanocrystalline diamond to nanocrystalline graphite at low thermal loads [less than or equal to 3.200 mA (FTS), 1.101 MW (SNS), or 1,715 K) and short beam exposures (4 minutes or less). If the beam exposure is increased (to approximately 8 minutes), the foil will transform from nanocrystalline diamond to nanocrystalline graphite at a lower thermal load (greater than or equal to 2.720 mA (FTS), 0.936 MW (SNS), or 1,635 K). If the thermal load is increased (greater than or equal to 3.760 mA (FTS), 1.239 MW (SNS), or 1,775K), the nanocrystalline diamond transforms directly to graphite with very little beam exposure (e.g., 1 minute).

When the foil is conditioned (e.g., Foil #1662), the foil transforms similarly to a foil that is not conditioned. As the thermal load is increased on the foil, the amorphous graphite peak at 1560 cm^{-1} decreases in intensity. When the FTS beam current is increased to 2.160 mA or greater (SNS equivalent of 0.743 MW or foil temperature of 1,535 K), the nanocrystalline diamond peak (1332 cm^{-1}) transforms into nanocrystalline graphite (1594 cm^{-1}). If the FTS beam current is increased to 3.200 mA or greater (SNS equivalent of 1.101 MW or foil

temperature of 1,715 K), the foil transforms from nanocrystalline graphite (1594 cm^{-1}) to graphite (1580 cm^{-1}). The transformation of the crystalline structure for a foil that undergoes conditioning is very similar to a foil that is not conditioned. This indicates that the change in the foil crystalline structure is more influenced by the peak temperature on the foil than time. However, if enough time is allowed, the foil will transform at a lower peak temperature (e.g., the foil transforms from nanocrystalline diamond to nanocrystalline graphite at a foil temperature of 1,635 K when the time is less than 5.0 minutes, but will transform into graphite if the time is increased to 8.0 minutes).

In addition to understanding how thermal load and time influence the mechanism at which a foil transforms, it was also important to understand how conditioning influenced foil lifetime. For foils that were conditioned, whether it was by the Gradual Ramp Up method or Stair Step method, the rate at which the foil transformed was steady and allowed the foil to gradually change over time. This gradual change inhibited the rate at which the foil developed holes and the overall damage to the foil. By conditioning the foil, the very rigid diamond foil was able to adapt to the dramatic changes that the it was undergoing. That is, as the foil area expanded when it went from diamond (density = 3.5 g/cm^3) to the graphite (density = 2.0 g/cm^3)). As this expansion occurred, the foil shape may

visibly contort, develop wrinkles, or shake. These physical changes and behaviors will be discussed further in Chapter 4.

Chapter 4. Foil Test Stand – Operational Issues of Stripper Foils

Since SNS began production in 2006, there have been several operational issues both pertaining to and not pertaining to the stripper foils. One of the major issue that has troubled the stripper foils at SNS is foil flutter. Foil flutter has been studied in depth with both the FTS and SNS. These studies were designed to determine the factors that influence foil flutter (e.g., mechanical, electrical, or a physical characteristic).

4.1 Stripper Foil Flutter

Stripper foil flutter is one of the major issues that affects SNS operations and the ability to provide the SNS users a steady supply of neutrons for experiments. Foil flutter occurs at series of random frequencies and shows no immediate correlation to the pulse frequency of SNS. Since the beam dynamics of SNS are finely tuned and dependent upon several different stages, having an aspect of the machine that is constantly changing increases the difficultly of operations. The foil is placed in a very exact location that allows for maximum stripping efficiency of the beam (H^- to H^+) and limits the amount of beam loss. Beam loss is when either sections or entire beams become adrift and can no longer be used for production. This is a significant problem because when the beam gets out of the designed area, it tends to impact beam pipes and the variety

of instrumentation used throughout SNS. This causes unattended beam areas to receive a very high activation, both decreasing the lifetime of equipment and increasing a radiation hazard to employees working in the area. Therefore, foil flutter is an important issue that needs to be resolved to ensure both the safety of employees and the success of future SNS upgrades.

4.1.1 Factors that influence foil flutter

Understanding the factors that influence foil flutter has been a difficult task. Since a limited number of foils can be tested per 6 month run cycle (changing stripper foils has a significant impact on the time available to SNS users), an alternative method is needed to probe the underlying basis of foil flutter. Therefore, it was decided that the FTS could provide some much needed insight. There have been several theories proposed of what causes foil flutter and potential solutions to decrease or eliminate foil flutter all together. Some of these theories include: mechanical effects, thermal effects, electrical charging, and interaction with secondary electrons.

Mechanical effects have been attributed to foil flutter because the stress distribution in the foil. The stress distribution is caused by defects in the foil crystalline structure, tears and rips in the foil, and defects in the box top lid going

around the freestanding portion of the diamond.

The thermal effects stem from the foils becoming very hot from the high intensity beam, causing the crystalline structure of the foil to change from diamond to graphite. As the crystalline structure of the foil changes (e.g., diamond to graphite), the area that is being heated is changing. This change in position on the foil, however slight, could be a source of forced oscillation (e.g., as the foil flutters, the spot on the foil that is heated changes). When the thermal expansion is coupled with the varying stress distribution in the foil, it could lead to foil movement.

The third theory proposed is electrical charging. As the foils are being bombarded with hydride ions, sputtering of the foil may lead to electrical charging on the foil. As that charge is dissipated or discharged, it can lead to foil flutter.

The last theory proposed is that the collector for convoy electrons (i.e., the secondary electron collector) is not capturing the electrons that are being stripped from the hydride ions after the electrons pass through the stripper foil. These stripped electrons (i.e., secondary electrons) are bouncing off the electron

collector and impacting the foil and the foil assembly. This additional impact on the foil could cause severe foil flutter and damage to the foil assembly that has been seen at higher beam powers.

4.1.1.1 Mechanical Effects

The stress distribution in the stripper foil causes a series of mechanical effects that may influence the stripper foil lifetime. The stress distribution is influenced by a series of defects in the foil, including defects in the crystalline structure and tears in various locations of the freestanding portion of the diamond. Mechanical effects have been studied in both the FTS and SNS. Within the FTS, it has been discovered that foils with tears and/or rips near the silicon handle have a higher tendency to flutter when impacted with an electron beam. This area of the foil near the silicon handle is the point of highest stress within the foil due to the thermal expansion that occurs during the development of the foils. The severity of the flutter is largely dependent upon the magnitude of the tear. Typically, tears greater than 1 to 2 mm will have a higher severity of flutter. Additionally, a tear has the tendency to increase while being handle or when impacted by the beam. This defect in the foil increases the probability of foil flutter, leading to more damage.

The second major mechanical issue is the defect in the box top lid going around the freestanding portion of the diamond (refer to Section 1.4.3). It has been found that foils without a full box top lid tend to be more prone to foil flutter. Since the box top lid gives added support and rigidity to the foil, any little defect will increase the chances that the foils will flutter. Studies on whether a foil needs a full or partial box top lid have also been researched. As depicted previously, a lack of a full box top lid tends to make a foil more prone to fluttering.

The last major mechanical issue is defects in the foil crystalline structure. It is very important that the growth of the diamond grown on the silicon substrate is uniform throughout. If imperfections exist on the silicon substrate prior to growth, these imperfections are exemplified when the diamond film is grown on the substrate. For example, if a piece of dirt or dust is on the silicon substrate, when the diamond film is grown this spot on the substrate can prevent growth and cause a hole in the film when the silicon substrate is etched away. Additionally, if growth of the diamond film on the silicon substrate occurs without holes but without uniform growth across the substrate, this leads to potential weak spots on the foil after the film is grown and the substrate etched away. These weak spots cause the film to tear, rip, or breakoff in areas that are

not of the same quality as the rest of the film. These tears and rips have been shown to be one of the major causes of foil flutter and are typically not used over other foils in SNS, if possible. Although nanocrystalline diamond is preferred over microcrystalline diamond, results within the FTS and SNS were inconclusive.

4.1.1.2 Thermal Effects

The next major issue that decreases stripper foil lifetime is brought on by the thermal conditions of the beam. Chapter 3 has shown that as the diamond foil receives increasing beam intensities, the foil undergoes carbon phase changes. The Raman spectroscopy study, both in the ultraviolet and visible region, indicates that the diamond foil is transforming into a graphite-like material. This causes stress that seems to be relieved by wrinkling of the foil. As the diamond film transform into a graphite-like material, it undergoes a material density change that causes it to expand in a confined space. This is based on the fact that the density of diamond is approximately 3.5 g/cm^3, and the density of graphite is approximately 2.0 g/cm^3. This large change in density causes the material to buckle out from the diamond film and causes ripples in the film from the added stress. The buckling and rippling that occurs causes the location in which the foil is heating to be constantly changing and uneven. This constant

change in foil location has the potential to lead to a forced oscillation of the foil.

4.1.1.3 Electrical Charging

The third major effect that potentially influences foil flutter is electrical charging, which results in discharging of the foil. Since the foils are stripping a H^- ion of its two electrons and allowing the resulting proton to pass through, it has been theorized that the foil is building up an electrical charge from sputtering. As the electrical charge reaches a certain threshold, it might be discharged and this discharging could be a source of foil flutter. The dissipation of charge in the diamond foils is expected to be limited because diamond is a poor electrical conductor, although it is a superior thermal conductor. This theory led to the proposal that the use of boron doped diamond films, boron carbide films, or HBC foils by Sugai, might eliminate foil flutter. Boron doped diamond films were tested and performed very well within SNS and the FTS. The boron doped diamond films were grown by a very similar process to the nanocrystalline diamond films developed by MPECVD at ORNL, with the addition of diborane gas as the boron dopant. While in the FTS, the boron doped diamond films still fluttered. The amount of foil flutter was comparable to that seen in both the nanocrystalline and microcrystalline diamond foils. Taking a closer look at the foils installed, it was found that the boron doped diamond foils

had physical defects including both tears and rips. Therefore, it was concluded that foil flutter was more influenced by both mechanical and thermal effects, as opposed to charging of the foil. Additionally, no relationship was found that indicated the foil was discharging at a particular oscillation frequency. Instead, foil flutter was random and sporadic, where the oscillation was influenced on the overall integrity of the foil.

4.1.1.4 Secondary Electron Issues

The last effect that could influence foil flutter and lifetime are stripped or convoy electrons not captured by the secondary electron collector. It has been established that the secondary electron collector is not sufficiently collecting the electrons stripped from the H^- beam. In principle, these electrons should be guided by several magnets in a conical spiral down to the electron collector, where the electron collector "collects" the electrons and prevents them from escaping to other parts of the system. Unfortunately, it has been shown in periodic photographs of the electron collector that not all electrons are being captured. Instead, the electrons are escaping and returning to the region around the foil and its assembly. These uncaptured electrons have been shown to cause severe damage to the foil assembly at high beam currents. In Figure 4.1, a picture of a titanium bracket used to mount the stripper foil in SNS prior to any

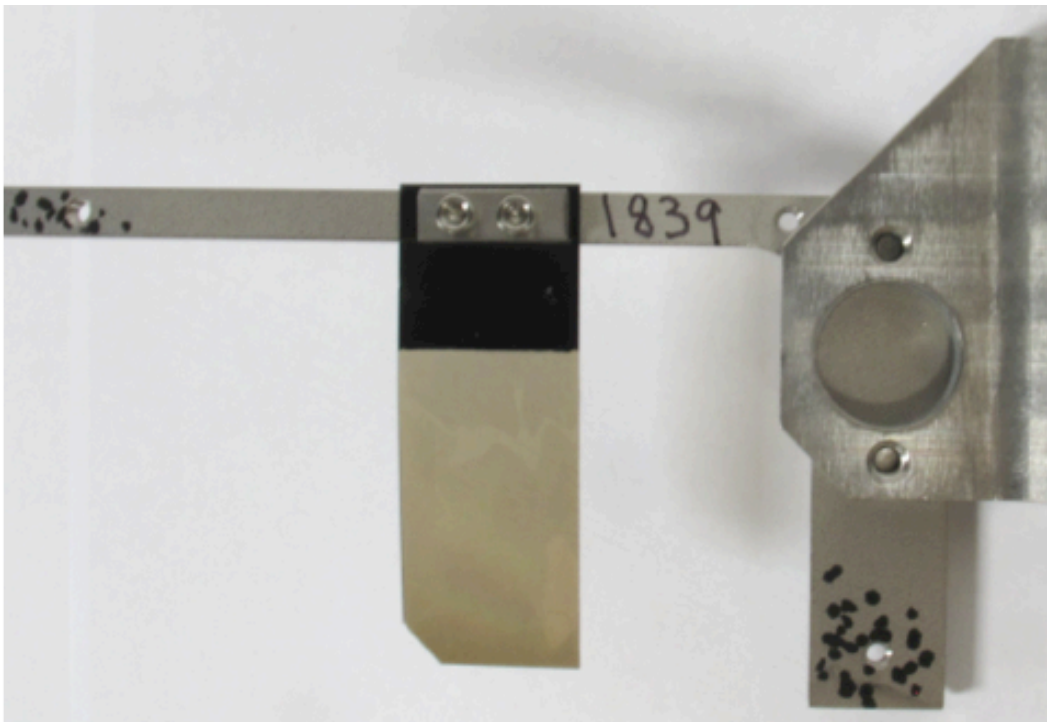

Figure 4.1 - Nanocrystalline diamond foil on titanium bracket prior to being inserted into SNS.

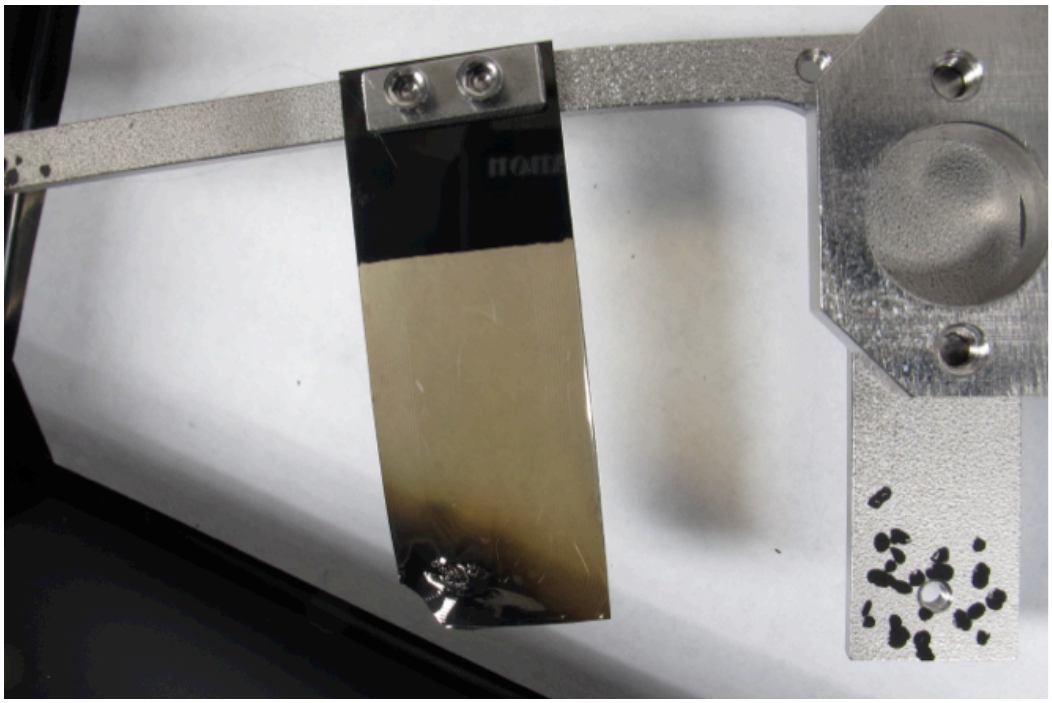

Figure 4.2 - Nanocrystalline diamond foil on titanium bracket after being removed from operation in SNS.

beam exposure is shown. In Figure 4.2, a picture of the foil bracket after being removed from operation in SNS illustrates how the titanium bracket begins to become etched and the foil bracket's arm begins to bend. This indicates that that these uncaptured electrons are causing damage to the foil and only increases as beam exposure and power increase. In retrospect, this damage to the foil bracket may have occurred since the very beginning of SNS. This was recently discovered when SNS increased its beam power and the damage to the foil assembly became more severe. Proposals have been discussed to determine the best method to remedy the issue with the electron collector. Unfortunately, the electron collector is located in an area of very high radiation. One method to decrease the effect seen from the secondary electrons that aren't captured was to change the location of the foil on the bracket assembly. The foil was placed on the backside of the bracket assembly, which allowed for an approximate 5 mm change in the foil position. This change in position showed less foil flutter, but it is not clear whether this is directly related to changes in convoy electron interactions with the foil and its assembly. Therefore, additional data must be accumulated to determine whether or not the foil position within SNS continues to have a substantial effect on flutter.

On the other hand, allowing the foil to interact with any uncaptured

secondary electrons might be beneficial to the overall SNS system. That is, radiation damage from the secondary electrons will continue to occur in the area surrounding the foils until the electrons are captured. Since the discovery was made that the secondary electrons weren't being fully captured, the ability to find a solution to this problem continues to be further complicated by additional radiation contamination. Since the foils are designed for relatively easy intermittent exchange compared to the other surrounding parts, it is of one thought to allow the secondary electrons to interact with the foil as opposed to another area of the chamber. This stance to allow the foils to capture the electrons is sustainable at current power levels in SNS (750 kW to 1.200 MW), but may not uphold as the power levels increase to the current design power (1.400 MW) and higher (2.0 MW). Therefore, further work must be employed in the electron collector's design to increase foil lifetime and performance at planned beam power increases.

4.1.1.5 Flutter comparison

The foil flutter in SNS and the FTS has been shown to be very similar in nature. Monitoring foil flutter within SNS is a difficult task due to the many obstacles discussed in previous sections. These obstacles include the foil being in a very highly activated area, a foil window that darkens with time, and a camera

that requires the use of several mirrors and a telescope to view the foil. The camera can still see foil flutter, but the clarity of the image is lacking. Additionally, the foil flutter is seen in the amount of beam loss, in which the beam loss increases as fluttering increases. Since it was rather difficult to view and monitor the foil flutter, the FTS could be used as an alternative for monitoring and testing conditions that influence flutter. The first thing was to determine if fluttering was a function of the 60 Hz pulsed beam. Therefore, a test was conducted within the FTS using a continuous wave (CW) beam, a 60 Hz pulsed (P) beam, and a pulsed and rastered (P/R) beam. In all three beam settings, fluttering occurred with a similar degree of intensity and at a random frequency. There appeared to be no direct relationship to the frequency of the pulse (i.e., 60 Hz pulse). The next test was to determine if it was a physical feature that influenced foil flutter. Fundamentally, foil flutter is influenced by the structural rigidity of the foil. Rips and tears, lithography pattern, and box top design affect these, and it was therefore a major part of this research to see how these patterns and imperfections influenced flutter. In this series of tests, a pulsed (P) and a pulsed/rastered (P/R) beam were used to determine what physical features influenced foil flutter. The first set of tests looked at physical defects that were caused by post-growth processing and handling. These include both tears and rips in the foil, with a horizontal tear in the diamond foil

increasing the likeliness of the foil fluttering (e.g., acts like a hinge). Once the foil would begin to flutter, it would continue to flutter until either the beam was turned off or the development of a wrinkle in the foil. The development of any wrinkles seemed to relieve stress within the foil when it underwent a transformational change (from diamond to that of graphite-like crystalline structure).

A vertical rip influence on foil flutter depended on the location of the rip. Typically, a rip in either the box-top lid or near the interface of the freestanding diamond and silicon handle would have the most influence on foil flutter. Similar to a horizontal tear discussion earlier, the fluttering of foil would tend to stop once the foil was either removed from the beam or if a wrinkle in the foil developed. The foil wrinkling and its influence on foil flutter may be clearly seen in digital evidence that was recorded by a JVC camera. By video recording the foil while being exposed to the electron beam, the foil can be seen fluttering very rapidly. The fluttering stops once wrinkles in the foil develop. The next couple of issues that have been theorized to be influencing foil flutter is charging of the foil and secondary electrons not be captured by the electron collector. Unfortunately, the FTS is unable to determine how these two issues influence foil flutter. Therefore, the FTS was used to determine how physical features,

lithography patterns, and chemical makeups influence foil flutter. These topics will be discussed in the proceeding sections

4.2 Stripper Foil Design

A major goal of the FTS was to determine how different physical features of foils influenced flutter and lifetime of foils at SNS. Two major design features of the foil have been tested, the lithography patterns and the box-top lid. A discussion of these two features will be discussed in the proceeding sections.

4.2.1 Lithography

A major design parameter that has been is the lithography pattern. Several designs have been implemented over the years; with certain patterns having more success. Some of the patterns that have been implemented were discussed in a preceding section, and include an U-shaped design with either 100 or 50 lines per inch, a checkerboard pattern in the shape of an U, a series of random ellipses covering the entire foil, a concentric ring design covering the entire foil, a series of sinusoidal waves in an U-shaped pattern, and an U-shaped pattern with square corners. In addition, a few of the 100 lines per inch U-shape design have had an increase depth of up to 4 times as deep compared to the

standard U-design. Each pattern has had a varying degree of success, with the U-shaped design, both the 100 and 50 lines per inch, being the most commonly used lithography pattern within SNS and the FTS. This pattern has proven to be very successful, providing the necessary rigidity to the foil to prevent curling of the foil after the silicon substrate is etched away, as well as keeping the foil flat to provide a uniform plane for stripping. A second lithography pattern that was very successful in the FTS was the concentric ring pattern. By having a lithography pattern covering the entire foil, it provided additional support that tended to all but eliminate foil flutter within the FTS. When this lithography pattern was implemented in SNS, it was not as successful. This lack of success in SNS can be because of several factors, and additional foils with this type of pattern should be tested in SNS to better quantify results. A third pattern that was also successful in the FTS was the full-U pattern. The full U-pattern, similar to the concentric ring pattern, provided the entire freestanding diamond portion of the foil with structure and support. This foil has not yet been tested in SNS, but seems very promising with the minimal foil flutter shown in the FTS at higher intensities. A comparison of four different lithography patterns in the FTS is shown in Figure 4.3. It was found that flutter is most severe with a random ellipses lithography pattern (purple line), where the flutter frequency ranged sporadically from approximately 50.0 Hz to 30.0 Hz while the foil was

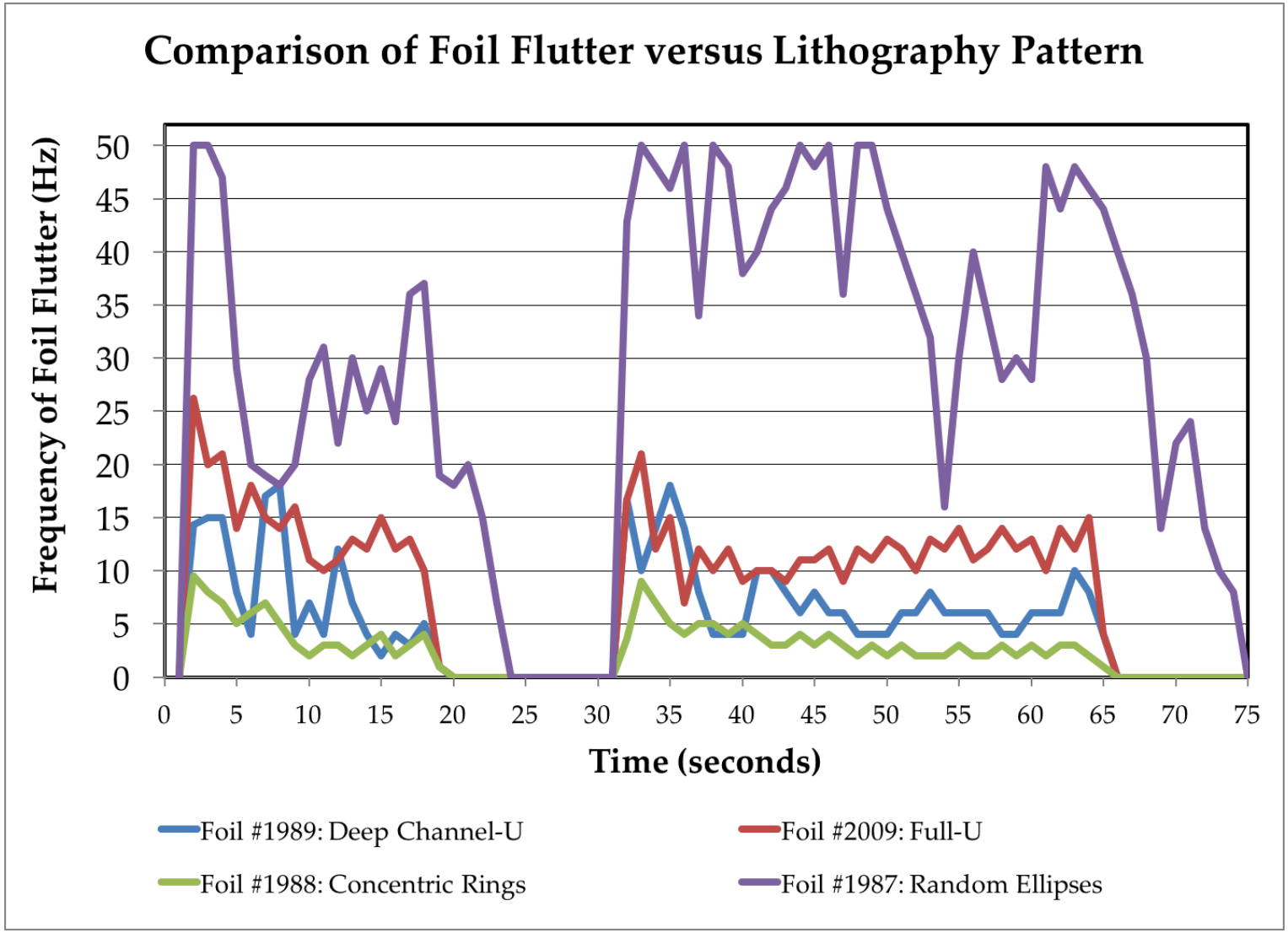

Figure 4.3 - Comparison of Foil Flutter versus Lithography Pattern.

undergoing tests. The fluttering was greatest at the initial start of the tests, and would later slow as the foil increased in temperature and stress in the foil was relieved from the development of wrinkles. Flutter improved greatly for the Full-U lithography pattern, which decreased in frequency to approximately 28.0 Hz – 10.0 Hz as shown in Figure 4.3 (red line). Improvement in foil flutter continued for both the Deep-Channel U (blue line) and Concentric Ring (green line) lithography patterns as shown in Figure 4.3. The Deep-Channel U lithography pattern decreased to 18.0 Hz – 5.0 Hz and the Concentric Ring decreased even further to 10.0 Hz – 2.0 Hz, where both of these lithography patterns had little to no observable fluttering. Additionally, all of these lithography patterns would have a higher initial flutter frequency before settling into a slower flutter frequency for reasons described above (e.g., development of wrinkles that seem to relieve stress in the foil and cause stabilization).

4.2.2 Box-top edge

The second major physical feature that seems to influence foil flutter is the box-top edge (also known as the "box-top lid"). There are a few designs to the box top lid that have been tried in both the FTS and SNS. These designs include: a full box-top lid around all of its edges both with and without the corner cut; a box-top lid around all edges except for where the corner has been cut post

growth; and a box-top lid around all edges except for where the bottom 1 mm of the foil that has been cut off post growth (refer to Figure 1.26 to Figure 1.29). It was found through multiple tests within the FTS that a foil with a full, continuous box-top lid around all of its edges performed much better than foils in which portions of the box-top lid were missing or removed. The box-top lid seems to provide additional support to the freestanding diamond portion, in conjunction with the lithography pattern. In addition, removal of the box-top lid post-growth (either at the corner or the bottom 1 mm), causes hairline fractures in the film. These fractures later become rips or tears when the silicon substrate is etched away. In addition, if a full box-top lid was intended but portions of it has either rips or tears, the foil still flutter similarly to a foil having a partial box-top lid. These results have been seen in SNS as well. Similar to the FTS, foils in SNS tend to flutter if there are any defects or if the box-top lid is non-continuous. Typically, any tear or rip in the box-top lid will act as a hinge point for the foil to flutter. This hinge point idea has been seen and recorded in the FTS, in which the foil tends to flutter below the hinge point and remain steady above it. Initially, it was theorized that the additional 1 μm thick box-top lid would lead to additional beam scattering and beam loss. After testing several foils, it has been found that this additional thickness actually had less effect on beam scattering and beam loss than foil flutter. Therefore, prior to any

loading of the foil, the foil's box-top lid is examined and notes are made of any imperfections. These notes are given to SNS operators, who use the descriptions of each foil to determine what foil to place into operation. This close communication between the operators and the Foil Development Team, has helped with the successful operation of the primary stripper foils at SNS.

4.3 Stripper Foil Chemical Make-up

There have been several types of stripper foils tested in both the FTS and SNS. These foils include: microcrystalline and nanocrystalline foils developed by MPECVD; nanocrystalline foils developed by hot-filament; boron-doped diamond foil developed by MPECVD; and HBC foils developed by CADAD method. The diamond foils developed by MPECVD and hot-filament have performed the best. One major reason for this success is the immense amount of effort and research placed into the development of these films to better fit the needs of SNS. Since their initial conception, several factors of these foils have changed. These changes include: increasing the size of the foil (both the vertical and horizontal direction); alternating the ratio of gases used to grow the films in the MPECVD chamber; optimizing the pre-growth handling of the foils to assure a clean and uniform surface for growth; determining the optimal

temperature and gas ratios; and enhancing the techniques and methods of handling the films post-growth. The large amount of resources placed into improving the diamond foils developed by either MPECVD and hot-filament has led to a very reliable foil, making it become the standard foil used within SNS and the FTS.

The boron-doped diamond foils developed by MPECVD at ORNL had quite the success as well. Development of these foils was ceased due to issues with the MPECVD chamber. The MPECVD chamber issues prevented the consistent growth of polycrystalline diamond films, both microcrystalline and nanocrystalline, from being developed. Since the polycrystalline films are vital to the success of SNS, the development of boron-doped diamond foils was placed on hold until a secondary MPECVD chamber could be obtained.

The HBC foils developed by Sugai had very little success within SNS and the FTS. The HBC foils seem to work quite well at J-PARC and other low intensity accelerator facilities. The HBC foils' growth method is thickness limited, meaning only a certain thickness of HBC foil can be grown. This thickness corresponds to an aerial density of approximately 175 $\mu g/cm^2$. Since SNS requires an aerial density of approximately 350 $\mu g/cm^2$, two HBC foils of

approximately 175 μg/cm^2 were placed back-to-back to meet the necessary thickness requirement for SNS (175 μg/cm^2+ 175 μg/cm^2 = 350 μg/cm^2). These two foils were held together by fibers (to provide support and keep the foils flat) and placed into SNS for production. Following a similar conditioning and beam ramp up protocol, two sets of HBC foils were tried and failed within a matter of hours. In addition to the failure in SNS, the HBC foils were placed into the FTS to see if more information could be gathered about the performance of the HBC foils under SNS conditions. Unfortunately, the tests were inconclusive since the bracket at the time could not accommodate the use of fiber supports. With the lack of fiber supports, the HBC foil flutter intensely when beam was placed onto the foil. Additionally, fluttering continued once the beam was removed from the foil. Since this test was conducted, the FTS has been modified and now allows for the addition of fiber supports. These tests were never repeated due to the two failures of the HBC foils within SNS.

Chapter 5. Discussion and Future Work

Since Earnest Rutherford developed the first accelerator, the field of accelerator physics and the technology associated with accelerators has grown immensely. One key piece that has been used at several accelerators over the years are stripper foils. The initial stripper foils developed were made of thin layers of carbon, and have proven very successful at low intensity beams. The success of these carbon foils at high intensity beams was unknown until the development of more powerful accelerator facilities.

In the late 1990's, the Spallation Neutron Source was being designed to become the world's most intense pulsed neutron beam accelerator facility. Once construction began on the facility, the development and design of new instrumentations and devices followed. One major focus was the development of a stripper foil that would be able to withstand the high intensities of SNS beam.

The Foil Development Team, comprising individuals from Oak Ridge National Laboratory, the Spallation Neutron Source, and the University of Tennessee at Knoxville, was assembled to meet SNS's stripper foil requirements. This group of individuals has a broad range of knowledge and experiences that include: chemical vapor deposition, accelerator physics, and thin films. This diversity

has had a positive influence on the development of stripper foils; leading to foils that are capable of withstanding a 1.4 MW SNS beam. Shaw (ORNL) and Feigerle (UTK) developed the capability of developing polycrystalline diamond films by utilizing plasma enhanced chemical vapor deposition, or more specifically microwave plasma-enhanced chemical vapor deposition (MPECVD). Initial research of polycrystalline films by MPECVD was developing microcrystalline diamond films, followed by development of nanocrystalline diamond films. Nanocrystalline diamond films were found to have greater success under the high intensity of SNS beam.

A typical polycrystalline diamond film is deposited on a corrugated silicon substrate by MPECVD with a dimension of 17 x 45 mm and an aerial density of 350 $\mu g/cm^2$ (corresponding to a thickness of 1 μm). After the growth of the diamond film, a 30 mm section of the silicon substrate is etched away, leaving a 15 mm silicon handle with a 30 mm freestanding diamond foil section. This silicon handle can then be used to provide the necessary support when inserting the foil into SNS. Each foil is typically used for a month of operation before being replaced by another foil. Periodically changing the foil helps ensure that SNS is reliable for all of the researchers that visit from around the world. Since SNS is used by such a wide array of individuals and companies, it is very

difficult and expensive to experiment with different foil properties that influence the lifetime.

Therefore, to better test foil properties, a test stand was designed and developed in 2009 that would allow researchers to characterize various stripper foil properties and help determine their potential performance in SNS. This test stand consists of a 30 keV electron gun, which was chosen because of its ability to replicate the thermal load on the stripper foils and still be a tabletop test stand. The electron gun has a maximum current of 5 mA and a focused beam size of 0.300 mm^2. The electron beam can be rastered simultaneously in the x- and y-directions at a frequency in both directions up to 15,000 Hz. By determining and comparing the stopping power of a 30 keV electron versus a 1 GeV proton, it was found that an electron beam that had a current density of 1.6 mA/mm^2 deposits the same power density on a diamond foil as a 1.4 MW SNS beam. A variety of experiments were conducted using the FTS to determine what influences foil flutter and lifetime. These experiments included researching how corrugation patterns, aerial densities, and foil crystallite size (microcrystalline vs. nanocrystalline) affected the overall expected lifetime of the foil. In addition to lifetime measurements, the FTS was used to measure the temperature and emissivity of the foil at a variety of beam settings. Finally,

experiments were conducted to determine how and under what beam conditions the nanocrystalline diamond converts into graphite.

5.1 Potential Modifications of FTS

Multiple experiments and modifications to the FTS have taken place since it was first conceptualized in 2009. Several of the designs have allowed researchers (SNS, ORNL, and UTK personnel) to test a wider array of foil types, along with determining more about what influences foil lifetime and foil flutter. Although there has been great success with the FTS, there are still areas of research into foils that can be explored with the FTS. One potential modification is to alter the sample holder to allow a foil to be rotated while in the FTS. The ability to rotate the foil has been theorized by some to increase the lifetime of the foil because the location of where the beam is hitting the foil is constantly changing. This constant movement would allow for potentially lower average temperatures on the foil than what is seen in a stationary foil. Another modification is to increase the maximum current output of the electron gun, along with the electron beam's focused spot size. By increasing both of these aspects, it would potentially eliminate the need to raster the beam to meet the necessary spot size requirement. Additionally, it would provide further insight into how the primary stripper foils will perform at future SNS upgrades.

5.2 Potential Upgrades to SNS

Several design modifications of SNS have taken place since it started production in 2006. With such a complex machine, additional modifications and designs have been planned to help the overall success and reliability of SNS. The major modifications that are of importance to the primary stripper foils include: modifying the secondary electron collector and replacing foils with lasers to strip the hydride beam of its electrons.

SNS scientists, Drs. Sarah Cousineau and Yun Li, are currently researching laser stripping. Their proposal will lay the groundwork for the implementation of laser stripping at SNS and other accelerator facilities. There are many obstacles and benefits to laser stripping compared to stripper foils. One of the major benefits is the significant decrease in the amount of radiation hazards that are formed. One of the major obstacles of laser stripping is the lack of technology and reliability of lasers. Since SNS is a user facility, it has very intense and stringent requirements that are difficult for current laser sources to meet. Therefore, additional research is ongoing to bridge this gap.

The second modification to SNS is the design and/or modification of the

secondary electron collector. Recent operation has been shown that the electron collector is not capturing all of the electrons that are being stripped from the foil. The uncaptured electrons, are reflected back up into the foil and its assembly. At low intensities, these uncaptured electrons tend to only influence foil flutter. However, at higher intensities it has led to parts of the titanium stripper foil assembly to melt and become significantly damaged. This damage is of great concern since it increases the likeliness of a foil failure, as well as additional radiation contamination.

5.3 Future Work with Stripper Foils

After several years of research on stripper foils, additional work is still being carried out to determine alternative foil designs and development methods to improve overall foil design. One of the most recent breakthroughs in stripper foil development is the use of nanocrystalline diamond foils developed by hot-filament deposition at BlueWave Semiconductor. The foils developed by BlueWave Semiconductor have shown to be very uniform and have performed very well in SNS. One major benefit to using hot-filament deposition is the relatively cheap cost of the system compared to a PECVD system. This has become an issue in recent months as the growth and fabrication facilities at

ORNL are being transplanted to SNS site. Prior to relocating the PECVD system from ORNL to SNS, it has been decided that a new PECVD system would be designed and purchased that would allow the growth of larger, more uniform foils. An additional benefit to having a second system is it would increase the capability to develop a wider array of foil types and still supply SNS with standard stripper foils.

Other design modifications to the stripper foils include the testing of different lithography patters. The recent success of a lithography patterns that covered the entire film has added additional interest in investigating how the depth of the lithography pattern influences foil rigidity. Other design parameters include looking at previous foil designs that were initially overlooked when first developed. This includes: development and testing of stripper foils with only two freestanding sides as opposed to the common three sides; adjusting the foil dimensions to determine how the overall size of the foil influence foil flutter.

Several of these issues with the stripper foils, SNS, and FTS are either currently under investigation or will be under investigation in the coming months and years. By continuing to experiment with foil properties and determining which aspects of the foil influence performance and lifetime, the development of a foil

that will be able to reliably withstand all of SNS power upgrades to 2.0 MW and 3.0 MW is within reach.

Bibliography

[1] H. Geiger and E. Marsden, "Containing Papers of a Mathematical and Physical Character," *Proceedings of the Royal Society of London. Series A* , vol. 82, no. 557, pp. 495 - 505, 31 July 1909.

[2] "Lawrence and the Cyclotron: AIP History Center Web Exhibit," 2015. [Online]. Available: AIP.org.

[3] A. R. Steere, "A Timeline of Major Particle Accelerators," 2005.

[4] R. J. Van De Graaff, "A 1,500,000 Volt Electrostatic Generator," *Physical Review,* vol. 38, p. 1919, 1931.

[5] A. J. Martins and H. M. Pinto, "Van de Graaff Generators," Braga, Portugal.

[6] R. Wideroe, *Archives fur Elektrot,* vol. 21, p. 387, 1929.

[7] P. M. Lapostolle and A. L. Septier, Linear Accelerators, Amsterdam: North Holland Publishing Company, 1970.

[8] D. W. Dupen, "The Story of Stanford's Two-Mile-Long Accelerator," 1996.

[9] T. Janssens, R. Hofstadter, E. B. Hughes and M. R. Yearian, "Proton Form Factors from Elastic Electron-Proton Scattering," *Physical Review,* vol. 142, no. 4, p. 141, 1966.

[10] R. Hofstadter, "Structure in the Proton and the Neutron," *Second United Nations International Conference on the Peaceful Use of Atomic Energy,* p. 1427, 1958.

[11] "History," 2015.

[12] B. G. Harvey, "Chapter 3 - Spallation," in *Progress in Nuclear Physics*, O. R. Frisch, Ed., Pergamon Press, 1959, pp. 90 - 120.

[13] I. Sugai, Y. Takeda, M. Oyaizu, H. Kawakami, H. Irie, Y. Arakida, K. Hara, H. Hattori, K. Kawasaki, J. Kamiya, M. Kinsho and K. Kuramochi, "Development of Thick Hybrid-Type Carbon Stripper Foils with High Durability at 1800K for RCS of J-PARC," *Nuclear Instruments and Methods in Physics Research A,* vol. 561, no. 1, pp. 16 - 23, 2006.

[14] K. Hasegawa, "Commissioning of the J-PARC LINAC," in *Proceedings of the 2007 Parcticle Accelerator Conference 2007 (PAC07)*, Albuquerque, N.M., 2007.

[15] "Accelerators - Facilities at J-PARC," 2015. [Online]. Available: J-parc.jp.

[16] W. T. Weng, "Accumulator Ring Design for the NSNS Project," in *Proceedings of the 1997 Particle Accelerator Conference 1997 (PAC97)*, Vancouver, B.C., 1997.

[17] J. Wei and et al., "Low-loss Design for the High-Intensity Accumulator Ring of the Spallation Neutron Source," *Physical Review Special Topics - Accelerators and Beams,* vol. 3, pp. 080101-01 - 080101-14, 2000.

[18] "Neutron Review," UT-Batelle, LLC, 2011.

[19] "Neutron Sciences," 2015. [Online]. Available: Neutrons.ornl.gov.

[20] S. J. Shukla, "Ion Source Development for the Spallation Neutron Source," 2003.

[21] M. White, "The Spallation Neutron Source (SNS)," in *Proceedings of the LINAC 2002*, Gyeongju, Korea, 2002.

[22] "In the OSTI Collections: Neutron Sources for Studying Matter," U.S. Department of Energy, Office of Scientific and Technical Information, 2015. [Online]. Available: OSTI.gov.

[23] E. Tanke and et al., "Commissioning Plans for the SNS DTL and CCL," in *Proceedings of the LINAC 2002*, Gyeongju, Korea, 2002.

[24] "Plasma & Ion Source Technology," 2015. [Online]. Available: LBT.LBL.gov.

[25] A. C. Jones and M. L. Hitchman, Chemical Vapour Deposition: Precursors, Process, and Application, Cambridge: Royal Society of Chemistry, 2009.

[26] N. Holtkamp, "The SNS Linac and Storage Ring: Challenges and Progress Towards Meeting Them," in *Proceedings of the 8th European Particle Accelerator Conference (EPAC02)*, Paris, France, 2002.

[27] "Startmap-Timing-Master," 2015. [Online]. Available: ICS-web.SNS.ORNL.gov.

[28] M. Lynch, W. Reass, D. Rees, A. Regan and P. Tallerico, "The Spallation Neutron Source (SNS) Linac RF System," in *Proceedings of the 2000 LINAC Conference*, Monterrey, 2000.

[29] N. R. Holtkamp, "The Spallation Neutron Source," 2005.

[30] "Spallation Neutron Source Target," 2004. [Online]. Available: Thelivingmoon.com.

[31] M. Plum and U. Wienands, "SNS Injection and Extraction Systems - Issues and Solutions," in *Proceedings of Hadron Beam 2008*, Nashville, TN, 2008.

[32] H. C. Hseuh, C. J. Liaw and M. Mapes, "Design of the SNS Accumulator Ring Vacuum Systems," in *Proceedings fo the 1999 Particle Accelerator Conference*, New York, NY, 1999.

[33] W. T. Weng, "SNS Accumulator Ring Design and Space Charge Considerations," in *Workshop on Space Charge Physics in High Intensity Hadron Rings*, 1998.

[34] H. C. Hseuh, "Carbon Wire Heating Due to Scattering in the SNS," in *Proceedings of the 2001 Particle Accelerator Conference (PAC2001)*, Chicago, IL, 2001.

[35] S. Cousineau, J. A. Holmes, M. A. Plum and W. Lu, "Dynamics of Uncaught Foil-Stripped Electrons in the Oak Ridge Spallation Neutron Source Accumulator Ring," *Physical Review Special Topics: Accelerator Beams,* vol. 14, p. 064001, 2011.

[36] "Targeting Mercury: SNS's High Energies Call for a Pioneering Target Source Design," 2015. [Online]. Available: Web.ORNL.gov.

[37] "SNS Instrument Systems - ORNL Neutron Sciences," 2015. [Online]. Available: Neutrons2.ornl.gov.

[38] M. A. Plum, J. A. Holmes, R. W. Shaw and C. S. Feigerle, "SNS Stripper Foil Development Program," *Nuclear Instruments and Methods in Physics Research A,* vol. 590, pp. 43 - 46, 2008.

[39] J. Galambos, "SNS Performance and the Next Generation of High Power Accelerators," in *Proceedings of the 2013 Particle Accelerator Conference (PAC2013)*, Pasadena, CA, 2013.

[40] J. R. Alonso, "The Spallation Neutron Source Project," in *Proceedings of the 1999 Particle Accelerator Conference (PAC99)*, New York, NY, 1999.

[41] "Spallation Neutron Source Features Superconducting Linac," *APS News,* vol. 9, no. 5, 2000.

[42] C. S. Feigerle, "Development of CVD Prepared Boron-Carbide and Boron Carbon Composite Stripper Foils for use in the Spallation Neutron Source," 2010.

[43] B. Schulte, H. Juergensen, P. Blackborow and E. Sevillano, "Flexibility of Microwave Plasma Chemical Vapour Deposition for Diamond Growth," *Surface and Coatings Technology,* Vols. 74 - 75, no. 2, pp. 634 - 636, 1995.

[44] C. J. Liaw, "Lifetime of Carbon Stripping Foils for the Spallation Neutron Source," in *Proceedings of the 2001 Particle Accelerator Conference (PAC2001)*, New York, NY, 2001.

[45] W. L. Wang, M. C. Polo, G. Sanchez, J. Cifre and J. Esteve, "Internal Stress and Strain in Heavily Boron-Doped Diamond Films Grown by Microwave Plasma and Hot Filament Chemical Vapor Deposition," *Journal of Applied Physics,* vol. 80, no. 3, pp. 1846 - 1850, 1996.

[46] C. J. Liaw, "Calculation of the Maximum Temperature on the Carbon Stripping Foil of the Spallation Neutron Source," in *Proceedings of the 1999 Particle Accelerator Conference (PAC99)*, New York, NY, 1999.

[47] R. W. Shaw, M. A. Plum, L. L. Wilson, C. S. Feigerle, M. J. Borden, Y. Irie, I. Sugai and A. Takagi, "Spallation Neutron Source (SNS) Diamond Stripper Foil Development," in *Proceedings of the 22nd Particle Accelerator Conference (PAC07)*, Albuquerque, NM, 2007.

[48] D. Zhou, T. G. McCauley, L. C. Qin, A. R. Krauss and D. M. Gruen, "Synthesis of Nanocrystalline Diamond Thin Films from an Ar-CH4 Microwave Plasma," *Journal of Applied Physics,* vol. 84, no. 1, pp. 540 - 543, 1998.

[49] K. E. Spear, "Diamond - Ceramic Coating of the Future," *Journal of American Ceramic Society,* vol. 72, no. 2, pp. 171 - 191, 1989.

[50] Y. C. Choi, Y. M. Shin, Y. H. Lee and B. S. Lee, "Controlling the Diameter, Growth Rate, and Density of Vertically Aligned Carbon Nanotubes Synthesized by Microwave Plasma-Enhanced Chemical Vapor Deposition," *Applied Physics Letters,* vol. 76, no. 17, p. 2367, 2000.

[51] P. W. May and Y. A. Mankelevich, "From Ultrananocrystalline Diamond to Single Crystal Diamond Growth in Hot Filament and Microwave Plasma-Enhanced CVD Reactors: a Unified Model for Growth Rates and Grain Sizes," *Journal of Physical Chemistry C,* vol. 112, no. 32, pp. 12432 - 12441, 2008.

[52] R. W. Shaw, A. D. Herr, C. S. Feigerle, M. E. Peretich and C. J. Liaw, "Thin Diamond Films for SNS H- Injection Stripping," in *Proceedings of 2003 Particle Accelerator Conference (PAC03)*, Portland, OR, 2003.

[53] R. W. Shaw, V. A. Davis, N. Potter, L. L. Wilson, C. S. Feigerle, M. E. Peretich and C. J. Liaw, "Corrugated Thin Diamond Foils for SNS H- Injection Stripping," in *Proceedings of 2005 Particle Accelerator Conference (PAC05)*, Knoxville, TN, 2005.

[54] L. H. Robins, L. P. Cook, E. N. Farabaugh and A. Feldman, "Cathodoluminescence of Defects in Diamond Films and Particles Grown by Hot-Filament Chemical-Vapor Deposition," *Physical Review B,* vol. 39, no. 18, pp. 13367 - 13377, 1989.

[55] Y. Liou, A. Inspektor, R. Weimer, D. Knight and R. Messier, "The Effect of Oxygen in Diamond Deposition by Microwave Plasma Enhanced Chemical Vapor Deposition," *Journal of Materials Research,* vol. 5, no. 11, pp. 2305 - 2312, 1990.

[56] Y. Liou, A. Inspektor, R. Weimer, D. Knight and R. Messier, "Low-Temperature Diamond Deposition by Microwave Plasma-Enhanced Chemical Vapor Deposition," *Applied Physic Letters,* vol. 55, no. 7, p. 631, 1989.

[57] S. Jiao, A. Sumant, M. A. Kirk, D. M. Gruen, A. R. Krauss and O. Auciello, "Microstructure of Ultrananocrystalline Diamond Films Grown by Microwave Ar-CH Plasma Chemical Vapor Deposition with or without Added H2," *Journal of Applied Physics,* vol. 90, no. 1, pp. 118 - 122, 2001.

[58] J. Lee, B. Hong, R. Messier and R. W. Collins, "Nucleation and Bulk Film Growth Kinetics of Nanocrystalline Diamond Prepared by Microwave Plasma-Enhanced Chemical Vapor Deposition on Silicon Substrates," *Applied Physics Letters,* vol. 69, no. 12, p. 1716, 1996.

[59] T.-S. Yang, J.-Y. Lai and M.-S. Wong, "Substrate Bias Effect on the Formation of Nanocrystalline Diamond Films by Microwave Plasma-Enhanced Chemical Vapor Deposition," *Journal of Applied Physics,* vol. 92, no. 4, pp. 2133 - 2138, 2002.

[60] B. R. Stoner and J. T. Glass, "Textured Diamond Growth on (100) Beta-SiC via Microwave Plasma Chemical Vapor Deposition," *Applied Physics Letters,* vol. 60, no. 6, pp. 698 - 700, 1991.

[61] S. Matsumoto, Y. Sato, M. Kamo and N. Setaka, "Vapor Deposition of Diamond Particles from Methane," *Japanese Journal of Applied Physics,* vol. 21, no. 4, pp. 183 - 185, 1982.

[62] S. K. Zeisler and V. Jaggi, "Production of Stripper Foils by Laser Ablation of Carbon-Boron Sputter Targets," *Nuclear Instruments and Methods in Physics Research A,* vol. 613, no. 3, pp. 434 - 435, 2010.

[63] T. Spikermann, M. J. Borden, R. J. Macek, R. W. Shaw, C. S. Feigerle and I. Sugai, "Comparison of Carbon and Corrugated Diamond Stripper Foil Under Operational Conditions at the Los Alamos PSR," *Nuclear Instruments and Methods in Physics Research A,* vol. 590, no. 1, pp. 25 - 31, 2008.

[64] T. Spikermann, T. Borden, M. J. Macek, R. J. Shaw, C. S. Feigerle and I. Sugia, "Comparison of Carbon Stripper Foil Under Operational Conditions at the Los Alamos PSR," 2008.

[65] C. S. Jolivet, S. A. Miller, P. Ladd and J. O. J. Stoner, "Carbon Stripper Foil Held in Place with Carbon Fibers," *Nuclear Instruments and Methods in Physics Research A,* vol. 590, no. 1, pp. 47 - 50, 2008.

[66] "Carbon Nanotubes and Other Carbon Materials Part 1 (Nanotechnology)," 2015. [Online]. Available: what-when-how.com.

[67] S. K. Zeisler and V. Jaggi, "Multilayer Carbon Foils for Cyclotron Beam Extraction," *Nuclear Instruments and Methods in Physics Research,* vol. 590, no. 1, pp. 18 - 21, 2008.

[68] P. G. Bricault, M. Dombsky, P. W. Schmor and G. Stanford, "Radioactive Ion Beams Facility at TRIUMF," *Nuclear Instruments and Methods in Physics Research B,* vol. 126, no. 3, pp. 231 - 235, 1997.

[69] "Nanodiamond Foil for SNS," 2015. [Online]. Available: Bluewavesemi.com.

[70] C. S. Feigerle, P. M. Menon, A. Edwards, R. W. Shaw, D. W. Coffey, L. Heatherly, R. E. Clausing, L. Robinson and D. C. Glasgow, "Filament Metal Contamination and Raman Spectra of Hot Filament Chemical Vapor Deposited Diamond Films," *Diamond and Related Materials,* vol. 8, pp. 101-109, 1999.

[71] M. Yoshimoto, P. K. Saha, Y. Yamazaki, M. Kawase, R. Saeki, N. Hayashi, K. Yamamoto, H. Hotchi, T. Ishiyama, M. Kinsho, I. Sugai and Y. Irie, "HBC Foil Beam Study and Long-term Observation at the 3-GeV RCS in J-PARC," in *15th International Conference on Thin Films (ICTF-15)*, 2013.

[72] Y. Yamazaki, M. Yoshimoto, O. Takeda, M. Kinsho, T. Taguchi, S. Yamamoto, T. Kurihara and I. Sugai, "Analysis of Hybrid Type Boron-Doped Carbon Stripper Foils in J-PARC RCS," in *15th International Conference on Thin Films (ICTF-15)*, 2013.

[73] Y. Yamazaki, M. Yoshimoto, O. Takeda, O. Kinsho and I. Sugai, "First Step Analysis of Hybrid Type Boron-Doped Carbon Stripper Foils for RCS of J-PARC," in *Proceedings of International Particle Accelerator Conference 2010 (IPAC'10)*, Kyoto, Japan, 2010.

[74] I. Sugai, Y. Takeda, M. Oyaizu, H. Kawakami, Y. Irie, A. Takagi, H. Hattori and K. Kawasaki, "Double-Layer Effects on the Lifetime of Newly Developed HBC-Foils for RCS of J-PARC," *Nuclear Instruments and Methods in Physics Research A,* vol. 613, no. 1, pp. 457 - 461, 2010.

[75] I. Sugai, Y. Takeda, M. Oyaizu, H. Kawakami, Y. Irie, A. Takagi, H. Hattori and K. Kawasaki, "Lifetime Comparison of Double and Single Layered HBC-Foils using 3.2 MeV Ne+ Ion," in *Proceedings of the 2008 European Particle Accelerator Conference (EPAC08)*, Genoa, Italy, 2008.

[76] Y. Takeda and I. Sugai, "Lifetime Measurements of HBC Stripper Foil Using 3.2 MeV Ne+ for RCS of J-PARC," in *Proceedings of 2010 International Particle Accelerator Conference (IPAC'10)*, Kyoto, Japan, 2010.

[77] I. Sugai, "Present Status of HBC Stripper Foil Development".

[78] R. W. Shaw, D. P. Bontrager, L. L. Wilson, C. S. Feigerle, C. F. Luck and M. A. Plum, "An Electron Beam SNS Foil Test Stand," in *Proceedings of 2009 Particle Accelerator Conference (PAC09)*, Vancouver, B.C., 2009.

[79] E. P. Barrowclough, C. S. Feigerle, C. F. Luck, L. L. Wilson, R. W. Shaw and M. A. Plum, "Analysis of Primary Stripper Foils at SNS by an Electron Beam Foil Test Stand," in *Proceedings of 2015 International Particle Accelerator Conference (IPAC2015)*, Richmond, VA, 2015.

[80] J. Galambos, "Progress with MW-Class Operation of the Spallation Neutron Source," in *Proceedings of 2009 Particle Accelerator Conference (PAC09)*, Vancouver, BC, 2009.

[81] "EMG-4215/EGPS-4215: Electron Gun and Power Supply System," 2008.

[82] O. W. Richardson, The Emission of Electricity from Hot Bodies, Second Edition ed., London: Longmans, Greem and Co., 1921.

[83] S. Dushman, "Electron Emission from Metals as a Function of Temperature," *Physical Review,* vol. 21, no. 6, pp. 623 - 636, 1923.

[84] O. W. Richardson, "Electron Emission from Metals as a Function of Temperature," *Physical Review,* vol. 23, no. 2, pp. 153 - 155, 1924.

[85] W. H. Aberth, R. Schnitzer and F. C. Engesser, "Construction of an Einzel Lens Capable of High Voltage Operation," *Review of Scientific Instruments,* vol. 45, no. 10, pp. 1289 - 1290, 1974.

[86] J. K. Fremerey, "Residual Gas: Traditional Understanding and New Experimental Results," *Vacuum,* vol. 53, no. 2, pp. 197 - 201, 1999.

[87] W. D. Swank, J. R. Fincke and D. C. Haggard, "Modular Enthalpy Probe and Gas Analyzer for Thermal Plasma Measurements," *Review of Scientific Instruments,* vol. 64, no. 1, pp. 56 - 62, 1993.

[88] "Residual Gas Analyzers," *Synchrotron Radiation News,* vol. 5, no. 5, p. 30, 1992.

[89] J. F. O'Hanlon, A User's Guide to Vacuum Technology, New York, NY: Wiley, 2004.

[90] "FLIR(R) Silver SC5000 MWIR Infrared Cameras for Research and Development," 2015. [Online]. Available: FLIR.com.

[91] "NIST Stopping-Power and Range Tables: Electrons, Protons, Helium Ions," 2015. [Online]. Available: NIST.gov.

[92] C. J. Liaw, Y. Y. Lee and J. Tuozzolo, "Lifetime of Carbon Stripping Foils for the Spallation Neutron Source," in *Proceedings of the 2001 Particle Accelerator Conference (PAC01)*, Chicago, IL, 2001.

[93] Y. Takeda and M. A. Plum, "SNS Foil Heating Report," March 14, 2013.

[94] "Emissivity Table," 2015. [Online]. Available: ThermoWorks.com.

[95] S. Edalatpour and M. Francoeur, "Size Effect on the Emissivity of Thin Films," *Journal of Quantitative Spectroscopy & Radiative Transfer,* vol. 118, pp. 75 - 85, 2013.

[96] R. Raman and A. Thakur, "Emissivity of Homogeneous Thin Films," *Thin Solid Films,* vol. 87, no. 2, pp. 101 - 111, 1982.

[97] "M305 - Light Weight Blackbody - Manual," LumaSense Technology, 2014.

[98] "FLIR SC7000 Series," 2015. [Online]. Available: www.flirmedia.com.

[99] D. C. Harris, "Properties of Diamond for Windows and Domes Applications," in *SPIE Conference Proceedings*, 1994.

[100] D. C. Harris, "Development of Chemical-Vapor-Deposited Diamond for Infrared Optical Applications. Status Report and Summary of Properties," July 1994.

[101] M. G. Krishna, R. G. Biswas and A. K. Bhattacharya, "On the Effects of Optical Constants and Physical Parameters on the Emittance of Thin-Film Selective Emitters for Thermophotovoltaic Applications," *Journal of Physics D: Applied Physics,* vol. 30, pp. 1167 - 1174, 1997.

[102] I. S. Habib, "The Effects of Radiation, Inclination, and Insulation Opacity on the Critical Radius for Radial Heat Transfer," *International Journal of Heat and Mass Transfer,* vol. 25, no. 10, pp. 1607 - 1609, 1982.

[103] R. Gardon, "The Emissivity of Transparent Materials," *Journal of the American Ceramic Society,* vol. 39, no. 8, pp. 278 - 287, 1956.

[104] G. Wu and D. Yu, "Preparation and Characterization of a New Low Infrared-Emissivity Coating Based on Modified Aluminum," *Progress in Organic Coatings,* vol. 76, no. 1, pp. 107 - 112, 2013.

[105] H. A. Hobbs and R. C. Folweiler, "Thermal Radiation Characteristics of Transparent, Semi-Transparent, and Translucent Materials Under Non-Isothermal Conditions," 1966.

[106] D. S. Knight and W. B. White, "Characterization of Diamond Films by Raman Spectroscopy," *Journal of Materials Research,* vol. 4, no. 2, pp. 385 - 393, 1989.

[107] S. Prawer and R. J. Nemanich, "Raman Spectroscopy of Diamond and Doped Diamond," *Philosophical Transactions of the Royal Society A,* vol. 362, no. 1,824, pp. 2,537 - 2,565, 2004.

[108] R. A. Khmelnitsky and A. A. Gippius, "Transformation of Diamond to Graphite Under Heat Transformation at Low Pressures," *Phase Transitions,* vol. 87, no. 2, pp. 175 - 192, 2014.

[109] A. C. Ferrari and J. Robertson, "Interpretation of Raman Spectra of Disordered and Amorphous Carbon," *Physical Review B,* vol. 61, no. 20, pp. 14,095 - 14,107, 2000.

[110] A. C. Ferrari and J. Robertson, "Origin of the 1150-cm-1 Raman Mode in Nanocrystalline Diamond," *Physical Review B,* vol. 63, no. 12, pp. 121405-1 - 121405-4, 2000.

[111] M. Rybachuk and J. M. Bell, "Electronic States of Trans-Polyacetylene, Poly(p-phenylene vinylene), and sp-Hybridised Carbon Species in Amorphous Hydrogenated Carbon Probed by Resonant Raman Scattering," *Carbon,* vol. 47, no. 10, pp. 2,481 - 2,490, 2009.

[112] J. Schwan, S. Ulrich, V. Batori, H. Ehrhardt and S. R. P. Silva, "Raman Spectroscopy on Amorphous Carbon Films," *Journal of Applied Physics,* vol. 80, no. 1, pp. 440 - 447, 1996.

[113] Z. Sun, J. R. Shi, B. K. Tay and S. P. Lau, "UV Raman Characteristics of Nanocrystalline Diamond Films with Different Grain Size," *Diamond and Related Materials,* vol. 9, no. 12, pp. 1,979 - 1,983, 2000.

[114] R. Pfeiffer, H. Kuzmany, P. Knoll, S. Bokova, N. Salk and B. Gunther, "Evidence for Trans-Polyacetylene in Nano-Crystalline Diamond Films," *Diamond and Related Materials,* vol. 12, no. 3, pp. 268 - 271, 2003.

[115] S. R. Sails, D. J. Gardiner, M. Bowden, J. Savage and D. Rodway, "Monitoring the Quality of Diamond Films using Raman Spectra Excited at 514.5 nm and 633 nm," *Diamond and Related Materials,* vol. 5, no. 6, pp. 589 - 591, 1996.

[116] K. W. R. Gilkes, S. Prawer, K. W. Nugent, J. Robertson, H. S. Sands, Y. Lifshitz and X. Shi, "Direct Quantitative Detection of the sp3 Bonding in Diamond-Like Carbon Films using Ultraviolet and Visible Raman Spectroscopy," *Journal of Applied Physics,* vol. 87, no. 10, pp. 7,283 - 7,289, 2000.

[117] K. W. R. Gilkes, H. S. Sands, D. N. Batchelder, J. Robertson and W. I. Milne, "Direct Observation of sp3 Bonding in Tetrahedral Amorphous

Carbon using Ultraviolet Raman Spectroscopy," *Applied Physics Letters,* vol. 70, no. 15, pp. 1,980 - 1,982, 1997.

[118] E. Anastassakis, S. Iwasa and E. Burstein, "Electric-Field-Induced Infrared Absorption in Diamond," *Physcial Review Letters,* vol. 17, no. 20, pp. 1,051 - 1,054, 1966.

[119] E. Anastassakis and E. Burstein, "Electric-Field-Induced Absorption and Raman Scattering in Diamond," *Physical Review B,* vol. 2, no. 6, pp. 1,952 - 1,965, 1970.

[120] A. A. Maradudin and E. Burstein, "Relation between Photoelasticity, Electrostriction, and First-Order Raman Effect in Crystals of the Diamond Structure," *Physical Review,* vol. 164, no. 3, pp. 1,081 - 1,099, 1967.

[121] A. K. McQuillan, W. R. L. Clemenets and B. P. Stoicheff, "Stimulated Raman Emission in Diamond - Spectrum, Gain, and Angular Distributionof Intensity," *Physical Review A,* vol. 1, no. 2, pp. 628 - 635, 1970.

[122] A. C. Ferrari, "Raman Spectroscopy of Graphene and Graphite/ Disorder, Electron–Phonon Coupling, Doping and Nonadiabatic Effects," *Solid State Communications,* vol. 143, no. 1, pp. 47 - 57, 2007.

[123] A. C. Ferrari and J. Robertson, "Raman Spectroscopy of Amorphous, Nanostructured, Diamond-Like Carbon, and Nanodiamond," *Philosophical Transactions of the Royal Society of London A,* vol. 362, no. 1,824, pp. 2,477 - 2,512, 2004.

[124] A. C. Ferrari and J. Robertson, "Resonant Raman Spectroscopy of Disordered, Amorphous, and Diamondlike Carbon," *Physical Review B,* vol. 64, no. 7, p. 075414, 2001.

[125] M. Profeta and F. Mauri, "Theory of Resonant Raman Scattering of Tetrahedral Amorphous Carbon," *Physical Review B,* vol. 63, no. 24, p. 245415, 2001.

[126] S. A. Asher, R. W. Bormett, X. G. Chen, D. H. Lemmon, N. Cho, P. Peterson, M. Arrigoni, L. Spinelli and J. Cannon, "UV Resonance Raman Spectroscopy Using a New CW Laser Source - Convenience and Experimental Simplicity," *Applied Spectroscopy,* vol. 47, no. 5, pp. 628 - 633, 1993.

[127] R. W. Bormett, S. A. Asher, R. E. Witowski, W. D. Partlow, R. Lizewski and F. Pettit, "Ultraviolet Raman Spectroscopy Characterizes Chemical Vapor Deposition Diamond Film Growth and Oxidation," *Journal of Applied Physics,* vol. 77, no. 11, pp. 5,916 - 5,923, 1995.

[128] R. Loudon, "The Raman Effect in Crystals," *Advances in Physics,* vol. 50, no. 7, pp. 813 - 864, 2001.

[129] N. R. Holtkamp, "Status of the SNS LINAC: An Overview," in *Proceedings of LINAC 2004*, Lubeck, Germany, 2004.

[130] T. C. Chieu and M. S. Dresselhaus, "Raman Studies of Benzene-Derived Graphite Fibers," *Physical Review B,* vol. 26, no. 10, pp. 5867 - 5877, 1982.

[131] J. Beebe-Wang, "Injection Carbon Stripping Foil Issues in the SNS Accumulator Ring," in *Proceedings of the 2001 Particle Accelerator Conference (PAC2001)*, New York, NY, 2001.

[132] "Lifetime Measurements of HBC Stripper Foil Using 3.2 MeV Ne+ for RC of J-PARC," in *Proceedings of 2010 International Particle Accelerator Conference (IPAC'10)*, Kyoto, Japan, 2010.

[133] "Development of Chemical-Vapor-Deposited Diamond for Infrared Optical Applications. Status Report and Summary of Properties," China Lake, CA, July 1994.

Vita

Eric Barrowclough was born in Johnson City, TN, to the parents of John and Ann Barrowclough. He is the fifth of six children: Matthew, Michael, Lauren, David, and Megan. He attended Science Hill High School in Johnson City, TN. While at Science Hill, he discovered his passion for chemistry. After graduation, he attended Auburn University in Auburn, AL. While at Auburn University, he performed research under Drs. Christian Goldsmith and Jimmy Mills. Additionally, he had the opportunity to attend a summer research program at Clemson University under Dr. Bill Pennington. During his tenure at Auburn University, he enjoyed many Saturdays full of football and friendship. He completed his Bachelor of Science in Chemistry in December 2009. Following graduation from Auburn University, he continued his passion and attended the University of Tennessee in Knoxville, TN. While at the University of Tennessee, he had the opportunity to perform research under Dr. Charles Feigerle at the University of Tennessee, Dr. Bob Shaw at Oak Ridge National Laboratory (ORNL), and Dr. Mike Plum at the Spallation Neutron Source (SNS). While working at ORNL and SNS, he had several mentors that helped shape his chemistry career. Some of these mentors include: Dr. Charles Feigerle of UTK, who educated me on the inner workings of a vacuum chamber and the analysis

of thin films; Chris Luck of SNS, who provided detailed insight into stripper foils, the Foil Test Stand, countless life advice, and a valued friendship; Dr. Mike Plum of SNS, who always offered great insight into the workings of the complexity of SNS; Dr. Bob Shaw and Leslie Wilson of ORNL, who provided one-on-one mentoring in the development of diamond films; Dr. Sarah Cousineau, who provided general guidance and an endless supply of expressos for a tired graduate student; as well as countless other colleagues and mentors at UTK, ORNL, and SNS.